FACULTY OF ENGINEERING
AND ARCHITECTURE

Novel Finite-Difference Time-Domain Techniques for Combined Electromagnetic and Quantum Mechanical Simulations

Pieter Decleer

Doctoral dissertation submitted to obtain the academic degree of
Doctor of Engineering Physics

Supervisors

Prof. Dries Vande Ginste, PhD* - Arne Van Londersele, PhD**

* Department of Information Technology
Faculty of Engineering and Architecture, Ghent University

** Trension

November 2022

GHENT
UNIVERSITY

ISBN 978-94-6355-639-2
NUR 928
Wettelijk depot: D/2022/10.500/80

Members of the Examination Board

Chair

Prof. Filip De Turck, PhD, Ghent University

Other members entitled to vote

Prof. Peter Bienstman, PhD, Ghent University
Prof. Dick Botteldooren, PhD, Ghent University
Prof. Vitaliy Lomakin, PhD, University of California San Diego, USA
Prof. Fernando Teixeira, PhD, The Ohio State University, USA

Supervisors

Prof. Dries Vande Ginste, PhD, Ghent University
Arne Van Londersele, PhD, Trensition

DANKWOORD

De afgelopen vier jaar kreeg ik vaak de vraag: “Wat doe jij nu eigenlijk?” En na vier jaar doctoreren, weet ik het zelf ook nog niet. Wel weet ik dat een doctoraat voor iedereen een heel andere ervaring is, maar steeds gepaard is met ups and downs. Ikzelf heb de vrijheid gekregen om er van te maken wat ik wil. Voor een klein deel begeleidde ik studenten bij projecten of bij hun masterthesissen, maar het grootste deel van mijn tijd zat ik gekluisterd voor mijn computerscherm code te schrijven of op papier een idee uit te werken. Het resultaat van al dit labeur is een handvol papers in wetenschappelijke tijdschriften en, uiteraard, dit boek. Ik hoop hierbij dat mijn werk een grote impact zal hebben en zal dienen ter inspiratie van veel toekomstig onderzoek. Hoewel de inhoud van dit werk nogal wiskundig is, hoop ik ook dat jij, als lezer, verder dan dit dankwoord zal raken want een goed idee kan overal ontstaan.

Naast het puur wetenschappelijk werk ben ik ook veel gegroeid door deze ervaring. Daarvoor wil ik eerst en vooral mijn promotoren bedanken: Dries en Arne. Al tijdens mijn master thesis stonden jullie paraat met sterk advies terwijl ik de vrijheid kreeg om uitdagende onderzoeksproblemen aan te pakken. Ook tijdens mijn vier jaar als doctoraatsstudent was dit het geval, maar ik heb ook de kans gekregen om jullie als persoon beter te leren kennen. Dries, ik vond het een hele eer om aanwezig te zijn bij het ontstaan van de onderzoeksgroep quest. en zal immer onze uitstap naar Odessa blijven herinneren. Arne, jouw doorgedreven drang naar resultaten, efficiëntie en praktische mindset zijn voor mij een bron van inspiratie. Ondanks de periodieke chaos en bijzondere hersenkronkels, verwacht ik steevast grootse dingen van u. Hiernaast, wil ik ook nog Hendrik bedanken. Tijdens mijn master thesis en de vroege jaren van mijn doctoraat hebben jouw inzichten mijn onderzoek tot een hoger niveau getild. *Furthermore, I would like to thank the jury for the constructive and interesting discussions during the internal defense and also for thoroughly reading the dissertation.*

Mijn periode als doctoraatsstudent zou heel wat minder aangenaam geweest zijn zonder de goede sfeer op kantoor met de collega’s. Dit heb ik in de eerste plaats te danken aan de oude garde. Dries, we zijn samen gestart en altijd tijdens deze tocht stond je klaar om te helpen bij ieders technische en minder technische problemen. Jouw gedetailleerde werkethiek legt de lat voor ons allemaal wat hoger. Duygu, ik heb vaak genoten van de goedlachsheid die je binnenbracht. Ik wens jou nog heel veel succes met jouw doctoraat af te ronden, de laatste loodjes wegen het zwaarst! Gert-Jan, ik heb altijd genoten van uw zelfrelativerend vermogen waardoor de sfeer in het bureau altijd wel wat beter was. Ook enkele long-running

pranks hoorden daar bij. Martijn, in sterk contrast met mijn thesisbegeleiders was jij degene die mij tijdens mijn eerste dagen begeleidde door de administratieve krochten van de UGent. Ook later was je altijd bereid om jouw postdoctorale wijsheden te delen. Daarnaast heb ik ook vaak genoten van onze discussies over boeken, Japans, D&D en zo veel meer. ありがとうございます。Michiel, jouw passie voor boardgames heeft er voor gezorgd dat ik mij onmiddellijk thuis voelde bij de collega's. De goedgeplaatste steken die we wel eens durfden uitwisselen, zijn sinds uw vertrek jammer genoeg tot een historisch laagtepunt gedaald. Simon, hoewel ik meermaals gewaarschuwd was voor jouw dictatoriaal bewind als bureauchef, zorgde jouw aanwezigheid in het bureau regelmatig voor een welkome afleiding. Daarnaast heb ik ook veelvuldig gebruikgemaakt van jouw extensieve Linux- en programmeerkennis, waarvoor dank. Thomas, jouw muzikale creativiteit en avontuurlijke spirit zorgen nog steeds voor een frisse wind door ons kantoor. Elke keer dat je op jouw longboard sprong of het dak beklom, was ik toch een beetje jaloers, met de gedachte: "Dat is nu eens onderzoek." Ook de nieuwere garde moet ik bedanken. Alessandro, ondanks je Italiaanse roots begin je toch een Vlaming te worden. Laten we ooit nog eens een Klokke Roeland gaan drinken. Arno, merci dat je altijd bereid was om een trage namiddag wat leuker te maken. Zo heb je de taak als bureauchef ten volle volbracht. Onze latere addities, Emile, Joryan, Jul & Maxim, waarvan sommigen hier toch ook al twee jaar doorbrengen, heb ik minder goed leren kennen dan ik wou. Maar ook jullie aanwezigheid zorgde voor de nodige dynamiek die nodig is in een goed draaiende onderzoeksomgeving. In het bijzonder wil ik de *Guitar Boys* al het beste toewensen: Geef niet op, de mentale dieptepunten zijn een essentieel onderdeel van een doctoraat. Bedankt dat jullie het kwantumgerelateerde onderzoek willen voortzetten. Ik heb enkel hoge verwachtingen!

In het andere bureau waren er ook heel wat mensen die hebben bijgedragen tot het slagen van dit doctoraat. Ze stonden allemaal klaar om straffe verhalen – al dan niet over thesisstudenten – te delen, mij tegen wil en dank iets bij te brengen over antennes, of om andere interessante gesprekken te voeren. Hiervoor mijn dank en hopelijk tot binnenkort: Bram, Dries V. B., Igor, Jelle, Kamil, Laura, Nick, Nicolas, Olivier, Quinten, Samuel, Seppe, Thomas D. en Victor.

Ook buiten de iGent toren zijn er heel wat mensen die dit werk mogelijk hebben gemaakt. Eerst en vooral mijn voormalige huisgenoten: de Potters. Meer dan twee jaar lang hebben we samen doorgebracht: samen gewerkt, gekookt, films gekeken, gefeest enz. Het was niet altijd makkelijk om zo dicht op elkaar te leven, maar we hebben ons er altijd wel doorgeslagen en ik zou onze tijd samen voor niets willen ruilen. Anke, merci om altijd vol enthousiasme over uw dag te vertellen. Ewoud, we zijn al zo lang vrienden en ik zie dit niet snel veranderen. Merci om er altijd te zijn, mijn deur staat altijd open. Ons avontuur in Indonesië zal ik blijven koesteren en ooit doen we wel eens plan A. Robbe, merci om de trap te doen daveren, uw oprechte lach en de straffe oneliners. Sara, merci voor uw gemeende

interesse en de rougekes. Sander, merci voor altijd voluit uzelf te zijn. Verder wil ik ook nog iedereen bedanken die mijn tijd na de werkuren verlicht heeft. De ontspanning was zeer welgekomen, de toffe gesprekken (al dan niet op café), de boardgames, de D&D sessies, de gamenights, de frietjes, de badminton, de padel, de (snowboard)reisjes, de trektochten...

Ten slotte wil ik ook nog mijn familie bedanken, zonder jullie was ik hier niet geraakt. Mama en papa, bedankt voor jullie steun en advies doorheen de jaren. De warme thuis heeft mij door mijn studie geholpen en nu ook door mijn doctoraat. Merci voor het vele nalezen en om te luisteren naar mijn exposities over mijn onderwerp. Marlies, je hebt me vaak gepusht maar je weet ook dat ik soms wel eens een duwtje in de rug kan gebruiken. Kristof, het is altijd toffer met u er bij en met jouw no-nonsense attitude gaat alles ook net een tikkeltje makkelijker. Jérôme, ook jij bedankt voor de toffe momenten en om de vragen te stellen over mijn doctoraat die niemand anders stelt. Ook de jongste telg kan hier niet ontbreken. César, zelfs al ben je er nog maar net bij, toch heb je al een sterke indruk achter gelaten. Ik ben benieuwd naar wat de toekomst in petto heeft!

Gent, oktober 2022
Pieter Decleer

"You gotta do the hop then move to the beat, you don't stop."

— A Tribe Called Quest

CONTENTS

SAMENVATTING

Met modelleringstools kunnen we steeds complexere systemen bestuderen en ontwerpen die leiden tot wetenschappelijke ontdekkingen en nieuwe doorbraaktechnologieën in een steeds veranderend wetenschappelijk landschap. Een belangrijk hulpmiddel dat wetenschappers en ingenieurs tegenwoordig ter beschikking hebben, is de computer. Computerondersteund ontwerp maakt een snellere overgang van het eerste concept naar het uiteindelijke product mogelijk.

De snelle evolutie van de stand van technologie en wetenschap leidt steeds tot nieuwe uitdagingen waar modelleringstools mee te kampen krijgen. Specifiek uit het domein van de elektronica is er een steeds verder doorgedreven miniaturisatie die leidt tot meer geavanceerde ontwerpen. In het verleden vereisten de hogere werkfrequenties zogenaamde *full-wave* modelleringsmethodes. Deze worden nu echter door complexere geometrieën ook tot hun limiet gedreven. Daarenboven worden er nieuwe types materialen gebruikt die een één- of tweedimensionaal karakter vertonen zoals nanodraden en kwantumgolfgeleiders. De kwantummechanische eigenschappen zijn door hun kleine dimensies prominenter waardoor deze ook in rekening gebracht moeten worden. Alzo hebben we te maken met een multifysisch (elektromagnetisch en kwantummechanisch) probleem waar de huidige generatie modelleringstools geen adequate oplossing voor biedt.

Om deze nieuwe soorten kwantumapparaten en hun toepassingen in de elektronica te bestuderen via computermodellering, moeten de vergelijkingen van Maxwell worden opgelost in combinatie met de Schrödingervergelijking. Deze vergelijkingen koppelen niet lineair en vinden plaats op verschillende spatiale en temporale schalen. Hierdoor is het probleem niet enkel multifysisch, maar ook multischaal.

De eindige-differentie-in-de-tijd of FDTD-methode is een veelgebruikte *full-wave* oplossingsmethode. Het vermogen om niet-lineaire media te modelleren maakt FDTD uitermate geschikt om multifysische problemen met betrekking tot elektromagnetisme (EM) en kwantummechanica (QM) aan te pakken. Ze discretiseert ruimte en tijd op een rooster en propageert de velden over kleine tijdsintervallen. De belangrijkste beperking is dat de maximaal toegestane tijdstap wordt beperkt door de Courantlimiet. In multischaal of multifysische problemen is deze tijdstap vaak te klein, wat de efficiëntie en dus de toepasbaarheid beperkt. Voor pure EM-problemen zijn geavanceerde technieken ontwikkeld om deze beperkingen te overwinnen. Deze kunnen echter niet rechtstreeks vertaald worden naar het ge-

koppelde EM/QM-systeem en zijn daardoor boeiende paden voor onderzoek.

Dit proefschrift bevat – naast een algemene inleiding tot elektromagnetisme, kwantummechanica en FDTD – verschillende methodes die tot doel hebben de huidige methodes voor het oplossen van de tijdsafhankelijke Schrödingervergelijking, met en zonder koppeling naar EM-velden, te verbeteren. Gezien de beperkingen van de huidige simulatietools om multifysische en multischaal problemen te modelleren, zijn de belangrijkste doelstellingen ofwel om de nauwkeurigheid van de methodes te verbeteren, ofwel om de efficiëntie te bevorderen in situaties waarin de tijdstapbeperkingen te problematisch worden. Hierdoor wordt hun toepasbaarheid aanzienlijk verhoogd. Bovendien worden de numerieke eigenschappen van de voorgestelde methodes grondig onderzocht met speciale aandacht voor hun stabiliteit. Verder hebben we onze methodes toegepast om systemen zoals kwantumdots, lateraal tunnelgekoppelde kwantumdraden en tunneldiodes te bestuderen. Door ze toe te passen in deze realistische simulatieopstellingen, hebben we gevalideerd dat hun numerieke eigenschappen zich ook vertalen in verbeteringen in praktijk.

Om de nauwkeurigheid van de FDTD-methode voor de tijdsafhankelijke Schrödingervergelijking te vergroten, stellen we een ruimtelijke discretisatie van hogere orde voor op niet-uniforme roosters (Hoofdstuk 4). Met een rigoureuze analyse van het stabiliteitscriterium vinden we een voorwaarde die minder beperkend is dan de gekende criteria in de limiet van uniforme roosters. De hogere-orde nauwkeurige schema's geven zowel een toename in nauwkeurigheid als efficiëntie aangezien een grover rooster kan gebruikt worden, wat resulteert in een grotere tijdstap. Bovendien kan de niet-uniforme spatiale discretisatie gebruikt worden om een optimale balans te vinden tussen de potentiaal, discretisatie en tijdstap.

Voor geometrieën die meerschalig zijn of sterke gradiënten van de potentialen vertonen, zijn toch kleine ruimtelijke stappen nodig waardoor enkel zeer kleine tijdstappen toegestaan zijn. De alternerende-richting hybride impliciete-expliciete of ADHIE-FDTD methode voor de Schrödingervergelijking heeft als doel dit te verhelpen (Hoofdstuk 5). Net als de gelijknamige methode voor het oplossen van de vergelijkingen van Maxwell, past deze lokale implicitisatie toe om de tijdstap te vergroten. Waar de ruimtelijke stappen klein zijn, wordt de golffunctie impliciet opgelost waardoor ADHIE-FDTD deze stappen uit het stabiliteitscriterium kan halen. Het resulterende schema laat grotere tijdstappen toe en bestaat uit makkelijk oplosbare impliciete lineaire systemen. In tegenstelling tot de vergelijkbare methode voor de wetten van Maxwell, is de volledig impliciete methode niet onvoorwaardelijk stabiel. Dit komt omdat de potentiaal niet wordt meegenomen in het impliciete deel van de berekening. De potentiaal limiteert de tijdstap eerder om een goede accuraatheid te bekomen dan uit stabiliteitsoverwegingen. Hierdoor is het schema stabiel voor elke redelijk gekozen tijdstap.

Een volgend deel van dit doctoraatsonderzoek is gewijd aan de koppeling tussen EM- en QM-systemen. Hiervoor stellen we een nieuwe methode voor om de minimaalgekoppelde Schrödingervergelijking met willekeurige ijkcondities te discretiseren (Hoofdstuk 6). De discretisatie wordt voorgesteld op niet-uniforme roosters voor lagere-orde accurate discretisaties en op uniforme roosters voor ruimtelijke differenties van tweede, vierde en zesde orde. De willekeurige aard van de EM-vectorpotentiaal bemoeilijkt de discretisatie aanzienlijk, maar door fysische symmetrieën in acht te nemen, resulteert de discretisatie in een elegant en aantoonbaar stabiel schema.

Verder onderzoeken we hoe QM-oplossingsmethodes kunnen geïntegreerd worden in EM-modelleringssoftware door verschillende FDTD-schema's voor te stellen die de EM-potentialen berekenen via de EM-velden (ook Hoofdstuk 6). Hoewel de EM-velden niet vereist zijn voor het QM-gedeelte van de berekening, vereenvoudigt de voorgestelde aanpak de integratie van QM-simulaties in bestaande code en laat hierdoor ook toe om meer geavanceerde methodes toe te passen die zijn ontwikkeld voor nano-elektronische componenten. De resulterende schema's vertonen zeer verschillende efficiënties en nauwkeurigheden die nauwgezet worden besproken.

De koppeling van EM- en QM-systemen resulteert in een grote discrepantie tussen de toegestane tijdstappen. Om de tijdstap van het EM-FDTD-schema te vergroten en het meer compatibel te maken met het QM-gedeelte, wenden we ons opnieuw tot de ADHIE-methode, maar nu voor de vergelijkingen van Maxwell (Hoofdstuk 7). Voor quasi 1-D QM-systemen zijn de ruimtelijke cellen in één enkele richting heel klein, wat de efficiëntie van het EM-deel beperkt. Door het ADHIE-schema voor de EM-velden uit te breiden naar de EM-potentialen met de Lorenz-ijkvoorwaarde vergroten we de toegestane tijdstap. Zo wordt de methode toepasbaar om de interactie tussen EM-velden en nanodraden te simuleren. In tegenstelling tot het oorspronkelijke schema bevat de nieuwe methode geen splitsingsparameter waardoor deze efficiënter en nauwkeuriger is.

De methodes die in dit werk worden gepresenteerd, zijn een aanzienlijke verbetering ten opzichte van bestaande methodes. Met talrijke voorbeelden tonen we aan dat ze nauwkeurig en efficiënt zijn. Door grondig de numerieke eigenschappen te onderzoeken zijn betere inzichten ontstaan die kunnen worden gebruikt om nog betere methodes te ontwikkelen. Deze moeten uiteindelijk leiden tot grootschalige berekeningen om de volgende generatie nanoelektronische componenten te ontwikkelen.

SUMMARY

Modeling tools allow us to interpret and design more complex systems, leading to new scientific discoveries and breakthrough technologies in an ever-changing landscape. Nowadays, an important tool that scientists and engineers have at their disposal, are computers. Computer-aided design (CAD) tools allow a faster transition from initial concept to final product.

The rapid evolution of the state-of-the-art in technology and science continues to create new challenges for modeling tools. Specifically in the field of electronics, there is an ever-increasing demand for miniaturization, which leads to the development of complex designs. In the past, the higher operating frequencies required so-called *full-wave* modeling techniques. These, however, are now also pushed to their limits by more complex geometries. Additionally, new types of materials are used that are quasi one- or two-dimensional such as nanowires and quantum waveguides where – due to their small dimensions – we also need to take their quantum mechanical properties into account. As such, we are dealing with a multiphysics (electromagnetic and quantum mechanical) problem for which the current generation of modeling tools offers no adequate solution.

To study these new types of quantum devices and their applications in electronics through computer modeling, Maxwell's equations must be solved in combination with the Schrödinger equation. These equations do not couple linearly and take place on different spatial and temporal scales. Therefore, the problem is not only multiphysics, but also multiscale.

The finite-difference time-domain (FDTD) method is a commonly used full-wave solver. Its ability to model nonlinear materials makes it the ideal candidate to tackle multiphysics problems involving electromagnetism (EM) and quantum mechanics (QM). The method discretizes space and time on a grid and propagates the fields in small time increments. Its main limitation is that the maximum allowed time step is limited by the Courant limit. In multiscale or multiphysics problems this time step is often overly restrictive, limiting the efficiency and thus applicability. For pure EM problems, advanced techniques have been developed to overcome these limitations. However, these do not directly translate to the coupled EM/QM system and are thus exciting avenues for investigation.

This dissertation contains – besides a general introduction to electromagnetism, quantum mechanics, and the FDTD method – several methods that aim to improve existing methods for solving the time-dependent Schrödinger equation with

and without coupling to EM fields. Given the lack of adequate simulation tools for multiphysics and multiscale problems, the main goals are either to increase the accuracy of the methods or to increase the efficiency in situations where the time step restrictions become too cumbersome. Consequently, we thereby increase their applicability. Furthermore, the proposed methods are thoroughly investigated with regards to their numerical properties, with special attention to the stability. Furthermore, we applied our methods to study systems such as quantum dots, laterally tunnel-coupled quantum wires and tunneling diodes. By applying them in these realistic simulation set-ups, we validated that their numerical properties also translate to real-world improvements.

To increase the accuracy of the FDTD method for the time-dependent Schrödinger equation we propose a higher-order spatially accurate discretization on nonuniform grids (Chapter 4). With a rigorous analysis of the stability criterion we retrieve a condition that is less restrictive than the known criteria in the limit of uniform grids. The higher-order accurate schemes effectuate both an increase in accuracy and efficiency since a coarser grid can be used which results in a larger time step. Additionally, the nonuniform discretization can be leveraged to attain an optimal balance between potential, discretization and time step.

For geometries that are multiscale or exhibit strong gradients of the potentials, small spatial steps are still required, which results in very small time steps. The alternating-direction hybrid implicit-explicit (ADHIE) method for the Schrödinger equation aims to remedy this (Chapter 5). Much like to the similarly named method for solving Maxwell's equations, it applies local implicitization to increase the time step. Where the spatial steps are small, the wave function is implicitly solved, thus removing these spatial steps from the stability criterion. As a result, the time step is increased and the resulting implicit systems are easily solved. Unlike the similar method for Maxwell's equations, the fully implicit method is not unconditionally stable since the potential is not included in the implicit part of the calculation. However, the time step is limited by the potential value more to obtain a high enough accuracy rather than to satisfy the stability criterion. Therefore, it is stable for every reasonable time step.

Another part of this doctoral research is devoted to the coupling between EM systems and QM systems. We propose a new method to discretize the minimally-coupled Schrödinger equation for arbitrary gauge conditions (Chapter 6). The discretization is proposed on nonuniform grids for lower-order accurate discretizations and on uniform grids for second-, fourth-, and sixth-order accurate spatial differences. The arbitrary nature of the EM vector potential significantly complicates the discretization but by keeping physical symmetries in mind, the discretization results in an elegant and provably stable scheme.

We further investigate the integration of QM solvers into EM computational methods by proposing several FDTD schemes that calculate the EM potentials from the EM fields (also Chapter 6). While the calculation of EM fields is not required for the QM part of the calculation, the proposed approach facilitates the integration of QM simulations into existing code, which also allows the application of more advanced methods developed for (nano)electronic devices. The resulting schemes exhibit very different efficiencies and accuracies, which are thoroughly discussed and illustrated.

The coupling of EM and QM systems results in a large mismatch between the allowed time steps. To increase the time step of the EM-FDTD scheme and make it more compatible with the QM part, we again turn towards the ADHIE method but now for Maxwell's equations (Chapter 7). For quasi 1-D QM systems, the spatial cells in a single direction are very small, thus limiting the efficiency of the EM part. By extending the ADHIE scheme for the EM fields to the EM potentials in the Lorenz gauge, we increase the overall time step. This makes the method applicable for the simulation of the interaction between EM fields and nanowires. In contrast to the original scheme, the new one does not require a splitting parameter, making it more efficient and more accurate.

The methods presented in this work considerably improve upon existing methods. Through numerous examples we show that they are accurate and efficient. The thorough numerical investigation of the methods has led to better insights which can be employed to develop even more specialized methods. These may eventually lead to large-scale computations to predict the behavior of the next generation of nanoelectronic devices.

List of abbreviations

ADHIE	alternating-direction hybrid implicit-explicit
ADI	alternating-direction implicit
ALDA	adiabatic local-density approximation
BiCGSTAB	biconjugate gradient stabilized
BV	boundary value
CAD	computer-aided design
CE	collocated explicit
CEM	computational electromagnetics
CFL	Courant-Friedrichs-Lewy
CFS	complex frequency shifted
CN	Crank-Nicolson
CPU	central processing unit
DFT	density-functional theory
EM	electromagnetism
FD	finite difference
FDTD	finite-difference time-domain
HIE	hybrid implicit-explicit
IBVP	initial-boundary-value problem
LDA	local-density approximation
MC	Monte-Carlo
MKS	Maxwell-Kohn-Sham
MS	Maxwell-Schrödinger
PDE	partial differential equation
PDF	probability density function
PEC	perfect electric conductor
PML	perfectly matched layer
QM	quantum mechanics
RTD	resonant-tunneling diode
RV	random variable
TDCDFT	time-dependent current-density-functional theory
TDDFT	time-dependent density-functional theory
TFSF	total-field scattered-field
UQ	uncertainty quantification
1-D	1-dimensional
2-D	2-dimensional
3-D	3-dimensional

List of symbols

$\jmath$	imaginary unit
∇	nabla operator
∇^2	Laplacian operator
$\frac{\mathrm{d}}{\mathrm{d}x}$	total derivative with respect to x
$\frac{\partial}{\partial x}$	partial derivative with respect to x
x^ν	4-D space-time coordinate
η_ρ	general field quantity
$\eta_{,\nu}$	partial derivative of η w.r.t. space-time coordinate x^ν
$\dot{\eta}$	temporal derivative of η
ε_{ijk}	Levi-Civita symbol
$\mathcal{L}$	Lagrangian density
$T_\mu{}^\nu$	energy-stress tensor
$\mathrm{Re}(x)$	real part of complex number x
$\mathrm{Im}(x)$	imaginary part of complex number x
$\|\boldsymbol{x}\|_p$	vector p-norm of $\boldsymbol{x}$
$\|A\|_p$	matrix p-norm of A
A^T	transpose of A
$s(A)$	spectrum of A
$\rho(A)$	spectral radius of A
$\sigma_{\max}(A)$	maximum singular value of A
$A \otimes B$	Kronecker product of A and B
$A \oplus B$	Kronecker sum of A and B
$A \circ B$	Hadamard or point-wise product of A and B
$\mathrm{diag}(\dots)$	diagonal matrix with specified elements
Θ	Heaviside function
$\forall i$	for all values of i
$i \in A$	i in set A

$\hbar$	reduced Planck's constant ($1.054\,571\,817 \times 10^{-34}\,\mathrm{J\,s}$)
e	elementary charge ($1.602\,176\,634 \times 10^{-19}\,\mathrm{C}$)
c	speed of light in vacuum ($299\,792\,458\,\mathrm{m\,s^{-1}}$)
ϵ_0	vacuum electric permittivity ($8.854\,187\,813 \times 10^{-12}\,\mathrm{F\,m^{-2}}$)
μ_0	vacuum magnetic permeability ($1.256\,637\,062 \times 10^{-6}\,\mathrm{N\,A^{-2}}$)
Z_0	impedance of free space ($376.730\,313\,668\,\Omega$)
m_e	electron rest mass ($9.109\,383\,702 \times 10^{-31}\,\mathrm{kg}$)
a_0	Bohr radius ($5.291\,772\,109 \times 10^{-11}\,\mathrm{m}$)
k_B	Boltzmann constant ($1.380\,649 \times 10^{-23}\,\mathrm{J\,K^{-1}}$)
γ	Euler-Mascheroni constant (0.577 215 665)

$\boldsymbol{E}$	continuous electric field vector
$\boldsymbol{H}$	continuous magnetizing field vector
$\boldsymbol{B}$	continuous magnetic field vector
$\boldsymbol{D}$	continuous electric displacement vector
$\boldsymbol{A}$	continuous electromagnetic vector potential
ϕ	continuous electromagnetic scalar potential
$\boldsymbol{e}$	row-major vectorized electric field
$\boldsymbol{h}$	row-major vectorized magnetizing field
$\boldsymbol{b}$	row-major vectorized magnetic field
$\boldsymbol{d}$	row-major vectorized electric displacement
$\boldsymbol{a}$	row-major vectorized electromagnetic vector potential
$\boldsymbol{\phi}$	row-major vectorized electromagnetic scalar potential
q	electric charge
ψ	continuous wave function
r	real part of the continuous wave function
s	imaginary part of the continuous wave function
$\boldsymbol{\psi}$	row-major vectorized wave function
$\boldsymbol{r}$	row-major vectorized real part of the wave function
$\boldsymbol{s}$	row-major vectorized imaginary part of the wave function
ρ	total electric charge density
$\boldsymbol{J}$	total electric current density

i	spatial index with respect to the x-axis
j	spatial index with respect to the y-axis
k	spatial index with respect to the z-axis
n	temporal index also, probability density
n_u	number of cells in the u-direction
m_u	number of dual cells in the u-direction ($m_u = n_u - 1$)
Δu	spatial step size in the u-direction
Δt	time step
$\Delta\tau$	time step normalized with the speed of light ($\Delta\tau = c\Delta t$)
$\Delta\eta$	time step normalized with $\hbar$ ($\Delta\eta = \Delta t/\hbar$)
$E\vert^n_{i,j,k}$	spatio-temporal evaluation of the variable E in the grid
$\boldsymbol{e}\vert_i$	i-th element of vector $\boldsymbol{e}$
$\boldsymbol{e}\vert^n_{(i,j,k)}$	spatio-temporal evaluation of the vector $\boldsymbol{e}$ in the grid

Articles in international journals

- Decleer, P., Van Londersele, A., Rogier, H. & Vande Ginste, D. Nonuniform and higher-order FDTD methods for the Schrödinger equation. *Journal of Computational and Applied Mathematics* **381,** 113023 (2021).
- Decleer, P., Van Londersele, A., Rogier, H. & Vande Ginste, D. An alternating-direction hybrid implicit-explicit finite-difference time-domain method for the Schrödinger equation. *Journal of Computational and Applied Mathematics* **403,** 113881 (2022).
- Decleer, P. & Vande Ginste, D. A Hybrid EM/QM Framework Based on the ADHIE-FDTD Method for the Modeling of Nanowires. *IEEE Journal on Multiscale and Multiphysics Computational Techniques* **7,** 236–251 (2022).

Articles in conference proceedings

- Decleer, P. & Vande Ginste, D. *Uncertainty quantification of charge transfer through a nanowire resonant-tunneling diode with an ADHIE-FDTD method* in *2021 IEEE 11th International Conference Nanomaterials: Applications & Properties (NAP)* Sept. 5–11, 2021 (Odessa, Ukraine, 2021), 1–5.

Novel Finite-Difference Time-Domain Techniques for Combined Electromagnetic and Quantum Mechanical Simulations

CHAPTER 1

INTRODUCTION

"If you only read the books that everyone else is reading,
you can only think what everyone else is thinking."

— HARUKI MURAKAMI, Norwegian Wood (1987)

1.1 Context and motivation

The world is nowadays dominated by an ever-increasing amount of "smart" devices. Even though some people try to eschew technology whenever possible, the amount of electronic devices and their capabilities will inevitably grow. They have enabled us to keep in touch with friends and family all over the planet, to design self-driving cars, to watch one's favorite movie or series in 4K resolution, and so much more.

At the core of all these new inventions lies our ability to interpret the world around us; make mental, theoretical, or physical models; and manipulate our surroundings in an advantageous manner. Physicists try to interpret the world using the "laws of physics" which are cast into a set of mathematical equations. While physicists typically want to understand, engineers typically aim to build. To design or optimize a device, we need to solve the corresponding equations but this is, unfortunately, extraordinarily hard. Therefore, we rely on simplified models of subsystems which are governed by some other set of approximated "laws". For example, Kirchhoff's current and voltage laws predict the current flowing through a device and by using these laws, we can modify the circuit parameters to optimize the delivered power.

There is obviously some positive feedback loop here, since well-built *approximate* models can help us to interpret the systems we wish to study. Since the advent of computer-aided design (CAD) tools, we can construct ever more complex models which help us to approximate reality more closely. These software tools support engineers in their endeavors by making a digital version of their designs. By prototyping in software, we can iterate faster through designs and also increase our understanding since we can access information that is unattainable in a physical prototype. Consequently, the final product will be available sooner and overall

better.

However, these CAD tools are only as good as the physical laws that we rely on. Therefore, we need to select the appropriate approximate laws, e.g., while Kirchhoff's laws can predict the amount of current flowing through a simple light bulb, they cannot predict how long it will take for a light bulb to turn on after the switch has been pressed. To calculate this, the telegrapher's equations – or even Maxwell's equations – need to be solved. Similarly, more advanced designs require us to solve more detailed equations which in turn requires more capable CAD tools.

The trend towards ever smaller electronic devices that operate at higher frequencies has historically led to the emergence of electromagnetic (EM) *full-wave solvers*, which solve Maxwell's equations. Some noteworthy examples are the finite-element method (FEM) [1], the method of moments (MoM) [2], and the finite-difference time-domain (FDTD) method [3]. Highly conductive media or magnetic materials, which are difficult to model, require ingenious modifications to the "standard" algorithms to be accurately described [4–9].

Furthermore, the increased miniaturization has led to the investigation and production of nanoscale electronics with dimensions smaller than 100 nm. Because of their small dimensions, unforeseen quantum mechanical (QM) effects such as quantum confinement become more important. An example that takes miniaturization to the extreme is a single molecule diode [10]. This *electronic* component is quantum mechanical by design and to model the EM behavior of these new kinds of quantum devices, we again require new solutions. One approach is to apply a simplified QM model of these materials, which describes their approximate frequency-dependent or anisotropic behavior, and try to incorporate it into the existing full-wave solvers. This has, e.g., been used to evaluate the shielding effectiveness of graphene [11]. Another approach is to integrate these materials on an *ab initio* level, i.e., by concurrently solving the Schrödinger equation which results in a nonlinear problem. Besides exhibiting QM effects, these new materials are also often low-dimensional. Some examples are thin-film MoS_2 transistors [12, 13], graphene inductors [14] or InGaAs nanowires [15]. Because of their discrepant sizes in different directions the problem is multiscale, which further complicates their modeling.

The FDTD method, which is the subject of this dissertation, can handle nonlinear materials, and is thus well-suited for modeling the QM and EM subsystems and their interaction. The method basically discretizes space on a grid while propagating the fields in small time increments. Even though QM CAD tools usually focus on the molecular modeling in the static or linear response regimes [16], several FDTD-based CAD tools have been developed that can model the behavior of various of nanoelectronic devices, such as quantum dots [17, 18], nanowires [19,

20], and quantum waveguides [21–23]. It is only more recently that the integration with full-wave EM solvers is investigated to describe the interactions at high frequencies or strong fields [24–36]. These kinds of techniques are still in their infancy and have to deal with the complicated behavior of coupled QM/EM systems which takes place at disparate length and spatial scales.

1.2 Goals

In this work, we focus on the FDTD method and propose new algorithms for quantum mechanical and electromagnetic simulations. We aim to make the existing methods applicable to the multiscale and multiphysics problems present in quantum device modeling. Generally speaking, we pursue this goal either by increasing the efficiency of an existing method without sacrificing accuracy, or by increasing the accuracy without sacrificing efficiency. To increase the accuracy, we have adopted higher-order accurate schemes. While, at first, this might seem to also increase the computation time, the inverse is true in practice. By using a higher-order scheme we reduce the number of grid samples which results in a reduced number of unknowns and simultaneously increases the time step. Alternatively, we also develop hybrid implicit-explicit methods which reduce the number of time steps at the cost of more complicated time stepping. We employ our methods to study, e.g., quantum dots, resonant tunneling diodes, and tunnel-coupled quantum wires. The methods are further verified either by comparing with an analytical solution, or by comparing with the methods we aim to improve. Furthermore, the conditional stability of the proposed methods is thoroughly investigated since a larger time step equals a more efficient method.

1.3 Outline

In Chapter 2, an overview is given of the EM and QM theory used in this work. Special attention is dedicated to the EM potentials and a Lagrangian formulation of QM and coupled EM/QM systems is presented. Chapter 3 introduces the FDTD method for Maxwell's equations and the Schrödinger equation along with some basic concepts such as conditional stability. The novel contributions start from Chapter 4. In Chapters 4 and 5, we deal with the single-particle Schrödinger equation and in Chapters 6 and 7, we treat the coupled EM/QM system.

Specifically, Chapter 4 presents an FDTD method for the Schrödinger equation on a nonuniform grid which employs higher-order spatial differences. In Chapter 5, this method is extended to apply hybrid implicit-explicit (HIE) updates to relax the time step in multiscale QM problems.

In Chapter 6 we study coupled EM/QM systems with fully explicit FDTD methods. The classic Yee algorithm is extended to include the EM potentials in various gauge conditions. Furthermore, a novel discretization of the minimally-coupled Schrödinger equation is proposed for nonuniform grids and also for uniform grids but leveraging higher-order spatial differences. In Chapter 7, we apply the concept of HIE updates based on the alternating-direction implicit (ADI) method to the EM potentials in the Lorenz gauge, resulting in the alternating-direction hybrid implicit-explicit (ADHIE) method. In combination with the ADHIE method for the EM fields, this results in a much increased time step for coupled EM/QM problems. This method is applied to quasi 1-D nanowires.

Finally, we present our conclusions and some promising avenues for future research in Chapter 8.

References

1. Jin, J.-M. *The Finite Element Method in Electromagnetics* (Wiley-IEEE Press, 2014).
2. Harrington, R. F. *Field Computation by Moment Methods* (Wiley-IEEE Press, 1993).
3. Taflove, A. & Hagness, S. C. *Computational electrodynamics: the finite-difference time-domain method* (Artech House, 2005).
4. Huynen, M., Gossye, M., De Zutter, D. & Vande Ginste, D. A 3-D Differential Surface Admittance Operator for Lossy Dipole Antenna Analysis. *IEEE Antennas and Wireless Propagation Letters* **16,** 1052–1055 (2017).
5. Van Londersele, A. *et al.* Systematic cell-by-cell FDTD subgridding in 3-D. *IEEE Microwave and Wireless Components Letters* **28,** 546–548 (2018).
6. Gossye, M. *et al.* A Calderón Preconditioner for High Dielectric Contrast Media. *IEEE Transactions on Antennas and Propagation* **66,** 808–818 (2018).
7. Gossye, M., Vande Ginste, D. & Rogier, H. Electromagnetic modeling of high magnetic contrast media using Calderón preconditioning. *Computers & Mathematics with Applications* **77,** 1626–1638 (2019).
8. Huynen, M. *et al.* Entire Domain Basis Function Expansion of the Differential Surface Admittance for Efficient Broadband Characterization of Lossy Interconnects. *IEEE Transactions on Microwave Theory and Techniques* **68,** 1217–1233 (2020).
9. Bosman, D. *et al.* A 2-D differential surface admittance operator for combined magnetic and dielectric contrast. *Computers & Mathematics with Applications* **102,** 175–186 (2021).
10. Zoldan, V. C., Faccio, R. & Pasa, A. A. n and p type character of single molecule diodes. *Scientific Reports* **5,** 1–8 (2015).
11. Van Londersele, A., De Zutter, D. & Vande Ginste, D. Full-wave analysis of the Shielding Effectiveness of Thin Graphene Sheets with the 3D Unidirectionally Collocated HIE-FDTD Method. *International Journal of Antennas and Propagation* **2017,** 1–8 (2017).
12. Kim, S. *et al.* High-mobility and low-power thin-film transistors based on multilayer MoS2 crystals. *Nature Communications* **3,** 1–7 (2012).
13. Sarkar, D. *et al.* MoS2 field-effect transistor for next-generation label-free biosensors. *ACS nano* **8,** 3992–4003 (2014).
14. Kang, J. *et al.* On-chip intercalated-graphene inductors for next-generation radio frequency electronics. *Nature Electronics* **1,** 46–51 (2018).
15. Tomioka, K., Yoshimura, M. & Fukui, T. A III–V nanowire channel on silicon for high-performance vertical transistors. *Nature* **488,** 189–192 (2012).

16. Castro, A. *et al.* Octopus: a tool for the application of time-dependent density functional theory. *Physica Status Solidi (b)* **243,** 2465–2488 (2006).

17. Sullivan, D. M. & Citrin, D. Determination of the eigenfunctions of arbitrary nanostructures using time domain simulation. *Journal of Applied Physics* **91,** 3219–3226 (2002).

18. Sudiarta, I. W. & Angraini, L. M. The finite difference time domain (FDTD) method to determine energies and wave functions of two-electron quantum dot. *AIP Conference Proceedings* **2023,** 020199 (2018).

19. Sullivan, D. M. & Wilson, P. M. Time-domain determination of transmission in quantum nanostructures. *Journal of Applied Physics* **112** (2012).

20. Sullivan, D. M., Mossman, S. & Kuzyk, M. G. Time-Domain Simulation of Three Dimensional Quantum Wires. *PLOS ONE* **11** (2016).

21. Sullivan, D. M. & Citrin, D. Determining quantum eigenfunctions in three-dimensional nanoscale structures. *Journal of Applied Physics* **97,** 104305 (2005).

22. Zheng, C. A perfectly matched layer approach to the nonlinear Schrödinger wave equations. *Journal of Computational Physics* **227,** 537–556 (2007).

23. Mennemann, J.-F. & Jüngel, A. Perfectly Matched Layers versus discrete transparent boundary conditions in quantum device simulations. *Journal of Computational Physics* **275,** 1–24 (2014).

24. Pierantoni, L., Mencarelli, D. & Rozzi, T. A new 3-D transmission line matrix scheme for the combined Schrödinger–Maxwell problem in the electronic/electromagnetic characterization of nanodevices. *IEEE Transactions on Microwave Theory and Techniques* **56,** 654–662 (2008).

25. Mennemann, J.-F., Jüngel, A. & Kosina, H. Transient Schrödinger–Poisson simulations of a high-frequency resonant tunneling diode oscillator. *Journal of Computational Physics* **239,** 187–205 (2013).

26. Takeuchi, T., Ohnuki, S. & Sako, T. Hybrid Simulation of Maxwell-Schrödinger Equations for Multi-Physics Problems Characterized by Anharmonic Electrostatic Potential. *Progress In Electromagnetics Research* **148,** 73–82 (2014).

27. Ryu, C. J., Liu, A. Y., Wei, E. & Chew, W. C. Finite-difference time-domain simulation of the Maxwell–Schrödinger system. *IEEE Journal on Multiscale and Multiphysics Computational Techniques* **1,** 40–47 (2016).

28. Chen, Y. P. *et al.* A unified Hamiltonian solution to Maxwell-Schrödinger equations for modeling electromagnetic field-particle interaction. *Computer Physics Communications* **215,** 63–70 (2017).

29. Zhang, L., Zeng, H. & Chen, R.-S. Full-quantum numerical scheme of finite difference time domain method for high-order harmonic generation. *IEEE Journal on Multiscale and Multiphysics Computational Techniques* **3,** 74–79 (2018).

30. Xiang, C., Kong, F., Li, K. & Liu, M. A high-order symplectic FDTD scheme for the Maxwell-Schrodinger system. *IEEE Journal of Quantum Electronics* **54,** 1–8 (2017).

31. Xie, G. *et al.* Universal vector–scalar potential framework for inhomogeneous electromagnetic system and its application in semiclassical quantum electromagnetics. *IEEE Transactions on Plasma Science* **49,** 3459–3471 (2021).

32. Sato, S. A. & Yabana, K. Maxwell+TDDFT multi-scale simulation for laser-matter interactions. *Journal of Advanced Simulation in Science and Engineering* **1,** 98–110 (2014).

33. Yamada, S., Noda, M., Nobusada, K. & Yabana, K. Time-dependent density functional theory for interaction of ultrashort light pulse with thin materials. *Physical Review B* **98,** 245147 (2018).

34. Yamada, A. & Yabana, K. Multiscale time-dependent density functional theory for a unified description of ultrafast dynamics: Pulsed light, electron, and lattice motions in crystalline solids. *Physical Review B* **99,** 245103 (2019).

35. Gabay, D. *et al.* Lorenz gauge formulation for time-dependent density functional theory. *Physical Review B* **101,** 235101 (2020).

36. Tancogne-Dejean, N. *et al.* Octopus, a computational framework for exploring light-driven phenomena and quantum dynamics in extended and finite systems. *The Journal of chemical physics* **152,** 124119 (2020).

CHAPTER 2

MAXWELL'S AND SCHRÖDINGER'S EQUATIONS OF MOTION

"Anything sufficiently weird must be fishy."

— LIU CIXIN, The Three Body Problem (2008)

In this chapter the basic equations that describe the interaction of electromagnetic radiation and matter are reviewed. These equations are fundamental to the description of nanoelectronic devices and therefore comprise the physical backbone of this dissertation. First, Maxwell's equations are presented in Section 2.1, starting from a microscopic viewpoint, where materials are considered as an amalgamation of moving charges. Next, in Section 2.2, we consider the Schrödinger equation, which describes matter on a quantum mechanical level. Subsequently, Section 2.3 introduces time-dependent density-functional theory (TDDFT), which is equivalent to the Schrödinger equation but results in a tractable way to deal with the many-body interactions present in real systems. Lastly, in Section 2.4, the fully coupled EM-QM system is considered.

2.1 Maxwell's equations

The propagation of electromagnetic (EM) waves is determined by Maxwell's equations, first proposed by J. C. Maxwell [1, 2]. In the context of nanoelectronic devices it is most natural to consider the microscopic formulation, where ρ is the total electric charge density and $\boldsymbol{J}$ is the total electric current density. For now, the only constraint we impose on physical matter is that charge should be conserved, which is expressed using the continuity equation:

$$\boldsymbol{\nabla} \cdot \boldsymbol{J} + \frac{\partial \rho}{\partial t} = 0. \tag{2.1}$$

The dynamics of the charges dictate the evolution of the electric field $\boldsymbol{E}$ and magnetic field $\boldsymbol{B}$ according to Maxwell's curl equations:

$$\boldsymbol{\nabla} \times \boldsymbol{E} = -\frac{\partial \boldsymbol{B}}{\partial t}, \tag{2.2a}$$

$$\boldsymbol{\nabla} \times \boldsymbol{B} = \mu_0 \left(\boldsymbol{J} + \epsilon_0 \frac{\partial \boldsymbol{E}}{\partial t} \right), \tag{2.2b}$$

where μ_0 and ϵ_0 are the permeability and permittivity of vacuum, respectively. The current density excites the initial-boundary-value problem (IBVP).

By taking the divergence of the curl equations (2.2) and using the starting conditions $\nabla \cdot \boldsymbol{B}(t_0) = 0$ and $\epsilon_0 \nabla \cdot \boldsymbol{E}(t_0) = \rho(t_0)$ at an arbitrary time t_0, Gauss' electric and magnetic laws are recovered:

$$\nabla \cdot \boldsymbol{E} = \frac{\rho}{\epsilon_0}, \tag{2.3a}$$

$$\nabla \cdot \boldsymbol{B} = 0, \tag{2.3b}$$

respectively.

In the microscopic formulation, materials only appear as charges and currents. As such, the dynamics of these charges should be treated self-consistently. However, in macroscopic problems, the description of *all* charge carriers quickly becomes intractable. Therefore, the – equally general – macroscopic equations are commonly used for EM applications which leverage the displacement field $\boldsymbol{D}$ and magnetizing field $\boldsymbol{H}$. The relationship between $(\boldsymbol{E}, \boldsymbol{B})$ and $(\boldsymbol{D}, \boldsymbol{H})$ for real materials is often determined empirically. For linear materials the response of the materials on the fields are given by the following constitutive equations:

$$\boldsymbol{D} = \epsilon \boldsymbol{E}, \tag{2.4a}$$

$$\boldsymbol{B} = \mu \boldsymbol{H}. \tag{2.4b}$$

The material permittivity ϵ and permeability μ can be inhomogeneous, dispersive and/or anisotropic (which results in tensorial $\boldsymbol{\epsilon}$ and $\boldsymbol{\mu}$). The resulting macroscopic Maxwell's equations are given by:

$$\nabla \times \boldsymbol{E} = -\frac{\partial \boldsymbol{B}}{\partial t}, \tag{2.5a}$$

$$\nabla \times \boldsymbol{H} = \boldsymbol{J}_f + \frac{\partial \boldsymbol{D}}{\partial t}, \tag{2.5b}$$

$$\nabla \cdot \boldsymbol{B} = 0, \tag{2.5c}$$

$$\nabla \cdot \boldsymbol{D} = \rho_f, \tag{2.5d}$$

where $\boldsymbol{J}_f$ and ρ_f are the *free* current and charge densities, respectively. These include externally impressed charges and currents. Another typical contribution to the free current density is the conduction current density $\boldsymbol{J}_c$. In a conductive material with conductivity σ, it is determined as:

$$\boldsymbol{J}_c = \sigma \boldsymbol{E}. \tag{2.6}$$

However, the media treated in this dissertation are lossless, homogeneous, non-dispersive and isotropic. Another contribution that is especially important in this

work is the quantum current density $\boldsymbol{J}_q$, which is discussed in Section 2.4.

Maxwell's equations can also be reformulated in terms of a vector potential $\boldsymbol{A}$ and a scalar potential ϕ. These are defined as:

$$\boldsymbol{B} = \boldsymbol{\nabla} \times \boldsymbol{A}, \tag{2.7a}$$

$$\boldsymbol{E} = -\frac{\partial \boldsymbol{A}}{\partial t} - \boldsymbol{\nabla}\phi. \tag{2.7b}$$

The substitution of (2.7) into Maxwell's equations yields:

$$\nabla^2\phi + \frac{\partial}{\partial t}(\boldsymbol{\nabla} \cdot \boldsymbol{A}) = -\frac{\rho}{\epsilon_0}, \tag{2.8a}$$

$$\left(\nabla^2\boldsymbol{A} - \frac{1}{c^2}\frac{\partial^2 \boldsymbol{A}}{\partial t^2}\right) - \boldsymbol{\nabla}\left(\boldsymbol{\nabla} \cdot \boldsymbol{A} + \frac{1}{c^2}\frac{\partial \phi}{\partial t}\right) = -\mu_0 \boldsymbol{J}. \tag{2.8b}$$

Since the electric and magnetic fields are unchanged under a *gauge* transformation the potentials are not uniquely defined:

$$\boldsymbol{A}' = \boldsymbol{A} + \boldsymbol{\nabla}\chi, \tag{2.9a}$$

$$\phi' = \phi - \frac{\partial \chi}{\partial t}. \tag{2.9b}$$

This freedom allows fixing the gauge with several conditions, and each gauge fixing condition has its pros and cons. An accessible but comprehensive overview of the electromagnetic potentials in any gauge is found in [3]. While the electromagnetic potentials seem nothing more than a mathematical trick at first, they do have physical significance as proven in [4].

Coulomb gauge

The first gauge we discuss, is the Coulomb gauge, which states:

$$\boldsymbol{\nabla} \cdot \boldsymbol{A} = 0. \tag{2.10}$$

The resulting equations from (2.8) are:

$$\nabla^2\phi = -\frac{\rho}{\epsilon_0}, \tag{2.11}$$

$$\left(\nabla^2\boldsymbol{A} - \frac{1}{c^2}\frac{\partial^2 \boldsymbol{A}}{\partial t^2}\right) = -\mu_0 \boldsymbol{J} + \frac{1}{c^2}\boldsymbol{\nabla}\left(\frac{\partial \phi}{\partial t}\right). \tag{2.12}$$

Hence, the Coulomb gauge condition results in the well-known Poisson equation for the scalar potential (2.11). Moreover, it has the advantage that the vector potential commutes with the quantum mechanical momentum operator $\hat{\boldsymbol{p}} = -\jmath\hbar\boldsymbol{\nabla}$,

which is discussed in Section 2.2. The scalar potential can also be calculated as an integral:

$$\phi(\boldsymbol{r},t) = \frac{1}{4\pi\epsilon_0}\int \frac{\rho(\boldsymbol{r}',t)}{|\boldsymbol{r}'-\boldsymbol{r}|}\,\mathrm{d}\boldsymbol{r}'\,. \tag{2.13}$$

The scalar potential in the Coulomb gauge propagates with infinite velocity as any change in ρ is instantly reflected in ϕ. However, because the resulting EM fields $\boldsymbol{E}$ and $\boldsymbol{B}$ still propagate at the speed of light, special relativity is not violated.

Gibbs gauge

The next gauge condition is the Gibbs gauge [5]:

$$\phi = 0. \tag{2.14}$$

The resulting equation for the vector potential $\boldsymbol{A}$ is simply an integral of $\boldsymbol{E}$:

$$\frac{\partial \boldsymbol{A}}{\partial t} = -\boldsymbol{E}. \tag{2.15}$$

This simple relation is particularly useful when the electric field is known and the vector potential has to be determined. However, since a constant electric field $\boldsymbol{E}$ results in an ever growing $\boldsymbol{A}$, the gauge is not always suited to numerical computations.

Lorenz gauge

The last gauge condition is the Lorenz gauge:

$$\boldsymbol{\nabla}\cdot\boldsymbol{A} + \frac{1}{c^2}\frac{\partial \phi}{\partial t} = 0. \tag{2.16}$$

The resulting equations from (2.8) are:

$$\nabla^2\boldsymbol{A} - \frac{1}{c^2}\frac{\partial^2\boldsymbol{A}}{\partial t^2} = -\mu_0\boldsymbol{J}, \tag{2.17a}$$

$$\nabla^2\phi - \frac{1}{c^2}\frac{\partial^2\phi}{\partial t^2} = -\frac{\rho}{\epsilon_0}. \tag{2.17b}$$

The scalar potential ϕ and all Cartesian components of the vector potential $\boldsymbol{A}$ are decoupled and satisfy the inhomogeneous wave equation. Moreover, the equations are (manifestly) Lorentz invariant. Note, however, that this does not make the Lorenz gauge any more valid than the alternative gauge conditions because the electric $\boldsymbol{E}$ and magnetic $\boldsymbol{B}$ fields are *always* Lorentz invariant, independent of the chosen gauge condition.

2.2 The Schrödinger equation

In 1926, E. Schrödinger presented his quantum theory to describe the wave-like behavior of matter [6]. The resulting equation is the famous Schrödinger equation. The time-dependent form for one particle is:[1]

$$\jmath\hbar\frac{\partial\psi}{\partial t} = \hat{H}\psi, \tag{2.18}$$

where $\hbar$ is the reduced Planck constant, ψ the wave function, and $\hat{H}$ the Hamiltonian operator. The wave function ψ encodes the state of a quantum mechanical system and the Schrödinger equation describes how the wave function evolves as a function of time. For example, the probability density n, which represents the probability of finding a particle in a certain region of space, is given by:

$$n = \psi^*\psi. \tag{2.19}$$

Here we assumed that the wave function is normalized. For a particle confined in a volume V, the probability of finding the particle anywhere in V equals 1:

$$\int_V n\,\mathrm{d}\boldsymbol{r} = 1. \tag{2.20}$$

For a particle subjected to a conservative force $\boldsymbol{F} = -\boldsymbol{\nabla}v$, the Hamiltonian operator is given by:

$$\hat{H} = \frac{1}{2m}\hat{\boldsymbol{p}}^2 + v = -\frac{\hbar^2}{2m}\nabla^2 + v, \tag{2.21}$$

where v is the potential and m is the particle mass.

Physical observables such as position, momentum, and energy are all represented by Hermitian operators with real eigenvalues. As such, the expectation value (in position space) for position, momentum, and energy are given by:

$$\langle\hat{\boldsymbol{r}}\rangle = \int \psi^*\boldsymbol{r}\psi\,\mathrm{d}\boldsymbol{r}\,, \tag{2.22a}$$

$$\langle\hat{\boldsymbol{p}}\rangle = -\jmath\hbar\int \psi^*\boldsymbol{\nabla}\psi\,\mathrm{d}\boldsymbol{r}\,, \tag{2.22b}$$

$$\left\langle\hat{H}\right\rangle = \int \psi^*\hat{H}\psi\,\mathrm{d}\boldsymbol{r}\,, \tag{2.22c}$$

respectively. The probability current density $\boldsymbol{J}_p$ can be derived from the Schrödinger equation and the continuity equation for probability:

$$\boldsymbol{\nabla}\cdot\boldsymbol{J}_p + \frac{\partial n}{\partial t} = 0, \tag{2.23}$$

[1] In this dissertation the wave function in position space is used, so $\psi = \psi(\boldsymbol{r}, t)$.

which states that probability is conserved. The resulting probability current density $\boldsymbol{J}_p$ is given by:

$$\boldsymbol{J}_p = \frac{1}{2m}(\psi^*\hat{\boldsymbol{p}}\psi - \psi\hat{\boldsymbol{p}}\psi^*) = -\jmath\frac{\hbar}{2m}(\psi^*\boldsymbol{\nabla}\psi - \psi\boldsymbol{\nabla}\psi^*). \tag{2.24}$$

Derivation from a Lagrangian density

The Schrödinger equation can also be derived from a Lagrangian density [7]. The advantage of using this formalism, is that it easily identifies several conserved quantities through application of Noether's theorem [8]. Further in this chapter, this formalism is developed for combined EM and QM systems, where the conservation properties might be less evident.

The notation used in this section is strongly inspired by [7]. The 4-D space components are introduced as $x^0 = ct$, $x^1 = x$, $x^2 = y$, and $x^3 = z$ along with generic field quantities η_ρ. The subscript ρ is only used to differentiate between different fields. Greek super- or subscripts refer to all four coordinates while Roman superscripts only refer to the three spatial coordinates. The coordinates x^ν are not generalized coordinates and are completely independent of each other. They enter only as explicit variables in the generalized coordinate $\eta(x^\nu)$. Therefore, derivatives of η w.r.t. x^ν can always be written as total derivatives, where we introduce the notation of a subscript ν separated from the field quantity by a comma, e.g.:

$$\eta_{,\nu} = \frac{\mathrm{d}\eta}{\mathrm{d}x^\nu}, \quad \text{and} \quad \eta_{,\nu\mu} = \frac{\mathrm{d}}{\mathrm{d}x^\nu}\frac{\mathrm{d}\eta}{\mathrm{d}x^\mu}. \tag{2.25}$$

We also adopt the Einstein summation convention where repeated indices are summed[2]. The general Euler-Lagrange equation for a Lagrangian density $\mathcal{L}$ is given by:

$$\frac{\mathrm{d}}{\mathrm{d}x^\nu}\left(\frac{\partial\mathcal{L}}{\partial\eta_{\rho,\nu}}\right) - \frac{\partial\mathcal{L}}{\partial\eta_\rho} = 0. \tag{2.26}$$

It can be shown that the energy-stress tensor $T_\mu{}^\nu$ defined by:

$$T_\mu{}^\nu = \frac{\partial\mathcal{L}}{\partial\eta_{\rho,\nu}}\eta_{\rho,\mu} - \mathcal{L}\delta_\mu{}^\nu, \tag{2.27}$$

satisfies:

$$T_\mu{}^\nu{}_{,\nu} = -\frac{\partial\mathcal{L}}{\partial x^\mu}, \tag{2.28}$$

[2]For example: The components A^i with $i \in \{1,2,3\}$ of the EM vector potential $\boldsymbol{A}$ are generalized coordinates whose values depend on the parameters x^ν. With the introduced notation, the Coulomb gauge condition ($\boldsymbol{\nabla}\cdot\boldsymbol{A} = 0$) is recast as $A^i{}_{,i} = 0$.

where $\delta_\mu{}^\nu$ is the Kronecker delta. If the Lagrangian density does not depend explicitly on x^μ then (2.28) results in a continuity equation:

$$\frac{1}{c}\frac{\mathrm{d}T_\mu{}^0}{\mathrm{d}t}+\frac{\mathrm{d}T_\mu{}^i}{\mathrm{d}x^i}=0, \tag{2.29}$$

and therefore implies a conserved quantity since:

$$\frac{1}{c}\frac{\mathrm{d}}{\mathrm{d}t}\int_V T_\mu{}^0\,\mathrm{d}\boldsymbol{r}+\int_V\frac{\mathrm{d}T_\mu{}^i}{\mathrm{d}x^i}\,\mathrm{d}\boldsymbol{r}=\frac{1}{c}\frac{\mathrm{d}}{\mathrm{d}t}\int_V T_\mu{}^0\,\mathrm{d}\boldsymbol{r}=\frac{1}{c}\frac{\mathrm{d}R_\mu}{\mathrm{d}t}=0, \tag{2.30}$$

where we have applied Gauss' divergence theorem, while also assuming that the fields vanish at the boundary of V, and introduced the integral quantity:

$$R_\mu=\int_V T_\mu{}^0\,\mathrm{d}\boldsymbol{r}\,. \tag{2.31}$$

For a single particle, the Lagrangian density is given by [7]:

$$\mathcal{L}_{\mathrm{qm}}=\frac{\jmath\hbar}{2}\left(\psi^*\dot{\psi}-\psi\dot{\psi}^*\right)-\frac{1}{2m}(\jmath\hbar\boldsymbol{\nabla}\psi^*)\cdot(-\jmath\hbar\boldsymbol{\nabla}\psi)-v\psi^*\psi, \tag{2.32}$$

where ψ and ψ^* are taken to be two independent field variables and where the dot represents the derivative w.r.t. time t. The Euler-Lagrange equation applied w.r.t. ψ^* yields:

$$\frac{\partial\mathcal{L}_{\mathrm{qm}}}{\partial\psi^*}=\frac{\jmath\hbar}{2}\dot{\psi}-v\psi, \tag{2.33a}$$

$$\frac{\mathrm{d}}{\mathrm{d}t}\frac{\partial\mathcal{L}_{\mathrm{qm}}}{\partial\dot{\psi}^*}=-\frac{\jmath\hbar}{2}\frac{\mathrm{d}}{\mathrm{d}t}\psi, \tag{2.33b}$$

$$\frac{\mathrm{d}}{\mathrm{d}x^i}\frac{\partial\mathcal{L}_{\mathrm{qm}}}{\partial\psi^*_{,i}}=-\frac{\hbar^2}{2m}\nabla^2\psi. \tag{2.33c}$$

As promised, the Schrödinger equation is recovered:

$$\jmath\hbar\frac{\mathrm{d}\psi}{\mathrm{d}t}=-\frac{\hbar}{2m}\nabla^2\psi+v\psi. \tag{2.34}$$

Now we calculate $T_0{}^0$:

$$T_0{}^0=\frac{\partial\mathcal{L}_{\mathrm{qm}}}{\partial\dot{\psi}}\dot{\psi}+\frac{\partial\mathcal{L}_{\mathrm{qm}}}{\partial\dot{\psi}^*}\dot{\psi}^*-\mathcal{L}_{\mathrm{qm}} \tag{2.35a}$$

$$=\frac{\hbar^2}{2m}(\boldsymbol{\nabla}\psi^*)\cdot(\boldsymbol{\nabla}\psi)+v\psi^*\psi \tag{2.35b}$$

which we can associate with the energy density. From (2.30) it is clear that if the Lagrangian $\mathcal{L}_{\text{qm}}$ and thus v does not explicitly depend on t, the energy defined as:

$$E = \int \left(-\frac{\hbar^2}{2m}\psi^* \nabla^2 \psi + v\psi^* \psi \right) \mathrm{d}\boldsymbol{r}\,, \tag{2.36}$$

is conserved as a function of time. Similarly, $T_i{}^0$ is determined:

$$T_i{}^0 = c\frac{\jmath\hbar}{2}\left(\psi^* \frac{\mathrm{d}\psi}{\mathrm{d}x^i} - \psi \frac{\mathrm{d}\psi^*}{\mathrm{d}x^i} \right) = -cmJ_{p,i}, \tag{2.37}$$

where $J_{p,i}$ is the i-th component of the probability current density $\boldsymbol{J}_p$ (2.24). Consequently, if the Lagrangian $\mathcal{L}_{\text{qm}}$ and thus potential v does not explicitly depend on x^i, then the total momentum $m\int_V J_{p,i}\,\mathrm{d}\boldsymbol{r}$ is conserved in that direction. The conservation properties of the energy-stress tensor are a special case of Noether's theorem. Similarly, probability conservation and the probability continuity equation (2.23) can be derived from Noether's theorem based on the invariance of the Lagrangian under a transformation $\psi' = \psi e^{\jmath\epsilon}$ and $\psi^{*\prime} = \psi^* e^{-\jmath\epsilon}$. The proof is omitted here.

Particle in electromagnetic fields

The influence of electromagnetic fields on a particle with charge q is included via the potentials $\boldsymbol{A}$ and ϕ by introducing minimal coupling. As such we neglect any coupling of the EM fields with the intrinsic magnetic moment of charged particles. The minimally coupled Lagrangian density $\mathcal{L}_{\text{mc}}$ is given by [9]:

$$\begin{aligned}\mathcal{L}_{\text{mc}} = {} & \frac{\jmath\hbar}{2}\left(\psi^*\dot{\psi} - \psi\dot{\psi}^*\right) \\ & - \frac{1}{2m}((\jmath\hbar\boldsymbol{\nabla} - q\boldsymbol{A})\psi^*)\cdot((-\jmath\hbar\boldsymbol{\nabla} - q\boldsymbol{A})\psi) - (v + q\phi)\psi^*\psi.\end{aligned} \tag{2.38}$$

The equations of motion are calculated using:

$$\frac{\partial \mathcal{L}_{\text{mc}}}{\partial \psi^*} = \frac{\jmath\hbar}{2}\dot{\psi} + \frac{q}{2m}\boldsymbol{A}\cdot(-\jmath\hbar\boldsymbol{\nabla} - q\boldsymbol{A})\psi - (v + q\phi)\psi, \tag{2.39a}$$

$$\frac{\mathrm{d}}{\mathrm{d}t}\frac{\partial \mathcal{L}_{\text{mc}}}{\partial \dot{\psi}^*} = -\frac{\jmath\hbar}{2}\frac{\mathrm{d}}{\mathrm{d}t}\psi, \tag{2.39b}$$

$$\frac{\mathrm{d}}{\mathrm{d}x^i}\frac{\partial \mathcal{L}_{\text{mc}}}{\partial \psi^*_{,i}} = -\frac{\hbar^2}{2m}\nabla^2\psi + \jmath\frac{q\hbar}{2m}\frac{\mathrm{d}}{\mathrm{d}x^i}(A_i\psi), \tag{2.39c}$$

such that the Euler-Lagrange equations (2.26) yield the minimally-coupled time-dependent single-particle Schrödinger equation:

$$\jmath\hbar\frac{\partial \psi}{\partial t} = \frac{1}{2m}(-\jmath\hbar\boldsymbol{\nabla} - q\boldsymbol{A})^2\psi + (v + q\phi)\psi. \tag{2.40}$$

Again, from the phase invariance of the Lagrangian $\mathcal{L}_{\text{mc}}$ (2.38), we can derive the continuity equation for probability density and current density (2.23) but with $\boldsymbol{J}_p$ now given by:

$$\begin{aligned}\boldsymbol{J}_p &= \frac{1}{2m}(\psi^*(-\jmath\hbar\boldsymbol{\nabla} - q\boldsymbol{A})\psi + \psi(\jmath\hbar\boldsymbol{\nabla} - q\boldsymbol{A})\psi^*) \\ &= -\jmath\frac{\hbar}{2m}(\psi^*\boldsymbol{\nabla}\psi - \psi\boldsymbol{\nabla}\psi^*) - \frac{q}{m}\boldsymbol{A}\psi^*\psi.\end{aligned} \tag{2.41a}$$

Similarly, we derive the energy density and momentum density as follows:

$$T_0{}^0 = \frac{1}{2m}((\jmath\hbar\boldsymbol{\nabla} - q\boldsymbol{A})\psi^*)\cdot((-\jmath\hbar\boldsymbol{\nabla} - q\boldsymbol{A})\psi) + (v + q\phi)\psi^*\psi, \tag{2.42}$$

$$T_i{}^0 = -cmJ_{p,i}. \tag{2.43}$$

The total energy and momentum will now be conserved only if v, ϕ, and $\boldsymbol{A}$ are time and space independent.

In Section 2.1, it was shown that the potentials $\boldsymbol{A}$ and ϕ are only defined up to a gauge transformation. Performing a gauge transformation like (2.9) will simultaneously transform the wave function as:

$$\psi' = \psi e^{\jmath\frac{q\chi}{\hbar}}. \tag{2.44}$$

The new wave function ψ' also satisfies the Schrödinger equation (2.40) but with the transformed potentials $\boldsymbol{A}'$ and ϕ'.

2.3 The Kohn-Sham equations

In this section, we succinctly introduce time-dependent density-functional theory (TDDFT) which proposes a scalable approach to treat the many-body interactions present in real systems. For now, the influence of magnetic fields is neglected.

2.3.1 The time-dependent Kohn-Sham equations

The many-particle Schrödinger equation for an N-electron problem is [10]:

$$\jmath\hbar\frac{\partial\psi(\boldsymbol{r}_1,\sigma_1,\ldots,\boldsymbol{r}_N,\sigma_N,t)}{\partial t} = \hat{H}\psi(\boldsymbol{r}_1,\sigma_1,\ldots,\boldsymbol{r}_N,\sigma_N,t), \tag{2.45}$$

with $\psi(\boldsymbol{r}_1,\sigma_1,\ldots,\boldsymbol{r}_N,\sigma_N,t)$ the anti-symmetric wave function, $\boldsymbol{r}_i$ and σ_i the position and spin variable of the i-th particle and $\hat{H}$ the Hamiltonian operator:

$$\hat{H} = -\frac{\hbar^2}{2m}\sum_{i=1}^{N}\nabla_i^2 + \frac{q^2}{4\pi\epsilon_0}\sum_{i=1}^{N}\sum_{j>i}\frac{1}{\left|\boldsymbol{r}_i - \boldsymbol{r}_j\right|} + \sum_{i=1}^{N}v(\boldsymbol{r}_i,t). \tag{2.46}$$

We only include the electronic degrees of freedom and assume that the atomic nuclei are clamped at certain positions, resulting in a static Coulomb potential that is included as part of the background potential v.

The probability density $n(\boldsymbol{r},t)$ for this many-particle system is determined as:

$$n(\boldsymbol{r},t) = \langle\psi|\sum_{i=1}^{N}\delta(\boldsymbol{r}-\boldsymbol{r}_i)|\psi\rangle\,. \tag{2.47}$$

Similar to the single-particle case, the probability density also satisfies the continuity equation (2.23) but with the probability current density $\boldsymbol{J}_p$ now given by:

$$\boldsymbol{J}_p = -\jmath\frac{\hbar}{2m}\langle\psi|(\boldsymbol{\nabla}_i\delta(\boldsymbol{r}-\boldsymbol{r}_i)+\delta(\boldsymbol{r}-\boldsymbol{r}_i)\boldsymbol{\nabla}_i)|\psi\rangle\,. \tag{2.48}$$

Given an initial state ψ_0, the Schrödinger equation maps any external potential $v(\boldsymbol{r},t)$ to a time-dependent wave function which is then mapped to a time-dependent density n. However, the Runge-Gross theorem [11] states that this mapping can be reversed where instead of the wave function, the time-dependent density determines the dynamics of the system:

Theorem 1 (Runge-Gross)**.** *For every single-particle potential $v(\boldsymbol{r},t)$ which can be expanded into a Taylor series with respect to the time coordinate around $t = t_0$, a map $\mathcal{G} : v(\boldsymbol{r},t) \to n(\boldsymbol{r},t)$ is defined by solving the time-dependent Schrödinger equation with a fixed initial state $\psi(t_0) = \psi_0$ and calculating the corresponding densities $n(\boldsymbol{r},t)$. This map can be inverted up to an additive, merely time-dependent function in the potential.*

As such, the Hamiltonian and wave function are functionals of the density. However, to make this relation useful in practice, we need the Van Leeuwen theorem [12]:

Theorem 2 (Van Leeuwen)**.** *For a time-dependent density $n(\boldsymbol{r},t)$ associated with a many-body system with a given particle-particle interaction $w(|\boldsymbol{r}-\boldsymbol{r}'|)$, external potential $v(\boldsymbol{r},t)$, and initial state ψ_0, there exists a different many-body system featuring an interaction $w'(|\boldsymbol{r}-\boldsymbol{r}'|)$ and a unique external potential $v'(\boldsymbol{r},t)$ – up to a purely time-dependent function $c(t)$ – which reproduces the same time-dependent density. The initial state ψ_0' in this system must be chosen such that it correctly yields the given density and its time derivative at the initial time.*

If the second interaction is set equal to zero, i.e., $w'(|\boldsymbol{r}-\boldsymbol{r}'|) = 0$, and we assume that there exists a noninteracting initial stateor ψ_0', then we know that there is a unique potential $v_{KS}(\boldsymbol{r},t)$ which produces $n(\boldsymbol{r},t)$ for all times $t > t_0$.

We now focus on systems which are in their ground state at $t = t_0$, and are excited by an external potential at $t > t_0$ such that the potential v is expressed as[3]:

$$v(\boldsymbol{r}, t) = v_0(\boldsymbol{r}) + v_1(\boldsymbol{r}, t)\Theta(t - t_0), \tag{2.49}$$

where Θ is the Heaviside function. For these systems, the wave function is given by a single Slater determinant [13]:

$$\psi(\boldsymbol{r}_1, \sigma_1, \ldots, \boldsymbol{r}_N, \sigma_N, t) = \frac{1}{\sqrt{N!}} \begin{vmatrix} \psi_1(\boldsymbol{r}_1, t) & \cdots & \psi_N(\boldsymbol{r}_1, t) \\ \vdots & & \vdots \\ \psi_1(\boldsymbol{r}_N, t) & \cdots & \psi_N(\boldsymbol{r}_N, t) \end{vmatrix}, \tag{2.50}$$

with $|\cdot|$ representing the determinant, and where the single-particle wave functions satisfy the time-dependent Kohn-Sham equations:

$$\jmath\hbar \frac{\partial \psi_i}{\partial t} = \left(-\frac{\hbar^2}{2m}\nabla^2 + v_{KS}[n] \right)\psi_i, \quad \forall i = 1, \ldots, N, \tag{2.51}$$

with the density determined by:

$$n(\boldsymbol{r}, t) = \sum_i |\psi_i(\boldsymbol{r}, t)|^2. \tag{2.52}$$

The time-dependent effective potential v_{KS} is given by [14]:

$$v_{KS}[n](\boldsymbol{r}, t) = v(\boldsymbol{r}, t) + \frac{q^2}{4\pi\epsilon_0} \int \frac{n(\boldsymbol{r}', t)}{|\boldsymbol{r}' - \boldsymbol{r}|}\, \mathrm{d}\boldsymbol{r}' + v_{\mathrm{xc}}[n](\boldsymbol{r}, t). \tag{2.53}$$

The second term on the r.h.s. is the Hartree potential v_H, which is readily identified with $q\phi$ where ϕ is the EM scalar potential in the Coulomb gauge (2.13). The last term *defines* the exchange-correlation potential $v_{\mathrm{xc}}[n](\boldsymbol{r}, t)$, which will be discussed below in Section 2.3.2.

The initial single-particle wave functions $\psi_i(\boldsymbol{r}, t = t_0)$ satisfy the static Kohn-Sham equations:

$$\left(-\frac{\hbar^2}{2m}\nabla^2 + v_{KS}[n(\boldsymbol{r}, t_0)] \right)\psi_i(\boldsymbol{r}, t_0) = \epsilon_i \psi_i(\boldsymbol{r}, t_0), \quad \forall i = 1, \ldots, N. \tag{2.54}$$

Only the wave functions that were initially occupied are propagated.

In principle, the time-dependent Kohn-Sham equations (2.51) reproduce the exact density for the many-particle system. However, the exchange-correlation potential is unknown and has to be approximated.

[3]Note that the static background potential $v_0(\boldsymbol{r})$ stems, e.g., from the Coulomb interaction with the nuclei and that the excitation potential $v_1(\boldsymbol{r}, t)$ stems, e.g., from an externally applied uniform electric field $v_1(\boldsymbol{r}, t) = -q\boldsymbol{r} \cdot \boldsymbol{E}(t)$.

2.3.2 Adiabatic local-density approximation

In this dissertation we will work in the adiabatic approximation, which implies that the time-dependent exchange-correlation potential at time t is calculated using the instantaneous density:

$$v_{\mathrm{xc}}^{\mathrm{adiabatic}}(\boldsymbol{r},t) = v_{\mathrm{xc}}^{0}[n'](\boldsymbol{r})|_{n'(\boldsymbol{r})\to n(\boldsymbol{r},t)}, \tag{2.55}$$

where v_{xc}^{0} is an exchange-correlation potential taken from static DFT. Although systems rarely evolve truly adiabatic, this approximation has proven to work remarkably well in many applications. Additionally, we will also adopt the local-density approximation (LDA), resulting in the adiabatic local-density approximation (ALDA). Within this approximation, the exchange-correlation energy $E_{\mathrm{xc}}^{\mathrm{ALDA}}$ is determined via the exchange-correlation energy per particle of a homogeneous electron gas $\epsilon_{\mathrm{xc}}^{h}$ evaluated at the local and instantaneous density:

$$E_{\mathrm{xc}}^{\mathrm{ALDA}}[n] = \int n(\boldsymbol{r},t)\epsilon_{\mathrm{xc}}^{h}(n(\boldsymbol{r},t))\,\mathrm{d}\boldsymbol{r}\,. \tag{2.56}$$

The corresponding exchange-correlation potential $v_{\mathrm{xc}}^{\mathrm{ALDA}}$ reads:

$$v_{\mathrm{xc}}^{\mathrm{ALDA}} = \frac{\delta E_{\mathrm{xc}}^{\mathrm{ALDA}}[n]}{\delta n(\boldsymbol{r},t)} = \frac{\partial(n(\boldsymbol{r},t)\epsilon_{\mathrm{xc}}^{\mathrm{ALDA}}(n(\boldsymbol{r},t)))}{\partial n(\boldsymbol{r},t)}, \tag{2.57}$$

where $\delta E_{\mathrm{xc}}^{\mathrm{ALDA}}[n]/\delta n$ is the functional derivative w.r.t. n. The exchange part is exactly known in the homogeneous case [15]. For the correlation energy, we use the parametrization proposed by Perdew and Zunger [16].

2.3.3 Time-dependent current-density-functional theory

To include magnetic fields into the theory, we have to upgrade TDDFT to time-dependent *current* density functional theory (TDCDFT), where instead of the density, the current density is the fundamental variable. This theory was developed in [17] but a simpler and more complete derivation was given in [18]. The resulting Kohn-Sham equations are given by:

$$\jmath\hbar\frac{\partial\psi_i}{\partial t} = \left(\frac{1}{2m}(-\jmath\hbar\boldsymbol{\nabla} - q\boldsymbol{A}_{KS})^2 + v_{KS}\right)\psi_i, \quad \forall i = 1,\ldots,N, \tag{2.58}$$

with a density n defined by (2.52) and the current density:

$$\boldsymbol{J}_p = \frac{-\jmath\hbar}{2m}\sum_{i=1}^{N}\left(\psi_i^*\boldsymbol{\nabla}\psi_i - \psi_i\boldsymbol{\nabla}\psi_i^*\right) - \frac{q}{m}\boldsymbol{A}_{KS}n, \tag{2.59}$$

where the exchange-correlation potentials are defined by the relations:

$$v_{KS} = v + v_H + v_{\mathrm{xc}}, \tag{2.60a}$$

$$\boldsymbol{A}_{KS} = \boldsymbol{A} + \boldsymbol{A}_{\mathrm{xc}}. \tag{2.60b}$$

In this work, we will neglect $\boldsymbol{A}_{\mathrm{xc}}$ in the assumption that the magnetic fields are weak, similar to [19–22].

We note here that this formulation of TDCDFT is not compatible with the original formulation of static CDFT, proposed in [23], which uses the density and *paramagnetic* current density (2.48) as the fundamental variables. However, it is possible to formulate static CDFT using the total current density (2.59) instead [24]. As such, this formulation can be used as the initial condition for TDCDFT. Still, if the initial state is an unperturbed ground state without a magnetic field, it is possible to use static DFT instead.

For further reading on TDDFT or TDCDFT the reader is referred to [10].

2.4 The Maxwell-Schrödinger and Maxwell-Kohn-Sham systems

In this section we consider the self-consistent coupling of EM and QM systems. This is a semiclassical approach, where matter is treated quantum mechanically while the EM fields are treated classically. First, we examine a single charged particle interacting with the EM field. Second, the theory of TDDFT from Section 2.3 is expanded to include the self-consistent coupling to EM fields. However, although we include magnetic fields, we do not fully upgrade the theory to TDCDFT as we do not introduce the current density as a fundamental variable. The resulting framework is a tractable way to describe the interaction between EM fields and quantum systems.

2.4.1 Maxwell-Schrödinger

To self-consistently couple the single-particle Schrödinger equation and Maxwell's equations, the following Lagrangian density is proposed:

$$\begin{aligned}\mathcal{L}_{\mathrm{ms}} = \frac{\jmath\hbar}{2}\left(\psi^*\dot{\psi} - \psi\dot{\psi}^*\right) - \frac{1}{2m}((\jmath\hbar\boldsymbol{\nabla} - q\boldsymbol{A})\psi^*)\cdot((-\jmath\hbar\boldsymbol{\nabla} - q\boldsymbol{A})\psi) \\ -(v + q\phi)\psi^*\psi + \frac{1}{2}\left(\epsilon_0\left(-\dot{\boldsymbol{A}} - \boldsymbol{\nabla}\phi\right)^2 - \frac{1}{\mu_0}(\boldsymbol{\nabla}\times\boldsymbol{A})^2\right).\end{aligned} \tag{2.61}$$

This is the sum of the minimally-coupled Lagrangian density for a single charged particle $\mathcal{L}_{\mathrm{mc}}$ (2.38) and the classical Lagrangian density for the EM field $\mathcal{L}_{\mathrm{em}}$:

$$\mathcal{L}_{\mathrm{em}} = \frac{1}{2}\left(\epsilon_0\boldsymbol{E}^2 - \frac{1}{\mu_0}\boldsymbol{B}^2\right) = \frac{1}{2}\left(\epsilon_0\left(-\dot{\boldsymbol{A}} - \boldsymbol{\nabla}\phi\right)^2 - \frac{1}{\mu_0}(\boldsymbol{\nabla}\times\boldsymbol{A})^2\right). \tag{2.62}$$

To derive the equations of motion, we consider $\boldsymbol{A}$, ϕ, ψ and ψ^* to be independent field variables. As before, the Euler-Lagrange equation (2.26) w.r.t. ψ^* yields the minimally-coupled Schrödinger equation (2.40). Next, (2.26) w.r.t. ϕ is calculated

and using:

$$\frac{\partial \mathcal{L}_{\text{ms}}}{\partial \phi} = -q\psi^*\psi, \quad \frac{\partial \mathcal{L}_{\text{ms}}}{\partial \dot{\phi}} = 0, \quad \text{and} \quad \frac{\partial \mathcal{L}_{\text{ms}}}{\partial \phi_{,i}} = -\epsilon_0 E^i, \tag{2.63}$$

results in Gauss' electric law:

$$\boldsymbol{\nabla} \cdot \boldsymbol{E} = \frac{\rho_q}{\epsilon_0}, \tag{2.64}$$

with $\rho_q = q\psi^*\psi$ the charge density. For the application of (2.26) w.r.t. the components of A_j of $\boldsymbol{A}$ we use:

$$\frac{\partial \mathcal{L}_{\text{ms}}}{\partial A_j} = \frac{q}{2m}\left(\psi^*\left(-\jmath\hbar\frac{\mathrm{d}}{\mathrm{d}x^j} - qA_j\right)\psi + \psi\left(\jmath\hbar\frac{\mathrm{d}}{\mathrm{d}x^j} - qA_j\right)\psi^*\right), \tag{2.65a}$$

$$\frac{\mathrm{d}}{\mathrm{d}t}\frac{\partial \mathcal{L}_{\text{ms}}}{\partial \dot{A}_j} = -\epsilon_0 \frac{\mathrm{d}E^j}{\mathrm{d}t}, \tag{2.65b}$$

$$\frac{\mathrm{d}}{\mathrm{d}x^i}\frac{\partial \mathcal{L}_{\text{ms}}}{\partial A_{j,i}} = \frac{1}{\mu_0}(\boldsymbol{\nabla} \times \boldsymbol{B})^j. \tag{2.65c}$$

The terms in (2.65) together with the expression (2.41) of the probability current density $\boldsymbol{J}_p$ yield Ampères law:

$$\boldsymbol{\nabla} \times \boldsymbol{B} = \mu_0\left(\boldsymbol{J}_q + \epsilon_0\frac{\partial \boldsymbol{E}}{\partial t}\right), \tag{2.66}$$

with the quantum current density $\boldsymbol{J}_q = q\boldsymbol{J}_p$ and the probability current density $\boldsymbol{J}_p$. The continuity equation (2.1) results again from the phase invariance of $\mathcal{L}_{\text{ms}}$. Faraday's law (2.2a) is retrieved by taking the curl of (2.7b) and Gauss' magnetic law (2.3b) by taking the divergence of (2.7a). As such, we retrieve the full set of Maxwell's equations (2.2)–(2.3).

If the potential v does not explicitly depend on time t, the total energy should be a conserved quantity. To obtain a gauge-invariant expression for this energy density, however, we have to add the extra term $\delta T_\mu{}^\nu$ [9]:

$$\delta T_\mu{}^\nu = \frac{1}{\mu_0}\frac{\mathrm{d}}{\mathrm{d}x^\lambda}\left(A_\mu F^{\nu\lambda}\right), \tag{2.67}$$

where $A^\mu = (\phi/c, \boldsymbol{A})$, $A_\mu = (-\phi/c, \boldsymbol{A})$, and $F^{\mu\nu}$ is the electromagnetic tensor:

$$F^{\mu\nu} = \begin{bmatrix} 0 & E_x/c & E_y/c & E_z/c \\ -E_x/c & 0 & B_z & -B_y \\ -E_y/c & -B_z & 0 & B_x \\ -E_z/c & B_y & -B_x & 0 \end{bmatrix}. \tag{2.68}$$

The added term $\delta T_\mu{}^\nu$ to the new energy-stress tensor $\epsilon_\mu{}^\nu = T_\mu{}^\nu + \delta T_\mu{}^\nu$ does not change its conservation properties because:

$$\delta T_\mu{}^\nu{}_{,\nu} = \frac{1}{\mu_0}\frac{\mathrm{d}}{\mathrm{d}x^\nu}\frac{\mathrm{d}}{\mathrm{d}x^\lambda}\big(A_\mu F^{\nu\lambda}\big), \tag{2.69a}$$

$$= -\frac{1}{\mu_0}\frac{\mathrm{d}}{\mathrm{d}x^\lambda}\frac{\mathrm{d}}{\mathrm{d}x^\nu}\big(A_\mu F^{\lambda\nu}\big), \tag{2.69b}$$

$$= -\frac{1}{\mu_0}\frac{\mathrm{d}}{\mathrm{d}x^\nu}\frac{\mathrm{d}}{\mathrm{d}x^\lambda}\big(A_\mu F^{\nu\lambda}\big) = 0, \tag{2.69c}$$

where we used that $F^{\mu\nu} = -F^{\nu\mu}$ and switched the order of the derivatives to go from (2.69a) to (2.69b). To go from (2.69b) to (2.69c) we simply relabeled λ and ν. As such, from (2.28), both $\epsilon_\mu{}^\nu$ and $T_\mu{}^\nu$ satisfy:

$$\epsilon_\mu{}^\nu{}_{,\nu} = T_\mu{}^\nu{}_{,\nu} = -\frac{\partial \mathcal{L}_{\mathrm{ms}}}{\partial x^\mu}. \tag{2.70}$$

The new energy density $\epsilon_0{}^0$ is given by:

$$\epsilon_0{}^0 = \frac{\partial \mathcal{L}_{\mathrm{ms}}}{\partial \dot{\psi}}\dot{\psi} + \frac{\partial \mathcal{L}_{\mathrm{ms}}}{\partial \dot{\psi}^*}\dot{\psi}^* + \frac{\partial \mathcal{L}_{\mathrm{ms}}}{\partial \dot{A}_\mu}\dot{A}_\mu - \mathcal{L}_{\mathrm{ms}} + \frac{1}{\mu_0}\frac{\mathrm{d}}{\mathrm{d}x^i}\big(A_0 F^{0i}\big) \tag{2.71a}$$

$$= \epsilon_0 \boldsymbol{E}\cdot(\boldsymbol{E} + \boldsymbol{\nabla}\phi) + \frac{1}{2m}((\imath\hbar\boldsymbol{\nabla} - q\boldsymbol{A})\psi^*)\cdot((-\imath\hbar\boldsymbol{\nabla} - q\boldsymbol{A})\psi) + (v + q\phi)\psi^*\psi - \frac{1}{2}\left(\epsilon_0\boldsymbol{E}^2 - \frac{1}{\mu_0}(\boldsymbol{\nabla}\times\boldsymbol{A})^2\right) - \epsilon_0\boldsymbol{\nabla}\cdot(\phi\boldsymbol{E}) \tag{2.71b}$$

$$= \frac{1}{2m}((\imath\hbar\boldsymbol{\nabla} - q\boldsymbol{A})\psi^*)\cdot((-\imath\hbar\boldsymbol{\nabla} - q\boldsymbol{A})\psi) + v\psi^*\psi + \frac{1}{2}\left(\epsilon_0\boldsymbol{E}^2 + \frac{1}{\mu_0}\boldsymbol{B}^2\right) + \epsilon_0\boldsymbol{E}\cdot\boldsymbol{\nabla}\phi + \epsilon_0\phi\,\boldsymbol{\nabla}\cdot\boldsymbol{E} - \epsilon_0\boldsymbol{\nabla}\cdot(\phi\boldsymbol{E}) \tag{2.71c}$$

$$= \frac{1}{2m}((\imath\hbar\boldsymbol{\nabla} - q\boldsymbol{A})\psi^*)\cdot((-\imath\hbar\boldsymbol{\nabla} - q\boldsymbol{A})\psi) + v\psi^*\psi + \frac{1}{2}\left(\epsilon_0\boldsymbol{E}^2 + \frac{1}{\mu_0}\boldsymbol{B}^2\right), \tag{2.71d}$$

where the scalar EM potential ϕ has been swallowed by the EM energy. The total energy is calculated as:

$$E = \int_V \left(\frac{1}{2m}\psi^*(-\imath\hbar\boldsymbol{\nabla} - q\boldsymbol{A})^2\psi + v\psi^*\psi + \frac{1}{2}\left(\epsilon_0\boldsymbol{E}^2 + \frac{1}{\mu_0}\boldsymbol{B}^2\right)\right)\mathrm{d}\boldsymbol{r}\,. \tag{2.72}$$

The first term in this expression can be easily derived by expanding the corresponding terms in (2.71d) and applying integration by parts. Momentum in a specific direction is conserved if v does not depend on the corresponding coordinate.

Therefore, we determine $\epsilon_i{}^0$ using:

$$c\left(\frac{\partial \mathcal{L}_{\text{ms}}}{\partial \dot{\psi}^*}\frac{\mathrm{d}\psi^*}{\mathrm{d}x^i}+\frac{\partial \mathcal{L}_{\text{ms}}}{\partial \dot{\psi}}\frac{\mathrm{d}\psi}{\mathrm{d}x^i}\right)=c\frac{\jmath\hbar}{2}\left(\psi^*\frac{\mathrm{d}}{\mathrm{d}x^i}\psi-\psi\frac{\mathrm{d}}{\mathrm{d}x^i}\psi^*\right), \tag{2.73a}$$

$$c\frac{\partial \mathcal{L}_{\text{ms}}}{\partial \dot{\phi}}\frac{\mathrm{d}\phi}{\mathrm{d}x^i}=0, \tag{2.73b}$$

$$c\frac{\partial \mathcal{L}_{\text{ms}}}{\partial \dot{A}_j}\frac{\mathrm{d}A_j}{\mathrm{d}x^i}=-\frac{E^j}{Z_0}\frac{\mathrm{d}A_j}{\mathrm{d}x^i}, \tag{2.73c}$$

$$\frac{1}{\mu_0}\left(A_{i,\mu}F^{0\mu}+A_iF^{0\mu}{}_{,\mu}\right)=\frac{1}{Z_0}\left(\frac{\mathrm{d}A_i}{\mathrm{d}x^j}E^j+A_i\frac{\mathrm{d}E^j}{\mathrm{d}x^j}\right)=\frac{E^j}{Z_0}\frac{\mathrm{d}A_i}{\mathrm{d}x^j}+c\rho_qA_i, \tag{2.73d}$$

where $Z_0=\sqrt{\mu_0/\epsilon_0}$ is the impedance of free space. Note that (2.73a) and the last term in (2.73d) can be combined using the probability density $\boldsymbol{J}_p$ from (2.41) as:

$$c\frac{\jmath\hbar}{2}\left(\psi^*\frac{\mathrm{d}}{\mathrm{d}x^i}\psi-\psi\frac{\mathrm{d}}{\mathrm{d}x^i}\psi^*\right)+c\rho_qA_i=-cmJ_{p,i}. \tag{2.74}$$

Summing (2.73c) and the remaining terms in (2.73d) yields:

$$-\frac{1}{Z_0}E^j\left(\frac{\mathrm{d}A_j}{\mathrm{d}x^i}-\frac{\mathrm{d}A_i}{\mathrm{d}x^j}\right)=-\frac{E^j}{Z_0}\left(\delta_i{}^a\delta_j{}^b-\delta_i{}^b\delta_j{}^a\right)\frac{\mathrm{d}A_b}{\mathrm{d}x^a} \tag{2.75a}$$

$$=-\frac{E^j}{Z_0}\varepsilon_{kij}\varepsilon^{kab}\frac{\mathrm{d}A_b}{\mathrm{d}x^a} \tag{2.75b}$$

$$=-\frac{1}{Z_0}\varepsilon_{kij}E^jB^k \tag{2.75c}$$

$$=-\frac{1}{Z_0}\varepsilon_{ijk}E^jB^k=-\frac{1}{Z_0}(\boldsymbol{E}\times\boldsymbol{B})_i, \tag{2.75d}$$

where ε_{ijk} is the Levi-Civita symbol. Adding (2.74) and (2.75) yields:

$$\epsilon_i{}^0=-c\left(mJ_{p,i}+\epsilon_0(\boldsymbol{E}\times\boldsymbol{B})_i\right). \tag{2.76}$$

We identify the momentum density:

$$\boldsymbol{p}=\frac{1}{2}(\psi^*(-\jmath\hbar\boldsymbol{\nabla})\psi+\psi(\jmath\hbar\boldsymbol{\nabla})\psi^*-2q\boldsymbol{A}\psi^*\psi)+\epsilon_0\boldsymbol{E}\times\boldsymbol{B}, \tag{2.77}$$

where the first term corresponds to the QM momentum density $\boldsymbol{p}_{\text{qm}}=m\boldsymbol{J}_p$ and the second term to the EM momentum $\boldsymbol{p}_{\text{em}}=\boldsymbol{S}/c^2$, where $\boldsymbol{S}=\boldsymbol{E}\times\boldsymbol{B}/\mu_0$ is the Poynting vector.

Background charge

In many applications encountered in literature [25–37], the Maxwell-Schrödinger system is initialized with a wave function ψ in an energy eigenstate of a static

potential v, thus satisfying the eigenvalue equation:

$$\left(-\frac{\hbar^2}{2m}\nabla^2 + v\right)\psi = E\psi. \tag{2.78}$$

The remaining field quantities $\boldsymbol{A}$, $\boldsymbol{B}$, $\boldsymbol{E}$, and ϕ are all zero. Subsequently, the system is excited by an external plane wave or current density to study the dynamical properties of interest. Note, however, that (2.64) is not satisfied in this case. To fix this, an extra term $\mathcal{L}' = qn_0\phi$ must be added to the Lagrangian $\mathcal{L}_{\text{ms}}$. This changes Gauss' electric law to:

$$\boldsymbol{\nabla}\cdot\boldsymbol{E} = \frac{\rho_q - qn_0}{\epsilon_0}, \tag{2.79}$$

while leaving all other equations of motion unaltered. By setting $n_0 = \rho_q(t=0)/q$, we can initialize our fields with zero $\boldsymbol{A}$, $\boldsymbol{B}$, $\boldsymbol{E}$, and ϕ. However, we have inadvertently added a fictional background charge to the model. Moreover, this background charge depends in most cases explicitly on the spatial coordinates x^i, such that momentum will *not* be conserved even in the case of $v = 0$.

2.4.2 Maxwell-Kohn-Sham

In this section, we present a model for the description of many-particle QM systems interacting with EM fields. The model is based on TDDFT as presented in Section 2.3 and also includes the influence of a vector potential $\boldsymbol{A}$. Similar systems have been discussed recently [20, 22, 38–42]. The influence of an exchange-correlation vector potential $\boldsymbol{A}_{\text{xc}}$ is neglected under the assumption of weak magnetic fields. Also, we use the ALDA approximation for the exchange-correlation potential and assume that the exchange-correlation energy density is a functional of the density only.

The proposed Lagrangian density for N electrons is given by:

$$\begin{aligned}\mathcal{L} = \sum_{i=1}^{N}\Bigg[&\frac{\jmath\hbar}{2}\left(\psi_i^*\dot{\psi}_i - \psi_i\dot{\psi}_i^*\right) - \psi_i^*(v + q\phi + \epsilon_{\text{xc}}[n])\psi_i \\ &- \frac{1}{2m}\left((\jmath\hbar\boldsymbol{\nabla} - q\boldsymbol{A})\psi_i^*\right)\cdot\left((-\jmath\hbar\boldsymbol{\nabla} - q\boldsymbol{A})\psi_i\right)\Bigg] \\ &+ \frac{1}{2}\left(\epsilon_0\left(-\dot{\boldsymbol{A}} - \boldsymbol{\nabla}\phi\right)^2 - \frac{1}{\mu_0}(\boldsymbol{\nabla}\times\boldsymbol{A})^2\right).\end{aligned} \tag{2.80}$$

The Hartree potential v_H from (2.53) is not included here since it is simply the static limit of $q\phi$. The same steps as in Section 2.4.1, but where ψ_i and ψ_i^* are treated as independent variables for all $i = 1,\ldots,N$, lead to the Maxwell-Kohn-

Sham equations:

$$\boldsymbol{\nabla}\cdot\boldsymbol{E}=\frac{\rho_q}{\epsilon_0}, \tag{2.81a}$$

$$\boldsymbol{\nabla}\times\boldsymbol{B}=\mu_0\left(q\boldsymbol{J}_p+\epsilon_0\frac{\partial\boldsymbol{E}}{\partial t}\right), \tag{2.81b}$$

$$\jmath\hbar\frac{\partial\psi_i}{\partial t}=\frac{1}{2m}(-\jmath\hbar\boldsymbol{\nabla}-q\boldsymbol{A})^2\psi_i+(q\phi+v+v_{\mathrm{xc}})\psi_i,\quad\forall i. \tag{2.81c}$$

with

$$\rho_q=q\sum_i\psi_i^*\psi_i, \tag{2.82a}$$

$$\boldsymbol{J}_p=\frac{1}{2m}\sum_i\left(\psi_i^*(-\jmath\hbar\boldsymbol{\nabla}-q\boldsymbol{A})\psi_i+\psi_i(\jmath\hbar\boldsymbol{\nabla}-q\boldsymbol{A})\psi_i^*\right). \tag{2.82b}$$

Again introducing a term $\delta T_\mu{}^\nu$ (2.67), the energy density is derived as:

$$\begin{aligned}\epsilon_0{}^0=\sum_i\Bigg(\frac{1}{2m}\left((\jmath\hbar\boldsymbol{\nabla}-q\boldsymbol{A})\psi_i^*\right)\cdot((-\jmath\hbar\boldsymbol{\nabla}-q\boldsymbol{A})\psi_i)+\psi_i^*v\psi_i\Bigg)\\+n\epsilon_{\mathrm{xc}}+\frac{1}{2}\left(\epsilon_0\boldsymbol{E}^2+\frac{1}{\mu_0}\boldsymbol{B}^2\right).\end{aligned} \tag{2.83}$$

The terms involving ϕ have again been swallowed by the electromagnetic energy. The resulting total energy is given by:

$$\begin{aligned}E=\sum_i\int\left(\frac{1}{2m}\psi_i^*(-\jmath\hbar\boldsymbol{\nabla}-q\boldsymbol{A})^2\psi_i+v\psi_i^*\psi_i\right)\mathrm{d}\boldsymbol{r}\\+E_{\mathrm{xc}}+\frac{1}{2}\int\left(\epsilon_0\boldsymbol{E}^2+\frac{1}{\mu_0}\boldsymbol{B}^2\right)\mathrm{d}\boldsymbol{r}\,.\end{aligned} \tag{2.84}$$

We further split the total energy to easily identify the single-particle energies ϵ_i:

$$E=\sum_i\epsilon_i-\int n(v_{\mathrm{xc}}+q\phi)\,\mathrm{d}\boldsymbol{r}+E_{\mathrm{xc}}+E_{\mathrm{em}}, \tag{2.85}$$

where ϵ_i is given by:

$$\epsilon_i=\langle\psi_i|\hat{H}_{KS}|\psi_i\rangle\,,\quad\text{and}\quad\hat{H}_{KS}=\frac{1}{2m}(-\jmath\hbar\boldsymbol{\nabla}-q\boldsymbol{A})^2+v+q\phi+v_{\mathrm{xc}}. \tag{2.86}$$

References

1. Maxwell, J. C. LI. On physical lines of force. *The London, Edinburgh, and Dublin Philosophical Magazine and Journal of Science* **21,** 338–348 (1861).
2. Maxwell, J. C. VIII. A dynamical theory of the electromagnetic field. *Philosophical transactions of the Royal Society of London,* 459–512 (1865).
3. Yang, K.-H. & McDonald, K. T. Formal expressions for the electromagnetic potentials in any gauge. *Princeton University, Princeton* (2015).
4. Aharonov, Y. & Bohm, D. Further considerations on electromagnetic potentials in the quantum theory. *Physical Review* **123,** 1511–1524 (1961).
5. Gibbs, J. W. Velocity of Propagation of Electrostatic Force. *Nature* **53,** 509–509 (1896).
6. Schrödinger, E. An undulatory theory of the mechanics of atoms and molecules. *Physical Review* **28,** 1049–1070 (1926).
7. Goldstein, H., Poole, C. & Safko, J. *Classical Mechanics* (Addison-Wesley, 2001).
8. Noether, E. Invariant variation problems. *Transport Theory and Statistical Physics* **1,** 186–207 (1971).
9. Rainer, D. *Advanced Quantum Mechanics: Materials and Photons* (Springer International, 2020).
10. Ullrich, C. A. *Time-Dependent Density-Functional Theory* (Oxford University Press, 2012).
11. Runge, E. & Gross, E. K. Density-functional theory for time-dependent systems. *Physical review letters* **52,** 997–1000 (1984).
12. Van Leeuwen, R. Mapping from densities to potentials in time-dependent density-functional theory. *Physical Review Letters* **82,** 3863–3866 (1999).
13. Atkins, P. *Molecular quantum mechanics parts I and II: An introduction to quantum chemistry* (Oxford University Press, 1977).
14. Kohn, W. & Sham, L. J. Self-consistent equations including exchange and correlation effects. *Physical review* **140,** A1133 (1965).
15. Martin, R. M. *Electronic Structure: Basic Theory and Practical Methods* (Cambridge University Press, 2004).
16. Perdew, J. P. & Zunger, A. Self-interaction correction to density-functional approximations for many-electron systems. *Physical Review B* **23,** 5048–5079 (1981).
17. Ghosh, S. K. & Dhara, A. K. Density-functional theory of many-electron systems subjected to time-dependent electric and magnetic fields. *Physical Review A* **38,** 1149–1158 (1988).

18. Vignale, G. Mapping from current densities to vector potentials in time-dependent current density functional theory. *Physical Review B* **70,** 201102 (2004).

19. Yabana, K. *et al.* Time-dependent density functional theory for strong electromagnetic fields in crystalline solids. *Physical Review B* **85,** 045134 (2012).

20. Yamada, S., Noda, M., Nobusada, K. & Yabana, K. Time-dependent density functional theory for interaction of ultrashort light pulse with thin materials. *Physical Review B* **98,** 245147 (2018).

21. Yamada, A. & Yabana, K. Multiscale time-dependent density functional theory for a unified description of ultrafast dynamics: Pulsed light, electron, and lattice motions in crystalline solids. *Physical Review B* **99,** 245103 (2019).

22. Gabay, D. *et al.* Lorenz gauge formulation for time-dependent density functional theory. *Physical Review B* **101,** 235101 (2020).

23. Vignale, G. & Rasolt, M. Density-functional theory in strong magnetic fields. *Physical Review Letters* **59,** 2360–2363 (1987).

24. Diener, G. Current-density-functional theory for a nonrelativistic electron gas in a strong magnetic field. *Journal of Physics: Condensed Matter* **3,** 9417 (1991).

25. Sui, W., Yang, J., Yun, X. & Wang, C. Including Quantum Effects in Electromagnetic System–An FDTD Solution to Maxwell-Schrödinger Equations. *2007 IEEE/MTT-S International Microwave Symposium,* 1979–1982 (2007).

26. Pierantoni, L., Mencarelli, D. & Rozzi, T. A new 3-D transmission line matrix scheme for the combined Schrödinger–Maxwell problem in the electronic/electromagnetic characterization of nanodevices. *IEEE Transactions on Microwave Theory and Techniques* **56,** 654–662 (2008).

27. Lopata, K. & Neuhauser, D. Nonlinear nanopolaritonics: Finite-difference time-domain Maxwell–Schrödinger simulation of molecule-assisted plasmon transfer. *The Journal of Chemical Physics* **131,** 014701 (2009).

28. Pierantoni, L., Mencarelli, D. & Rozzi, T. Boundary immittance operators for the Schrödinger–Maxwell problem of carrier dynamics in nanodevices. *IEEE transactions on Microwave Theory and Techniques* **57,** 1147–1155 (2009).

29. Ahmed, I., Khoo, E. H., Li, E. & Mittra, R. A hybrid approach for solving coupled Maxwell and Schrödinger equations arising in the simulation of nanodevices. *IEEE Antennas and Wireless Propagation Letters* **9,** 914–917 (2010).

30. Ohnuki, S. *et al.* Coupled analysis of Maxwell–Schrödinger equations by using the length gauge: harmonic model of a nanoplate subjected to a 2D electromagnetic field. *International Journal of Numerical Modelling: Electronic Networks, Devices and Fields* **26,** 533–544 (2013).

31. Takeuchi, T., Ohnuki, S. & Sako, T. Hybrid Simulation of Maxwell-Schrödinger Equations for Multi-Physics Problems Characterized by Anharmonic Electrostatic Potential. *Progress In Electromagnetics Research* **148,** 73–82 (2014).

32. Takeuchi, T., Ohnuki, S. & Sako, T. Comparison between Maxwell–Schrödinger and Maxwell–Newton hybrid simulations for multi-well electrostatic potential. *IEEE Journal of Quantum Electronics* **50,** 334–339 (2014).

33. Ryu, C. J., Liu, A. Y., Wei, E. & Chew, W. C. Finite-difference time-domain simulation of the Maxwell–Schrödinger system. *IEEE Journal on Multiscale and Multiphysics Computational Techniques* **1,** 40–47 (2016).

34. Chen, Y. P. *et al.* A unified Hamiltonian solution to Maxwell-Schrödinger equations for modeling electromagnetic field-particle interaction. *Computer Physics Communications* **215,** 63–70 (2017).

35. Xiang, C., Kong, F., Li, K. & Liu, M. A high-order symplectic FDTD scheme for the Maxwell-Schrodinger system. *IEEE Journal of Quantum Electronics* **54,** 1–8 (2017).

36. Xie, G., Huang, Z., Fang, M. & Wei, E. Simulating Maxwell–Schrödinger equations by high-order symplectic FDTD algorithm. *IEEE Journal on Multiscale and Multiphysics Computational Techniques* **4,** 143–151 (2019).

37. Xie, G. *et al.* Universal vector–scalar potential framework for inhomogeneous electromagnetic system and its application in semiclassical quantum electromagnetics. *IEEE Transactions on Plasma Science* **49,** 3459–3471 (2021).

38. Sato, S. A. & Yabana, K. Maxwell+TDDFT multi-scale simulation for laser-matter interactions. *Journal of Advanced Simulation in Science and Engineering* **1,** 98–110 (2014).

39. Sato, S. *et al.* Time-dependent density functional theory of high-intensity short-pulse laser irradiation on insulators. *Physical Review B* **92,** 205413 (2015).

40. Li, Y., He, S., Russakoff, A. & Varga, K. Accurate time propagation method for the coupled Maxwell and Kohn-Sham equations. *Physical Review E* **94,** 023314 (2016).

41. Otobe, T. Multi-Scale Simulation for Transient Absorption Spectroscopy under Intense Few-Cycle Pulse Laser. *MDPI Photonics* **3,** 63 (2016).

42. Covington, C. *et al.* Time propagation of the coupled Maxwell and Kohn-Sham equations using the Riemann-Silberstein formalism. *Physical Review E* **100,** 053301 (2019).

CHAPTER 3

THE FINITE-DIFFERENCE TIME-DOMAIN METHOD

"The most important step a man can take. It's not the first one, is it?
It's the next one. Always the next one."

— BRANDON SANDERSON, Oathbringer (2017)

To find solutions to the equations presented in Chapter 2 for realistic set-ups, we need to rely on approximated solutions provided by computers. However, coaxing these machines to produce accurate solutions in a reasonable time frame still requires a lot of human ingenuity.

3.1 Introduction

In this chapter, we present the finite-difference time-domain (FDTD) method. In a computational EM (CEM) context, this method is best known in the form proposed by K. Yee in 1966 [1], which is deservedly called the *Yee algorithm*. However, finite differences (FDs) comprise a much wider class of methods and are used in many other fields of physics. Already in 1928, R. Courant [2] described the use of FDs for boundary-value (BV) problems and discussed the conditional stability of explicit FD schemes. In 1947, J. Crank and P. Nicolson proposed the *Crank-Nicolson* method for equations of the heat-conduction type [3]. An explicit FDTD method was used in 1950 by J. Von Neumann and R. D. Richtmyer to model hydrodynamic shocks. J. Douglas Jr. presented a more efficient variation of the Crank-Nicolson method in 1962 which he called the *alternating-direction implicit* method [4]. The FDTD method also made its way into quantum mechanics, when in 1967 A. Goldberg applied the Crank-Nicolson method to the time-dependent Schrödinger equation [5].

This limited and non-exhaustive historical overview attests to the popularity of the FDTD method even before the term 'FDTD' existed. We list several properties that attribute to its applicability. First, it is conceptually simple, i.e., differential equations are discretized with relative ease by subdividing space and time into a finite grid. Furthermore, the resulting system of linear equations can either be explicit or implicit. The former are solved without any linear algebra making them easy to implement and very fast whereas the latter results in relatively simple sparse matrix systems. Second, FDTD leads to well-ordered memory and easily lends itself to parallelization. Last, owing to its time-domain nature, it can obtain wide-band

data from a single run and also treat nonlinear behavior with ease.

One of the main drawbacks of the "classic" FDTD method is its limited geometric flexibility. Space and time are subdivided into cuboids leading to ill-defined edges or staircasing. For this reason, other techniques such as the finite-integration or finite-element methods have been called into life, which allow for much more geometric flexibility and often have a higher accuracy. They come, however, at a much increased computational cost.

Because there exist legion implementations and fields of application, we limit ourselves in this chapter to discussing finite differences in basic terms and apply it to the Yee algorithm [1] for EM problems and the explicit method of [6] for the Schrödinger equation. With this brief summary we aim to impart a sense of the intricacies that might arise from such a seemingly simple method. For a more in-depth view, we recommend the book of J. D. Hoffman [7].

3.2 Finite differences

The "classic" FDTD method discretizes the unknown field variables on a regular cuboid grid with node coordinates $x_i = i\Delta x$, $y_j = j\Delta y$, and $z_k = k\Delta z$, for small spatial steps Δx, Δy, and Δz. As such, we identify a short-hand notation for a field variable $f(x,y,z)$ at a certain position as:

$$f\left(x_i, y_j, z_k\right) = f(i\Delta x, j\Delta y, k\Delta z) = f|_{i,j,k}. \tag{3.1}$$

Field variables at half-integer locations are similarly noted:

$$f\left(x_{i+\frac{1}{2}}, y_j, z_k\right) = f\left(\frac{1}{2}(x_{i+1} + x_i), j\Delta y, k\Delta z\right) = f|_{i+\frac{1}{2},j,k}. \tag{3.2}$$

To discretize a partial differential equation (PDE), we need to find approximate expressions for the partial derivatives in terms of the field variables. As an example, we give the expressions for a forward, central, and backward difference approximation for a first-order derivative in 1 dimension (1-D):

$$\left.\frac{\partial f}{\partial x}\right|_i \approx \frac{f|_{i+1} - f|_i}{\Delta x}, \qquad \text{(forward)}, \tag{3.3}$$

$$\left.\frac{\partial f}{\partial x}\right|_i \approx \frac{f|_{i+\frac{1}{2}} - f|_{i-\frac{1}{2}}}{\Delta x}, \qquad \text{(central)}, \tag{3.4}$$

$$\left.\frac{\partial f}{\partial x}\right|_i \approx \frac{f|_i - f|_{i-1}}{\Delta x}, \qquad \text{(backward)}, \tag{3.5}$$

and the central difference approximation for a second-order derivative:

$$\left.\frac{\partial^2 f}{\partial x^2}\right|_i \approx \frac{f|_{i+1} - 2f|_i + f|_{i-1}}{\Delta x^2}. \tag{3.6}$$

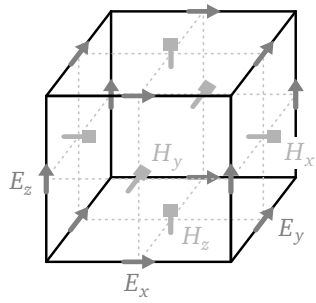

Figure 3.1: The electric $\boldsymbol{E}$ and magnetization $\boldsymbol{H}$ fields are staggered in space in accordance with the Yee cell and indicated with triangle-topped and square-topped arrows, respectively. The electric field components are anchored at the center of their corresponding edge and the magnetization field components at the center of their normal plane. The fields are updated in a leapfrog manner with $\boldsymbol{E}$ discretized at integer time steps $t = n\Delta t$ and $\boldsymbol{H}$ at half-integer time steps $t = (n+1/2)\Delta t$.

By substituting the Taylor expansions for f_{i+1}, $f_{i+\frac{1}{2}}$, $f_{i-\frac{1}{2}}$, and f_{i-1} into (3.3)–(3.6), we can show that (3.3) and (3.5) are first-order accurate while (3.4) and (3.6) are second-order accurate, e.g.:

$$\frac{f|_{i+1} - f|_i}{\Delta x} = \left.\frac{\partial f}{\partial x}\right|_i + \frac{\Delta x}{2}\left.\frac{\partial^2 f}{\partial x^2}\right|_i + \frac{\Delta x^2}{6}\left.\frac{\partial^3 f}{\partial x^3}\right|_i + \mathcal{O}\big(\Delta x^3\big), \tag{3.7}$$

$$\frac{f|_{i+1} - 2f|_i + f|_{i-1}}{\Delta x^2} = \left.\frac{\partial^2 f}{\partial x^2}\right|_i + \frac{\Delta x^2}{12}\left.\frac{\partial^4 f}{\partial x^4}\right|_i + \frac{\Delta x^4}{360}\left.\frac{\partial^6 f}{\partial x^6}\right|_i + \mathcal{O}\big(\Delta x^6\big). \tag{3.8}$$

The accuracy of the finite differences (3.4) and (3.5) can be shown analogously. The time axis is discretized in a similar fashion, with time steps Δt and time index n, but where the shorthand notation positions the time index – for no reason other than notational simplicity – in superscript:

$$f(x_i, y_j, z_k, t_n) = f(i\Delta x, j\Delta y, k\Delta z, n\Delta t) = f|^n_{i,j,k}. \tag{3.9}$$

Turning a set of PDEs into an FDTD method, usually boils down to applying the difference equations (3.3)–(3.6) to the spatial and temporal derivatives and combining them in such a way that yields a consistent, accurate and stable scheme.

Maxwell's equations

The Yee algorithm discretizes the two curl equations (2.5a) and (2.5b). The discretization is performed using the Yee cell which is shown in Fig. 3.1. We will only consider the lossless case here, hence where the conductivity $\sigma = 0$.

The electric and magnetization fields are discretized in a leapfrog fashion, alternately updating the electric field at integer time steps $t = n\Delta t$ as:

$$E_x\big|^{n}_{i+\frac{1}{2},j,k} = E_x\big|^{n-1}_{i+\frac{1}{2},j,k} + \frac{\Delta t}{\epsilon_{i+\frac{1}{2},j,k}}\left(\frac{H_z\big|^{n-\frac{1}{2}}_{i+\frac{1}{2},j+\frac{1}{2},k} - H_z\big|^{n-\frac{1}{2}}_{i+\frac{1}{2},j-\frac{1}{2},k}}{\Delta y} - \frac{H_y\big|^{n-\frac{1}{2}}_{i+\frac{1}{2},j,k+\frac{1}{2}} - H_y\big|^{n-\frac{1}{2}}_{i+\frac{1}{2},j,k-\frac{1}{2}}}{\Delta z} - J_x\big|^{n-\frac{1}{2}}_{i+\frac{1}{2},j,k}\right), \tag{3.10a}$$

$$E_y\big|^{n}_{i,j+\frac{1}{2},k} = E_y\big|^{n-1}_{i,j+\frac{1}{2},k} + \frac{\Delta t}{\epsilon_{i,j+\frac{1}{2},k}}\left(\frac{H_x\big|^{n-\frac{1}{2}}_{i,j+\frac{1}{2},k+\frac{1}{2}} - H_x\big|^{n-\frac{1}{2}}_{i,j+\frac{1}{2},k-\frac{1}{2}}}{\Delta z} - \frac{H_z\big|^{n-\frac{1}{2}}_{i+\frac{1}{2},j+\frac{1}{2},k} - H_z\big|^{n-\frac{1}{2}}_{i-\frac{1}{2},j+\frac{1}{2},k}}{\Delta x} - J_y\big|^{n-\frac{1}{2}}_{i,j+\frac{1}{2},k}\right), \tag{3.10b}$$

$$E_z\big|^{n}_{i,j,k+\frac{1}{2}} = E_z\big|^{n-1}_{i,j,k+\frac{1}{2}} + \frac{\Delta t}{\epsilon_{i,j,k+\frac{1}{2}}}\left(\frac{H_y\big|^{n-\frac{1}{2}}_{i+\frac{1}{2},j,k+\frac{1}{2}} - H_y\big|^{n-\frac{1}{2}}_{i-\frac{1}{2},j,k+\frac{1}{2}}}{\Delta x} - \frac{H_x\big|^{n-\frac{1}{2}}_{i,j+\frac{1}{2},k+\frac{1}{2}} - H_x\big|^{n-\frac{1}{2}}_{i,j-\frac{1}{2},k+\frac{1}{2}}}{\Delta y} - J_z\big|^{n-\frac{1}{2}}_{i,j,k+\frac{1}{2}}\right), \tag{3.10c}$$

and the magnetization field at half-integer time steps $t = (n+1/2)\Delta t$ as:

$$H_x\big|^{n+\frac{1}{2}}_{i,j+\frac{1}{2},k+\frac{1}{2}} = H_x\big|^{n-\frac{1}{2}}_{i,j+\frac{1}{2},k+\frac{1}{2}} - \frac{\Delta t}{\mu_{i,j+\frac{1}{2},k+\frac{1}{2}}}\left(\frac{E_z\big|^{n}_{i,j+1,k+\frac{1}{2}} - E_z\big|^{n}_{i,j,k+\frac{1}{2}}}{\Delta y} - \frac{E_y\big|^{n}_{i,j+\frac{1}{2},k+1} - E_y\big|^{n}_{i,j+\frac{1}{2},k}}{\Delta z}\right), \tag{3.11a}$$

$$H_y\big|^{n+\frac{1}{2}}_{i+\frac{1}{2},j,k+\frac{1}{2}} = H_y\big|^{n-\frac{1}{2}}_{i+\frac{1}{2},j,k+\frac{1}{2}} - \frac{\Delta t}{\mu_{i+\frac{1}{2},j,k+\frac{1}{2}}}\left(\frac{E_x\big|^{n}_{i+\frac{1}{2},j,k+1} - E_x\big|^{n}_{i+\frac{1}{2},j,k}}{\Delta z} - \frac{E_z\big|^{n}_{i+1,j,k+\frac{1}{2}} - E_z\big|^{n}_{i,j,k+\frac{1}{2}}}{\Delta x}\right), \tag{3.11b}$$

$$H_z\big|^{n+\frac{1}{2}}_{i+\frac{1}{2},j+\frac{1}{2},k} = H_z\big|^{n-\frac{1}{2}}_{i+\frac{1}{2},j+\frac{1}{2},k} - \frac{\Delta t}{\mu_{i+\frac{1}{2},j+\frac{1}{2},k}}\left(\frac{E_y\big|^{n}_{i+1,j+\frac{1}{2},k} - E_y\big|^{n}_{i,j+\frac{1}{2},k}}{\Delta x} - \frac{E_x\big|^{n}_{i+\frac{1}{2},j+1,k} - E_x\big|^{n}_{i+\frac{1}{2},j,k}}{\Delta y}\right). \tag{3.11c}$$

Equations (3.10) and (3.11) form the Yee algorithm for the electric $\boldsymbol{E}$ and magnetization $\boldsymbol{H}$ field and the free currents $\boldsymbol{J}$, where we have dropped the subscript f. In case nonhomogeneous media are used, the material properties ϵ and μ should be properly averaged. Since only central differences were used to construct the Yee scheme, it is second-order accurate in time and space.

For the general case, and a more in-depth introduction to the FDTD method for computational electromagnetics, the reader is referred to the book by A. Taflove and S. C. Hagness [8]. Besides [8], a good introduction to the FDTD method in computational electromagnetics is presented by Stephen D. Gedney [9] or with more implementational details by John B. Schneider [10].

Schrödinger equation

There are several implementations of the FDTD method for the Schrödinger equation, but here we present the explicit method of A. Askar [6] for a 1-D wave function. The extension to 3-D is trivial. The method is constructed by applying a central difference for the time derivative spanning two (temporal) cells and the central difference for the Laplacian (3.6). The result is given by:

$$\psi|_i^{n+1} = \psi|_i^{n-1} + \jmath\frac{\hbar\Delta t}{m}\frac{\psi|_{i+1}^n - 2\psi|_i^n + \psi|_{i-1}^n}{\Delta x^2} - \jmath\frac{2\Delta t}{\hbar}v|_i\psi|_i^n. \tag{3.12}$$

As such, the wave function is iterated based on two previous time steps. In Chapter 4, we present a generalization of this method and we discuss advantages and disadvantages of alternative methods in Chapters 4 and 5.

3.3 Numerical properties

To analyze an FDTD method, several features need to be considered. According to [7], there are four: consistency, order, stability, and convergence. In this section, we explain what they mean and how they apply to the Yee algorithm (3.10)–(3.11) and to (3.12) for the Schrödinger equation. Additionally, we also consider the numerical dispersion relation since this is a very common method to analyze FDTD schemes in the CEM community.

3.3.1 Consistency and order

Consistency implies that the difference between the PDE and the difference equation vanishes as grid spacings go to zero independently. The order is the rate at which the global error (the truncation terms) decreases as the grid sizes approach zero.

To determine the order and consistency, Warming and Hyett [11] proposed the modified differential equation method, where the Taylor expansion of each term is inserted into the difference equation around a specific base point. The truncation error is then given by the terms that do not appear in the original PDE. By studying these errors, the consistency and order can be determined simultaneously. In fact, this method was already applied in (3.7)–(3.8) for a first- and second-order partial derivative, respectively. The application of this method to the difference schemes for Maxwell and Schrödinger, directly shows that both are consistent and second-order accurate in space and time.

3.3.2 Stability

Another aspect that needs to be analyzed for every FDTD method is its stability. For a stable PDE, the numerical method is stable if it produces a bounded output and unstable if it produces an unbounded output. The concept of conditional stability was first discussed by R. Courant, K. Friedrichs, and H. Lewy [2]. Conditional stability implies that the time step Δt has to be smaller than a certain prescribed value in order to ensure stability. This condition is now often called the Courant-Friedrichs-Lewy (CFL) or simply Courant condition with a maximum allowed time step given by Δt_{CFL}.

One method for determining the stability was developed by J. von Neumann during World War II but published in 1950 by G. O'Brien [12] with his permission. The *von Neumann* method assumes that all the coefficients are constant, which can be a drawback in some cases. In the 1-D case, the following steps need to be taken:

1. Substitute $f|_i^n = f_0 e^{\alpha n\Delta t + \jmath i\beta\Delta x}$ into the difference equation, where β is real and α is complex.
2. Transform the result to obtain a value for $\xi = e^{\alpha\Delta t}$.
3. The stability condition now reads $|\xi| \leq 1$. Otherwise, the solution will grow every iteration.

In the case of (3.12) with constant v, we substitute $\psi|_i^n = \psi_0 e^{\alpha n\Delta t + \jmath i\beta\Delta x}$, resulting in:

$$e^{\alpha\Delta t} = e^{-\alpha\Delta t} + \jmath\frac{\Delta t}{\hbar}\left(\frac{\hbar^2}{m}\frac{e^{\jmath\beta\Delta x} - 2 + e^{-\jmath\beta\Delta x}}{\Delta x^2} - 2v\right), \tag{3.13}$$

such that we need to solve the following equation for ξ:

$$\xi^2 + \jmath\gamma\xi - 1 = 0, \tag{3.14}$$

with

$$\gamma = \frac{2\Delta t}{\hbar}\left(\frac{2\hbar^2}{m\Delta x^2}\sin^2\left(\frac{\beta\Delta x}{2}\right) + v\right). \tag{3.15}$$

The solutions for ξ are thus given by:

$$\xi_{\pm} = \frac{1}{2}\Big(-\jmath\gamma \pm \sqrt{4-\gamma^2}\Big). \tag{3.16}$$

In order for $|\xi_{\pm}| \leq 1$ we get the condition:

$$\Delta t \leq \frac{\hbar}{\left|\frac{2\hbar^2}{m\Delta x^2}\sin^2\Big(\frac{\beta\Delta x}{2}\Big) + \nu\right|}, \tag{3.17}$$

but since β and ν can be any combination of real numbers, the stability condition is often approximated as:

$$\Delta t \leq \frac{\hbar}{\frac{2\hbar^2}{m}\frac{1}{\Delta x^2} + |\nu|}. \tag{3.18}$$

In Chapter 4, we will show that this stability criterion can be relaxed. A similar approach for the Yee algorithm, but where every field component is expanded as:

$$E_x|^n_{i,j,k} = E_{x0}e^{\alpha n\Delta t + \jmath\left(i\beta_x\Delta x + j\beta_y\Delta y + k\beta_z\Delta z\right)}, \tag{3.19a}$$

$$E_y|^n_{i,j,k} = E_{y0}e^{\alpha n\Delta t + \jmath\left(i\beta_x\Delta x + j\beta_y\Delta y + k\beta_z\Delta z\right)}, \tag{3.19b}$$

$$E_z|^n_{i,j,k} = E_{z0}e^{\alpha n\Delta t + \jmath\left(i\beta_x\Delta x + j\beta_y\Delta y + k\beta_z\Delta z\right)}, \tag{3.19c}$$

$$H_x|^n_{i,j,k} = H_{x0}e^{\alpha n\Delta t + \jmath\left(i\beta_x\Delta x + j\beta_y\Delta y + k\beta_z\Delta z\right)}, \tag{3.19d}$$

$$H_y|^n_{i,j,k} = H_{y0}e^{\alpha n\Delta t + \jmath\left(i\beta_x\Delta x + j\beta_y\Delta y + k\beta_z\Delta z\right)}, \tag{3.19e}$$

$$H_z|^n_{i,j,k} = H_{z0}e^{\alpha n\Delta t + \jmath\left(i\beta_x\Delta x + j\beta_y\Delta y + k\beta_z\Delta z\right)}, \tag{3.19f}$$

and with a uniform background medium, yields the well known CFL stability criterion:

$$\Delta t \leq \frac{1}{\frac{1}{\sqrt{\epsilon\mu}}\sqrt{\frac{1}{\Delta x^2} + \frac{1}{\Delta y^2} + \frac{1}{\Delta z^2}}}. \tag{3.20}$$

In practice, when the background media are not uniform, the highest occurring phase velocity $v_{\text{ph}} = 1/\sqrt{\epsilon\mu}$ and potential energy $|\nu|$ is taking for (3.20) and (3.18), respectively. It can be shown that this indeed yields a valid but underestimated time step [13].

3.3.3 Convergence

A last important aspect is the convergence, i.e., the solution of the difference equation should approach the exact solution of the differential equation as the grid sizes approach zero. According to the Lax equivalence theorem [14], the stability of a *consistent* FDTD scheme is a necessary and sufficient condition for convergence.

3.3.4 Numerical dispersion

A benchmark feature of any FDTD method is the error introduced by the discretization. To characterize this error we introduce a known signal on the grid and study how the error varies with the spatio-temporal discretization. As such, a spatial and temporal discretization can be proposed that keeps the error below a certain threshold. One such commonly used signal is a monochromatic plane wave:

$$g(\boldsymbol{r}, t) = g_0 e^{\jmath(\omega t - \boldsymbol{k}\cdot\boldsymbol{r})}. \tag{3.21}$$

The substitution into the differential equation yields a relation between the wavelength $\lambda = 2\pi/\|k\|$ and the radial frequency $\omega = 2\pi f$, called the dispersion relation. Doing the same for the difference equation yields the numerical dispersion relation.

Schrödinger equation

The dispersion relation for the 1-D Schrödinger equation with constant potential v is given by:

$$\hbar\omega = \frac{\hbar^2 k^2}{2m} + v. \tag{3.22}$$

Substituting $\psi|_{i,j,k}^{n} = \psi_0 \exp\big(-\jmath\big(n\omega\Delta t - i\tilde{k}\Delta x\big)\big)$ into (3.12) yields:

$$\frac{\hbar}{\Delta t}\sin(\omega\Delta t) = \frac{2\hbar^2}{m\Delta x^2}\sin^2\left(\frac{k\Delta x}{2}\right) + v. \tag{3.23}$$

We can see that in the limit of $\omega\Delta t \to 0$ and $\tilde{k}\Delta x \to 0$ the analytical dispersion relation (3.22) is recovered. As such, we have shown that the numerical solution converges to the analytical solution for decreasing spatial and temporal steps. The derivation of (3.23) in the general 3-D case is given in Chapter 4, where we will also consider the influence of the angle of propagation.

Maxwell's equations

The dispersion relation for the Yee algorithm is a bit more complicated. We again insert (3.19) into the Yee scheme (3.10)–(3.11) for a homogeneous medium with phase velocity v_{ph} but now with $\alpha = \jmath\omega$ and $\beta_u = -\tilde{k}_u$ for $u \in \{x, y, z\}$. The resulting numerical dispersion relation is given by [8]:

$$\left(\frac{\sin\left(\frac{\omega\Delta t}{2}\right)}{v_{\text{ph}}\Delta t}\right)^2 = \left(\frac{\sin\left(\frac{\tilde{k}_x\Delta x}{2}\right)}{\Delta x}\right)^2 + \left(\frac{\sin\left(\frac{\tilde{k}_y\Delta y}{2}\right)}{\Delta y}\right)^2 + \left(\frac{\sin\left(\frac{\tilde{k}_z\Delta z}{2}\right)}{\Delta z}\right)^2, \tag{3.24}$$

which again reduces to the analytical relation:

$$\left(\frac{\omega}{v_{\text{ph}}}\right)^2 = k_x^2 + k_y^2 + k_z^2, \tag{3.25}$$

for small spatial and temporal steps. From (3.24) we can see that FDTD is dispersive and anisotropic despite the fact that Maxwell's equations in free space are nondispersive an isotropic. To have an acceptable error, a spatial discretization of $\Delta \leq \lambda/20$ should be chosen [9].

In 1-D, the EM FDTD scheme – which is used in, e.g., the simulation of transmission lines – knows the concept of a *magic* time step. The 1-D dispersion relation reduces to:

$$\cos(\omega \Delta t) = \frac{v_{\text{ph}}^2 \Delta t^2}{\Delta x^2}\left(\cos\left(\tilde{k}_x \Delta x\right) - 1\right) + 1, \tag{3.26}$$

and the stability criterion reads:

$$\Delta t \leq \frac{\Delta x}{v_{\text{ph}}}. \tag{3.27}$$

Note that if $\Delta t = \Delta x / v_{\text{ph}} = \Delta t_{\text{magic}}$ the dispersion relation (3.26) reduces to the exact relation $\omega = \tilde{k}_x v_{\text{ph}}$, hence the name magic time step. Alas, this relation does not hold in the 3-D case nor for the 1-D Schrödinger equation. However, the error for these schemes is generally minimized by choosing the time step as close as possible to the stability criterion.

References

1. Yee, K. Numerical solution of initial boundary value problems involving Maxwell's equations in isotropic media. *IEEE Transactions on antennas and propagation* **14,** 302–307 (1966).
2. Courant, R., Friedrichs, K. & Lewy, H. Über die partiellen Differenzengleichungen der mathematischen Physik. *Mathematische Annalen* **100,** 32–74 (Dec. 1928).
3. Crank, J. & Nicolson, P. A practical method for numerical evaluation of solutions of partial differential equations of the heat-conduction type. *Mathematical Proceedings of the Cambridge Philosophical Society* **43,** 50–67 (1947).
4. Douglas Jr., J. Alternating direction methods for three space variables. *Numerische Mathematik* **4,** 41–63 (1962).
5. Goldberg, A., Schey, H. M. & Schwartz, J. L. Computer-generated motion pictures of one-dimensional quantum-mechanical transmission and reflection phenomena. *American Journal of Physics* **35,** 177–186 (1967).
6. Askar, A. & Cakmak, A. S. Explicit integration method for the time-dependent Schrödinger equation for collision problems. *The Journal of Chemical Physics* **68,** 2794–2798 (1978).
7. Hoffman, J. D. *Numerical Methods for Engineers and Scientists* (Marcel Dekker, 2001).
8. Taflove, A. & Hagness, S. C. *Computational electrodynamics: the finite-difference time-domain method* (Artech House, 2005).
9. Gedney, S. D. *Introduction to the Finite-Difference Time-Domain (FDTD) Method for Electromagnetics* (Morgan & Claypool, 2011).
10. Schneider, J. B. *Understanding the FDTD method* `www.eecs.wsu.edu/~schneidj/ufdtd` (2010).
11. Warming, R. F. & Hyett, B. J. The modified equation approach to the stability and accuracy analysis of finite-difference methods. *Journal of Computational Physics* **14,** 159–179 (1974).
12. O'Brien, G. G., Hyman, M. A. & Kaplan, S. A Study of the Numerical Solution of Partial Differential Equations. *Journal of Mathematics and Physics* **29,** 223–251 (1950).
13. Denecker, B., Knockaert, L., Olyslager, F. & De Zutter, D. A new state-space-based algorithm to assess the stability of the finite-difference time-domain method for 3D finite inhomogeneous problems. *AEU-International Journal of Electronics and Communications* **58,** 339–348 (2004).
14. Lax, P. D. Weak solutions of nonlinear hyperbolic equations and their numerical computation. *Communications on Pure and Applied Mathematics* **7,** 159–193 (1954).

CHAPTER 4

NONUNIFORM AND HIGHER-ORDER METHODS FOR THE SCHRÖDINGER EQUATION

Two finite-difference time-domain (FDTD) methods are developed for solving the Schrödinger equation on nonuniform tensor-product grids. The stability is derived based on discrete-time stability theory, which yields an upper bound for the time step. Several numerical experiments demonstrate the applicability of the proposed schemes on nonuniform grids.

The theory and examples in this chapter are based on "Nonuniform and Higher-order FDTD Methods for the Schrödinger Equation" by Pieter Decleer, Arne Van Londersele, Hendrik Rogier, and Dries Vande Ginste, as published in *Journal of Computational and Applied Mathematics*, **381**, 113023 (2021).

4.1 Introduction

As discussed in Chapter 3, the FDTD method applied to the Schrödinger equation discretizes the wave function on a space-time structured grid. Many different implementations exist, depending on the spatial discretization and the time propagation, each having their strengths and weaknesses. Depending on the discretization of the temporal derivative, the resulting scheme is either implicit or explicit. The former can be unconditionally stable [1] but has the drawback of requiring expensive matrix inversions, whereas the latter only requires elementary arithmetic operations but is only conditionally stable [2–6]. The linear numerical complexity of explicit methods often makes them favorable over implicit methods when it comes to computationally large problems.

To lower the computational cost pertaining to explicit schemes, one can reduce the number of spatial variables or the number of time iterations. Higher-order accurate spatial schemes employ coarser grids that effectuate both at the same time, as a coarser grid is used, which in turn support a larger time step. These higher-order accurate spatial schemes are highly effective because they can be interpreted as a sum-accelerated pseudospectral method [7].

Complex nanostructures require large grids with very small spatial steps, resulting in an unreasonable amount of unknowns. The high accuracy, however, is only required in specific areas of the structure. To increase the accuracy in these areas, it is possible to use nonuniform tensor product grids, meaning that each spatial step can vary along its axis. The nonuniform discretization and higher-order accurate spatial schemes drastically reduce the number of spatial variables. In [8], such a scheme is proposed, where a mapping function is used to convert a nonuniform grid into a uniform grid and where extended stencils are used. However, the mapping function does not support higher-order accurate spatial schemes.

In this chapter, two explicit schemes are presented that solve the Schrödinger equation on a nonuniform grid without explicitly needing a mapping function and, as such, allow for much more flexibility in the used grid. The first scheme modifies the second-order accurate central difference scheme to a nonuniform grid by introducing a dual grid. The second scheme is higher-order accurate, allowing for coarser spatial discretization and, consequently, a larger time step. Both are dubbed the *collocated-explicit* (CE) method. While these two schemes are very efficient owing to the explicit updates and the reduction in unknowns, they are still limited by restrictions on the time step, with small spatial steps and high potential energies leading to small time steps. Therefore, we thoroughly investigate the stability in order to select the highest possible time step while still ensuring the stability. Additionally, the numerical dispersion error is derived and investigated. While the nonuniform and higher-order spatial discretization is applied for one possible temporal discretization, it is equally applicable to other temporal discretizations [1, 5, 6, 9, 10]. Numerical experiments attest to the accuracy and efficiency of the proposed methods.

In Section 4.2, the definition of the grid is given and the two update schemes are derived. The stability condition for both schemes is determined in Section 4.3. In Section 4.4, the numerical dispersion error is studied as a function of the propagation direction, the spatial discretization and the time step. The theoretical derivations are verified through numerical experimentation in Section 4.5. In Section 4.6, the results are summarized.

4.2 Discretization of the Schrödinger equation

The equation to be solved is the continuous time-dependent Schrödinger equation (2.34).

4.2.1 Spatial discretization

The wave function ψ is defined on the internal nodes of a 3-D nonuniform tensor product grid containing $n_x \times n_y \times n_z$ cells. The wave function at position (x_i, y_j, z_k)

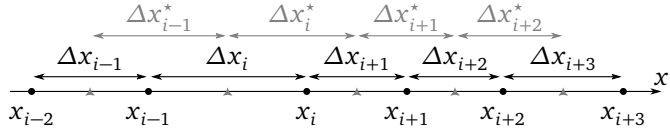

Figure 4.1: The primary grid steps Δx_i are defined as the distance between two primary grid points $\Delta x_i = x_{i+1} - x_i$ and the dual grid steps are defined as $\Delta x^\star_i = (\Delta x_i + \Delta x_{i-1})/2$. The positions of the primary grid points x_i are denoted by dots and the positions of the dual grid points are denoted by the pointed triangles.

is denoted by $\psi|_{i,j,k}$, corresponding to node (i,j,k). We also introduce the row-major vectorized wave function $\boldsymbol{\psi}$ with elements $\boldsymbol{\psi}|_{(im_y+j)m_z+k} = \psi|_{i,j,k}$. Similarly, we define the notation $\boldsymbol{\psi}|_{(i,j,k)}$, which is the spatial evaluation of the row-major discretized vector $\boldsymbol{\psi}$ in the grid. With Dirichlet boundary conditions, the wave function is discretized on $n_\psi = m_x m_y m_z$ nodes where $m_x = n_x - 1$ are the number of dual cells in the x-direction, and similarly for y and z. The spatial grid variables are defined in Fig. 4.1 for the x-direction.

The FD approximation of the second-order derivative is obtained by solving for the coefficients $c^x_1|_i$ and $c^x_{-1}|_i$ of the Taylor expansion:

$$c^x_1|_i\ \psi|_{i+1,j,k} + c^x_{-1}|_i\ \psi|_{i-1,j,k} = \sum_{n=0}^{\infty} \frac{1}{n!}\left(c^x_1|_i\,(\Delta x_{i+1})^n + c^x_{-1}|_i\,(-\Delta x_i)^n\right) \left.\frac{\partial^n \psi}{\partial x^n}\right|_{i,j,k},$$

such that the first-order derivative drops out. The resulting approximation is:

$$\left.\frac{\partial^2 \psi}{\partial x^2}\right|_{i,j,k} = \frac{\psi|_{i+1,j,k} - \psi|_{i,j,k}}{\Delta x_{i+1}\Delta x^\star_i} - \frac{\psi|_{i,j,k} - \psi|_{i-1,j,k}}{\Delta x^\star_i \Delta x_i} + \mathcal{O}(\Delta x_{i+1} - \Delta x_i). \tag{4.1}$$

Hence, the first-order accurate approximation to the Laplacian of ψ, written as a matrix vector product $L_L\boldsymbol{\psi}$, is given by:

$$\begin{aligned}(L_L\boldsymbol{\psi})|_{(i,j,k)} = &\frac{\psi|_{i+1,j,k} - \psi|_{i,j,k}}{\Delta x_{i+1}\Delta x^\star_i} - \frac{\psi|_{i,j,k} - \psi|_{i-1,j,k}}{\Delta x^\star_i \Delta x_i} \\ &+ \frac{\psi|_{i,j+1,k} - \psi|_{i,j,k}}{\Delta y_{j+1}\Delta y^\star_j} - \frac{\psi|_{i,j,k} - \psi|_{i,j-1,k}}{\Delta y^\star_j \Delta y_j} \\ &+ \frac{\psi|_{i,j,k+1} - \psi|_{i,j,k}}{\Delta z_{k+1}\Delta z^\star_k} - \frac{\psi|_{i,j,k} - \psi|_{i,j,k-1}}{\Delta z^\star_k \Delta z_k}.\end{aligned} \tag{4.2}$$

The exact form of the matrix L_L is given when we discuss the stability in Section 4.3. For a uniform grid, this scheme is second-order accurate. Moreover, if

a rather smoothly varying grid is used, the scheme will be close to second-order accurate. The subscript L indicates the lower-order nature as to distinguish it from the higher-order scheme that will be proposed next.

The higher-order accurate spatial scheme is derived by also including $\psi|_{i+2,j,k}$, and $\psi|_{i-2,j,k}$ in the Taylor expansion. We first introduce $\gamma_n^x\big|_i$:

$$\begin{aligned}\gamma_n^x\big|_i = d_2^x|_i\,(x_{i+2}-x_i)^n + d_1^x|_i\,(x_{i+1}-x_i)^n \\ + d_{-1}^x|_i\,(x_{i-1}-x_i)^n + d_{-2}^x|_i\,(x_{i-2}-x_i)^n,\end{aligned} \tag{4.3}$$

and the still unknown coefficients $d_2^x|_i$, $d_1^x|_i$, $d_{-1}^x|_i$, $d_{-2}^x|_i$, such that the resulting Taylor series expansion yields:

$$\begin{aligned}&d_2^x|_i\;\psi|_{i+2,j,k} + d_1^x|_i\;\psi|_{i+1,j,k} + d_{-1}^x|_i\;\psi|_{i-1,j,k} + d_{-2}^x|_i\;\psi|_{i-2,j,k} \\ &\quad = \sum_{n=0}^{\infty} \frac{1}{n!}\gamma_n^x|_i\;\frac{\partial^n\psi}{\partial x^n}\bigg|_{i,j,k}.\end{aligned} \tag{4.4}$$

The coefficients are determined by requiring that the first-, third- and fourth-order derivative drop out. Additionally, we require that the coefficient for the second-order derivative equals 1. As such, we obtain the following set of equations:

$$\gamma_1^x\big|_i = 0, \quad \gamma_2^x\big|_i = 2, \quad \gamma_3^x\big|_i = 0, \quad \text{and} \quad \gamma_4^x\big|_i = 0. \tag{4.5}$$

The solution to (4.5) is obtained with a linear algebra package and is given by:

$$d_{-2}^x|_i = \frac{2\Delta x_{i+1}^\star(\Delta x_{i+1}-\Delta x_i)-\Delta x_{i+1}\Delta x_i}{2\Delta x_{i-1}\Delta x_{i-1}^\star\left(2\Delta x_{i-1}^\star+\Delta x_{i+1}\right)\left(\Delta x_{i-1}^\star+\Delta x_{i+1}^\star\right)}, \tag{4.6a}$$

$$d_{-1}^x|_i = \frac{2\left(\Delta x_{i+2}\Delta x_{i-1}^\star+2\Delta x_{i-1}^\star\Delta x_{i+1}-\Delta x_{i+1}\Delta x_{i+1}^\star\right)}{\Delta x_i^\star\Delta x_i\Delta x_{i-1}\left(2\Delta x_i^\star+\Delta x_{i+2}\right)}, \tag{4.6b}$$

$$d_1^x|_i = \frac{2\left(\Delta x_{i-1}\Delta x_{i+1}^\star+2\Delta x_{i+1}^\star\Delta x_i-\Delta x_i\Delta x_{i-1}^\star\right)}{\Delta x_i^\star\Delta x_{i+1}\Delta x_{i+2}\left(2\Delta x_i^\star+\Delta x_{i-1}\right)}, \tag{4.6c}$$

$$d_2^x|_i = \frac{2\Delta x_{i-1}^\star(\Delta x_i-\Delta x_{i+1})-\Delta x_{i+1}\Delta x_i}{2\Delta x_{i+2}\Delta x_{i+1}^\star\left(2\Delta x_{i+1}^\star+\Delta x_i\right)\left(\Delta x_{i-1}^\star+\Delta x_{i+1}^\star\right)}. \tag{4.6d}$$

Eq. (4.4) is rearranged using (4.6), resulting in:

$$\begin{aligned}\frac{\partial^2\psi}{\partial x^2}\bigg|_{i,j,k} &= d_2^x|_i\left(\psi|_{i+2,j,k}-\psi|_{i,j,k}\right) + d_1^x|_i\left(\psi|_{i+1,j,k}-\psi|_{i,j,k}\right) \\ &\quad + d_{-1}^x|_i\left(\psi|_{i-1,j,k}-\psi|_{i,j,k}\right) + d_{-2}^x|_i\left(\psi|_{i-2,j,k}-\psi|_{i,j,k}\right) + \mathcal{E}|_i,\end{aligned} \tag{4.7}$$

with the error term:

$$\mathcal{E}|_i = \sum_{n=5}^{\infty}\frac{2}{n!}\frac{\gamma_n|_i}{\gamma_2|_i}\;\frac{\partial^n\psi}{\partial x^n}\bigg|_{i,j,k}. \tag{4.8}$$

According to [11], to check the consistency and obtain the order of accuracy, the expressions for $d_2^x|_i$, $d_1^x|_i$, $d_{-1}^x|_i$ and $d_{-2}^x|_i$ are plugged into the $m = 5$ term of the error. The result is simplified using a linear algebra package and rewritten as a function of the primary grid cells. As such it can be seen that the second-order derivative is correct up to third order:

$$\begin{aligned}\mathcal{E}|_i = \mathcal{O}\big(2\Delta x_{i+1}\Delta x_i((\Delta x_{i-1}+\Delta x_i)-(\Delta x_{i+1}+\Delta x_{i+2}))\\ +\Delta x_i\Delta x_{i+2}(\Delta x_{i-1}+\Delta x_i)\\ -\Delta x_{i+1}\Delta x_{i-1}(\Delta x_{i+1}+\Delta x_{i+2})\big).\end{aligned} \tag{4.9}$$

The third-order correct approximation of the Laplacian, denoted L_H, is fourth-order accurate on uniform grids and is given by:

$$\begin{aligned}(L_H\boldsymbol{\psi})|_{(i,j,k)} = {} & d_2^x|_i\left(\psi|_{i+2,j,k}-\psi|_{i,j,k}\right)+d_1^x|_i\left(\psi|_{i+1,j,k}-\psi|_{i,j,k}\right)\\ & +d_{-1}^x|_i\left(\psi|_{i-1,j,k}-\psi|_{i,j,k}\right)+d_{-2}^x|_i\left(\psi|_{i-2,j,k}-\psi|_{i,j,k}\right)\\ & +d_2^y|_j\left(\psi|_{i,j+2,k}-\psi|_{i,j,k}\right)+d_1^y|_j\left(\psi|_{i,j+1,k}-\psi|_{i,j,k}\right)\\ & +d_{-1}^y|_j\left(\psi|_{i,j-1,k}-\psi|_{i,j,k}\right)+d_{-2}^y|_j\left(\psi|_{i,j-2,k}-\psi|_{i,j,k}\right)\\ & +d_2^z|_k\left(\psi|_{i,j,k+2}-\psi|_{i,j,k}\right)+d_1^z|_k\left(\psi|_{i,j,k+1}-\psi|_{i,j,k}\right)\\ & +d_{-1}^z|_k\left(\psi|_{i,j,k-1}-\psi|_{i,j,k}\right)+d_{-2}^z|_k\left(\psi|_{i,j,k-2}-\psi|_{i,j,k}\right).\end{aligned} \tag{4.10}$$

4.2.2 Temporal discretization

A second-order accurate central difference is used for the temporal discretization [12]:

$$\left.\frac{\partial\psi}{\partial t}\right|^n = \frac{\psi|^{n+1}-\psi|^{n-1}}{2\Delta t}+\mathcal{O}\big(\Delta t^2\big), \tag{4.11}$$

where n denotes the temporal index.

The combination of the spatial and temporal discretizations yields following CE update scheme:

$$\psi|_{i,j,k}^{n+1} = \psi|_{i,j,k}^{n-1}+\jmath\frac{\hbar\Delta t}{m}\,(L\boldsymbol{\psi})|_{(i,j,k)}^{n}-\jmath\frac{2\Delta t}{\hbar}v|_{i,j,k}\;\psi|_{i,j,k}^{n}, \tag{4.12}$$

where L is either L_L or L_H, for the lower- or higher-order scheme, respectively. The CE update scheme (4.12) naturally leads to two independent *leapfrog* schemes, as the real and imaginary parts at even and odd time steps, respectively, are decoupled from the real and imaginary parts at odd and even time steps, respectively (Fig. 4.2). With r and s the real and imaginary parts of the wave function, the

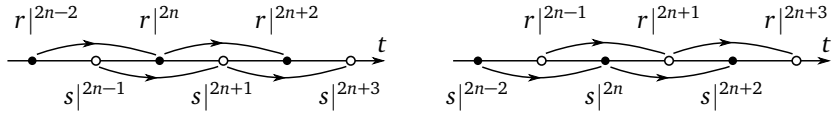

Figure 4.2: The update scheme for the Schrödinger equation (4.12) results in two intertwined but independent leapfrog schemes. The left scheme (4.13), with the real part r at even and the imaginary part s at odd time steps, is decoupled from the right scheme (4.14), with the real part at odd and imaginary part at even time steps. In the numerical implementation, it is twice as efficient to solve only one of both decoupled schemes.

update equations are given by:

$$r|_{i,j,k}^{2n} = r|_{i,j,k}^{2n-2} - \frac{\hbar\Delta t}{m}\,(L\boldsymbol{s})|_{(i,j,k)}^{2n-1} + \frac{2\Delta t}{\hbar} v|_{i,j,k}\, s|_{i,j,k}^{2n-1}, \tag{4.13a}$$

$$s|_{i,j,k}^{2n+1} = s|_{i,j,k}^{2n-1} + \frac{\hbar\Delta t}{m}\,(L\boldsymbol{r})|_{(i,j,k)}^{2n} - \frac{2\Delta t}{\hbar} v|_{i,j,k}\, r|_{i,j,k}^{2n}, \tag{4.13b}$$

and

$$r|_{i,j,k}^{2n+1} = r|_{i,j,k}^{2n-1} - \frac{\hbar\Delta t}{m}\,(L\boldsymbol{s})|_{(i,j,k)}^{2n} + \frac{2\Delta t}{\hbar} v|_{i,j,k}\, s|_{i,j,k}^{2n}, \tag{4.14a}$$

$$s|_{i,j,k}^{2n+2} = s|_{i,j,k}^{2n} + \frac{\hbar\Delta t}{m}\,(L\boldsymbol{r})|_{(i,j,k)}^{2n+1} - \frac{2\Delta t}{\hbar} v|_{i,j,k}\, r|_{i,j,k}^{2n+1}. \tag{4.14b}$$

For notational simplicity, it is easier to write the wave function as the complex scalar equation, as in the CE scheme (4.12). However, for computational efficiency, the real and imaginary parts should be split and only one of both leapfrog schemes should be computed, either (4.13) or (4.14), as was also proposed in [2]. Even though we only consider the CE scheme (4.12) in the remainder of this chapter, the results are also valid for the leapfrog schemes.

The proposed nonuniform and higher-order spatial discretization can be combined with other temporal schemes such as the Crank-Nicolson (CN) method [1] or the alternating-direction implicit (ADI) method [9]. It is also possible to combine it with higher-order temporal schemes, e.g., the generalized FDTD method [5] or a higher-order symplectic scheme [6].

The proposed schemes can incorporate a perfectly matched layer (PML) [13] for unbounded domains. The PML technique for the Schrödinger equation, where a coordinate stretching is performed into the complex plane [14–17], is applied to (4.12) both for the lower-order and higher-order accurate scheme. The cells have to be stretched as:

$$\Delta x_{i,\mathrm{PML}} = \Delta x_i\big(1 + \alpha\,\sigma|_{i-1/2}\big), \tag{4.15a}$$

$$\Delta x^{\star}_{i,\mathrm{PML}} = \Delta x^{\star}_i\big(1 + \alpha\,\sigma|_i\big), \tag{4.15b}$$

where α is a complex number and σ the absorption function. The absorption function increases as a function of the depth inside the PML and α determines the ratio of real versus imaginary stretch [18]. If the complex cell sizes are used directly in the Laplacian L, it becomes a complex-valued matrix. This mixes the two independent leapfrog schemes (4.13a)–(4.13b) and (4.14a)–(4.14b), and renders the scheme unstable, as will be discussed in Section 4.3. To remedy this, the approach described in [16] is applied, resulting in:

$$\begin{aligned}\psi|_{i,j,k}^{n+1} = \psi|_{i,j,k}^{n-1} + \jmath\frac{\hbar\Delta t}{m}\left(L_{\mathrm{Re}}\boldsymbol{\psi}\right)|_{(i,j,k)}^{n} - \jmath\frac{2\Delta t}{\hbar}v|_{i,j,k}\,\psi|_{i,j,k}^{n} \\ - \frac{\hbar\Delta t}{m}\left(L_{\mathrm{Im}}\boldsymbol{\psi}\right)|_{(i,j,k)}^{n-1},\end{aligned} \tag{4.16}$$

where L_{Re} and L_{Im} are the real and imaginary parts of L, respectively.

4.3 Stability

The stability analysis of the Schrödinger equation is customarily performed as in Chapter 3 with a von Neumann analysis and where the grid is assumed uniform and the potential constant [6]. This approach was further verified for the Schrödinger equation in [3], where a more rigorous criterion was determined by explicitly allowing the potential to vary. For nonuniform grids, however, the stability condition cannot be derived in this way. Instead, discrete-time stability analysis for matrices is applied to derive a rigorous stability condition [19]. Additionally, this analysis generates more profound insights into the true time step stability bound, which is dictated by the eigenvalues of the iteration matrix, even in the limit of uniform grids.

The update equation (4.12) is written in matrix form as:

$$\boldsymbol{f}|^{n} = A\boldsymbol{f}|^{n-1}, \tag{4.17}$$

with

$$\boldsymbol{f}|^{n} = \begin{bmatrix}\boldsymbol{\psi}|^{n} \\ \boldsymbol{\psi}|^{n-1}\end{bmatrix}, \quad \text{and} \quad A = \begin{bmatrix}-\jmath\frac{2\Delta t}{\hbar}H & I_{n_\psi} \\ I_{n_\psi} & 0\end{bmatrix}. \tag{4.18}$$

The Hamiltonian matrix H is defined as:

$$H \triangleq -\frac{\hbar^2}{2m}L + V, \tag{4.19}$$

with L either L_L or L_H and where V is the diagonal matrix containing the potential energy v. To guarantee stability, the eigenvalues z of the iteration matrix A cannot lie outside the unit circle, i.e., $|z| \leq 1$ [19–21]. The eigenvalues z are related to the eigenvalues w of H through:

$$z^2 + z\left(\jmath\frac{2\Delta t}{\hbar}w\right) - 1 = 0. \tag{4.20}$$

Since $\det\left(zI_{2n_\psi} - A\right) = \det\left(zI_{n_\psi}\right)\det\left(zI_{n_\psi} + (\jmath 2\Delta t H/\hbar) - z^{-1}I_{n_\psi}\right)$ [19]. Note that this equation (4.20) has the same structure as (3.14). As such, the eigenvalues z lie in the closed unit circle if and only if the eigenvalues w of H are real and for Δt satisfying:

$$\Delta t \leq \frac{\hbar}{\max(|w|)}, \tag{4.21}$$

where by definition $\rho(H) = \max(|w|)$ is the spectral radius of H. Provided that this is true, the eigenvalues z will all lie on the unit circle. For complex values of w or for Δt not satisfying (4.21), some eigenvalues will have a norm greater than 1, yielding an unstable scheme. Therefore, we can conclude that the FDTD scheme (4.17) is stable if and only if the eigenvalues of H are real and the time step satisfies the relation:

$$\Delta t \leq \frac{\hbar}{\rho(H)}. \tag{4.22}$$

This stability criterion is very general as it is valid for *any* consistent spatial scheme that uses the CE scheme (4.12) or the equivalent staggered in time schemes (4.13) or (4.14). For example, it would be possible to use a Hamiltonian matrix based on the nonuniform grid mapping presented in [8], a higher-order compact difference scheme [22], or apply different boundary conditions.

We now check that the eigenvalues of H_L using Dirichlet boundary conditions are indeed real. First, the Laplacian matrix for the lower-order scheme L_L is decomposed as:

$$L_L = L_{Lx} \oplus L_{Ly} \oplus L_{Lz} \tag{4.23a}$$

$$= -(\delta_x^{\star -1} D_x \delta_x{}^{-1} D_x{}^T) \oplus (\delta_y^{\star -1} D_y \delta_y{}^{-1} D_y{}^T) \oplus (\delta_z^{\star -1} D_z \delta_z{}^{-1} D_z{}^T), \tag{4.23b}$$

where $\oplus$ is the Kronecker sum, and D_u the discrete differentiator:

$$D_u = \begin{bmatrix} -1 & 1 & & & & \\ & -1 & 1 & & & \\ & & \ddots & \ddots & & \\ & & & -1 & 1 & \\ & & & & -1 & 1 \end{bmatrix}_{m_u \times n_u}, \tag{4.24}$$

and δ_u and $\delta_u^\star$ are the diagonal matrices containing the n_u primary and m_u dual grid steps in the u-direction ($u \in \{x, y, z\}$). Next, a similarity transformation is

applied to H_L:

$$\tilde{H}_L = Q^{\frac{1}{2}}\, H_L\, Q^{-\frac{1}{2}}, \tag{4.25a}$$

$$= -\frac{\hbar^2}{2m} Q^{\frac{1}{2}}\, L_L\, Q^{-\frac{1}{2}} + V \tag{4.25b}$$

$$= -\frac{\hbar^2}{2m} \tilde{L}_L + V \tag{4.25c}$$

where the diagonal transformation matrix Q is defined as:

$$Q \triangleq \delta_x^\star \otimes \delta_y^\star \otimes \delta_z^\star, \tag{4.26}$$

where $\otimes$ is the Kronecker product. Next, the Laplacian L_L is expanded as:

$$\begin{aligned} L_L = &-\left(\delta_x^{\star\,-1} D_x \delta_x{}^{-1} D_x{}^T \otimes I_{m_y} \otimes I_{m_z}\right) \\ &-\left(I_{m_x} \otimes \delta_y^{\star\,-1} D_y \delta_y{}^{-1} D_y{}^T \otimes I_{m_z}\right) \\ &-\left(I_{m_x} \otimes I_{m_y} \otimes \delta_z^{\star\,-1} D_z \delta_z{}^{-1} D_z{}^T\right). \end{aligned} \tag{4.27}$$

Lastly, we show that $\tilde{L}_L$ is real symmetric, by using the mixed-product property of the Kronecker sum $(A \otimes B)(C \otimes D) = (AC) \otimes (BD)$ [19], such that $\tilde{L}_L$ is given by:

$$\tilde{L}_L = -\left(\tilde{D}_x \tilde{D}_x{}^T \oplus \tilde{D}_y \tilde{D}_y{}^T \oplus \tilde{D}_z \tilde{D}_z{}^T\right), \tag{4.28}$$

where $\tilde{D}_u$ is defined as:

$$\tilde{D}_u \triangleq \left(\delta_u^\star\right)^{-\frac{1}{2}} D_u \delta_u{}^{-\frac{1}{2}}, \quad \text{for} \quad u \in \{x, y, z\}. \tag{4.29}$$

Since real symmetric matrices have real eigenvalues, L_L and H_L only have real eigenvalues. This discussion can be directly repeated for periodic boundary conditions with only minor changes, i.e., add an extra row to D_u as follows:

$$D_u^{\text{periodic}} = \begin{bmatrix} -1 & 1 & & & \\ & -1 & 1 & & \\ & & \ddots & \ddots & \\ & & & -1 & 1 \\ 1 & & & & -1 \end{bmatrix}_{n_u \times n_u},$$

and replace $\delta_u^\star$ by $\mathrm{diag}(\Delta u_1^\star, \ldots, \Delta u_{n_u}^\star)$, where $\mathrm{diag}(\ldots)$ constructs a diagonal matrix with the specified elements.

This stability analysis also shows why the direct implementation of a PML with complex cell sizes would lead to an unstable scheme. In that case, the matrix

L is similar to a complex symmetric matrix instead of a real symmetric or complex Hermitian matrix, which does not necessarily yield real eigenvalues. Therefore, we adopt the alternative PML implementation (4.16) from [16] with complex stretched cells (4.15) and numerical experiments show that this method is indeed stable.

The Laplacian L_H of the higher-order scheme can also be decomposed as the Kronecker sum $L_H = L_{Hx} \oplus L_{Hy} \oplus L_{Hz}$ with L_{Hx}, L_{Hy} and L_{Hz} the discretized third-order accurate second-order derivatives in the x-, y- and z-directions, respectively. However, it is not possible to decompose this further and prove its similarity to a real symmetric matrix of H_H in a straightforward manner. In the case of a uniform grid, H_H is real and symmetric since L_{Hx}, L_{Hy} and L_{Hz} are real symmetric, which implies that the eigenvalues are real. Hence, the inequality (4.22) will guarantee stability. In the next section, however, we will assume that H_H has only real eigenvalues, even in the nonuniform case, which is supported by numerical calculations provided in Section 4.5.

A Courant-like stability criterion

Calculating the eigenvalues of H numerically is computationally expensive for large grids. In most practical cases, the time step is based on an easily calculable formula, such as the Courant-Friedrichs-Lewy condition, which we discussed in Section 3 but which makes a (slight) underestimate of the stability limit [23–25]. In order to obtain a similar condition, an estimate of the spectral radius of the Hamiltonian matrix H is made.

The spectral radius is bounded by any induced norm, e.g., the infinity norm [26]:

$$\rho(H) \leq \|H\|_\infty = \max_m \sum_n \left|[H]_{m,n}\right|. \tag{4.30}$$

To derive a Courant-like stability criterion for the lower-order scheme, the structure of the lower-order Hamiltonian matrix H_L has to be considered. Row $m = \big(im_y + j\big)m_z + k$ with $m \in \{1,\ldots,m_x m_y m_z)\}$, $i \in \{1,\ldots,m_x\}$, $j \in \{1,\ldots,m_y\}$, and $k \in \{1,\ldots,m_z\}$ of the Hamiltonian matrix looks like:

$$\begin{aligned}
&\Bigg[\ldots, -\frac{\hbar^2}{2m} c_{-1}^x|_i, \ldots, -\frac{\hbar^2}{2m} c_{-1}^y|_j, \ldots, -\frac{\hbar^2}{2m} c_{-1}^z|_k, \\
&-\frac{\hbar^2}{2m}\Big(-c_{-1}^x|_i - c_1^x|_i - c_{-1}^y|_j - c_1^y|_j - c_{-1}^z|_k - c_1^z|_k\Big) + v|_{i,j,k}, \\
&-\frac{\hbar^2}{2m} c_1^z|_k, \ldots, -\frac{\hbar^2}{2m} c_1^y|_j, \ldots, -\frac{\hbar^2}{2m} c_1^x|_i, \ldots \Bigg],
\end{aligned} \tag{4.31}$$

where the "…" represent an appropriate number of zeros. The column indexes n of the nonzero elements are in order: $n = m - m_z m_y$, $n = m - m_z$, $n = m - 1$,

$n = m$, $n = m + 1$, $n = m + m_z$ and $n = m + m_z m_y$.

The row m for which the sum of the absolute values of these elements is maximal, yields the infinity norm:

$$\|H_L\|_\infty = \max_{i,j,k}\left(\left[\left|\frac{\hbar^2}{2m}\left(\frac{1}{\lambda_{i,j,k}}\right)^2 + v|_{i,j,k}\right| + \frac{\hbar^2}{2m}\left(\frac{1}{\lambda_{i,j,k}}\right)^2\right]\right), \tag{4.32}$$

where $\lambda_{i,j,k}$ is defined by:

$$\begin{aligned}\left(\frac{1}{\lambda_{i,j,k}}\right)^2 \triangleq\ & \frac{1}{\Delta x_i^\star}\left(\frac{1}{\Delta x_i} + \frac{1}{\Delta x_{i+1}}\right) \\ & + \frac{1}{\Delta y_j^\star}\left(\frac{1}{\Delta y_j} + \frac{1}{\Delta y_{j+1}}\right) + \frac{1}{\Delta z_k^\star}\left(\frac{1}{\Delta z_k} + \frac{1}{\Delta z_{k+1}}\right).\end{aligned} \tag{4.33}$$

As such, the Courant-like stability criterion for the lower-order scheme is:

$$\Delta t_L^C \leq \min_{i,j,k}\left(\left[\left|\frac{\hbar}{2m}\left(\frac{1}{\lambda_{i,j,k}}\right)^2 + \frac{1}{\hbar}v|_{i,j,k}\right| + \frac{\hbar}{2m}\left(\frac{1}{\lambda_{i,j,k}}\right)^2\right]^{-1}\right). \tag{4.34}$$

A similar reasoning leads to the Courant-like stability criterion for the higher-order scheme, for which we introduce:

$$\mu_{i,j,k} = \sum_{(u,l)\in\{(x,i),(y,j),(z,k)\}} d_{-2}^u|_l + d_{-1}^u|_l + d_1^u|_l + d_2^u|_l, \tag{4.35}$$

$$\tilde{\mu}_{i,j,k} = \sum_{(u,l)\in\{(x,i),(y,j),(z,k)\}} \left|d_{-2}^u|_l\right| + \left|d_{-1}^u|_l\right| + \left|d_1^u|_l\right| + \left|d_2^u|_l\right|. \tag{4.36}$$

The resulting stability condition is given by:

$$\Delta t_H^C \leq \min_{i,j,k}\left(\left[\left|\frac{\hbar}{2m}\left(\mu_{i,j,k}\right) + \frac{1}{\hbar}v|_{i,j,k}\right| + \frac{\hbar}{2m}\left(\tilde{\mu}_{i,j,k}\right)\right]^{-1}\right). \tag{4.37}$$

On uniform grids, the Hamiltonian matrix H is symmetric and, hence, all its eigenvalues are real. In this case, the stability conditions simplify to:

$$\Delta t_l \leq \min_{i,j,k} \frac{\hbar}{\left|\frac{\hbar^2}{m}\left(\frac{1}{\Delta x^2} + \frac{1}{\Delta y^2} + \frac{1}{\Delta z^2}\right) + v|_{i,j,k}\right| + \frac{\hbar^2}{m}\left(\frac{1}{\Delta x^2} + \frac{1}{\Delta y^2} + \frac{1}{\Delta z^2}\right)}, \tag{4.38}$$

$$\Delta t_h \leq \min_{i,j,k} \frac{\hbar}{\left|\frac{5\hbar^2}{4m}\left(\frac{1}{\Delta x^2} + \frac{1}{\Delta y^2} + \frac{1}{\Delta z^2}\right) + v|_{i,j,k}\right| + \frac{17\hbar^2}{12m}\left(\frac{1}{\Delta x^2} + \frac{1}{\Delta y^2} + \frac{1}{\Delta z^2}\right)}, \tag{4.39}$$

for the lower- and higher-order scheme, respectively. On this uniform grid, these schemes are second- and fourth-order accurate, respectively. Also note that (4.38) is less stringent than (3.18) for negative potentials.

In many practical cases the potential satisfies the relation:

$$v|_{i,j,k} \geq -\frac{\hbar^2}{m}\left(\frac{1}{\Delta x^2}+\frac{1}{\Delta y^2}+\frac{1}{\Delta z^2}\right), \quad \forall i,j,k, \tag{4.40}$$

simplifying the time steps to:

$$\Delta t_l \leq \frac{\hbar}{\frac{2\hbar^2}{m}\left(\frac{1}{\Delta x^2}+\frac{1}{\Delta y^2}+\frac{1}{\Delta z^2}\right)+\max(v)}, \tag{4.41}$$

$$\Delta t_h \leq \frac{\hbar}{\frac{8\hbar^2}{3m}\left(\frac{1}{\Delta x^2}+\frac{1}{\Delta y^2}+\frac{1}{\Delta z^2}\right)+\max(v)}, \tag{4.42}$$

which is consistent with results in [2–6] when using only one of the two independent leapfrog schemes in Fig. 4.2.

From (4.34)–(4.42) it is clear that the scheme can be tuned to achieve a trade-off between efficiency (large time step) and accuracy (small spatial step). For example, (4.34) states that the grid can be made coarser (i.e. larger $\lambda_{i,j,k}$) at locations where $v|_{i,j,k}$ is larger. This property is exploited and demonstrated in Section 4.5. Also, while (4.41) and (4.42) indicate that the higher-order scheme requires a smaller time step, the added accuracy will in practice allow us to use a coarser grid, which in turn results in a larger time step.

4.4 Numerical dispersion

In this section, the numerical dispersion error is derived and analyzed for both new schemes. The dispersion error is characterized by the difference between the physical propagation of a plane wave and the one calculated by the FDTD algorithm. To derive this error, the grid is assumed uniform and infinite with a constant potential v, such that the following plane-wave solution can be substituted into the update equations:

$$\psi|_{i,j,k}^{n} = e^{-\jmath(\tilde{\omega}n\Delta t - k_x i\Delta x - k_y j\Delta y - k_z k\Delta z)}, \tag{4.43}$$

where $\tilde{\omega}$ is the numerical angular frequency, and k_x, k_y, and k_z, are the x-, y-, and z-components of the wave vector $\boldsymbol{k}$, respectively. This plane wave corresponds to the solution of the Schrödinger equation that is enforced on the space-time discretized grid. The substitution of this plane wave into the lower-order scheme

yields:

$$\frac{1}{2\Delta t}\left(e^{-\jmath\tilde{\omega}\Delta t}-e^{\jmath\tilde{\omega}\Delta t}\right)= \jmath\frac{\hbar}{2m}\left[\frac{e^{\jmath k_x\Delta x}-2+e^{-\jmath k_x\Delta x}}{\Delta x^2}+\frac{e^{\jmath k_y\Delta y}-2+e^{-\jmath k_y\Delta y}}{\Delta y^2} + \frac{e^{\jmath k_z\Delta z}-2+e^{-\jmath k_z\Delta z}}{\Delta z^2}\right]-\jmath\frac{v}{\hbar}. \tag{4.44}$$

This simplifies to the numerical dispersion relation:

$$s_t=\frac{\hbar}{2m}\left(p_x^2+p_y^2+p_z^2\right)+\frac{v}{\hbar}, \tag{4.45}$$

where

$$s_t\triangleq\frac{1}{\Delta t}\sin(\tilde{\omega}\Delta t),\quad\text{and}\quad p_u\triangleq\frac{2}{\Delta x}\sin\left(\frac{k_u\Delta u}{2}\right), \tag{4.46}$$

for $u\in\{x,y,z\}$. The substitution of (4.43) into the higher-order scheme, after some simplifications, yields:

$$s_t=\frac{\hbar}{2m}\left(\frac{1}{3}\left(4p_x^2-s_x^2\right)+\frac{1}{3}\left(4p_y^2-s_y^2\right)+\frac{1}{3}\left(4p_z^2-s_z^2\right)\right)+\frac{v}{\hbar}, \tag{4.47}$$

where

$$s_u\triangleq\frac{1}{\Delta x}\sin(k_u\Delta u),\quad\text{for}\quad u\in\{x,y,z\}. \tag{4.48}$$

In the limit of $\tilde{\omega}\Delta t\to 0$ and $\|\boldsymbol{k}\|\Delta\to 0$, both (4.45) and (4.47) reduce to the analytical relation:

$$\hbar\omega=\frac{\hbar^2\|\boldsymbol{k}\|^2}{2m}+v. \tag{4.49}$$

An error measure is defined as:

$$\mathcal{E}=\frac{\omega-\tilde{\omega}}{\omega}, \tag{4.50}$$

which measures the relative difference between the numerical and the exact energy. We investigate the directional dependence of the error $\mathcal{E}$ by writing the wave vector in spherical coordinates and solving (4.45) and (4.47) for $\tilde{\omega}$.

We start by studying the influence of the ratio of kinetic and potential energy. A discretization of 20 samples per wavelength $\lambda=2\pi/\|\boldsymbol{k}\|$ is considered with the time steps chosen at the upper bound of (4.41) and (4.42) for the lower- and

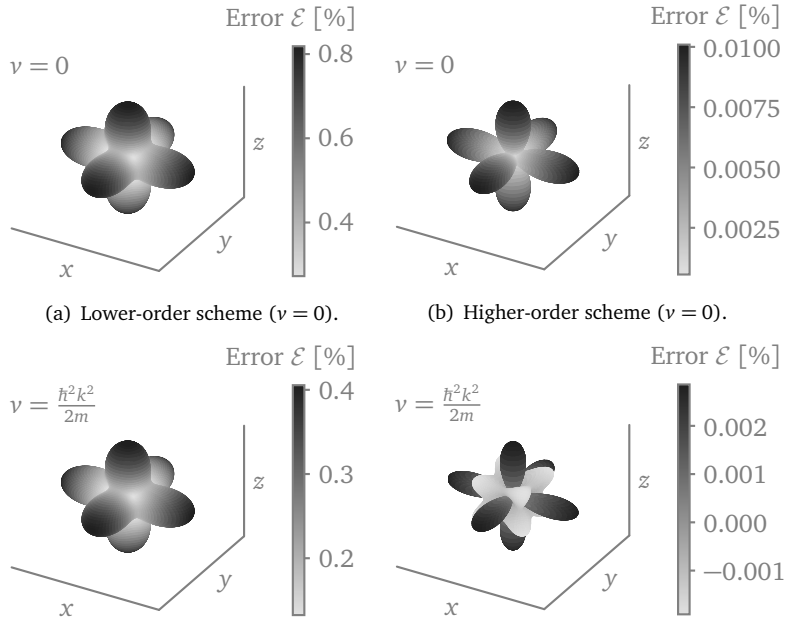

(a) Lower-order scheme ($v = 0$).

(b) Higher-order scheme ($v = 0$).

(c) Lower-order scheme ($v = \hbar^2 k^2/2m$).

(d) Higher-order scheme($v = \hbar^2 k^2/2m$).

Figure 4.3: The numerical dispersion error $\mathcal{E}$ (4.50) for the higher-order scheme has a much reduced overall error. A discretization of 20 samples per wavelength is adopted and the time step is chosen at the upper bound of (4.41) and (4.42). For a free particle ($v = 0$) shown in Figs. 4.3(a) and 4.3(b), the lower-order scheme has a maximum error that is approximately 80 times larger compared to the higher-order scheme. For equal kinetic and potential energy ($v = \hbar^2 k^2/2m$) shown in Figs. 4.3(c) and 4.3(d), the higher-order scheme is almost 200 times more accurate.

higher-order scheme, respectively. First, the dispersion error for a free particle $v = 0$ is given in Figs. 4.3(a) and 4.3(b). The lower-order scheme has a maximum error that is approximately 80 times larger than for the higher-order scheme. For both schemes, the body diagonals are the directions of least error, but for neither scheme does the error reduce to zero. The higher-order scheme is more anisotropic, but this is easily compensated by the overall decrease in error.

Next, the potential is set equal to the kinetic energy $v = \hbar^2 k^2/2m$ whereas the other variables remain unchanged in Figs. 4.3(c) and 4.3(d). The lower-order scheme has a maximum error that is approximately 200 times larger compared to the higher-order scheme. The directional dependence is more intricate as the numerical angular frequency $\tilde{\omega}$ can now also outpace the analytical angular frequency ω, yielding a negative $\mathcal{E}$.

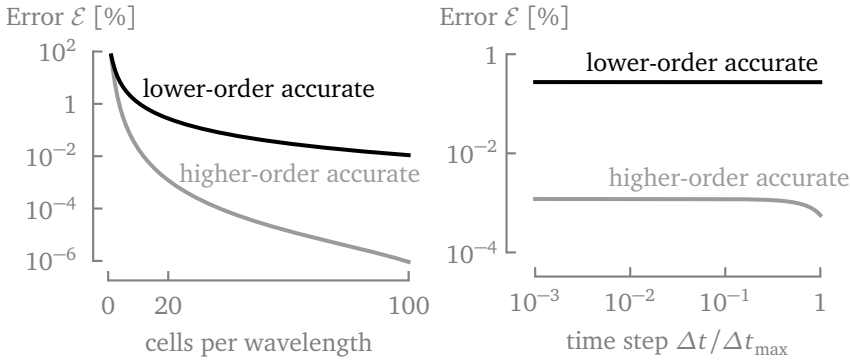

(a) Varying the spatial and time steps.

(b) Varying only the time steps.

Figure 4.4: Increasing the number of cells per wavelength (and simultaneously decreasing the time step Δt) drastically decreases the numerical dispersion error $\mathcal{E}$ whereas only decreasing Δt has little effect. The error was computed along the body diagonal, i.e., $\phi = \pi/4$ and $\theta = \text{atan}\big(\sqrt{2}\big)$, as a function of (a) the spatial step at the upper bound of (4.41) and (4.42), denoted by Δt_{max}, and (b) the time step at 20 samples per wavelength for a free particle $v = 0$.

In Fig. 4.4, the numerical dispersion error is plotted along the body diagonal for a free particle. The higher-order scheme is seen to perform orders of magnitude better compared to the lower-order scheme. Moreover, it is shown in Fig. 4.4(a), that the error decreases much faster upon reducing the spatial step. In contrast, decreasing the time step Δt does not improve the accuracy, as shown in Fig. 4.4(b). As such, it is beneficial both for computational efficiency as accuracy, to set the time step as close to the maximum allowed time step.

4.5 Numerical validation

The results discussed in this section were all obtained on an Intel(R) Core(TM) i7-8650U CPU @ 1.90 GHz with 15.5 GiB of RAM memory. The simulations were implemented in C code because of its low-level computations and memory compactness.

4.5.1 Eigenvalues of A and H

In this section, the eigenvalues of the iteration matrix A (4.18) and Hamiltonian matrix H (4.19) are studied as a function of the cell sizes, the chosen time step and the potential energy. By visualizing how the eigenvalues change, we expose the origin of instabilities. The contribution of an eigenvector corresponding to eigenvalues outside the unit circle will grow at every time step, resulting in an

unstable scheme. Even if the contributions of all unstable eigenvectors are zero at the start of the simulation, it is possible that the scheme becomes unstable due to numerical rounding errors. The uniform grid with $v = 0$ is used for reference situation after which we investigate the cases where $v \neq 0$ and for a nonuniform grid. This demonstrates that the new stability criterion (4.22) yields a tighter upper bound compared to the Courant limit, both on uniform and on nonuniform grids.

Consider a grid of $10\,\mathrm{nm} \times 10\,\mathrm{nm} \times 10\,\mathrm{nm}$ divided into $10 \times 10 \times 10$ cells. The wave function at the edge is set to zero.

Further, consider the simplest case of a uniform grid, i.e., $\Delta x = \Delta y = \Delta z = 1\,\mathrm{nm}$, with $v = 0$ and $m = m_\mathrm{e}$, where m_e is the electron mass. This corresponds to an electron trapped in a 3-D infinite well. The time steps Δt_L^C and Δt_H^C denote the upper bounds of the time steps, calculated by (4.34) and (4.37) respectively, and Δt_L^ρ and Δt_H^ρ, the upper bounds of the time steps calculated by (4.22) for the lower- and higher-order scheme, respectively. These time steps are given by:

$$\Delta t_L^C = 1.439\,665\,\mathrm{fs}, \quad \Delta t_L^\rho = 1.475\,779\,\mathrm{fs}, \tag{4.51a}$$

$$\Delta t_H^C = 1.079\,749\,\mathrm{fs}, \quad \Delta t_H^\rho = 1.112\,937\,\mathrm{fs}. \tag{4.51b}$$

The eigenvalues for both proposed schemes are shown in Fig. 4.5 for different time steps. The eigenvalues accumulate in $z = -1$ as the time step is chosen closer to the stability condition (4.22). Even for this very basic grid, the Courant-like stability limit is an underestimation of the true maximum time step. In Fig. 4.5(b), some eigenvalues lie outside the unit circle because the time step is larger than Δt_H^ρ, resulting in an unstable scheme.

The addition of a potential modifies the allowed time step. For simplicity, the case where the potential is constant, is considered. The zero-point energy of the potential is arbitrary and should have no influence on any physical parameters calculated from the wave function. However, as was shown in Sections 4.3 and 4.4, both the stability criterion and the numerical dispersion error change. The time steps for a uniform potential of $v = 0.3\,\mathrm{eV}$ are:

$$\Delta t_L^C = 8.692\,734 \times 10^{-1}\,\mathrm{fs}, \quad \Delta t_L^\rho = 8.823\,096 \times 10^{-1}\,\mathrm{fs}, \tag{4.52a}$$

$$\Delta t_H^C = 7.236\,302 \times 10^{-1}\,\mathrm{fs}, \quad \Delta t_H^\rho = 7.383\,864 \times 10^{-1}\,\mathrm{fs}. \tag{4.52b}$$

Fig. 4.6 reveals that the behavior of the eigenvalues is similar to the $v = 0$ case. Still, it is observed that the potential increases the energy of the eigenstates, thus pushing the eigenvalues towards $z = -1$, resulting in a decreased time step.

A negative potential does the inverse. It pushes the eigenvalues of the iteration matrix away from $z = -1$ towards $z = 1$. This is shown in Fig. 4.7 for a uniform

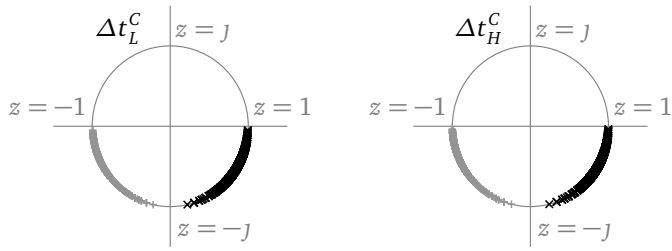

(a) Lower-order scheme.

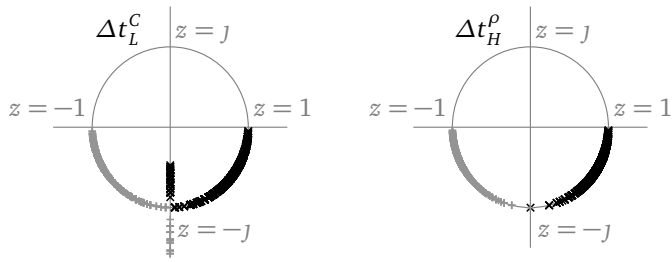

(b) Higher-order scheme.

Figure 4.5: The eigenvalues z of the iteration matrix A for a uniformly discretized grid and zero potential all lie in the lower half plane. The lower-order scheme, shown in 4.5(a) results in a stable scheme both for $\Delta t = \Delta t_L^C$ and $\Delta t = \Delta t_H^C$. The higher-order scheme in 4.5(b) is unstable for a time step $\Delta t = \Delta t_L^C$ but is stable for $\Delta t = \Delta t_H^\rho$. The latter has a double pole in $z = -\jmath$. The black $\times$ and the grey $+$ are the plus and minus solutions to (4.20), respectively.

potential $v = -0.3\,\mathrm{eV}$, resulting in the time steps:

$$\Delta t_L^C = 2.194\,040\,\mathrm{fs}, \quad \Delta t_L^\rho = 2.279\,034\,\mathrm{fs}, \tag{4.53a}$$

$$\Delta t_H^C = 1.946\,798\,\mathrm{fs}, \quad \Delta t_H^\rho = 2.258\,646\,\mathrm{fs}. \tag{4.53b}$$

Fig. 4.7 illustrates that increasing the time step pushes the eigenvalues with positive imaginary part towards $z = \jmath$ and those with negative imaginary part towards $z = -\jmath$. The maximum allowed time step is reached when either of these points is reached, at (4.22). Note that the time steps (4.53) are significantly larger than (4.52) even though (3.18) would yield the same time step in both cases. The zero energy point is arbitrary from a physical point of view such that the efficiency of the proposed schemes can be increased by lowering the potential. Note that in this case, the time step calculated by (4.41) for the lower-order scheme, which is used in [2, 4, 6], yields the incorrect time step $\Delta t = 4.187\,156\,\mathrm{fs}$, as (4.40) is violated. This would lead to an unstable scheme. The resulting instability is addressed in [3], where the absolute value of v is considered. However, this stability criterion

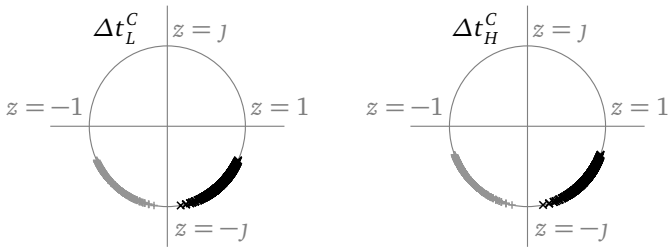

(a) Lower-order scheme.

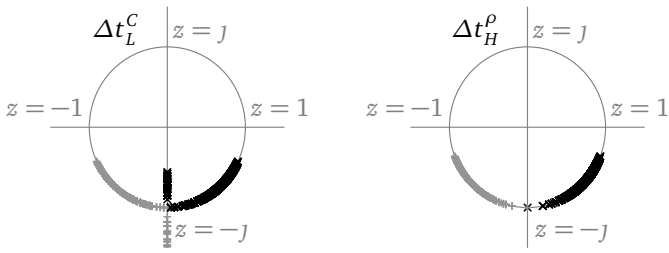

(b) Higher-order scheme.

Figure 4.6: A positive potential $v = 0.3\,\text{eV}$ pushes the eigenvalues of the iteration matrix A towards $z = -\jmath$. The lower-order scheme in Fig. 4.6(a) is stable both for $\Delta t = \Delta t_L^C$ and $\Delta t = \Delta t_H^C$. The higher-order scheme in 4.6(b) is unstable for a time step $\Delta t = \Delta t_L^C$ but is stable for $\Delta t = \Delta t_H^\rho$. The latter has a double pole in $z = -\jmath$. The black $\times$ and the grey $+$ are the plus and minus solutions to (4.20), respectively.

leads to an underestimation of the time step, namely $\Delta t = 8.692\,734 \times 10^{-1}\,\text{fs}$.

To verify whether the eigenvalues of the Hamiltonian matrix H are real, consider a highly nonuniform grid with randomly distributed grid points. The calculated time steps for this generated grid, shown in Fig. 4.8(a), are:

$$\Delta t_L^C = 1.171\,590 \times 10^{-2}\,\text{fs}, \quad \Delta t_L^\rho = 1.403\,755 \times 10^{-2}\,\text{fs}, \tag{4.54a}$$

$$\Delta t_H^C = 1.601\,756 \times 10^{-2}\,\text{fs}, \quad \Delta t_H^\rho = 3.976\,790 \times 10^{-2}\,\text{fs}. \tag{4.54b}$$

As illustrated in Fig. 4.8, numerical stability is guaranteed since the eigenvalues lie on the unit circle. Moreover, for such a nonuniform grid, the Courant-like stability criterions (4.34) and (4.37) are found to be a more substantial underestimation of the time step. The eigenvalue plots for the lower-order scheme are omitted as they are very similar to the higher-order scheme.

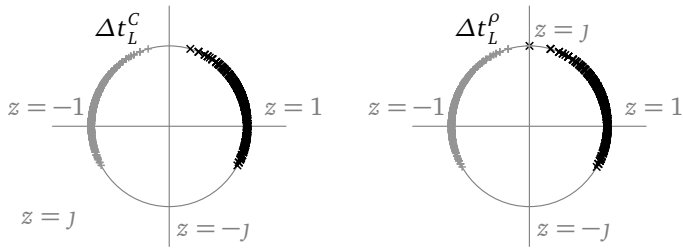

(a) Lower-order scheme.

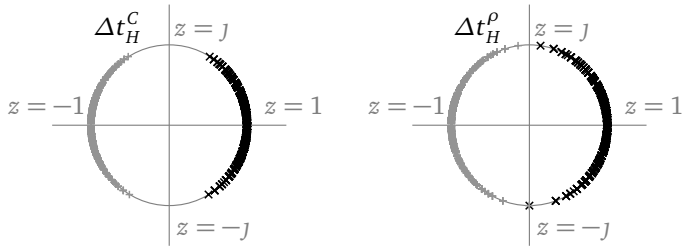

(b) Higher-order scheme.

Figure 4.7: A negative potential $v = -0.3\,\mathrm{eV}$ pushes the eigenvalues of the iteration matrix A towards $z = \jmath$. Increasing the Courant-like time step Δt^C from (4.34) and (4.37) to Δt^ρ determined by (4.22) moves the eigenvalues towards $z = \jmath$ and $z = -\jmath$, for both the lower- and higher-order schemes. The black $\times$ and the grey $+$ are the plus and minus solutions to (4.20), respectively.

4.5.2 A particle-in-a-3-D-box

In this section, a particle-in-a-3-D-box is considered. The eigenenergies of an electron in a cavity are calculated through a long-time simulation using both schemes and compared with the analytical result. The cavity is a cube with sides 8 nm and $m = m_\mathrm{e}$. The cube is uniformly discretized with $\Delta x = \Delta y = \Delta z = 0.2\,\mathrm{nm}$ resulting in a grid of $40 \times 40 \times 40$ cells.

The time steps calculated with the Courant-like stability criterion (4.34) and (4.37) are:

$$\Delta t_L^C = 5.758\,662 \times 10^{-2}\,\mathrm{fs}, \quad \text{and} \quad \Delta t_H^C = 4.318\,996 \times 10^{-2}\,\mathrm{fs}. \tag{4.55}$$

The time steps calculated with (4.22) are given by:

$$\Delta t_L^\rho = 5.767\,551 \times 10^{-2}\,\mathrm{fs}, \quad \text{and} \quad \Delta t_H^\rho = 4.327\,287 \times 10^{-2}\,\mathrm{fs}. \tag{4.56}$$

To determine the eigenenergies of the electron in the cavity, the method proposed in [27] is applied, where a narrow Gaussian function centered at an arbitrary posi-

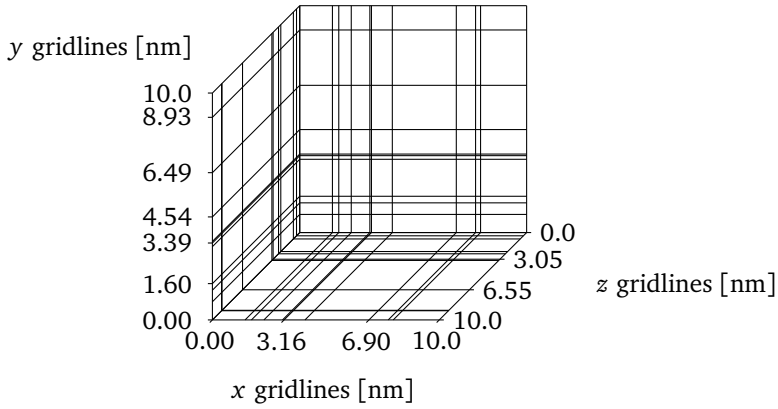

(a) Grid with randomly generated grid points

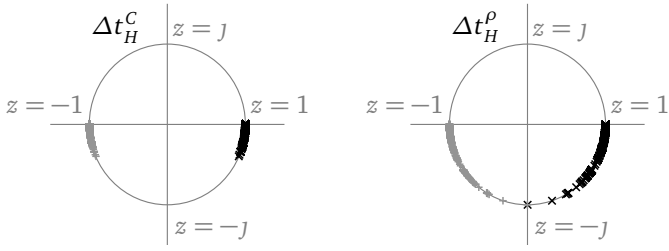

(b) Higher-order scheme.

Figure 4.8: The iteration matrix A for the higher-order order scheme on a randomly distributed grid only has eigenvalues on the unit circle as long as $\Delta t \leq \Delta t_H^\rho$.

tion is used as the initial wave function. The eigenenergies are extracted from the simulation by performing a Fourier transform of the time-domain data. Instead of looking at the data in a few points, the method in [8] is applied, where the time-domain data at every point is multiplied by a random number between −0.5 and 0.5 and summed. This is done to ensure that most eigenstates are found.

The simulation is run for 30.0 ps using the initial wave function:

$$\psi(x,y,z,t=0) = \left(\frac{1}{\pi\sigma^2}\right)^{3/4} e^{-\frac{(x-x')^2+(y-y')^2+(z-z')^2}{2\sigma^2}}, \tag{4.57}$$

with $\sigma = 0.5\,\text{nm}$, $x' = 1.0\,\text{nm}$, $y' = -2.0\,\text{nm}$ and $z' = -0.5\,\text{nm}$. The used time steps are (4.56), resulting in 520 151 and 693 274 iterations for the lower- and higher-order scheme, respectively. A Hamming window is applied to the time-domain signal to ensure that the peaks are well resolved.

Table 4.1: The comparison between the calculated and the analytical eigenvalues shows that the higher-order scheme predicts the eigenenergies with a much higher accuracy than the lower-order scheme. For each eigenmode, defined by its three quantum numbers n_1, n_2, and n_3, we give the analytical eigenenergies $\epsilon_{\text{analytic}}$, and the eigenvalues obtained with the lower-order and higher-order schemes, ϵ_L and ϵ_H, respectively. Moreover, we give the relative error of ϵ_L and ϵ_H w.r.t. $\epsilon_{\text{analytic}}$. Note that the lower-order scheme predicts different eigenenergies for modes 511 and 333 although they have the same analytical eigenenergy. It was assumed that the largest error corresponds to the mode with the highest maximum mode number, i.e., 511. The same is true for eigenmodes 522 and 441 and for 611 and 532. The error of the higher-order scheme is so small that the eigenenergies remain degenerate.

$n_1n_2n_3$	$\epsilon_{\text{analytic}}$ [eV]	ϵ_L [eV]	Error [%]	ϵ_H [eV]	Error [%]
111	0.0176264	0.0176454	0.11	0.0176455	0.11
211	0.0352528	0.0351529	0.28	0.0352910	0.11
221	0.0528792	0.0527983	0.15	0.0529365	0.11
311	0.0646302	0.0643781	0.39	0.0646543	0.04
222	0.0705057	0.0703059	0.28	0.0704442	0.09
321	0.0822566	0.0820235	0.28	0.0822998	0.05
322	0.0998830	0.0995310	0.35	0.0999453	0.06
411	0.1057585	0.1050452	0.67	0.1057353	0.02
331	0.1116340	0.1111108	0.47	0.1116631	0.03
421	0.1233849	0.1225528	0.67	0.1233808	0.00
332	0.1292604	0.1287562	0.39	0.1293086	0.04
422	0.1410113	0.1401981	0.58	0.1410263	0.01
431	0.1527623	0.1517779	0.64	0.1527440	0.01
511	0.1586377	0.1567407	1.20	0.1586718	0.02
333	0.1586377	0.1578436	0.50	0.1586718	0.02
432	0.1703887	0.1692855	0.65	0.1703896	0.00
521	0.1762641	0.1743861	1.07	0.1761795	0.05
522	0.1938906	0.1918936	1.03	0.1938250	0.03
441	0.1938906	0.1923072	0.82	0.1938250	0.03
433	0.1997660	0.1985107	0.63	0.1997528	0.01
531	0.2056415	0.2034734	1.05	0.2055428	0.05
442	0.2115170	0.2099526	0.74	0.2114705	0.02
611	0.2232679	0.2193267	1.77	0.2231883	0.04
532	0.2232679	0.2211188	0.96	0.2231883	0.04

In Fig. 4.9, the spectrum is shown for both the lower- and higher-order schemes. The values for the peaks are compared to the analytical values in Table 4.1. It can be seen that the higher-order scheme computes the eigenenergies with much higher accuracy. In fact, a large part of the error is due to the limited resolution of the Fourier transform. The simulation of this resonant cavity problem over many time steps confirms the accuracy of the proposed methods, particularly of the higher-order scheme, which exhibits very low numerical dispersion.

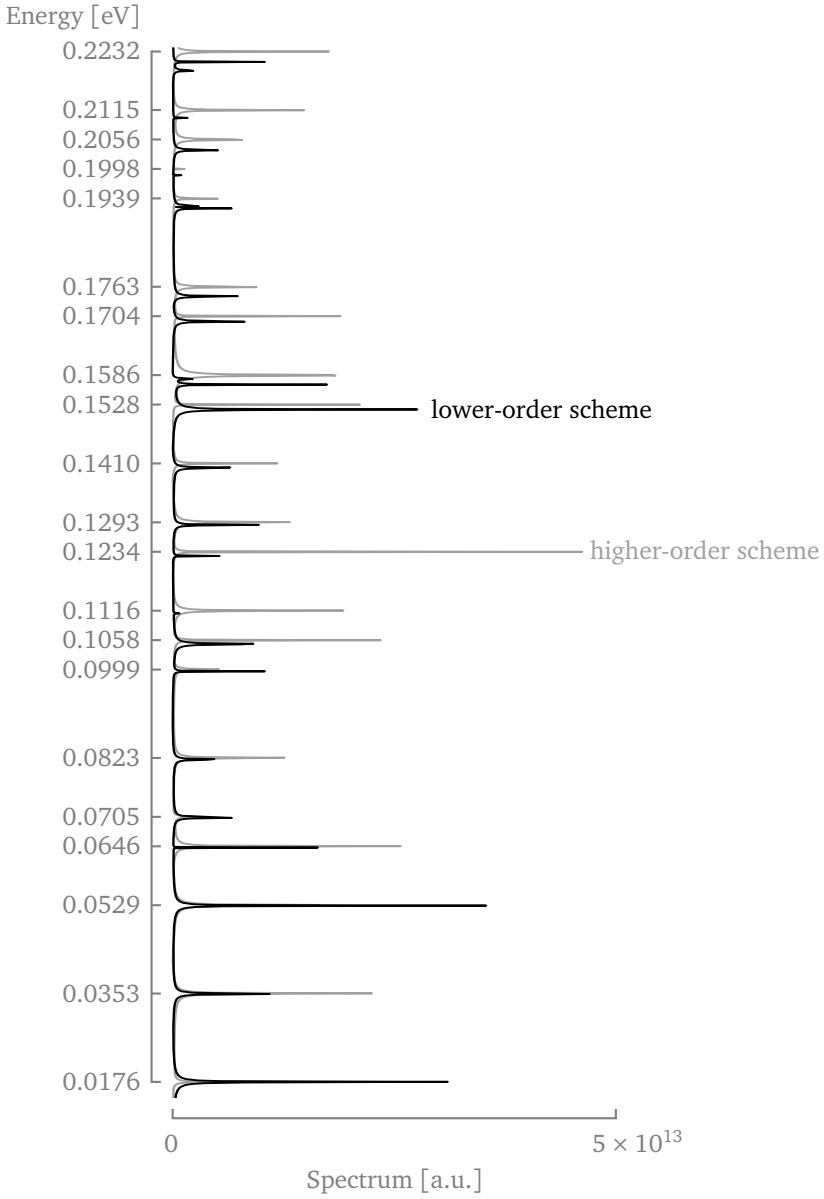

Figure 4.9: The higher-order scheme can predict the eigenenergies of the particle-in-a-3-D-box with a much higher accuracy and over a larger energy range. The tickmarks on the energy scale indicate the values for the higher-order scheme.

4.5.3 Coherent states

In this section, a simulation of a coherent state is performed. A short review of coherent states is provided at the end of this chapter in Appendix 4.A . Modeling the behavior of a coherent state over a long time is quite challenging as many energy eigenstates propagate simultaneously with different amplitudes. Small errors in the time evolution and amplitude of each eigenstate will gradually build up and result in decoherence. As such, the accuracy of the schemes is very visible, even for this highly dynamical simulation, since both the expectation value of the position and the shape of the probability distribution can be compared with the analytic result. The efficiency and accuracy of the higher-order scheme is compared with the lower-order scheme and the nonuniform grid is evaluated based on the speedup with respect to uniform grids.

A grid of 24 nm × 12 nm × 12 nm is constructed. The harmonic oscillator potential is defined as:

$$v(x,y,z) = \frac{1}{2}m\kappa^2\left(x^2+y^2+z^2\right), \tag{4.58}$$

with $m = 0.023\,m_\mathrm{e}$ and $\kappa = 1.984\times10^{15}\,\mathrm{rad\,s^{-1}}$. This artificial atom model was obtained from [28] which was based on a quantum dot in [29]. A normalized coherent state is initialized by shifting the ground state wave function to $x' = -5.0\,\mathrm{nm}$, which corresponds to a coherent state with quantum numbers:

$$\left(\alpha_x,\alpha_y,\alpha_z\right) = (-2.2197,0,0). \tag{4.59}$$

The resulting initial state is given by (4.57) with $\sigma^2 = \hbar/m\kappa$, and $y' = z' = 0\,\mathrm{nm}$. The accuracy of the two proposed schemes is evaluated for this set-up by comparing the analytical expectation value of the position $\langle\hat{x}(t)\rangle_\mathrm{ana}$ (4.A.6) to the numerically determined expectation value $\langle\hat{x}(t)\rangle_\mathrm{num}$ using the error measure:

$$\mathcal{E}_\mathrm{coh} = \frac{1}{\langle\hat{x}\rangle_\mathrm{max}}\sqrt{\frac{1}{T}\int_0^T\left(\langle\hat{x}(\tau)\rangle_\mathrm{ana}-\langle\hat{x}(\tau)\rangle_\mathrm{num}\right)^2\mathrm{d}\tau}, \tag{4.60}$$

where $\langle\hat{x}\rangle_\mathrm{max} = \max_t\langle\hat{x}(t)\rangle_\mathrm{ana} = 5.0\,\mathrm{nm}$. The numerical expectation value of the position (2.22a) and the integral in (4.60) are numerically evaluated by means of the trapezoidal rule. Deviations from the norm conservation will contribute to the overall error since the wave function is only normalized at initialization.

In Table 4.2, the parameters of the performed simulations are provided. The simulations are indicated by either an `L` or an `H` for the lower- and higher-order schemes, respectively. Furthermore, the simulations are numbered with a subscript. Simulations $\mathtt{L}_1$–$\mathtt{L}_3$ and $\mathtt{H}_1$–$\mathtt{H}_3$ are performed using a uniform grid such that the lower-order

Table 4.2: The grid parameters are compared to the accuracy and efficiency of the performed coherent state simulations. The `L` or `H` indicates the lower- or higher-order scheme, respectively, and the subscript indicates the simulation number. The tilde indicates that a nonuniform grid was used. Every grid has equal discretization in y- and z-directions such that $\Delta z = \Delta y$ and $n_z = n_y$. The nonuniform grids are defined in the x-direction by (4.61) and apply a constant grading ratio in the y- and z-directions of 1.05. The reported cell sizes correspond to the smallest cell sizes. We also report the total CPU time T_{CPU}, the error according to (4.60) and – where applicable – the order of convergence (OOC) using (4.62).

Sim.	$(\Delta x,\ \Delta y)$ [nm]	$(n_x,\ n_y)$	Δt [as]	T_{CPU} [s]	$\mathcal{E}_{\text{coh}}$ [%]	OOC
$\mathtt{L}_1$	(0.3, 0.3)	(80, 40)	2.44	113	49.4	—
$\mathtt{L}_2$	(0.2, 0.2)	(120, 60)	1.20	785	23.4	1.843
$\mathtt{L}_3$	(0.1, 0.1)	(240, 120)	0.32	24 225	5.94	1.928
$\mathtt{H}_1$	(0.3, 0.3)	(80, 40)	1.93	181	3.03	—
$\mathtt{H}_2$	(0.2, 0.2)	(120, 60)	0.92	1250	0.504	4.424
$\mathtt{H}_3$	(0.1, 0.1)	(240, 120)	0.24	34 111	0.0292	4.225
$\tilde{\mathtt{L}}_1$	(0.174, 0.2)	(97, 36)	1.21	208	27.0	—
$\tilde{\mathtt{L}}_2$	(0.174, 0.2)	(97, 36)	1.26	199	27.0	—
$\tilde{\mathtt{H}}_1$	(0.174, 0.2)	(97, 36)	0.92	319	0.388	—
$\tilde{\mathtt{H}}_2$	(0.174, 0.2)	(97, 36)	0.96	309	0.376	—

Table 4.3: The parameters for the discretization of the nonuniform grid in the x-direction are defined by (4.61).

a_1[nm]	b_1	a_2[nm]	b_2	a_3[nm]	b_3
2.214×10^{-5}	81.53	0.1739	−8.348 nm	1.969×10^{-5}	12.21

scheme is second-order accurate and the higher-order scheme is fourth-order accurate. Simulations $\tilde{\mathtt{L}}_1$, $\tilde{\mathtt{L}}_2$, $\tilde{\mathtt{H}}_1$, and $\tilde{\mathtt{H}}_2$ are performed using a nonuniform grid, with grid points along the x-direction given by:

$$x_i = \begin{cases} a_1(i-b_1)^3, & i < 25, \\ a_2\, i + b_2, & 25 \le i < 71, \\ a_3(i-b_3)^3, & \text{elsewhere}, \end{cases} \tag{4.61}$$

where the parameters are defined in Table 4.3. Along the y- and z-directions, the cell sizes are scaled from the center outward by a constant grading ratio of 1.05. The cell sizes denoted in Table 4.2 correspond to the smallest cell size.

The time steps are calculated using (4.34) and (4.37), except for simulations $\tilde{\mathtt{L}}_2$ and $\tilde{\mathtt{H}}_2$ where the spectral-radius-based upper bound is used (4.22). The total simulated time is 25 fs. In Fig. 4.10, we show $\langle \hat{x}(t) \rangle$ for the simulations in Table 4.2, except for $\tilde{\mathtt{L}}_2$ and $\tilde{\mathtt{H}}_2$ because these overlap too closely with $\tilde{\mathtt{L}}_1$ and $\tilde{\mathtt{H}}_1$, respectively.

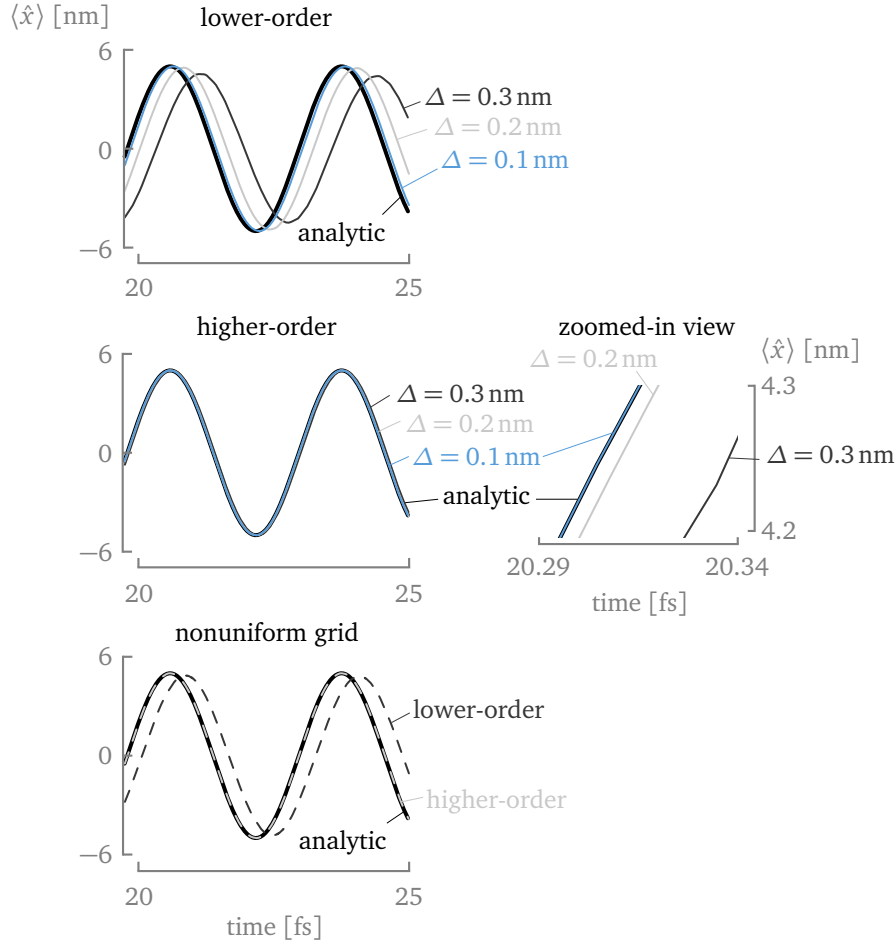

Figure 4.10: The calculated position $\langle \hat{x}(t) \rangle_{\text{num}}$ shows that higher-order scheme more closely coincides with the analytical solution compared to the lower-order method even on coarse grids ($\Delta = 0.3\,\text{nm}$). The lower-order results correspond to simulations $\mathtt{L}_1$–$\mathtt{L}_3$ from Table 4.2, the higher-order results with $\mathtt{H}_1$–$\mathtt{H}_3$ and the nonuniform grid results with $\tilde{\mathtt{L}}_2$ and $\tilde{\mathtt{H}}_2$. The results for $\tilde{\mathtt{L}}_1$ and $\tilde{\mathtt{H}}_1$ were omitted because they overlapped with $\tilde{\mathtt{L}}_2$ and $\tilde{\mathtt{H}}_2$. The different simulation results for the higher-order scheme can be differentiated in the zoomed-in view.

The error (4.60) corresponding to the simulations, is given in the one but last column of Table 4.2. The error indicates the average distance from the analytic solution during the first 25 fs. It can be seen that the higher-order scheme using the coarsest uniform grid $\mathtt{H}_1$ already outperforms the lower-order scheme using the finest grid $\mathtt{L}_3$, even though the latter has roughly 160 times more unknowns due to the increase in grid nodes and the superlinear decrease in time step. The accuracy of the higher-order scheme is excellent for spatial steps of 0.2 nm and 0.1 nm with an error below 1 % (see $\mathtt{H}_2$ and $\mathtt{H}_3$). In the rightmost column of Table 4.2 we give the order of convergence (OOC), which is calculated as:

$$\mathrm{OOC} = \frac{\log\left(\mathcal{E}_{\mathrm{coh,\,fine}}\right) - \log\left(\mathcal{E}_{\mathrm{coh,\,coarse}}\right)}{\log(\Delta x_{\mathrm{fine}}) - \log(\Delta x_{\mathrm{coarse}})}. \tag{4.62}$$

The coarse grid is either $\mathtt{L}_1$ or $\mathtt{H}_1$, depending on the used scheme, and the fine grid is given in the leftmost column of Table 4.2. This method of calculating the OOC is not applicable to nonuniform grids. As expected, the lower-order scheme exhibits approximately second-order convergence and the higher-order scheme exhibits approximately fourth-order convergence.

Snapshots of the particle propagating through the computational domain are given in Fig. 4.11 for simulations $\mathtt{L}_1$, $\mathtt{H}_1$, $\tilde{\mathtt{L}}_1$, and $\tilde{\mathtt{H}}_1$. By comparing simulations $\mathtt{L}_1$ and $\mathtt{H}_1$, it is clear that the higher-order scheme is able to maintain the Gaussian probability distribution for long time propagation in contrast to the lower-order scheme. Although the nonuniform discretization retains the coherence much better, the lower-order scheme $\tilde{\mathtt{L}}_1$ still gradually loses its Gaussian probability distribution compared to the higher-order scheme $\tilde{\mathtt{H}}_1$.

The nonuniform grid decreases the computation time in two distinct ways. First, it significantly decreases the number of spatial variables, resulting in 125 712 cells compared to 432 000 cells for the medium uniform grid, which has approximately the same accuracy. Furthermore, it has less cells than the uniform coarse grid which contains 128 000 cells. Second, the time step is increased (or at least unchanged) compared to the medium uniform grid even though the minimum cell size is decreased. These two effects are capable of reducing the CPU time by a factor 4 without compromising the accuracy. In fact, the higher-order scheme using the nonuniform grid $\tilde{\mathtt{H}}_2$ is even slightly more accurate than the higher-order uniform scheme $\tilde{\mathtt{H}}_2$ due to a decrease in cell size where necessary. As such the combination of a nonuniform grid and the rigorously derived time step allows to cleverly refine the grid. Where uniform refinement would quickly lead to an infeasible amount of calculations, a “smart” refinement – using a nonuniform grid and bearing (4.22) in mind – can limit the amount of spatial variables and limit the decrease of the time step.

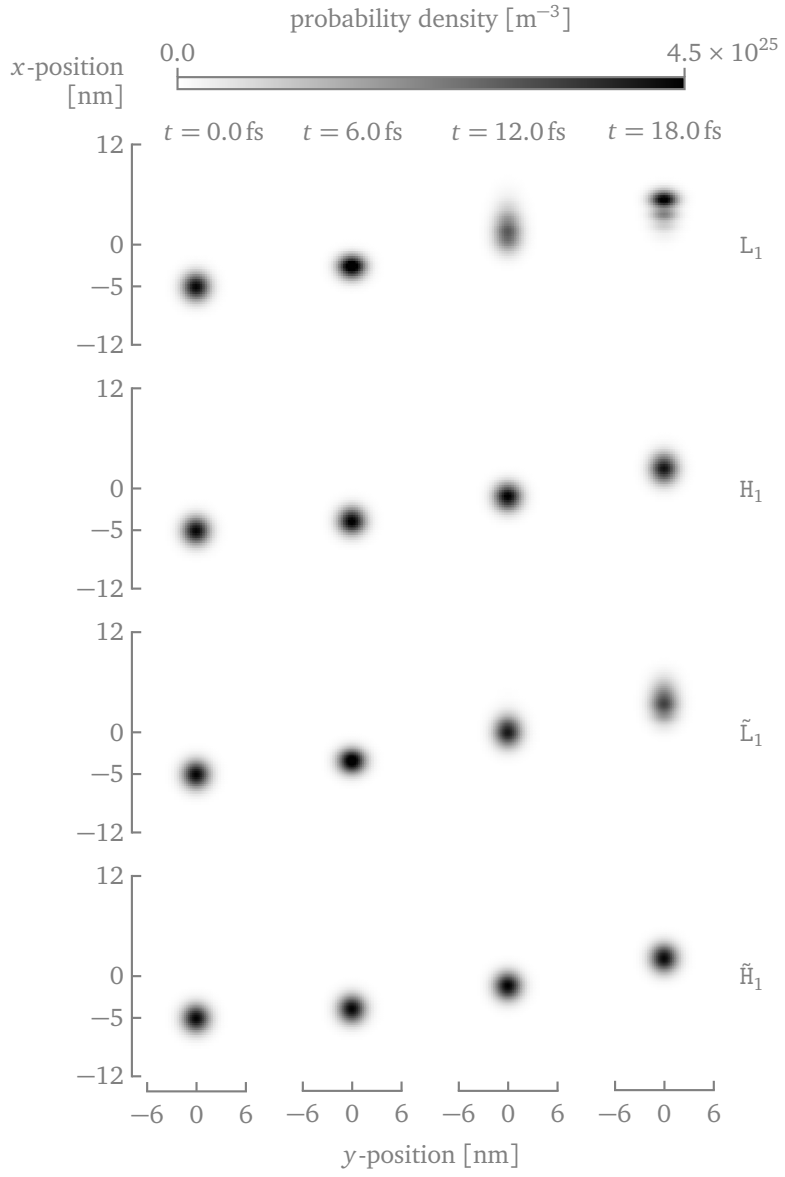

Figure 4.11: Snapshots of the particle in a harmonic oscillator propagating through the computational domain show that the higher-order scheme (in $\mathtt{H}_1$ and $\tilde{\mathtt{H}}_1$) is much better at preserving the Gaussian shape than the lower-order scheme (in $\mathtt{L}_1$ and $\tilde{\mathtt{L}}_1$). The nonuniform grid (in $\tilde{\mathtt{L}}_1$ and $\tilde{\mathtt{H}}_1$) also succeeds in preserving the shape at only a modest increase in the computational load as seen in Table 4.2

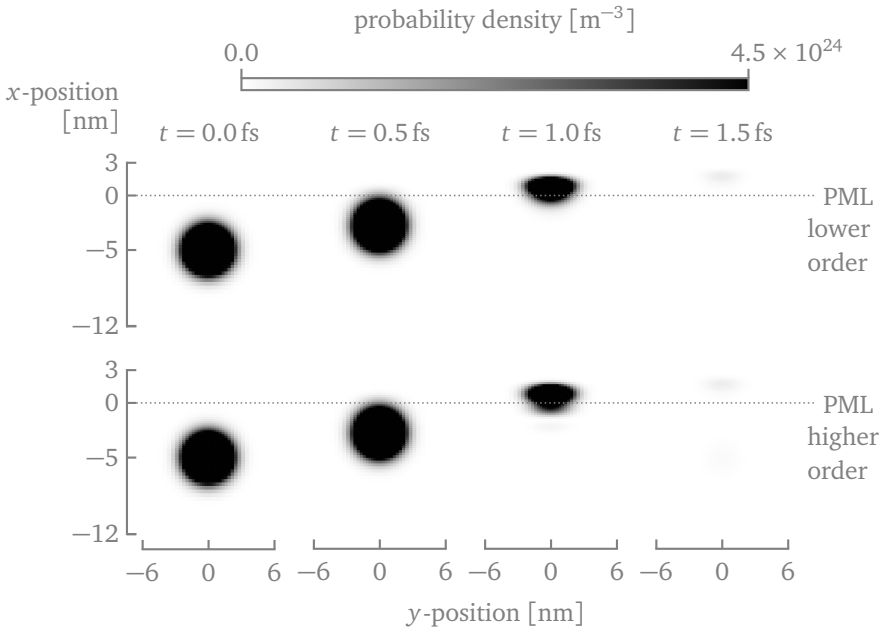

Figure 4.12: The PML absorbs the particle in a harmonic oscillator for both the lower- and higher-order schemes. The snapshots of the probability density at $z = 0$ are shown and the color axis maximum is fixed at $4.5 \times 10^{24}\,\mathrm{m}^{-3}$ (approximately 1/10th of the maximum). The dotted line at $x = 0$ indicates the start of the 3 nm thick PML layer. From $x = -12\,\mathrm{nm}$ to $x = 0\,\mathrm{nm}$, the nonuniform discretization is used.

In Fig. 4.12 the propagation of the particle is shown using the nonuniform grid where the area beyond $x > 0.0\,\mathrm{nm}$ is replaced with a 3 nm thick PML layer that is terminated with Dirichlet boundary conditions. The cells inside the PML are scaled as (4.15) with:

$$\alpha = e^{j\frac{\pi}{4}}, \quad \text{and} \quad \sigma(x) = 3\left(\frac{x}{d}\right)^2, \tag{4.63}$$

where $d = 3\,\mathrm{nm}$ is the thickness of the PML layer. Update scheme (4.16) is used inside the PML. The snapshots are given at times $t = 0.0\,\mathrm{fs}$, 0.5 fs, 1.0 fs, and 1.5 fs, thus spanning approximately half an oscillation of the harmonic oscillator. Both the lower- and higher-order schemes are able to completely absorb the incoming particle. To estimate the error introduced by this PML, the reflection error as a function of time is presented in Fig. 4.13. The reflection error is calculated as:

$$\mathcal{E}_{\mathrm{PML}} = \sqrt{\frac{\int_{-12\,\mathrm{nm}}^{0\,\mathrm{nm}} \mathrm{d}x \int \mathrm{d}y \int \mathrm{d}z\,(n_{\mathrm{HO}} - n_{\mathrm{PML}})^2}{\int_{-12\,\mathrm{nm}}^{12\,\mathrm{nm}} \mathrm{d}x \int \mathrm{d}y \int \mathrm{d}z\,(n_{\mathrm{HO}})^2}}, \tag{4.64}$$

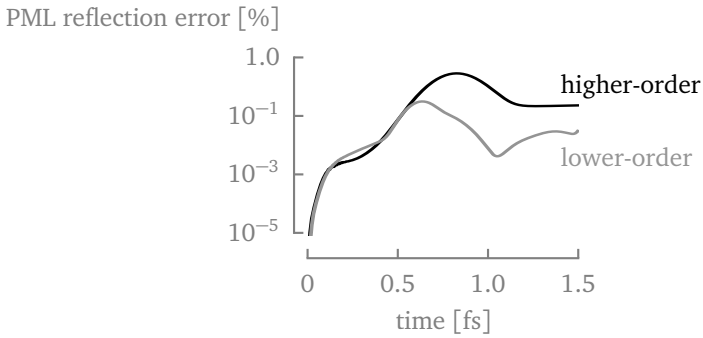

Figure 4.13: The reflection error caused by the PML is below 1 % for both schemes. The error was calculated with (4.64). While the higher-order scheme results in an overall more accurate discretization, the PML implementation induces a larger error.

where n_{HO} is the probability density of the original HO – without a PML – and n_{PML} is the probability density with the PML. It can be seen that the error for both schemes remains below 1 %.

4.6 Conclusions

In this chapter, two novel collocated-explicit (CE) update schemes were introduced for solving the Schrödinger equation on nonuniform tensor product grids. The two schemes are first- and third-order spatially accurate, becoming second- and fourth-order accurate on uniform grids. The spatial discretization scheme can incorporate a perfectly matched layer to simulate unbounded domains. Rigorous stability conditions were derived and it was shown that these are consistent with the known results on uniform grids. It was also demonstrated that a Courant-like stability criterion yields an underestimation of the true maximum time step on uniform grids. Moreover, it is possible to shift the zero-point energy of a potential in order to obtain a larger time step and increase the overall computational efficiency. The numerical dispersion error was derived for both schemes and studied as a function of the propagation direction, discretization, and the time step. The higher-order scheme was shown to exhibit stronger anisotropic behavior while increasing the accuracy substantially.

Numerical experimentation and comparison with analytical solutions have confirmed the accuracy and efficiency of the proposed CE methods. The higher-order accurate scheme is able to predict the dynamical behavior of a particle in a harmonic oscillator with a reasonable amount of computer resources and with great accuracy. Nonuniform grids were able to decrease the computation time by a factor four by both reducing the number of spatial unknowns and increasing the time step, and this without compromising the accuracy.

4.A Appendix: Coherent states theory

This appendix will briefly explain the theory of coherent states and is strongly based on [30]. A coherent state is a state of the harmonic oscillator most closely resembling the classical harmonic oscillator. The probability distribution is represented by an oscillating Gaussian distribution. It is composed of a superposition of many energy eigenstates of the harmonic oscillator, making it a broadband state. The potential for the 3-D harmonic oscillator is defined as:

$$v(x,y,z) = \frac{1}{2}m\kappa^2\left(x^2+y^2+z^2\right), \tag{4.A.1}$$

where m is the particle's mass and κ the angular frequency. The eigenfunctions in 3-D are characterized by the set of three quantum numbers (n_x, n_y, n_z) and defined in the coordinate representation by a product of the three 1-D eigenfunctions:

$$\phi_{n_x,n_y,n_z}(x,y,z) = \phi_{n_x}(x)\phi_{n_y}(y)\phi_{n_z}(z), \tag{4.A.2}$$

where the 1-D eigenfunctions are given by:

$$\phi_n(x) = \frac{1}{\sqrt{2^n n!}}\left(\frac{m\kappa}{\pi\hbar}\right)^{1/4} e^{-\frac{m\kappa x^2}{2\hbar}}\, H_n\left(\sqrt{\frac{m\kappa}{\hbar}}x\right), \tag{4.A.3}$$

illustrated in the x-direction and with H_n the n-th Hermite polynomial. A coherent state χ_α is defined in 1-D as the eigenvector of the creation operator with eigenvalue $\alpha_u \in \mathbb{C}$. The time evolution of a coherent state can be written as a superposition of the energy eigenstates:

$$\chi_\alpha(x,t) = e^{-\frac{1}{2}|\alpha|^2} e^{-\jmath\frac{\kappa t}{2}} \sum_n \frac{(\alpha e^{-\jmath\kappa t})^n}{\sqrt{n!}}\phi_n(x). \tag{4.A.4}$$

It is again possible to write a coherent state in 3-D as a product of 1-D coherent states as:

$$\chi_{\alpha_x,\alpha_y,\alpha_z}(x,y,z,t) = \chi_{\alpha_x}(x,t)\chi_{\alpha_y}(y,t)\chi_{\alpha_z}(z,t), \tag{4.A.5}$$

such that a 3-D coherent state is characterized by the three quantum numbers $(\alpha_x, \alpha_y, \alpha_z)$. The ground state of the harmonic oscillator is a coherent state with $\alpha_x = \alpha_y = \alpha_z = 0$. The expectation value of the position behaves as a classical point particle in a harmonic oscillator. For the x-dimension, this yields:

$$\langle\hat{x}(t)\rangle = |\alpha_x|\sqrt{\frac{2\hbar}{m\kappa}}\cos(\varphi_x - \kappa t), \tag{4.A.6}$$

where φ_x is the phase of α_x as $\alpha_x = |\alpha_x|\exp(\jmath\varphi_x)$. Moreover, the probability density is an unchanging oscillating Gaussian distribution:

$$\left|\chi_{\alpha_x}\right|^2 = \sqrt{\frac{m\kappa}{\pi\hbar}} e^{-\frac{m\kappa}{\hbar}\left(x-\sqrt{\frac{2\hbar}{m\kappa}}|\alpha_x|\cos(\varphi_x-\kappa t)\right)^2}. \tag{4.A.7}$$

It is possible to initialize a coherent state with real α_x by shifting the ground state wave function $\phi_0(x)$ to a starting position:

$$x' = \sqrt{\frac{2\hbar}{m\kappa}}\alpha_x. \tag{4.A.8}$$

References

1. Goldberg, A., Schey, H. M. & Schwartz, J. L. Computer-generated motion pictures of one-dimensional quantum-mechanical transmission and reflection phenomena. *American Journal of Physics* **35,** 177–186 (1967).
2. Visscher, P. A fast explicit algorithm for the time-dependent Schrödinger equation. *Computers in Physics* **5,** 596–598 (1991).
3. Dai, W., Li, G., Nassar, R. & Su, S. On the stability of the FDTD method for solving a time-dependent Schrödinger equation. *Numerical Methods for Partial Differential Equations: An International Journal* **21,** 1140–1154 (2005).
4. Pierantoni, L., Mencarelli, D. & Rozzi, T. A new 3-D transmission line matrix scheme for the combined Schrödinger–Maxwell problem in the electronic/electromagnetic characterization of nanodevices. *IEEE Transactions on Microwave Theory and Techniques* **56,** 654–662 (2008).
5. Moxley III, F. I., Zhu, F. & Dai, W. A Generalized FDTD Method with Absorbing Boundary Condition for Solving a Time-Dependent Linear Schrödinger Equation. *American Journal of Computational Mathematics* **2,** 163–172 (2012).
6. Shen, J. *et al.* High-order symplectic FDTD scheme for solving a time-dependent Schrödinger equation. *Computer Physics Communications* **184,** 480–492 (2013).
7. Guantes, R. & Farantos, S. C. High order finite difference algorithms for solving the Schrödinger equation in molecular dynamics. *The Journal of Chemical Physics* **111,** 10827–10835 (1999).
8. Bigaouette, N., Ackad, E. & Ramunno, L. Nonlinear grid mapping applied to an FDTD-based, multi-center 3D Schrödinger equation solver. *Computer Physics Communications* **183,** 38–45 (2012).
9. Xu, Y. & Zhang, L. Alternating direction implicit method for solving two-dimensional cubic nonlinear Schrödinger equation. *Computer Physics Communications* **183,** 1082–1093 (2012).
10. Eskar, R., Huang, P. & Feng, X. A new high-order compact ADI finite difference scheme for solving 3D nonlinear Schrödinger equation. *Advances in Difference Equations* **2018,** 1–15 (2018).
11. Warming, R. F. & Hyett, B. J. The modified equation approach to the stability and accuracy analysis of finite-difference methods. *Journal of Computational Physics* **14,** 159–179 (1974).
12. Askar, A. & Cakmak, A. S. Explicit integration method for the time-dependent Schrödinger equation for collision problems. *The Journal of Chemical Physics* **68,** 2794–2798 (1978).
13. Berenger, J.-P. A perfectly matched layer for the absorption of electromagnetic waves. *Journal of Computational Physics* **114,** 185–200 (1994).

14. Zheng, C. A perfectly matched layer approach to the nonlinear Schrödinger wave equations. *Journal of Computational Physics* **227,** 537–556 (2007).

15. Nissen, A. & Kreiss, G. An Optimized Perfectly Matched Layer for the Schrödinger Equation. *Communications in Computational Physics* **9,** 147–179 (2011).

16. Sullivan, D. M. & Wilson, P. M. Time-domain determination of transmission in quantum nanostructures. *Journal of Applied Physics* **112** (2012).

17. Mennemann, J.-F. & Jüngel, A. Perfectly Matched Layers versus discrete transparent boundary conditions in quantum device simulations. *Journal of Computational Physics* **275,** 1–24 (2014).

18. Berènger, J.-P. *Perfectly Matched Layer (PML) for Computational Electromagnetics* first (Morgan & Claypool, 2007).

19. Bernstein, D. S. *Matrix Mathematics* (Princeton University Press, 2009).

20. Remis, R. F. On the Stability of the Finite-Difference Time-Domain Method. *Journal of Computational Physics* **163,** 249–261 (2000).

21. Wang, S. & Teixeira, F. Some Remarks on the Stability of Time-Domain Electromagnetic Simulations. *IEEE Transactions on Antennas and Propagation* **52,** 895–898 (2004).

22. Caplan, R. M. & Carretero-González, R. A two-step high-order compact scheme for the Laplacian operator and its implementation in an explicit method for integrating the nonlinear Schrödinger equation. *Journal of computational and applied mathematics* **251,** 33–46 (2013).

23. Taflove, A. & Hagness, S. C. *Computational electrodynamics: the finite-difference time-domain method* (Artech House, 2005).

24. Denecker, B., Knockaert, L., Olyslager, F. & De Zutter, D. A new state-space-based algorithm to assess the stability of the finite-difference time-domain method for 3D finite inhomogeneous problems. *AEU-International Journal of Electronics and Communications* **58,** 339–348 (2004).

25. Van Londersele, A., De Zutter, D. & Vande Ginste, D. An in-depth stability analysis of nonuniform FDTD combined with novel local implicitization techniques. *Journal of Computational Physics* **342,** 177–193 (2017).

26. Horn, R. A. & Johnson, C. R. *Matrix analysis* 3rd (Cambridge University Press, 1990).

27. Sullivan, D. M. & Citrin, D. Determination of the eigenfunctions of arbitrary nanostructures using time domain simulation. *Journal of Applied Physics* **91,** 3219–3226 (2002).

28. Ryu, C. J., Liu, A. Y., Wei, E. & Chew, W. C. Finite-difference time-domain simulation of the Maxwell–Schrödinger system. *IEEE Journal on Multiscale and Multiphysics Computational Techniques* **1,** 40–47 (2016).

29. Warburton, R. J. Single spins in self-assembled quantum dots. *Nature Materials* **12,** 483–493 (2013).

30. Bertlmann, R. A. & Friis, N. Theoretical physics T2 quantum mechanics. *T2-Script of Summer Semester* (2008).

Chapter 5

An alternating-direction hybrid implicit-explicit FDTD method for the Schrödinger equation

"It is at this point that normal language gives up, and goes and has a drink."

— Terry Pratchett, The Colour of Magic (1983)

A hybrid implicit-explicit (HIE) FDTD method for the time-dependent Schrödinger equation is developed to alleviate the computation time for multiscale geometries in the design of nanoscale devices.

This chapter is based on "An alternating-direction hybrid implicit-explicit finite-difference time-domain method for the Schrödinger equation" by Pieter Decleer, Arne Van Londersele, Hendrik Rogier, and Dries Vande Ginste, as published in *Journal of Computational and Applied Mathematics*, **403**, 113881 (2022), and "Uncertainty Quantification of Charge Transfer through a Nanowire Resonant-Tunneling diode with an ADHIE-FDTD Method" by Pieter Decleer and Dries Vande Ginste, as published in the proceedings of the *2021 IEEE 11th International Conference Nanomaterials: Applications and Properties (NAP-2021)*, Sept. 5–11, 2021 (Odessa, Ukraine, 2021), 1–5.

5.1 Introduction

In Chapter 4, we presented a new explicit method for the Schrödinger equation. This method – and explicit finite-difference methods in general – have the advantage that the computational complexity scales linearly with the size of the system, making them ideally suited to tackle large problems. However, small spatial steps and high potential energies lead to small time steps. Therefore, we implemented nonuniform grids and higher-order spatial differences to have high accuracy on coarse grids and thereby decreased the number of spatial variables and increased the time step. However, the time step can still be a limiting factor when small geometric details are present.

Alternatively, unconditionally stable schemes can be applied. In fact, one of the first time-integration methods applied to the Schrödinger equation was the Crank-Nicolson (CN) method [1, 2]. Because the method is unitary and stable independent of the time step, it is still widely used to this day [3–5]. The unconditional stability comes at the cost of implicit time integration for which a system of linear equations has to be solved at every iteration. In 1-D systems, this does not pose a large restriction on its applicability because the system is tridiagonal for second-order accurate finite differences and the number of operations to solve this system scales linearly with its size. However, in 3-D, the system is not solved as easily and will not scale linearly. This makes the CN method excessively slow, particularly for large systems.

Another frequently used implicit method is the alternating-direction implicit (ADI) method [6–8]. It is an adaptation of the CN method that is also unconditionally stable but can retain the linear complexity scaling in higher dimensions by solving multiple tridiagonal systems. It is thus better suited for tackling large problems. There are already several different implementations that can deal with the Schrödinger or related equations [9–12].

While these methods are usually defined on uniform grids, they are easily adapted to nonuniform grids by using the techniques described in Chapter 4. However, even on nonuniform grids, implicit methods still result in too expensive time stepping. HIE methods combine the best of both worlds. Explicit updates are applied in one part of the grid with large cells and implicit updates are applied in the other part. Whereas HIE methods have already been developed and applied successfully for Maxwell's equations [13–21], similar methods for the Schrödinger equation are still lacking.

In this chapter, a HIE method for solving the linear time-dependent Schrödinger equation on nonuniform grids is proposed. It is based on the ADI method and retains the desirable linear time complexity of an explicit update scheme making it attractive for large problems and long-time propagation. The resulting ADHIE scheme tailors the grid to the structure and lowers the number of spatial variables in regions of less interest. The flexibility of this scheme enables us to optimize simulations by balancing implicit with explicit updates. Small spatial steps are updated implicitly and are thus removed from the stability criterion, drastically increasing the time step and decreasing the computation time.

First, Section 5.2 describes the spatial and temporal discretization resulting in the ADHIE scheme. Next, Section 5.3 derives how the scheme eliminates spatial steps from the stability criterion. The accuracy and efficiency of the method is illustrated with several examples in Section 5.4. Finally, Section 5.5 highlights the most important results and presents some challenges expected in future research.

5.2 The ADHIE scheme

In this section, we discuss the spatial and temporal discretization of ADHIE scheme.

5.2.1 Discretization

The Schrödinger equation (2.34) is spatially discretized on the same 3-D nonuniform tensor product grid as in Chapter 4, resulting in:

$$j\hbar\frac{\partial}{\partial t}\boldsymbol{\psi} = (T+V)\boldsymbol{\psi}. \tag{5.1}$$

The discrete kinetic energy matrix $T \in \mathbb{R}^{n_\psi \times n_\psi}$ is defined as:

$$T = -\frac{\hbar^2}{2m}L_L, \tag{5.2}$$

where L_L is the lower-order accurate Laplacian matrix from (4.23). In the remainder of this dissertation the subscript L is dropped. The ADI method [9, 10, 12, 22] is modified and applied *locally* to the explicit update scheme in [23–26]. Taking some inspiration from Section 4.2.2, we split the wave function $\boldsymbol{\psi}$ into its real part $\boldsymbol{r}$ and its imaginary part $\boldsymbol{s}$ and stagger them in time. This is unlike other ADI methods and allows us to combine explicit with implicit updates. The proposed ADHIE scheme is:

$$G\boldsymbol{s}\big|^n = G\boldsymbol{s}\big|^{n-1} - \Delta\eta H\boldsymbol{r}\big|^{n-\frac{1}{2}}, \tag{5.3a}$$

$$G\boldsymbol{r}\big|^{n+\frac{1}{2}} = G\boldsymbol{r}\big|^{n-\frac{1}{2}} + \Delta\eta H\boldsymbol{s}\big|^{n}, \tag{5.3b}$$

where

$$G = \bigotimes_{u\in\{x,y,z\}}\left(I_{m_u} + \frac{\Delta\eta}{2}S_u\right), \tag{5.4}$$

The discretized Hamiltonian matrix is given by:

$$H = T_x \oplus T_y \oplus T_z + V, \tag{5.5}$$

and $\Delta\eta$ is the normalized time step $\Delta\eta = \Delta t/\hbar$. The 1-D kinetic energy operator T_u and the implicitized 1-D kinetic energy operator S_u are defined as:

$$T_u = \frac{\hbar^2}{2m}\big(\delta_u^{\star -1} D_u {\delta_u}^{-1} {D_u}^T\big), \tag{5.6a}$$

$$S_u = \frac{\hbar^2}{2m}\big(\delta_u^{\star -1} D_u \big(I_{n_u} - P_u\big) {\delta_u}^{-1} {D_u}^T\big), \tag{5.6b}$$

where $P_u \in \mathbb{R}^{n_u \times n_u}$ is the diagonal projection matrix such that:

$$[P_u]_{i,i} = \begin{cases} 0, & \text{if } \Delta u_i \text{ yields an implicit contribution,} \\ 1, & \text{if } \Delta u_i \text{ yields an explicit contribution.} \end{cases}. \tag{5.7}$$

The real and imaginary parts are also combined into a single vector $\boldsymbol{x}$:

$$\boldsymbol{x}|^n = \begin{bmatrix} \boldsymbol{s}|^n \\ \boldsymbol{r}|^{n+\frac{1}{2}} \end{bmatrix}. \tag{5.8}$$

The update scheme is compactly written as:

$$\begin{bmatrix} G & 0 \\ -\Delta\eta\, H & G \end{bmatrix} \boldsymbol{x}|^n = \begin{bmatrix} G & -\Delta\eta\, H \\ 0 & G \end{bmatrix} \boldsymbol{x}|^{n-1}. \tag{5.9}$$

Note that choosing $[P_u]_{i,i} = 1$ for all u and i, produces the fully explicit leapfrog scheme of lower-order described in Chapter 4 with only one of the staggered schemes, which we will henceforth simply call *the leapfrog method*. In contrast, setting $[P_u]_{i,i} = 0$ for all u and i leads to the fully implicit ADI scheme. When using the ADHIE method, $[P_u]_{i,i}$ is carefully chosen to reduce the overall computation time whilst maintaining high accuracy. However, note that the ADHIE method introduces an extra error compared to the explicit method usually called the *splitting error* [27]. However, because the implicitization is only applied locally, the error is reduced compared to fully implicit methods.

To maintain linear time complexity when inverting the matrix in the l.h.s. of (5.9), it is necessary to exploit the structure of the matrices. This results in a multi-step method, similar to early ADI schemes for Maxwell [15, 28]. However, unlike those schemes, the number of intermediate steps is equal to the number of implicitized dimensions. The update equations become:

$$\left[\left(I_{m_x} + \frac{\Delta\eta}{2} S_x\right) \otimes I_{m_y} \otimes I_{m_z}\right] \boldsymbol{s}|^{(1)} = -\Delta\eta\, H \boldsymbol{r}|^{n-\frac{1}{2}}, \tag{5.10a}$$

$$\left[I_{m_x} \otimes \left(I_{m_y} + \frac{\Delta\eta}{2} S_y\right) \otimes I_{m_z}\right] \boldsymbol{s}|^{(2)} = \boldsymbol{s}|^{(1)}, \tag{5.10b}$$

$$\left[I_{m_x} \otimes I_{m_y} \otimes \left(I_{m_z} + \frac{\Delta\eta}{2} S_z\right)\right] \boldsymbol{s}|^{(3)} = \boldsymbol{s}|^{(2)}, \tag{5.10c}$$

$$\boldsymbol{s}|^n = \boldsymbol{s}|^{(3)} + \boldsymbol{s}|^{n-1}, \tag{5.10d}$$

$$\left[\left(I_{m_x} + \frac{\Delta\eta}{2} S_x\right) \otimes I_{m_y} \otimes I_{m_z}\right] \boldsymbol{r}|^{(1)} = \Delta\eta H \boldsymbol{s}|^n, \tag{5.11a}$$

$$\left[I_{m_x} \otimes \left(I_{m_y} + \frac{\Delta\eta}{2} S_y\right) \otimes I_{m_z}\right] \boldsymbol{r}|^{(2)} = \boldsymbol{r}|^{(1)}, \tag{5.11b}$$

$$\left[I_{m_x} \otimes I_{m_y} \otimes \left(I_{m_z} + \frac{\Delta\eta}{2} S_z\right)\right] \boldsymbol{r}|^{(3)} = \boldsymbol{r}|^{(2)}, \tag{5.11c}$$

$$\boldsymbol{r}|^{n+\frac{1}{2}} = \boldsymbol{r}|^{(3)} + \boldsymbol{r}|^{n-\frac{1}{2}}. \tag{5.11d}$$

The matrices to be inverted are only nonzero on three of their diagonals and can, hence, be solved by the tridiagonal matrix algorithm of order $\mathcal{O}(n)$ [29]. Even

though the separation into real and imaginary parts increases the number of update equations compared to the fully implicit Schrödinger method [10], our novel ADHIE method does not require more storage or more floating-point operations, as no complex arithmetic is required.

5.2.2 2-D update equations in scalar notation

The method is further clarified by treating the 2-D case and writing it in the more common scalar notation. We first introduce the update coefficients:

$$\zeta_x|_i = \frac{1-p_x|_{i+1}}{\Delta x_{i+1}\Delta x_i^\star}, \quad \theta_x|_i = \frac{1-p_x|_i}{\Delta x_i^\star \Delta x_i}, \quad \text{and} \quad \eta_x|_i = -\zeta_x|_i - \theta_x|_i. \tag{5.12}$$

The 2-D equivalent of (5.10) becomes in scalar notation:

$$\begin{aligned} s|_{i,j}^{(0)} = \frac{\hbar\Delta t}{2m}\Bigg(& \frac{r|_{i+1,j}^{n-\frac{1}{2}} - r|_{i,j}^{n-\frac{1}{2}}}{\Delta x_{i+1}\Delta x_i^\star} - \frac{r|_{i,j}^{n-\frac{1}{2}} - r|_{i-1,j}^{n-\frac{1}{2}}}{\Delta x_i^\star \Delta x_i} \\ & + \frac{r|_{i,j+1}^{n-\frac{1}{2}} - r|_{i,j}^{n-\frac{1}{2}}}{\Delta y_{j+1}\Delta y_j^\star} - \frac{r|_{i,j}^{n-\frac{1}{2}} - r|_{i,j-1}^{n-\frac{1}{2}}}{\Delta y_j^\star \Delta y_j}\Bigg) - \frac{\Delta t}{\hbar} v|_{i,j}\, r|_{i,j}^{n-\frac{1}{2}}, \end{aligned} \tag{5.13a}$$

$$s|_{i,j}^{(1)} - \frac{\hbar\Delta t}{4m}\Big(\zeta_x|_i\, s|_{i+1,j}^{(1)} + \eta_x|_i\, s|_{i,j}^{(1)} + \theta_x|_i\, s|_{i-1,j}^{(1)}\Big) = s|_{i,j}^{(0)}, \tag{5.13b}$$

$$s|_{i,j}^{(2)} - \frac{\hbar\Delta t}{4m}\Big(\zeta_y|_j\, s|_{i,j+1}^{(2)} + \eta_y|_j\, s|_{i,j}^{(2)} + \theta_y|_j\, s|_{i,j-1}^{(2)}\Big) = s|_{i,j}^{(1)}, \tag{5.13c}$$

$$s|_{i,j}^{n} = s|_{i,j}^{(2)} + s|_{i,j}^{n-1}. \tag{5.13d}$$

For (5.11) we get:

$$\begin{aligned} r|_{i,j}^{(0)} = -\frac{\hbar\Delta t}{2m}\Bigg(& \frac{s|_{i+1,j}^{n} - s|_{i,j}^{n}}{\Delta x_{i+1}\Delta x_i^\star} - \frac{s|_{i,j}^{n} - s|_{i-1,j}^{n}}{\Delta x_i^\star \Delta x_i} \\ & + \frac{s|_{i,j+1}^{n} - s|_{i,j}^{n}}{\Delta y_{j+1}\Delta y_j^\star} - \frac{s|_{i,j}^{n} - s|_{i,j-1}^{n}}{\Delta y_j^\star \Delta y_j}\Bigg) + \frac{\Delta t}{\hbar} v|_{i,j}\, s|_{i,j}^{n}, \end{aligned} \tag{5.14a}$$

$$r|_{i,j}^{(1)} - \frac{\hbar\Delta t}{4m}\Big(\zeta_x|_i\, r|_{i+1,j}^{(1)} + \eta_x|_i\, r|_{i,j}^{(1)} + \theta_x|_i\, r|_{i-1,j}^{(1)}\Big) = r|_{i,j}^{(0)}, \tag{5.14b}$$

$$r|_{i,j}^{(2)} - \frac{\hbar\Delta t}{4m}\Big(\zeta_y|_j\, r|_{i,j+1}^{(2)} + \eta_y|_j\, r|_{i,j}^{(2)} + \theta_y|_j\, r|_{i,j-1}^{(2)}\Big) = r|_{i,j}^{(1)}, \tag{5.14c}$$

$$r|_{i,j}^{n+\frac{1}{2}} = r|_{i,j}^{(2)} + r|_{i,j}^{n-\frac{1}{2}}. \tag{5.14d}$$

The scalar $p_u|_i$ is the i-th diagonal element of the matrix P_u, $u \in \{x, y\}$, and is either 0 or 1. It is now easily seen that if, e.g., $p_x|_i = p_x|_{i+1} = 1$ for a certain i, (5.13b) and (5.14b) are solved explicitly since $\zeta_x|_i = \eta_x|_i = \theta_x|_i = 0$. In contrast, if $p_x|_i = 0$ then (5.13b) is solved implicitly because the value of $s|_{i,j}^{(1)}$ depends on

the unknown value $s|_{i-1,j}^{(1)}$ and vice versa. The same reasoning applies to $r|_{i,j}^{(1)}$ and $r|_{i-1,j}^{(1)}$ in (5.14b). Furthermore, in Section 5.3, it is shown that the spatial step Δx_i is removed from the stability criterion. Lastly, (5.13)–(5.14) clearly illustrate that the implicitization requires at most the solution of a tridiagonal system, which can be done efficiently with the tridiagonal matrix algorithm [30].

By studying (5.13)–(5.14), we can easily recognize that the novel ADHIE update scheme is a direct extension of the lower-order accurate explicit leapfrog scheme.

5.3 Stability

In this section, the time step for which the ADHIE scheme is stable is derived. The resulting formula enables the user to tune the time step by selectively removing small spatial steps.

First, the update equations are symmetrized using the diagonal transformation matrix Q (4.26). Left multiplication of (5.9) with $I_2 \otimes Q^{1/2}$ results in:

$$\begin{aligned}\begin{bmatrix} Q^{\frac{1}{2}} & \\ & Q^{\frac{1}{2}} \end{bmatrix}\begin{bmatrix} G & 0 \\ -\Delta\eta H & G \end{bmatrix}\begin{bmatrix} Q^{-\frac{1}{2}} & \\ & Q^{-\frac{1}{2}} \end{bmatrix}\begin{bmatrix} Q^{\frac{1}{2}} & \\ & Q^{\frac{1}{2}} \end{bmatrix}\boldsymbol{x}|^{n} \\ = \begin{bmatrix} Q^{\frac{1}{2}} & \\ & Q^{\frac{1}{2}} \end{bmatrix}\begin{bmatrix} G & -\Delta\eta H \\ 0 & G \end{bmatrix}\begin{bmatrix} Q^{-\frac{1}{2}} & \\ & Q^{-\frac{1}{2}} \end{bmatrix}\begin{bmatrix} Q^{\frac{1}{2}} & \\ & Q^{\frac{1}{2}} \end{bmatrix}\boldsymbol{x}|^{n-1},\end{aligned} \tag{5.15}$$

which simplifies to the symmetrized update equation:

$$\begin{bmatrix} \tilde{G} & 0 \\ -\Delta\eta\, \tilde{H} & \tilde{G} \end{bmatrix}\tilde{\boldsymbol{x}}|^{n} = \begin{bmatrix} \tilde{G} & -\Delta\eta\, \tilde{H} \\ 0 & \tilde{G} \end{bmatrix}\tilde{\boldsymbol{x}}|^{n-1}. \tag{5.16}$$

with

$$\tilde{\boldsymbol{x}}|^{n} = \begin{bmatrix} Q^{\frac{1}{2}}\boldsymbol{s}|^{n} \\ Q^{\frac{1}{2}}\boldsymbol{r}|^{n+\frac{1}{2}} \end{bmatrix}, \quad \tilde{H} = \tilde{T}_x \oplus \tilde{T}_y \oplus \tilde{T}_z + V, \tag{5.17}$$

$$\tilde{G} = \bigotimes_{u\in\{x,y,z\}} \left(I_{m_u} + \frac{\Delta\eta}{2}\tilde{S}_u \right), \quad \tilde{T}_u = \frac{\hbar^2}{2m}\tilde{D}_u\tilde{D}_u{}^{T}, \tag{5.18}$$

and

$$\tilde{S}_u = \frac{\hbar^2}{2m}\tilde{D}_u\big(I_{n_u} - P_u\big)\tilde{D}_u{}^{T}, \tag{5.19}$$

where $\tilde{D}_u$ is defined in (4.29). The similarity transformation leaves the eigenvalues and eigenvectors unaltered, so that the stability of (5.9) is guaranteed if (5.16) is

stable.

By following the approach in [17, 31], we recast the symmetrized scheme (5.16) as:

$$(E+F)\tilde{\boldsymbol{x}}|^n = (E-F)\tilde{\boldsymbol{x}}|^{n-1}, \tag{5.20}$$

with

$$E=\begin{bmatrix} \tilde{G} & -\frac{\Delta\eta}{2}\tilde{H} \\ -\frac{\Delta\eta}{2}\tilde{H} & \tilde{G} \end{bmatrix}, \quad \text{and} \quad F=\begin{bmatrix} 0 & \frac{\Delta\eta}{2}\tilde{H} \\ -\frac{\Delta\eta}{2}\tilde{H} & 0 \end{bmatrix}. \tag{5.21}$$

Since E is real symmetric and F is real, it is possible to use the results in [31], stating that the scheme is stable if E is positive definite and $F+F^T$ is positive semi-definite. The latter condition is trivially satisfied because $F+F^T$ is the zero matrix. The former is satisfied if the time step satisfies:

$$\Delta t < \frac{2\hbar}{\left\|\tilde{U}_x \oplus \tilde{U}_y \oplus \tilde{U}_z + V\right\|_2}, \tag{5.22}$$

where the matrix $\tilde{U}_u$ is defined as:

$$\tilde{U}_u = \frac{\hbar^2}{2m}\tilde{D}_u P_u \tilde{D}_u{}^T = \tilde{T}_u - \tilde{S}_u, \tag{5.23}$$

and $\|\cdot\|_2$ denotes the matrix 2-norm. To prove this, E is expanded into six parts $E=\sum_{i=1}^{6} E_i$. Because the Kronecker product is distributive over the matrix sum, matrix $\tilde{G}$ can be expanded as:

$$\begin{aligned} \tilde{G} = \; & I_{n_\psi} + \frac{\Delta\eta}{2}\left(\tilde{S}_x \otimes I_{m_y} \otimes I_{m_z} + I_{m_x} \otimes \tilde{S}_y \otimes I_{m_z} + I_{m_x} \otimes I_{m_y} \otimes \tilde{S}_z\right) \\ & + \left(\frac{\Delta\eta}{2}\right)^2 \left(\tilde{S}_x \otimes \tilde{S}_y \otimes I_{m_z} + \tilde{S}_x \otimes I_{m_y} \otimes \tilde{S}_z + I_{m_x} \otimes \tilde{S}_y \otimes \tilde{S}_z\right) \\ & + \left(\frac{\Delta\eta}{2}\right)^3 \left(I_2 \otimes \tilde{S}_x \otimes \tilde{S}_y \otimes \tilde{S}_z\right). \end{aligned} \tag{5.24}$$

By also considering that:

$$\tilde{T}_x \oplus \tilde{T}_y \oplus \tilde{T}_z = \tilde{U}_x \oplus \tilde{U}_y \oplus \tilde{U}_z + \tilde{S}_x \oplus \tilde{S}_y \oplus \tilde{S}_z, \tag{5.25}$$

it is straightforward to obtain the six expansion terms:

$$E_1 = \begin{bmatrix} I_{n_\psi} & -\frac{\Delta\eta}{2}\left(\tilde{U}_x \oplus \tilde{U}_y \oplus \tilde{U}_z + V\right) \\ -\frac{\Delta\eta}{2}\left(\tilde{U}_x \oplus \tilde{U}_y \oplus \tilde{U}_z + V\right) & I_{n_\psi} \end{bmatrix}, \tag{5.26a}$$

$$E_2 = \left(\frac{\Delta\eta}{2}\right)\begin{bmatrix} 1 & -1 \\ -1 & 1 \end{bmatrix} \otimes \left(\tilde{S}_x \oplus \tilde{S}_y \oplus \tilde{S}_z\right), \tag{5.26b}$$

$$E_3 = \left(\frac{\Delta\eta}{2}\right)^2 \left(I_2 \otimes \tilde{S}_x \otimes \tilde{S}_y \otimes I_{m_z}\right), \tag{5.26c}$$

$$E_4 = \left(\frac{\Delta\eta}{2}\right)^2 \left(I_2 \otimes \tilde{S}_x \otimes I_{m_y} \otimes \tilde{S}_z\right), \tag{5.26d}$$

$$E_5 = \left(\frac{\Delta\eta}{2}\right)^2 \left(I_2 \otimes I_{m_x} \otimes \tilde{S}_y \otimes \tilde{S}_z\right), \tag{5.26e}$$

$$E_6 = \left(\frac{\Delta\eta}{2}\right)^3 \left(I_2 \otimes \tilde{S}_x \otimes \tilde{S}_y \otimes \tilde{S}_z\right). \tag{5.26f}$$

The matrices $\tilde{S}_u$ are all positive semi-definite since:

$$\begin{aligned} \boldsymbol{x}^T \tilde{S}_u \boldsymbol{x} &= \frac{\hbar^2}{2m} \boldsymbol{x}^T \tilde{D}_u \left(I_{n_u} - P_u\right) \tilde{D}_u{}^T \boldsymbol{x} \\ &= \frac{\hbar^2}{2m} \left(\left(I_{n_u} - P_u\right) \tilde{D}_u{}^T \boldsymbol{x}\right)^T \left(I_{n_u} - P_u\right) \tilde{D}_u{}^T \boldsymbol{x} \\ &= \frac{\hbar^2}{2m} \left\| \left(I_{n_u} - P_u\right) \tilde{D}_u{}^T \boldsymbol{x} \right\|_2^2 \geq 0 \quad \forall \boldsymbol{x} \in \mathbb{R}^n. \end{aligned} \tag{5.27}$$

By considering that:

$$s(A \oplus B) = \{a + b : a \in s(A) \quad \text{and} \quad b \in s(B)\}, \tag{5.28a}$$

$$s(A \otimes B) = \{ab : a \in s(A) \quad \text{and} \quad b \in s(B)\}, \tag{5.28b}$$

and

$$s\left(\begin{bmatrix} 1 & -1 \\ -1 & 1 \end{bmatrix}\right) = \{0, 2\}, \tag{5.29}$$

where $s(\cdot)$ denotes the spectrum, it is clear that matrices E_2 to E_6 are all positive semi-definite.

As such, it only remains to be proven if E_1 is positive definite. This is true if and only if:

$$\boldsymbol{x}^T E_1 \boldsymbol{x} = \|\boldsymbol{x}\|_2^2 - \boldsymbol{x}^T \check{E}_1 \boldsymbol{x} > 0 \quad \forall \boldsymbol{x} \in \mathbb{R}^{2n_\psi} \setminus \mathbf{0}, \tag{5.30}$$

where $\check{E}_1$ is defined as:

$$\check{E}_1 \triangleq \frac{\Delta\eta}{2} \begin{bmatrix} 0 & 1 \\ 1 & 0 \end{bmatrix} \otimes \left(\tilde{U}_x \oplus \tilde{U}_y \oplus \tilde{U}_z + V\right). \tag{5.31}$$

The inequality (5.30) is equivalent to:

$$\max_{\boldsymbol{x} \in \mathbb{R}^{2n_\psi} \setminus \mathbf{0}} \frac{\boldsymbol{x}^T \check{E}_1 \boldsymbol{x}}{\|\boldsymbol{x}\|_2^2} = \lambda_{\max}(\check{E}_1) < 1, \tag{5.32}$$

where we have used [32, eq. 8.4.3]. The maximum eigenvalue of $\check{E}_1$ is equal to:

$$\lambda_{\max}(\check{E}_1) = \frac{\Delta\eta}{2}\lambda_{\max}\left(\begin{bmatrix} & \tilde{U}_x \oplus \tilde{U}_y \oplus \tilde{U}_z + V \\ \tilde{U}_x \oplus \tilde{U}_y \oplus \tilde{U}_z + V & \end{bmatrix}\right) \tag{5.33}$$

$$= \frac{\Delta\eta}{2}\rho(\tilde{U}_x \oplus \tilde{U}_y \oplus \tilde{U}_z + V). \tag{5.34}$$

Since the matrix $\tilde{U}_x \oplus \tilde{U}_y \oplus \tilde{U}_z + V$ is not necessarily positive definite, the transition from $\lambda_{\max}$ to spectral radius ρ, is significant. Given that the spectral radius of a symmetric matrix is equal to the 2-norm of the matrix [30, Cor. 1.8], the combination of (5.32) and (5.34) yields (5.22), which concludes the proof. From Chapter 4, we already know that the time step scales with the square of the spatial step, which highlights the need for a Schrödinger HIE scheme that can eliminate the small steps from the stability criterion. Unsurprisingly, (5.22) for the leapfrog scheme is a factor 2 bigger than (4.22) for the fully explicit lower-order scheme presented in Chapter 4. This is because we have effectively halved the step we take in a single iteration.

We now derive a Courant-like stability criterion in the 2-D case for ease of notation. The 2-D stability criterion is approximated by first considering that:

$$\rho(\tilde{U}_x \oplus \tilde{U}_y + V) = \rho(U_x \oplus U_y + V), \tag{5.35}$$

and then approximate the spectral radius with the infinity norm ($\rho(\cdot) \leq \|\cdot\|_\infty$), so that:

$$\begin{aligned} \Delta t &< \frac{2\hbar}{\left\|U_x \oplus U_y + V\right\|_\infty} \\ &= \frac{2\hbar}{\max\limits_k\left(\sum\limits_l \left|[U_x \oplus U_y + V]_{k,l}\right|\right)}, \quad \text{for} \quad k,l \in \{0,\ldots,m_x m_y\} \\ &= \frac{2\hbar}{\max\limits_{i,j}\left(\frac{\hbar^2}{2m}\left(\frac{1}{\kappa_{i,j}}\right)^2 + \left|\frac{\hbar^2}{2m}\left(\frac{1}{\kappa_{i,j}}\right)^2 + v|_{i,j}\right|\right)} \end{aligned} \tag{5.36}$$

with

$$\left(\frac{1}{\kappa_{i,j}}\right)^2 = \frac{1}{\Delta x_i^\star}\left(\frac{p_x|_i}{\Delta x_i} + \frac{p_x|_{i+1}}{\Delta x_{i+1}}\right) + \frac{1}{\Delta y_j^\star}\left(\frac{p_y|_j}{\Delta y_j} + \frac{p_y|_{j+1}}{\Delta y_{j+1}}\right). \tag{5.37}$$

By assuming $v|_{i,j} > -\hbar^2/(2m{\kappa_{i,j}}^2)$, we can simplify (5.36) as:

$$\Delta t < \frac{2\hbar}{\max\limits_{i,j}\left(\frac{\hbar^2}{m}\left(\frac{1}{\kappa_{i,j}}\right)^2 + v|_{i,j}\right)}. \tag{5.38}$$

In contrast, the time step for the fully explicit method has to satisfy:

$$\Delta t < \frac{2\hbar}{\max\limits_{i,j}\left(\frac{\hbar^2}{m}\left(\frac{1}{\lambda_{i,j}}\right)^2 + v|_{i,j}\right)}, \tag{5.39}$$

with $\lambda_{i,j}$ the 2-D equivalent of (4.33):

$$\left(\frac{1}{\lambda_{i,j}}\right)^2 = \frac{1}{\Delta x_i^\star}\left(\frac{1}{\Delta x_i} + \frac{1}{\Delta x_{i+1}}\right) + \frac{1}{\Delta y_j^\star}\left(\frac{1}{\Delta y_j} + \frac{1}{\Delta y_{j+1}}\right). \tag{5.40}$$

This clearly shows that the hybrid scheme can remove specific Δx_i or Δy_j from the stability criterion by setting $p_x|_i = 0$ and $p_y|_j = 0$, respectively. Moreover, because (5.40) is always greater than or equal to (5.37), the stability criterion for the ADHIE scheme (5.36) is certainly *less* restrictive than for the fully explicit method. Consequently, the hybrid scheme can support much higher time steps, granted that the smallest cells are removed from the stability criterion.

5.4 Examples

In this section, first, two possibilities for a hybrid implicit-explicit scheme are theoretically discussed to elucidate the method further. Second, we investigate the hybrid implicit-explicit interface. Finally, the method is demonstrated numerically via application to two relevant examples.

5.4.1 Implicitization of a single direction

Consider a grid that is discretized very densely in a single direction, e.g., the x-direction. By choosing $P_x = 0$, matrix $\tilde{U}_x$ is reduced to the zero matrix. Consequently, the time step must satisfy:

$$\Delta t < \frac{2\hbar}{\left\| I_{m_x} \otimes \left(\tilde{T}_y \oplus \tilde{T}_z\right) + V \right\|_2}. \tag{5.41}$$

The matrix $I_{m_x} \otimes \left(\tilde{T}_y \oplus \tilde{T}_z\right) + V$ is block diagonal where each block corresponds to a slice in the yz-plane. Consequently, it is easy to see that the time step must satisfy a 2-D stability condition for every slice. Moreover, solving a single direction implicitly simplifies the update equations significantly compared to the traditional multistep 3-D ADI schemes mentioned above. Indeed, starting from (5.9) with $P_x = I_{n_x}$, $P_y = 0$ and $P_z = 0$ (i.e., the x-direction is fully implicitized and the updates in the yz-plane are fully explicit), we get:

$$\left[\left(I_{m_x} + \frac{\Delta\eta}{2} T_x\right) \otimes I_{m_y} \otimes I_{m_z}\right]\left(\boldsymbol{s}|^n - \boldsymbol{s}|^{n-1}\right) = -\Delta\eta H \boldsymbol{r}|^{n-\frac{1}{2}}, \tag{5.42}$$

Table 5.1: The time steps for the successively refined grids in Section 5.4.3 are calculated with (5.36).

Δx [nm]	Δt[fs]
2.0	17.276
1.0	4.3190
0.5	1.0797
0.25	0.269 94

and

$$\left[\left(I_{m_x}+\frac{\Delta\eta}{2}T_x\right)\otimes I_{m_y}\otimes I_{m_z}\right]\left(\boldsymbol{r}\,|^{n+\frac{1}{2}}-\boldsymbol{r}\,|^{n-\frac{1}{2}}\right)=\Delta\eta H\boldsymbol{s}\,|^{n}. \tag{5.43}$$

5.4.2 Local 1-D implicitization

When the discretization is chosen nonuniform along a single direction (chosen to be the x-direction, as in the previous subsection), it is unnecessary to completely solve this direction implicitly. Such local grid refinement can be used to resolve small geometric details. The update scheme for this local implicitization, and leaving the yz-plane fully explicit, is again the leapfrog scheme (5.42) and (5.43) with T_x replaced by S_x. This renders the matrix on the left-hand sides sparser still.

5.4.3 Convergence at the implicit-explicit interface

In this section, we will study the convergence order of the hybrid FDTD scheme. Therefore a 2-D free wave packet with mass $m = m_e$ is simulated traveling diagonally along $x = y$, on a uniform grid of 1100 nm × 1100 nm. The convergence of the hybrid implicit-explicit scheme is studied by successively refining the grid with spatial steps $\Delta x = \Delta y \in \{2.0\,\text{nm}, 1.0\,\text{nm}, 0.5\,\text{nm}, 0.25\,\text{nm}\}$. The wave function is updated fully explicitly from $x = 0.0$ nm to $x = 500.0$ nm. In the other part of the grid, i.e., from $x = 500.0$ nm to $x = 1100.0$ nm, the wave function is updated with implicitization in the x-direction. The simulation set-up is sketched in Fig. 5.1. The time step is calculated with the Courant-like stability criterion (5.36). Because the grid is uniform, local implicitization does not affect the time step. As such, only the accuracy is studied. The efficiency is sufficiently tested in Sections 5.4.4 and 5.4.5. The resulting time steps are given in Table 5.1. The initial wave function is given by:

$$\psi(x,y)=\frac{\pi}{\sigma}e^{-j\frac{\sqrt{2mE_c}}{\hbar}\left((x-x')+(y-y')\right)}e^{-\frac{1}{4}\frac{(x-x')^2+(y-y')^2}{\sigma^2}}, \tag{5.44}$$

with

$$E_c = 0.02\,\text{eV}, \quad \sigma = 30.0\,\text{nm}, \quad \text{and} \quad x' = y' = 300.0\,\text{nm}. \tag{5.45}$$

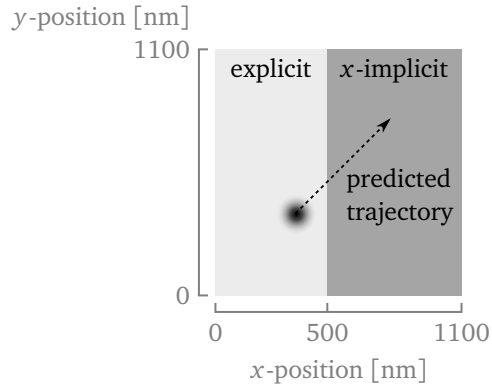

Figure 5.1: The square grid of 1100 nm × 1100 nm is split into a fully explicit part and a part that is updated with implicitization in the x-direction. The interface between these two regions is positioned at $x = 500\,\text{nm}$. A free Gaussian wave packet is initialized at $x = y = 300\,\text{nm}$ traveling along the diagonal $x = y$ toward the x-implicit part of the grid.

To quantify the convergence of the ADHIE scheme, the expectation value of the position is tracked as a function of time and compared to the analytic result. The time-averaged error is given by:

$$\mathcal{E} = \sqrt{\frac{1}{T}\int_0^T \|\langle \hat{\boldsymbol{r}}_{\text{calc}}(t)\rangle - \langle \hat{\boldsymbol{r}}_{\text{ana}}(t)\rangle\|^2 \,\mathrm{d}t}, \tag{5.46}$$

where $T = 6000\,\text{fs}$ is the total simulation time, $\langle \hat{\boldsymbol{r}}_{\text{ana}}(t)\rangle$ is the analytical position and $\langle \hat{\boldsymbol{r}}_{\text{calc}}(t)\rangle$ is the calculated position. At the interface $x = 500.0\,\text{nm}$ of the explicit and HIE parts of the grid, artificial reflection of the wave function might appear. To quantify this spurious reflection, the probability of finding the particle in the area $0\,\text{nm} < x < 500\,\text{nm}$ is calculated at time $t = 5000\,\text{fs}$. At that time the analytical wave packet in front of the barrier ($x < 500\,\text{nm}$) is negligible and the particle has passed the interface at $x = 500\,\text{nm}$ completely. Hence, the reflection coefficient R is calculated as:

$$R = \int_{0\,\text{nm}}^{500\,\text{nm}} \mathrm{d}x \int_{0\,\text{nm}}^{1100\,\text{nm}} \mathrm{d}y\, |\psi(x,y)|^2. \tag{5.47}$$

The errors $\mathcal{E}$ and reflection coefficients R for the varying cell sizes are given in Fig. 5.2. For this example, the error $\mathcal{E}$ converges approximately as $\mathcal{O}\big(\Delta x^{2.85}\big)$ and the reflection probability R decreases as $\mathcal{O}\big(\Delta x^{5.06}\big)$. This shows that the ADHIE method scales very well with decreasing cell sizes.

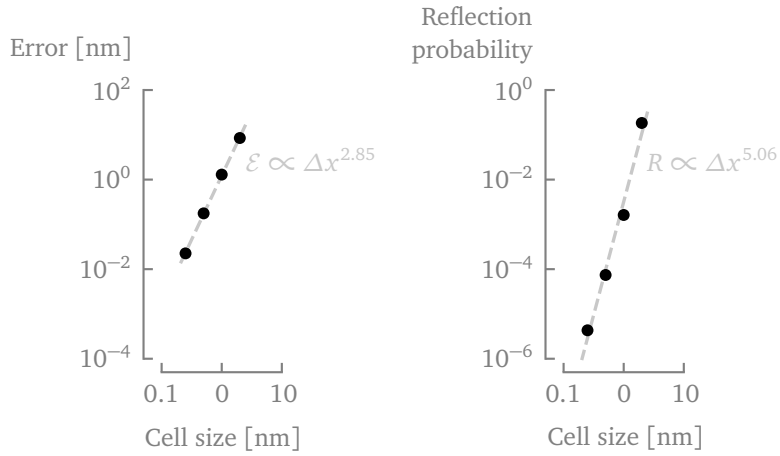

(a) Error convergence.

(b) Reflection probability.

Figure 5.2: The time-averaged error $\mathcal{E}$ and spurious reflection coefficient R scale very well with the cell sizes. For the tested cell sizes of $\Delta x = 2.0\,\text{nm}$, $1.0\,\text{nm}$, $0.5\,\text{nm}$ and $0.25\,\text{nm}$, the error $\mathcal{E}$ converges as $\mathcal{O}\left(\Delta x^{2.85}\right)$ and the reflection probability R decreases as $\mathcal{O}\left(\Delta x^{5.06}\right)$.

5.4.4 Flying qubit in laterally tunnel-coupled quantum wires

In this section, a flying qubit interferometer is simulated in the time domain. The calculations were performed on an Intel(R) Core(TM) i7-8650U CPU @ 1.90 GHz with 15 GiB of RAM memory and the methods were implemented in Python 3. These kinds of devices have been numerically investigated in [33–36] and also fabricated in, e.g., [37]. The active region is constructed on the interface of a GaAs/AlGaAs heterostructure, creating a 2-D electron gas. The device itself is shown in Fig. 5.3 and consists of two parallel quantum wires separated by a thin and high barrier, and a central scattering region of length w where the barrier height is variable. An electron in the upper or lower channel is denoted by $|\uparrow\rangle$ or $|\downarrow\rangle$, respectively. In the central region, it is possible for an electron originally in state $|\downarrow\rangle$ to tunnel from the lower channel to the upper channel $|\uparrow\rangle$. The final state of the electron will be a superposition of the $|\uparrow\rangle$ and $|\downarrow\rangle$ state, depending on the length w of the interaction region, and the – possibly time-dependent – barrier height.

The device geometry studied here is very similar to the geometry presented in [35]. A first set of calculations compares the leapfrog method with the ADHIE method and the CN method for several values of the barrier height. The parameters which

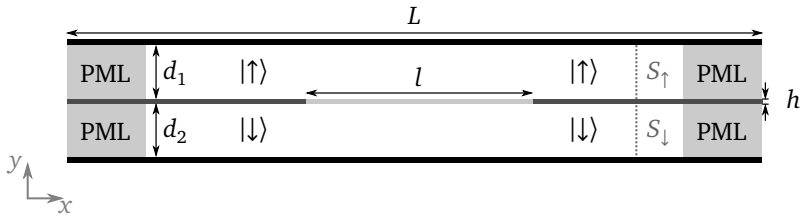

Figure 5.3: The channels of a 2-D flying qubit interferometer are separated by a thin barrier of width h. The upper and lower channels have a width of d_1 and d_2, respectively. A central scattering region of length l with variable barrier height v_b allows interaction between both channels. The channels are terminated on both sides by a PML. An electron originally in the lower channel (state $|\downarrow\rangle$) will leave the channel in a superposition of $|\uparrow\rangle$ and $|\downarrow\rangle$ being both in the upper and lower channels with a certain probability. The probability density current is calculated through the surfaces $S_\uparrow$ and $S_\downarrow$.

remain constant throughout the simulations are:

$$L = 1970\,\text{nm}, \quad l = 250\,\text{nm}, \quad d_1 = d_2 = 28\,\text{nm},$$
$$h = 2.0\,\text{nm}, \quad \Delta x = 1.0\,\text{nm}, \quad \text{and} \quad \Delta y_{\text{ch}} = 1.0\,\text{nm},$$

where Δy_{ch} is the cell size in the two channels. We utilize a nonuniform discretization where the barrier is uniformly discretized with $\Delta y_{\text{bar}} = 0.2\,\text{nm}$. This fine spatial discretization is required to resolve the thin barrier accurately. To verify this, we compare to the explicit scheme using a coarse uniform discretization such that $\Delta y_{\text{bar}} = 1.0\,\text{nm}$. Along the length of the channel, the simulation domain is truncated by a 50 nm thick PML as explained in Chapter 4 to simulate an unbounded domain and the channels are terminated by Dirichlet boundary conditions in the y-direction. The potential for the barrier outside of the central region is set to $v = 0.5\,\text{eV}$ whereas the potential in the central region v_b is variable. The mass of the wave packet is set to $m = 0.067\,m_{\text{e}}$. The static barrier starts at $x = 500\,\text{nm}$.

For the explicit method, the small cells that are used to resolve the barrier limit the allowed time step significantly. This leads to an oversampling in time and thus decreases the efficiency. The CN method does not suffer from this limitation because of its unconditional stability. However, due to its implicit nature, every update is more expensive. Therefore, the largest possible time step should be chosen while still ensuring enough temporal samples per oscillation.

For the ADHIE method, only the small cells in the y-direction are implicitly solved, similar to what was proposed in Section 5.4.2. This strongly increases the allowed

time step. The resulting time steps are:

$$\Delta t_{\text{leapfrog,coarse}} = 270.0\,\text{as}, \quad \Delta t_{\text{leapfrog,fine}} = 22.65\,\text{as}, \tag{5.48a}$$

$$\Delta t_{\text{ADHIE}} = 289.4\,\text{as}, \quad \Delta t_{\text{CN}} = 700.0\,\text{as}. \tag{5.48b}$$

Three things are interesting to note here. First, $\Delta t_{\text{exp,coarse}}$ is larger than the time step obtained using the traditional Courant limit in [38], i.e., $\Delta t = 260.4\,\text{as}$. This is because the Courant-like stability criterion derived with the infinity norm, underestimates the true stability limit. Second, despite using smaller cells with the ADHIE method, the time step Δt_{ADHIE} is larger than $\Delta t_{\text{exp,coarse}}$. This is a consequence of the well-chosen implicitization. Third, the larger time step for the CN scheme will slightly reduce the accuracy compared to the ADHIE or explicit methods but will close the gaps in efficiency. As such, it should present a fair comparison.

The initial wave packet is entirely confined in the lower channel $|\downarrow\rangle$ and defined by:

$$\psi(x,y) = \begin{cases} \psi_0 \cos\left(\frac{\pi y}{d_1}\right) e^{-\beta^2 - j\alpha}, & 0.0\,\text{nm} < y < 29.0\,\text{nm}, \\ 0, & \text{otherwise}, \end{cases} \tag{5.49}$$

where

$$\psi_0 = \sqrt{\frac{2\pi}{d_1 \sigma^2}}, \quad \beta = \frac{x - x'}{2\sigma}, \quad \text{and} \quad \alpha = \frac{\sqrt{2mE_c}}{\hbar}(x - x'), \tag{5.50}$$

and with parameters:

$$E_c = 0.2\,\text{eV}, \quad \sigma = 30.0\,\text{nm}, \quad \text{and} \quad x' = 200.0\,\text{nm}.$$

The x-dependence of the wave function represents a Gaussian wave packet traveling in the positive x-direction and the y-dependence is the ground state wave function of a particle-in-a-box of width d_1. In Fig. 5.4, the probability of finding the electron in the upper or lower channel as a function of the barrier height is shown. These probabilities are derived as:

$$N_{\uparrow(\downarrow)} = \frac{1}{N_0} \int_0^{t_{\max}} \int_{S_{\uparrow(\downarrow)}} \boldsymbol{J}_p \cdot \boldsymbol{u}_n \, \mathrm{d}S \, \mathrm{d}t \,, \tag{5.51}$$

with $\boldsymbol{u}_n$ the normal unit vector to the surface $S_{\uparrow(\downarrow)}$ in the upper (or lower) channel, N_0 the total particle number and $\boldsymbol{J}_p$ the probability current density (2.24). As such, the total charge that passes through that channel during the simulation is calculated instead of the instantaneous charge at an arbitrary point in time. Eq. (5.51) is evaluated at the plane $x = 1200\,\text{nm}$.

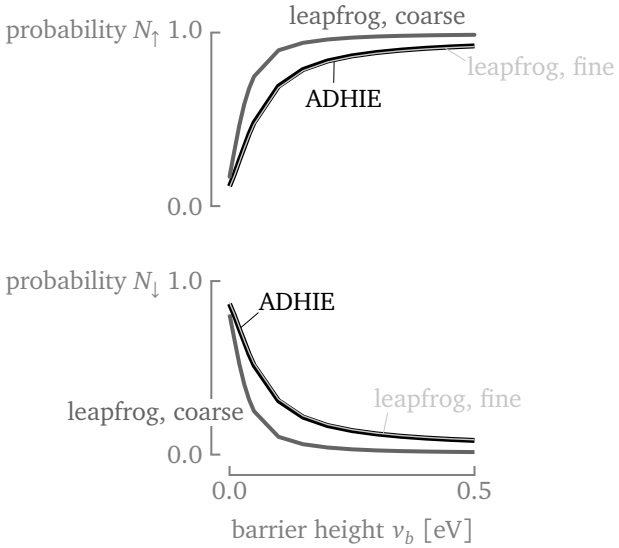

Figure 5.4: Probability of finding an electron in the upper $N_\uparrow$ or lower $N_\downarrow$ channel for an electron originally injected into the lower channel. The results with the different methods using the fine grid are very close. The CN method is not shown because it overlaps nigh perfectly with the leapfrog method.

Table 5.2: The single-core calculation times for the different methods with either a static or variable barrier. The calculation times for the static barrier are averaged over 15 simulations, each with a different barrier height.

	static barrier	variable barrier
leapfrog, coarse	26 s	32 s
leapfrog, fine	247 s	302 s
ADHIE	35 s	44 s
CN	171 s	3118 s

It can be seen that all the simulations, except the one using the coarse grid, have matching results. The main difference between the simulations is their calculation time. The computation times for the different methods are given in Table 5.2. The ADHIE method can almost effortlessly increase the efficiency by increasing the time step making it 7 times faster than the explicit calculation and almost 5 times faster than the CN method. For the ADHIE and CN schemes, the implicit calculations were performed by first calculating the LU decomposition prior to the FDTD loop. The computation time needed for the LU decomposition is included in the number shown in Table 5.2.

In Fig. 5.5, the probability density $n = |\psi|^2$ is plotted for different values of the

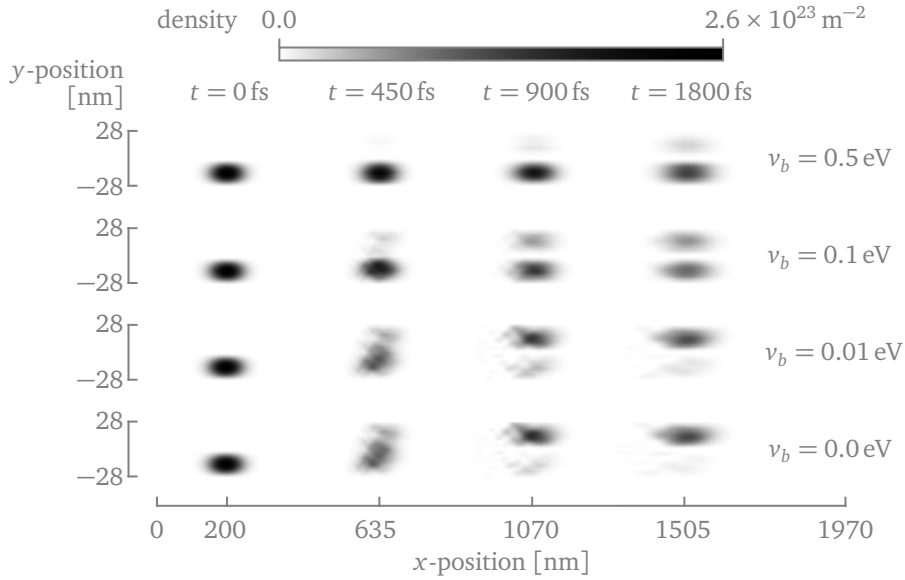

Figure 5.5: A flying qubit traveling through laterally tunnel-coupled quantum wires is simulated with the ADHIE method for different values of the barrier height v_b in the central region between 500 nm and 750 nm. The probability density $n = |\psi|^2$ of the wave packet is shown every 450 fs.

barrier height v_b as the particle propagates from the lower left to the right, calculated with the ADHIE method. It can be seen that the wave packet spreads out over time in the direction of propagation and tunnels from the lower to the upper channel depending on the barrier height v_b.

The second set of calculations considers a time-dependent barrier height in the central region. The scattering region again starts 500 nm from the left side but now has length $w = 1000\,\text{nm}$. The barrier height is modulated in time as:

$$v_b(t) = 0.25\,\text{eV}\,(1 + \cos(\omega t)), \tag{5.52}$$

with $\omega = 20.0 \times 10^{12}\,\text{rad}\,\text{s}^{-1}$. Hence, at $t = 0$ the barrier in the central region is the same as the barrier height separating the 2 channels.

In Fig. 5.6, the probability current:

$$I_{\uparrow(\downarrow)} = \int_{S_{\uparrow(\downarrow)}} \boldsymbol{J}_P \cdot \boldsymbol{u}_n \,\mathrm{d}S\,, \tag{5.53}$$

through the upper $I_\uparrow$ and lower $I_\downarrow$ channel at position $x = 1700\,\text{nm}$ is plotted as a function of time for the various methods. Again, the coarse grid is unable to

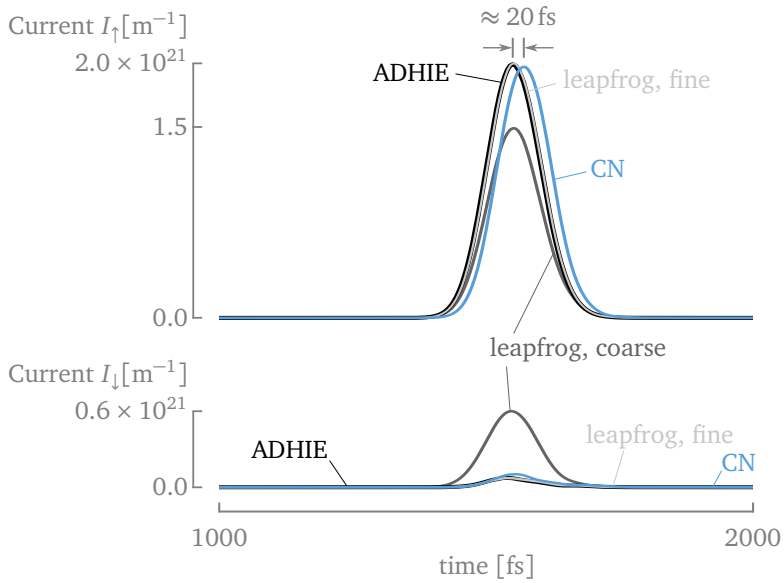

Figure 5.6: The probability current as a function of time through the plane $x = 1700\,\mathrm{nm}$ in the upper $I_\uparrow$ and lower $I_\downarrow$ channels is calculated with the various methods for a time-varying barrier $v_b(t)$.

correctly predict the behavior of the wave packet. While the other three methods yield similar results, the CN method has the largest deviation from the other two. Even though the method is stable for every time step, $\Delta t_{\mathrm{CN}} = 700\,\mathrm{fs}$ is slightly too large to obtain accurate calculations. These results are confirmed in Fig. 5.7 where the probability density $n = |\psi|^2$ is plotted every 450 fs for the various calculation methods.

Only the ADHIE scheme can compute the LU-factorization of the matrices prior to the FDTD loop, when a time-dependent potential is applied. For the CN scheme the potential enters the matrix that has to be inverted. Hence, the linear system of equations has to be solved from scratch at every time step which drastically increases the computation time. The resulting calculation times for the four simulations are also shown in Table 5.2. The ratios of the computation times stay approximately the same for all simulations except for CN. The latter is approximately 70 times slower than the ADHIE method, as ADHIE can still utilize predetermined LU factors. Moreover, the leapfrog method now easily outperforms the CN method, but it is still considerably slower than the ADHIE method.

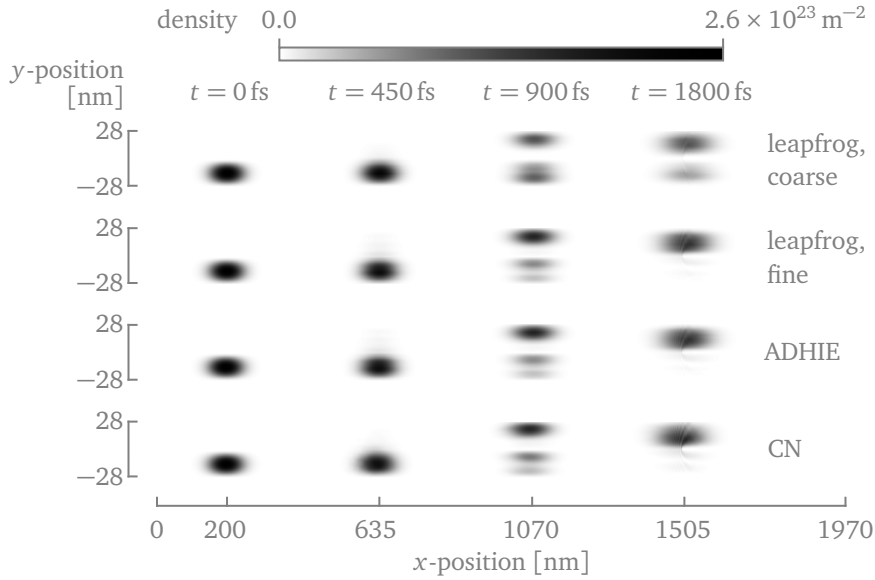

Figure 5.7: A flying qubit traveling through laterally tunnel-coupled quantum wires is computed with several simulation methods. The probability density $n = |\psi|^2$ of the wave packet is shown every 450 fs. A time-varying barrier height is used according to (5.52) between 500 nm and 1500 nm. The coarse grid yields a different result compared to the other simulations using the nonuniform discretization. The CN method yields approximately the same behavior for the wave packet, but it lags somewhat behind.

5.4.5 Nanowire resonant-tunneling diode

In this section, the transmission probability through a nanowire double-barrier resonant-tunneling diode (RTD) is calculated. The simulations were performed on an Intel(R) Xeon(R) Gold 6136 CPU @ 3.00 GHz with 125 GiB of RAM memory. The structure discussed here is similar to the one discussed in [39, 40] and constructed in [41]. The RTD is defined by two InP barriers of height $v = 0.6\,\text{eV}$ in an InAs nanowire. The nanowire has a square cross section with 40 nm long sides and it has a longitudinal potential profile as shown in Fig. 5.8, where V_{CE} is the applied voltage. For now, the barrier widths are set to $a = c = 5.0\,\text{nm}$ and $b = 15.0\,\text{nm}$. The effective masses in InAs and InP are $m_{\text{InAs}} = 0.023\,m_\text{e}$ and $m_{\text{InP}} = 0.077\,m_\text{e}$, respectively. The extension of the presented ADHIE method to include a variable mass is presented at the end of this chapter in Appendix 5.A.

A wave packet is inserted in the nanowire using a total-field scattered-field (TFSF) boundary [4]. As such, the computational domain can be smaller than the wave packet, expediting the computation. A Gaussian wave packet is inserted with central energy $E = 0.08\,\text{eV}$ and width $\sigma = 10\,\text{nm}$. The wave packet is in the transversal

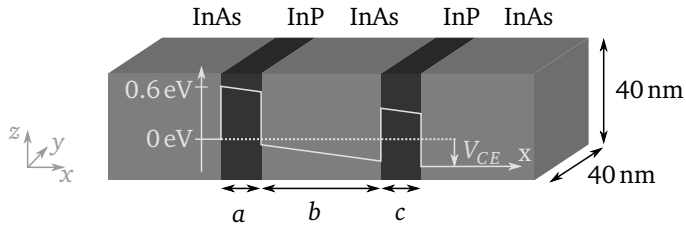

Figure 5.8: An infinitely extended InAs/InP/InAs/InP/InAs nanowire resonant-tunneling diode is biased with a voltage V_{CE} across a double barrier structure. The nanowire is assumed infinite in the x-direction and has a square cross section with 40 nm sides. The two InP barriers separated by a distance b have a height of 0.6 eV. The barriers have a width a and c for the left and right barrier, respectively. The biasing voltage results in a linear decrease of the potential energy. The effective mass in InAs and InP are $m_{\text{InAs}} = 0.023\, m_e$ and $m_{\text{InP}} = 0.077\, m_e$, respectively.

ground state.

The transmission probability, as a function of the injected energy at a particular bias voltage V_{CE}, is calculated by averaging the outgoing wave function over the transversal direction, taking the Fourier transform of this signal and dividing it by the analytical signal when no barrier or bias is present:

$$T(E, V_{CE}) = \left| \frac{\Psi_{\text{calc}}(E, V_{CE})}{\Psi_{\text{analytic}}(E)} \right|^2 . \tag{5.54}$$

The current is calculated as in [42] with:

$$I(V_{CE}) = \frac{2e}{\pi\hbar} \sqrt{E_0} \int_{E_0}^{\infty} \frac{T(E, V_{CE})(f_{\text{FD}}(E) - f_{\text{FD}}(E - eV_{CE}))}{\sqrt{E - E_0}} \, \mathrm{d}E \,, \tag{5.55}$$

with $f_{\text{FD}}(E)$ the Fermi-Dirac distribution function:

$$f_{\text{FD}}(E) = \frac{1}{1 + \exp\left(\frac{E - E_F}{k_B T}\right)}, \tag{5.56}$$

and where $E_0 = 20.436$ meV is the transversal ground state energy.

The transmission is calculated by performing a time-dependent simulation and using (5.54) for every applied voltage V_{CE}. The Fermi level E_F was determined to be 2 meV above the first subband minimum, such that $E_F = 22.436$ meV [40].

Several simulations are performed. Simulations S_1 to S_4 use the leapfrog method with a uniformly discretized x-direction. Simulation S_5 also uses the leapfrog

Table 5.3: The different simulations parameters corresponding to S_1 to S_6. The discretization, calculation method, time step and resulting average single-core CPU times per applied voltage are given. The time step was calculated with (5.22) using the infinity norm instead of the 2-norm.

	S_1	S_2	S_3	S_4	S_5	S_6
Method	leapfrog	leapfrog	leapfrog	leapfrog	leapfrog	ADHIE
Δx [nm]	2.5	1.0	0.5	0.25	—	—
Δt [as]	301.0	132.4	44.14	12.04	12.04	256.5
T_{CPU}	57 s	296 s	1839 s	14 701 s	2364 s	167 s

method but with a nonuniform discretization and S_6 uses the ADHIE method on the same nonuniform grid. For all simulations, the y- and z-directions are uniformly meshed with 20 cells of width 2 nm and the x-direction is discretized from $x = -200\,\text{nm}$ to $x = 200\,\text{nm}$. The cells in the x-direction are $\Delta x = 2.5\,\text{nm}$, $\Delta x = 1.0\,\text{nm}$, $\Delta x = 0.5\,\text{nm}$, and $\Delta x = 0.25\,\text{nm}$ for S_1, S_2, S_3, and S_4, respectively. The nonuniform grid is discretized as follows: from $x = -200.0\,\text{nm}$ to $-30.0\,\text{nm}$ and from $x = 30.0\,\text{nm}$ to $200.0\,\text{nm}$, the grid has uniform cells of width $\Delta x = 2.0\,\text{nm}$. Between $x = -12.5\,\text{nm}$ and $12.5\,\text{nm}$, the grid consists of cells of width $\Delta x = 0.25\,\text{nm}$. In the intermediate areas, the cell sizes are graded with a constant grading ratio resulting in a total of 312 cells. The wave function is inserted using a TFSF boundary at $x = -40\,\text{nm}$ with an initial pulse center at $x = -240.0\,\text{nm}$. As such, there is no particle in the active domain at initialization. On both sides, there is a 150 nm thick PML.

The ADHIE method only implicitizes the x-direction from $-30.0\,\text{nm}$ to $30.0\,\text{nm}$. The various simulation parameters are summarized in Table 5.3, with the average single-core CPU time T_{CPU} per applied voltage. Each simulation terminates after a physical simulation time of 10.0 ps. However, because transmission through the double barriers is a resonant process, the decay time is very long. As such, the signal is extrapolated using the matrix-pencil method [43] until it has mostly decayed.

In Fig. 5.9(a), the transmission coefficients $T(E, V_{CE})$ calculated by (5.54) at applied voltages $V_{CE} = 0.0\,\text{mV}$ and $V_{CE} = 73.0\,\text{mV}$ are shown. The resulting IV-characteristic of the device using (5.55) is shown in Fig. 5.9(b). The IV-curve for S_1 misjudges the amplitude of the peak current by over an order of magnitude. The curves for S_2 and S_3 seem to converge to the value obtained for S_4. The results for S_5 are not shown as they overlapped almost exactly with S_5. The results for S_6 are in very close agreement with S_4. Moreover, the peak voltage of $V_{CE} = 72\,\text{mV}$ obtained for S_4 and S_6 is close to the value of 72.4 mV for a cylindrical wire, obtained from a 1-D transfer matrix calculation in both [40] and [42]. The computation

times listed in Table 5.3 show that uniform refinement greatly increases the computation time. Simulation S_4 takes, for example, more than 250 times longer than S_1. Using a nonuniform grid can decreases the computation time considerably as S_5 is already 6 times faster than S_4 at no cost to the accuracy. The small time step hindering S_5 can be increased by using the ADHIE method. As such, S_6 is 14 times faster than S_5, making it almost 90 times faster than S_4. Hence, it is clear that the ADHIE method outperforms the explicit method for balancing accuracy with efficiency in cases where the grid is very nonuniform.

Uncertainty quantification

One challenge associated with these kinds of devices is related to the uncertainty introduced through imperfect production processes or variable operating conditions [44]. To ensure the proper working of a device, it is crucial to assess how strongly manufacturing variability influences its behavior. This uncertainty quantification (UQ) can be done by constructing a stochastic model. One approach is to use a brute-force Monte Carlo (MC) method [45], which is essentially a sampling technique. It is a popular method as it is robust, reliable and easy to implement. Unfortunately, it requires a large number of samples, thus necessitating very efficient methods to obtain these samples. As such, UQ of the RTD diode seems like an ideal candidate to further validate the proposed ADHIE method.

For simplicity, we limit the uncertainty to the random variables (RVs) a and c and fix the width of the middle region $b = 20\,\text{nm} - (a+c)/2$. All other parameters remain unchanged. An MC run is performed for 4000 samples where the RVs are picked from a bivariate normal distribution with means $\mu_a = \mu_c = 5.0\,\text{nm}$ and standard deviations $\sigma_a = \sigma_c = 0.1\,\text{nm}$ with a correlation coefficient $\rho = 0.8$. The rather high correlation coefficient reflects that uncertainties in the production process result in similar deviations for the nominal value for both barriers. Note that the presented UQ method is in no way restricted to this specific probability distribution of a and c. Other distributions, e.g., acquired by measuring the physical dimensions of many manufactured RTDs, can also be dealt with.

We will only perform simulations with the ADHIE method and the following nonuniform discretization, which is modified for every sample. From $x = -200\,\text{nm}$ to $-30\,\text{nm}$ and from $x = 30\,\text{nm}$ to $200\,\text{nm}$, the grid consists of uniform cells of width $\Delta x = 2.0\,\text{nm}$. The narrow InP barriers, however, are finely discretized with 20 cells each and the intermediate InAs region with 60 cells. The remaining regions are again scaled with a constant grading ratio. At the nominal case $a = c = 5.0\,\text{nm}$ and $b = 15.0\,\text{nm}$, the discretization is identical to the nonuniform grid presented above. Since the nonuniform grid does not alter the time step, it is the same for all samples $\Delta t = 256.5\,\text{as}$.

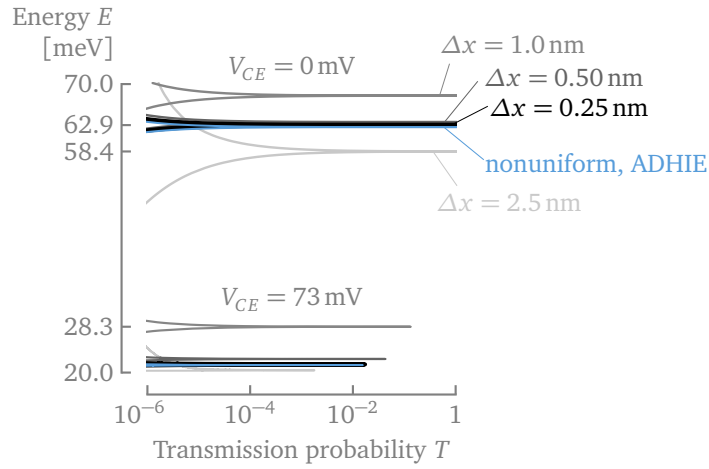

(a) Transmission probability.

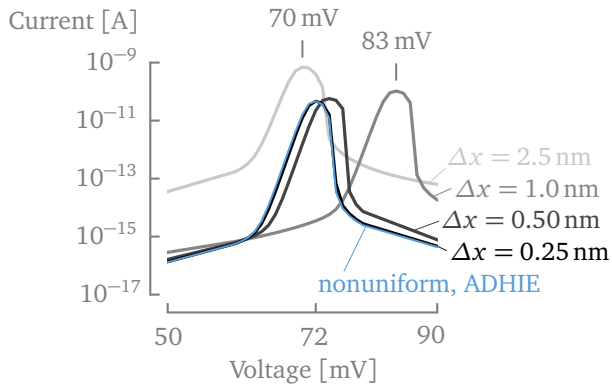

(b) IV-characteristic.

Figure 5.9: The calculated transmission probability T (5.54) and IV-characteristics (5.55) show that the ADHIE method with the uniform discretization yields results very close to the finest uniform leapfrog calculation. In Fig. 5.9(a), the transmission probabilities are shown for voltages of $V_{CE} = 0\,\mathrm{mV}$ and $V_{CE} = 73\,\mathrm{mV}$. In Fig. 5.9(b), the resulting IV-characteristics are shown. The results for S_5 are omitted as they almost exactly overlap with S_4.

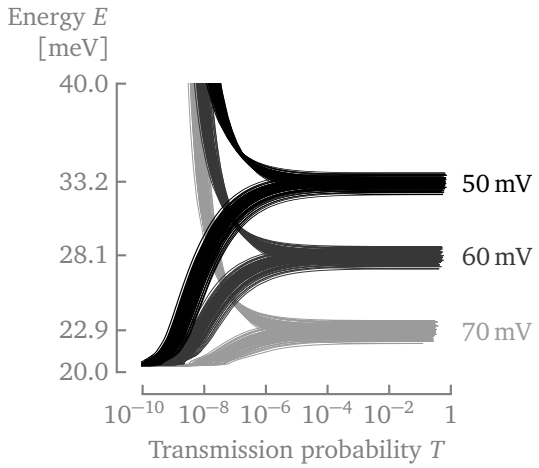

Figure 5.10: The position of the transmission peaks exhibits a large variability. Specifically, the transmission probability T as function of energy E for V_{CE} at 50 mV, 60 mV and 70 mV for 100 out of the 4000 MC samples is shown. The tick marks on the ordinate represent the mean peak position μ_T for the different applied voltages.

The transmission probability as a function of the energy for 100 out of the 4000 samples is shown in Fig. 5.10 at three different applied voltages $V_{CE} = 50\,\text{mV}$, 60 mV, and 70 mV. The transmission exhibits very fine peaks due to a very sharp resonance and the position of these peaks is very sensitive to the dimensions of the barriers. Moreover, we can see that the peak position decreases, on average, approximately 5 meV when the voltage V_{CE} is increased by 10 mV. The probability density function (PDF) of the position of the peak is shown in Fig. 5.11 for an applied voltage of $V_{CE} = 50\,\text{mV}$. The distribution is approximately Gaussian with a mean of $\mu_T = 33.12\,\text{meV}$ and standard deviation $\sigma_T = 0.37\,\text{meV}$. Increasing the applied voltage by 1 mV shifts the mean value of the peak by approximately 0.5 meV implying that the $\mu_T \pm \sigma_T$ regions for two applied voltages differing by 1 mV partially overlap. Consequently, the device cannot be expected to reliably operate within 1 mV of accuracy.

The convergence of the MC analysis is assessed by calculating the relative error of the mean μ_T and standard deviation σ_T. The relative error is shown for an applied voltage of 50 mV in Fig. 5.12 as a function of the number of MC samples N. The expected decrease of the error as $1/\sqrt{N}$ is clearly observed. Note that many samples – here 4000 – are needed to have an error of less than 1 % on the standard deviation.

The resulting current voltage characteristics of the device are shown in Fig. 5.13 for 100 samples. Similar to the nominal case, the mean IV-curve μ_I shows a

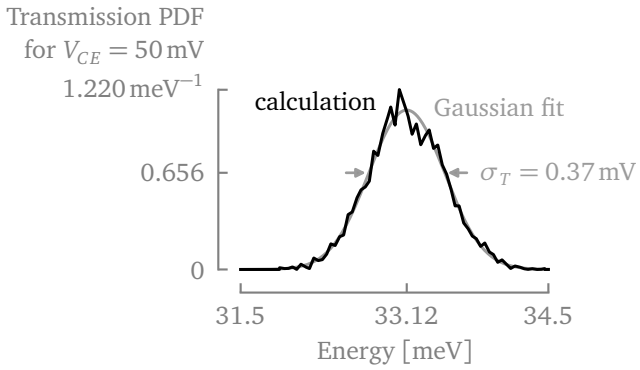

Figure 5.11: The position of the transmission peak as a function of energy has a Gaussian PDF for an applied voltage of $V_{CE} = 50\,\mathrm{meV}$. The mean position for the transmission peak is $\mu_T = 33.12\,\mathrm{meV}$ with a standard deviation of $\sigma_T = 0.37\,\mathrm{meV}$. The fitted curve is a Gaussian with the same mean and standard deviation. A similar graph is obtained for other applied voltages.

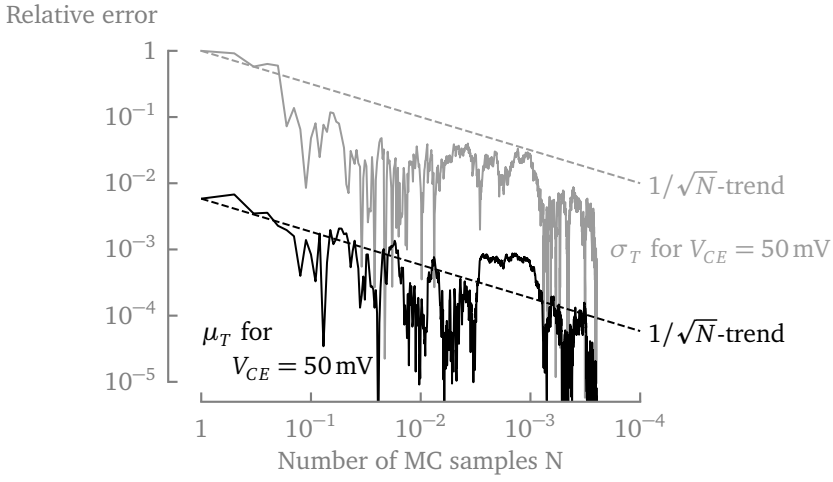

Figure 5.12: The relative error of the mean position of the transmission peak μ_T and its standard deviation σ_T decreases as 1 over the square root of the number of Monte Carlo samples N. This is illustrated for the applied voltage of $V_{CE} = 50\,\mathrm{mV}$.

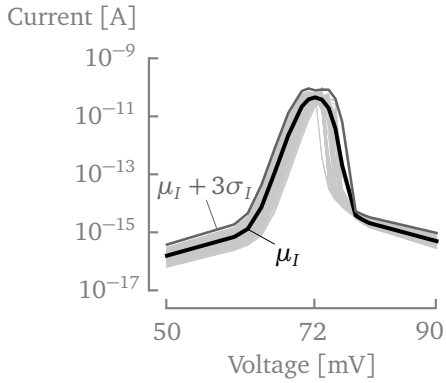

Figure 5.13: The current-voltage curves of 100 out of 4000 MC samples are characteristic of a resonant-tunneling diode. The thick black line indicates the mean μ_I and the thinner dark grey line indicates $\mu_I + 3\sigma_I$, where σ_I is the standard deviation. The mean has a maximum current at 72 mV.

strong peak at $V_{CE} = 72$ mV followed by a region of negative differential resistance, characteristic of an RTD. It is also seen that there is a large variance in the position of the current peak and the region of negative differential resistance. These are two very important quantities for obtaining a correctly functioning device. As such, it is crucial that we assess how much fabrication uncertainties affect device operation. Moreover, there is also a large variance in the amplitude of the current at any given voltage V_{CE}.

In Fig. 5.14, the PDFs for the current at applied voltages of 50 mV and 70 mV are shown. Both distributions are very skew, with rather long tails towards high currents. For example, in 10 % of the cases, the current for an applied voltage of 70 mV will exceed approximately triple the mean value of the current. Hence it is clear that, instead of merely estimating the mean and standard deviation, the full quantification of the statistics, including the distribution's tail, is essential for a design engineer. It allows to assess in how many cases the device will carry too much current, possibly leading to failure of other components. As such, the ADHIE method in combination with MC may be used for yield analysis.

5.5 Conclusions

In this chapter, an alternating-direction hybrid implicit-explicit (ADHIE) FDTD method for the time-dependent Schrödinger equation on nonuniform tensor-product grids was proposed. The method combines implicit with explicit updates to increase the overall time step imposed by the explicit scheme. A rigorous stability analysis has shown that it is possible to easily and efficiently remove small cells

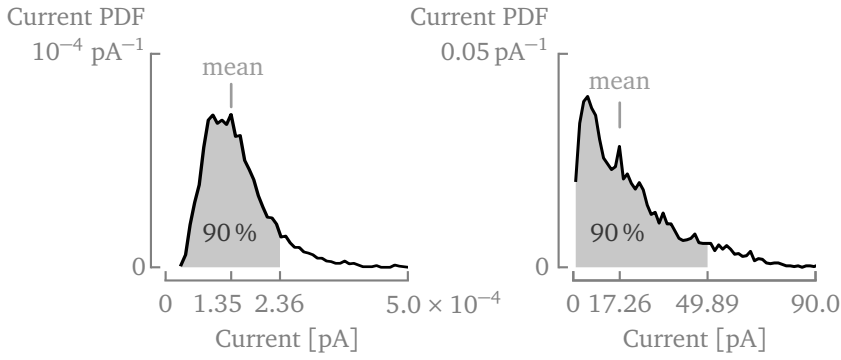

(a) $V_{CE} = 50\,\text{mV}$. (b) $V_{CE} = 70\,\text{mV}$.

Figure 5.14: The probability density functions show that the current exhibits a large variance. This is illustrated for an applied voltage $V_{CE} = 50\,\text{mV}$ in (a) and 70 mV in (b). In both cases the distributions are very skew with a long tail towards high currents. In 10 % of the cases the current will exceed almost double the mean current for (a) and almost triple the mean current for (b).

from the stability criterion. By treating the different directions separately and only solving part of the grid implicitly, the performed simulations show that this yields a much reduced computational cost compared to fully implicit methods.

Note that the ADI method – upon which the ADHIE method is based – is not unconditionally stable unlike other implicit methods. Instead, it is limited by the maximum absolute value of the potential energy v. This does not prove a limitation in practice because the time step has to be small solely based on accuracy. More importantly, v is not included in the implicit part of the calculation. Hence, a time-varying potential can be easily added without changing the implicit part of the calculation. This is unlike other implicit methods, such as the Crank-Nicolson method, where a linear system of equations has to be solved from scratch at every time step. The inclusion of a time-dependent potential is important for simulating transient behavior in nanodevices or when including the Coulomb interaction between different particles.

We have shown that uncertainty quantification using the Monte Carlo method of nanoscale devices becomes tractable because of the increased efficiency of the ADHIE method. The analysis also showed that, to asses the robustness of a design, it is crucial to have knowledge of the full statistics of the device's behavior.

5.A Appendix: ADHIE-FDTD for the variable mass Schrödinger equation

The Schrödinger equation for a variable mass is given by:

$$\jmath\hbar\frac{\partial\psi}{\partial t} = -\frac{\hbar^2}{2}\nabla\cdot\left(\frac{1}{m}\nabla\psi\right) + v\psi. \tag{5.A.1}$$

For simplicity, we only consider a mass which is variable in a single direction, here the x-direction. Also, only implicitization along the x-direction is considered. The resulting spatial discretization yields:

$$\jmath\hbar\frac{\partial}{\partial t}\boldsymbol{\psi} = \big(T_x + T_y + T_z + V\big)\boldsymbol{\psi}, \tag{5.A.2}$$

with

$$T_x = \frac{\hbar^2}{2}\big(\delta_x^{\star\,-1} D_x m^{\star\,-1} \delta_x{}^{-1} D_x{}^T\big) \otimes I_{m_y} \otimes I_{m_z}, \tag{5.A.3a}$$

$$T_y = \frac{\hbar^2}{2} m^{-1} \otimes \Big(\delta_y^{\star\,-1} D_y \delta_y{}^{-1} D_y{}^T\Big) \otimes I_{m_z}, \tag{5.A.3b}$$

$$T_z = \frac{\hbar^2}{2} m^{-1} \otimes I_{m_y} \otimes \big(\delta_z^{\star\,-1} D_z \delta_z{}^{-1} D_z{}^T\big), \tag{5.A.3c}$$

with m the diagonal matrix containing the variable mass in the x-direction on the vertices of the primary grid, excluding the edge of the grid, and $m^\star$ containing the mass harmonically averaged from the masses on the primary grid.

The resulting ADHIE scheme is given by:

$$\begin{bmatrix} G & 0 \\ -\Delta\eta H & G \end{bmatrix} \boldsymbol{x}\big|^n = \begin{bmatrix} G & -\Delta\eta H \\ 0 & G \end{bmatrix} \boldsymbol{x}\big|^{n-1}, \tag{5.A.4}$$

where $\boldsymbol{x}$ is defined as in (5.8), H and G are given by:

$$H = T_x + T_y + T_z + V, \tag{5.A.5a}$$

$$G = \left(I_{m_x} + \frac{\Delta\eta}{2} S_x\right) \otimes I_{m_y} \otimes I_{m_z}, \tag{5.A.5b}$$

and

$$S_x = \frac{\hbar^2}{2}\big(\delta_x^{\star\,-1} D_x m^{\star\,-1} \big(I_{n_x} - P_x\big) \delta_x{}^{-1} D_x{}^T\big). \tag{5.A.5c}$$

The same method to prove the stability as in Section 5.3 is used. First, the equations are symmetrized using Q, defined in (4.26), resulting in:

$$\begin{bmatrix} \tilde{G} & 0 \\ -\Delta\eta\, \tilde{H} & \tilde{G} \end{bmatrix} \tilde{\boldsymbol{x}}\big|^n = \begin{bmatrix} \tilde{G} & -\Delta\eta\, \tilde{H} \\ 0 & \tilde{G} \end{bmatrix} \tilde{\boldsymbol{x}}\big|^{n-1}, \tag{5.A.6}$$

with

$$\tilde{H} = \tilde{T}_x + \tilde{T}_y + \tilde{T}_z + V, \tag{5.A.7a}$$

$$\tilde{G} = \left(I_{m_x} + \frac{\Delta\eta}{2} \tilde{S}_x \right) \otimes I_{m_y} \otimes I_{m_z}, \tag{5.A.7b}$$

$$\tilde{T}_x = \frac{\hbar^2}{2} \left(\tilde{D}_x m^{\star -1} \tilde{D}_x{}^T \right) \otimes I_{m_y} \otimes I_{m_z}, \tag{5.A.7c}$$

$$\tilde{T}_y = \frac{\hbar^2}{2} m^{-1} \otimes \left(\tilde{D}_y \tilde{D}_y{}^T \right) \otimes I_{m_z}, \tag{5.A.7d}$$

$$\tilde{T}_z = \frac{\hbar^2}{2} m^{-1} \otimes I_{m_y} \otimes \left(\tilde{D}_z \tilde{D}_z{}^T \right), \tag{5.A.7e}$$

and

$$\tilde{S}_x = \frac{\hbar^2}{2} \left(\tilde{D}_x m^{\star -1} \left(I_{n_x} - P_x \right) \tilde{D}_x{}^T \right). \tag{5.A.8}$$

The symmetrized update scheme (5.A.6) can be rewritten in exactly the same way as (5.20). Again, stability is guaranteed when E in (5.21) is positive definite. For the system (5.A.6), E is rewritten as:

$$\begin{aligned} E = &\begin{bmatrix} I_{n_\psi} & -\frac{\Delta\eta}{2} \left(\tilde{U}_x + \tilde{T}_y + \tilde{T}_z + V \right) \\ -\frac{\Delta\eta}{2} \left(\tilde{U}_x + \tilde{T}_y + \tilde{T}_z + V \right) & I_{n_\psi} \end{bmatrix} \\ &+ \left(\frac{\Delta\eta}{2} \right) \begin{bmatrix} \tilde{S}_x & -\tilde{S}_x \\ -\tilde{S}_x & \tilde{S}_x \end{bmatrix} \otimes I_{m_y} \otimes I_{m_z}. \end{aligned} \tag{5.A.9}$$

with

$$\tilde{U}_x = \left(\tilde{T}_x - \tilde{S}_x \right) \otimes I_{m_y} \otimes I_{m_z} \tag{5.A.10a}$$

$$= \left(\tilde{D}_x m^{\star -1} P_x \tilde{D}_x{}^T \right) \otimes I_{m_y} \otimes I_{m_z}. \tag{5.A.10b}$$

Matrix $\tilde{S}_x$ can be proven to be positive semi-definite in the same way as (5.27). This immediately shows, by virtue of (5.28)–(5.29), that the second term in (5.A.9) is positive semi-definite as well. It is now straightforward to show that the first term in (5.A.9) is positive definite for:

$$\Delta t < \frac{2\hbar}{\left\| \tilde{U}_x + \tilde{T}_y + \tilde{T}_z + V \right\|_2}. \tag{5.A.11}$$

As such, the update scheme is stable for a time step satisfying (5.A.11).

References

1. Crank, J. & Nicolson, P. A practical method for numerical evaluation of solutions of partial differential equations of the heat-conduction type. *Mathematical Proceedings of the Cambridge Philosophical Society* **43,** 50–67 (1947).
2. Goldberg, A., Schey, H. M. & Schwartz, J. L. Computer-generated motion pictures of one-dimensional quantum-mechanical transmission and reflection phenomena. *American Journal of Physics* **35,** 177–186 (1967).
3. Mennemann, J.-F., Jüngel, A. & Kosina, H. Transient Schrödinger–Poisson simulations of a high-frequency resonant tunneling diode oscillator. *Journal of Computational Physics* **239,** 187–205 (2013).
4. Mennemann, J.-F. & Jüngel, A. Perfectly Matched Layers versus discrete transparent boundary conditions in quantum device simulations. *Journal of Computational Physics* **275,** 1–24 (2014).
5. Bian, L., Pang, G., Tang, S. & Arnold, A. ALmost EXact boundary conditions for transient Schrödinger–Poisson system. *Journal of Computational Physics* **313,** 233–246 (2016).
6. Douglas Jr., J. Alternating direction methods for three space variables. *Numerische Mathematik* **4,** 41–63 (1962).
7. Zhai, S., Feng, X. & Weng, Z. New high-order compact ADI algorithms for 3D nonlinear time-fractional convection-diffusion equation. *Mathematical Problems in Engineering* **2013,** 1–11 (2013).
8. Zhai, S., Feng, X. & He, Y. A new high-order compact ADI method for 3-D unsteady convection-diffusion problems with discontinuous coefficients. *Numerical Heat Transfer, Part B: Fundamentals* **65,** 376–391 (2014).
9. Xu, Y. & Zhang, L. Alternating direction implicit method for solving two-dimensional cubic nonlinear Schrödinger equation. *Computer Physics Communications* **183,** 1082–1093 (2012).
10. Eskar, R., Huang, P. & Feng, X. A new high-order compact ADI finite difference scheme for solving 3D nonlinear Schrödinger equation. *Advances in Difference Equations* **2018,** 1–15 (2018).
11. Dehghan, M. Finite difference procedures for solving a problem arising in modeling and design of certain optoelectronic devices. *Mathematics and Computers in Simulation* **71,** 16–30 (2006).
12. Tay, W. C. & Tan, E. L. Pentadiagonal alternating-direction-implicit finite-difference time-domain method for two-dimensional Schrödinger equation. *Computer Physics Communications* **185,** 1886–1892 (2014).
13. Chen, J. & Wang, J. A 3D hybrid implicit-explicit FDTD scheme with weakly conditional stability. *Microwave and Optical Technology Letters* **48,** 2291–2294 (2006).

14. Zhang, Q., Zhou, B. & Wang, J. A novel hybrid implicit–explicit FDTD algorithm with more relaxed stability condition. *IEEE Antennas and Wireless Propagation Letters* **12,** 1372–1375 (2013).

15. Wang, J. *et al.* A novel 3-D HIE-FDTD method with one-step leapfrog scheme. *IEEE transactions on microwave theory and techniques* **62,** 1275–1283 (2014).

16. Van Londersele, A., De Zutter, D. & Vande Ginste, D. A new hybrid implicit–explicit FDTD method for local subgridding in multiscale 2-D TE scattering problems. *IEEE Transactions on Antennas and Propagation* **64,** 3509–3520 (2016).

17. Van Londersele, A., De Zutter, D. & Vande Ginste, D. An in-depth stability analysis of nonuniform FDTD combined with novel local implicitization techniques. *Journal of Computational Physics* **342,** 177–193 (2017).

18. Van Londersele, A., De Zutter, D. & Vande Ginste, D. Full-wave analysis of the Shielding Effectiveness of Thin Graphene Sheets with the 3D Unidirectionally Collocated HIE-FDTD Method. *International Journal of Antennas and Propagation* **2017,** 1–8 (2017).

19. Van Londersele, A., De Zutter, D. & Vande Ginste, D. A Collocated 3-D HIE-FDTD Scheme With PML. *IEEE Microwave and Wireless Components Letters* **27,** 609–611 (2017).

20. Chen, J., Li, J. & Liu, Q. H. Designing graphene-based absorber by using HIE-FDTD method. *IEEE Transactions on Antennas and Propagation* **65,** 1896–1902 (2017).

21. Chen, J., Guo, J. & Tian, C. Analyzing the shielding effectiveness of a graphene-coated shielding sheet by using the HIE-FDTD method. *IEEE Transactions on Electromagnetic Compatibility* **60,** 362–367 (2017).

22. Dehghan, M. A new ADI technique for two-dimensional parabolic equation with an integral condition. *Computers & Mathematics with Applications* **43,** 1477–1488 (2002).

23. Visscher, P. A fast explicit algorithm for the time-dependent Schrödinger equation. *Computers in Physics* **5,** 596–598 (1991).

24. Sullivan, D. M. & Citrin, D. Determination of the eigenfunctions of arbitrary nanostructures using time domain simulation. *Journal of Applied Physics* **91,** 3219–3226 (2002).

25. Soriano, A., Navarro, E. A., Portí, J. A. & Such, V. Analysis of the finite difference time domain technique to solve the Schrödinger equation for quantum devices. *Journal of Applied Physics* **95,** 8011–8018 (2004).

26. Sullivan, D. M. & Citrin, D. Determining quantum eigenfunctions in three-dimensional nanoscale structures. *Journal of Applied Physics* **97,** 104305 (2005).

27. Wang, S., Teixeira, F. L. & Chen, J. An iterative ADI-FDTD with reduced splitting error. *IEEE Microwave and Wireless Components Letters* **15,** 92–94 (2005).

28. Yang, S.-C., Chen, Z., Yu, Y. & Yin, W.-Y. An unconditionally stable one-step arbitrary-order leapfrog ADI-FDTD method and its numerical properties. *IEEE transactions on antennas and propagation* **60,** 1995–2003 (2012).

29. Süli, E. & Mayers, D. F. *An Introduction to Numerical Analysis* (Cambridge University Press, 2008).

30. Varga, R. S. *Matrix Iterative Analysis* (Springer, 2000).

31. Denecker, B., Knockaert, L., Olyslager, F. & De Zutter, D. A new state-space-based algorithm to assess the stability of the finite-difference time-domain method for 3D finite inhomogeneous problems. *AEU-International Journal of Electronics and Communications* **58,** 339–348 (2004).

32. Bernstein, D. S. *Matrix Mathematics* (Princeton University Press, 2009).

33. Bertoni, A. *et al.* Quantum logic gates based on coherent electron transport in quantum wires. *Physical Review Letters* **84,** 5912–5915 (2000).

34. Gaury, B. *et al.* Numerical simulations of time-resolved quantum electronics. *Physics Reports* **534,** 1–37 (2014).

35. Weston, J. & Waintal, X. Towards realistic time-resolved simulations of quantum devices. *Journal of Computational Electronics* **15,** 1148–1157 (2016).

36. Rossignol, B., Kloss, T., Armagnat, P. & Waintal, X. Toward flying qubit spectroscopy. *Physical Review B* **98,** 205302 (2018).

37. Yamamoto, M. *et al.* Electrical control of a solid-state flying qubit. *Nature Nanotechnology* **7,** 247–251 (2012).

38. Dai, W., Li, G., Nassar, R. & Su, S. On the stability of the FDTD method for solving a time-dependent Schrödinger equation. *Numerical Methods for Partial Differential Equations: An International Journal* **21,** 1140–1154 (2005).

39. Zervos, M. & Feiner, L.-F. Electronic structure of piezoelectric double-barrier InAs/InP/InAs/InP/InAs (111) nanowires. *Journal of Applied Physics* **95,** 281–291 (2004).

40. Zervos, M. & Pelekanos, N. Current transport in semiconductor nanowires with built-in barriers based on a 1D transfer matrix calculation. *Journal of Applied Physics* **104,** 054302 (2008).

41. Björk, M. *et al.* Nanowire resonant tunneling diodes. *Applied Physics Letters* **81,** 4458–4460 (2002).

42. Ragi, R., da Nobrega, R. V. & Romero, M. A. Modeling of peak voltage and current of nanowire resonant tunneling devices: case study on InAs/InP double-barrier heterostructures. *International Journal of Numerical Modelling: Electronic Networks, Devices and Fields* **26,** 506–517 (2013).

43. Ritter, J. & Amdt, F. Efficient FDTD/matrix-pencil method for the full-wave scattering parameter analysis of waveguiding structures. *IEEE Transactions on Microwave Theory and Techniques* **44,** 2450–2456 (1996).

44. Krantz, P. *et al.* A quantum engineer's guide to superconducting qubits. *Applied Physics Reviews* **6,** 021318 (2019).

45. Kalos, M. H. & Whitlock, P. A. *Monte Carlo Methods* (John Wiley & Sons, 2009).

CHAPTER 6

FDTD FOR COMBINED ELECTROMAGNETIC AND QUANTUM MECHANICAL PROBLEMS

"Life's simplest answers are often the easiest to overlook."

— STEPHEN KING, 11/22/63 (2011)

In this chapter, we present several explicit FDTD methods that are aimed at simulating coupled EM/QM systems. The three pieces that need to be discretized are: the electromagnetic fields, the minimally coupled Schrödinger equation, and the quantum current density.

6.1 Introduction

Up to now, many methods have been developed that deal with either the EM problem or the QM problem. As already mentioned, the Yee algorithm is the most popular (time-dependent) method for EM problems by virtue of the second-order accurate staggered grid resulting in fast explicit time integration. In the previous chapters, it was shown that the FD approach is also a viable option in computational QM, and it has been applied to the Schrödinger and Kohn-Sham equations with many variations [1–5]. As such, the FDTD method looks like an excellent approach to couple these two sets of equations.

To couple the QM problem and the EM problem, many implementations exist, where, depending on the problem at hand, an effective-mass Schrödinger equation [6–13] or the *ab initio* Kohn-Sham equation [14–19] is considered. One of the major differences of coupled QM/EM methods, compared to regular EM methods, is that the former require the computation of the EM potentials, which results in different schemes depending on the chosen gauge condition. In [9, 12, 19], the potentials are directly calculated from the current and charge density. Alternatively, the EM potentials may be calculated from the EM fields, rendering computational methods that are more compatible with traditional EM techniques [13, 20]. Therefore, we have opted to use the latter approach.

Further, we develop a new leapfrog method for the minimally-coupled Schrödinger equation, where the real and imaginary parts of the wave function are alternately

updated. The spatial discretization is performed on nonuniform tensor-product grids, similar to the lower-order scheme presented in Chapter 4. Additionally, fourth-order and sixth-order accurate spatial discretizations are derived on uniform grids. The stability of the scheme is rigorously proven for arbitrary spatial variations of the potentials. It is shown that the stability of the scheme does not depend on the spatial gradients of the potentials, but only on the magnitude.

The remainder of this chapter is organized as follows. In Section 6.2, the Yee algorithm is presented on nonuniform tensor-product grids with inclusion of the electromagnetic potentials in three different gauges: Coulomb, Gibbs, and Lorenz. Next, in Section 6.3, the novel leapfrog scheme for the minimally-coupled Schrödinger equation is presented and its stability is discussed. The self-consistent coupling and discretization of the quantum current density is performed in Section 6.4. In Section 6.5, some of the results obtained with the presented methods are discussed. Lastly, we make some concluding remarks in Section 6.6.

6.2 The electromagnetic fields

6.2.1 The Yee algorithm

The EM schemes presented in this chapter all start from the *lossless* Yee algorithm for the EM fields (3.10)–(3.11), but now defined on the nonuniform tensor-product grid defined in Chapters 4 and 5. Therefore, we will briefly restate the update equations for a grid consisting of $n_x \times n_y \times n_z$ cells terminated by a perfectly electric conducting (PEC) boundary. The discretized fields and current densities are row-major vectorized and collected as:

$$\boldsymbol{e} = \begin{bmatrix} \boldsymbol{e}_x \\ \boldsymbol{e}_y \\ \boldsymbol{e}_z \end{bmatrix}, \quad \boldsymbol{h} = \begin{bmatrix} \boldsymbol{h}_x \\ \boldsymbol{h}_y \\ \boldsymbol{h}_z \end{bmatrix}, \quad \text{and} \quad \boldsymbol{s} = \begin{bmatrix} \boldsymbol{j}_x \\ \boldsymbol{j}_y \\ \boldsymbol{j}_z \end{bmatrix}. \tag{6.1}$$

The total length n_e of $\boldsymbol{e}$ and $\boldsymbol{s}$ is:

$$n_e = n_x m_y m_z + m_x n_y m_z + m_x m_y n_z, \tag{6.2}$$

and the total length n_h of $\boldsymbol{h}$ is:

$$n_h = m_x n_y n_z + n_x m_y n_z + n_x n_y m_z. \tag{6.3}$$

The resulting scheme is compactly written as:

$$\begin{bmatrix} \frac{M_\epsilon}{\Delta t} & 0 \\ C^T & \frac{M_\mu}{\Delta t} \end{bmatrix} \begin{bmatrix} \hat{\boldsymbol{e}}|^n \\ \hat{\boldsymbol{h}}|^{n+\frac{1}{2}} \end{bmatrix} = \begin{bmatrix} \frac{M_\epsilon}{\Delta t} & C \\ 0 & \frac{M_\mu}{\Delta t} \end{bmatrix} \begin{bmatrix} \hat{\boldsymbol{e}}|^{n-1} \\ \hat{\boldsymbol{h}}|^{n-\frac{1}{2}} \end{bmatrix} + \begin{bmatrix} \hat{\boldsymbol{s}}|^{n-\frac{1}{2}} \\ 0 \end{bmatrix}, \tag{6.4}$$

where $\hat{\boldsymbol{e}}$ and $\hat{\boldsymbol{h}}$ are the scaled electric and magnetic field:

$$\hat{\boldsymbol{e}} = \begin{bmatrix} \delta_x \otimes I_{m_y} \otimes I_{m_z} & & \\ & I_{m_x} \otimes \delta_y \otimes I_{m_z} & \\ & & I_{m_x} \otimes I_{m_y} \otimes \delta_z \end{bmatrix} \begin{bmatrix} \boldsymbol{e}_x \\ \boldsymbol{e}_y \\ \boldsymbol{e}_z \end{bmatrix}, \tag{6.5a}$$

$$\hat{\boldsymbol{h}} = \begin{bmatrix} \delta_x^\star \otimes I_{n_y} \otimes I_{n_z} & & \\ & I_{n_x} \otimes \delta_y^\star \otimes I_{n_z} & \\ & & I_{n_x} \otimes I_{n_y} \otimes \delta_z^\star \end{bmatrix} \begin{bmatrix} \boldsymbol{h}_x \\ \boldsymbol{h}_y \\ \boldsymbol{h}_z \end{bmatrix}. \tag{6.5b}$$

The source term $\hat{\boldsymbol{s}}$ is given by:

$$\hat{\boldsymbol{s}} = -\begin{bmatrix} I_{n_x} \otimes \delta_y^\star \otimes \delta_z^\star & & \\ & \delta_x^\star \otimes I_{n_y} \otimes \delta_z^\star & \\ & & \delta_x^\star \otimes \delta_y^\star \otimes I_{n_z} \end{bmatrix} \begin{bmatrix} \boldsymbol{j}_x \\ \boldsymbol{j}_y \\ \boldsymbol{j}_z \end{bmatrix}, \tag{6.6}$$

where $\boldsymbol{j}$ can be an impressed current source or the current density arising from a quantum system. The dimensionless curl matrix C is given by:

$$C = \begin{bmatrix} 0 & -I_{n_x} \otimes I_{m_y} \otimes D_z & I_{n_x} \otimes D_y \otimes I_{m_z} \\ I_{m_x} \otimes I_{n_y} \otimes D_z & 0 & -D_x \otimes I_{n_y} \otimes I_{m_z} \\ -I_{m_x} \otimes D_y \otimes I_{n_z} & D_x \otimes I_{m_y} \otimes I_{n_z} & 0 \end{bmatrix}. \tag{6.7}$$

The material matrices M_ϵ and M_μ are defined as:

$$M_\mu = M\big[\mu\big], \quad \text{and} \quad M_\epsilon = M^\star\big[\epsilon\big], \tag{6.8}$$

where the diagonal matrices $\big[\epsilon\big]$ and $\big[\mu\big]$ contain the correctly averaged permittivity ϵ and permeability μ, as described in, e.g., [21]. The matrices M and $M^\star$ are given by:

$$M = \begin{bmatrix} (\delta_x^\star)^{-1} \otimes \delta_y \otimes \delta_z & & \\ & \delta_x \otimes (\delta_y^\star)^{-1} \otimes \delta_z & \\ & & \delta_x \otimes \delta_y \otimes (\delta_z^\star)^{-1} \end{bmatrix}, \tag{6.9a}$$

$$M^\star = \begin{bmatrix} (\delta_x)^{-1} \otimes \delta_y^\star \otimes \delta_z^\star & & \\ & \delta_x^\star \otimes (\delta_y)^{-1} \otimes \delta_z^\star & \\ & & \delta_x^\star \otimes \delta_y^\star \otimes (\delta_z)^{-1} \end{bmatrix}. \tag{6.9b}$$

In [22], the Yee algorithm is proven stable for Δt satisfying:

$$\Delta t < \frac{2}{\left\| M_\epsilon^{-\frac{1}{2}} C M_\mu^{-\frac{1}{2}} \right\|_2}. \tag{6.10}$$

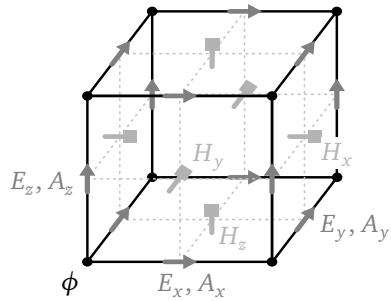

Figure 6.1: The EM vector potential $\boldsymbol{A}$ (indicated with triangle-topped arrows) is discretized at the same spatial locations as $\boldsymbol{E}$ in the regular Yee cell, and the scalar EM potential ϕ at the nodes of the grid, indicated with circles. The temporal discretization fixes $\boldsymbol{E}$ and ϕ at integer time indices and $\boldsymbol{H}$ and $\boldsymbol{A}$ at half-integer time indices, resulting in leapfrog iterations.

6.2.2 Discretization of the potentials

The EM potentials $\boldsymbol{A}$ and ϕ are computed from the EM fields $\boldsymbol{E}$ and $\boldsymbol{H}$. In the following, three different schemes are presented corresponding to three possible gauges.

The Coulomb gauge condition

The first gauge is the Coulomb gauge ($\boldsymbol{\nabla} \cdot \boldsymbol{A} = 0$). The vector potential $\boldsymbol{A}$ is discretized on the same spatial positions as the electric field and row-major vectorized:

$$\boldsymbol{a}|^{n+\frac{1}{2}} = \begin{bmatrix} \boldsymbol{a}_x|^{n+\frac{1}{2}} \\ \boldsymbol{a}_y|^{n+\frac{1}{2}} \\ \boldsymbol{a}_z|^{n+\frac{1}{2}} \end{bmatrix}, \tag{6.11}$$

and the scalar potential ϕ is discretized on the $n_\phi = m_x m_y m_z$ internal nodes of the grid, resulting in $\boldsymbol{\phi}$. The Yee cell with the EM potentials is shown in Fig. 6.1. The straightforward discretization of (2.7b) using central differences, results in:

$$\boldsymbol{a}|^{n+\frac{1}{2}} = \boldsymbol{a}|^{n-\frac{1}{2}} + \Delta t D^T \boldsymbol{\phi}|^n - \Delta t \boldsymbol{e}|^n, \tag{6.12}$$

with D defined as:

$$D = \begin{bmatrix} D_1 & D_2 & D_3 \end{bmatrix}, \tag{6.13}$$

and where

$$D_1 = D_x {\delta_x}^{-1} \otimes I_{m_y} \otimes I_{m_z}, \tag{6.14a}$$

$$D_2 = I_{m_x} \otimes D_y {\delta_y}^{-1} \otimes I_{m_z}, \tag{6.14b}$$

$$D_3 = I_{m_x} \otimes I_{m_y} \otimes D_z {\delta_z}^{-1}. \tag{6.14c}$$

The scalar potential ϕ satisfies the Poisson equation:

$$\nabla^2 \phi = -\frac{\rho}{\epsilon_0}, \tag{6.15}$$

where ρ is the total charge. For now, we assume that this charge distribution is known. The discretization of (6.15) is directly given by:

$$L\boldsymbol{\phi}|^n = -\frac{1}{\epsilon_0}\boldsymbol{\rho}|^n, \tag{6.16}$$

where L is the discretized Laplacian operator defined in Chapter 4. However, the matrix L assumes Dirichlet boundary conditions which would require very large grids because of the long range of the Coulomb potential. To overcome this issue, the multipole-corrections method is applied [23]. This method introduces an auxiliary charge distribution ρ_{aux} centered at the origin, which is calculated from the multipole moments of the true charge distribution. Since the Coulomb potential ϕ_{aux} for ρ_{aux} has an analytical expression, it can easily be calculated. The remaining charge density $\rho_{\text{diff}} = \rho - \rho_{\text{aux}}$ has a short-range Coulomb potential ϕ_{diff} which is calculated with (6.16). We used spherical harmonics up to degree 4 to obtain this effect. The update for $\boldsymbol{\phi}$ is schematically summarized as:

$$\boldsymbol{\rho}_{\text{aux}}|^n = \text{Multipoles}\left(\boldsymbol{\rho}|^n\right), \tag{6.17a}$$

$$\boldsymbol{\phi}_{\text{aux}}|^n = \text{Expansion}\left(\boldsymbol{\rho}_{\text{aux}}|^n\right), \tag{6.17b}$$

$$L\boldsymbol{\phi}_{\text{diff}}|^n = -\frac{\boldsymbol{\rho}_{\text{diff}}|^n}{\epsilon_0}, \tag{6.17c}$$

where the exact form of Multipoles and Expansion is given in [23]. In conclusion, the Coulomb gauge has a straightforward update equation for the vector potential, but has to solve a linear system of equations (6.17c) at every iteration in addition to calculating the multipoles and expansion functions.

As an alternative, the scalar potential can be determined as an integral (2.13). This sidesteps the problem with boundary conditions but instead has a very poor scaling of $\mathcal{O}\left(n_\phi^2\right)$ when the integral is directly calculated. Clever techniques can reduce this computational cost, as proposed in [19, 24].

The Gibbs gauge condition

The Gibbs gauge condition ($\phi = 0$) results directly in the update scheme:

$$\boldsymbol{a}|^{n+\frac{1}{2}} = \boldsymbol{a}|^{n-\frac{1}{2}} - \Delta t \boldsymbol{e}|^{n}. \tag{6.18}$$

The Lorenz gauge condition

In the Lorenz gauge ($c\boldsymbol{\nabla}\cdot\boldsymbol{A} + \partial\phi/\partial t = 0$), the update for $\boldsymbol{a}$ is the same as for the Coulomb gauge (6.12) while the update for $\boldsymbol{\phi}$ becomes:

$$\boldsymbol{\phi}|^{n+1} = \boldsymbol{\phi}|^{n} - c^2 \Delta t D^{\star} \boldsymbol{a}|^{n+\frac{1}{2}}, \tag{6.19}$$

where

$$D^{\star} = \begin{bmatrix} D_1^{\star} & D_2^{\star} & D_3^{\star} \end{bmatrix}, \tag{6.20}$$

with

$$D_1^{\star} = \delta_x^{\star -1} D_x \otimes I_{m_y} \otimes I_{m_z}, \tag{6.21a}$$

$$D_2^{\star} = I_{m_x} \otimes \delta_y^{\star -1} D_y \otimes I_{m_z}, \tag{6.21b}$$

$$D_3^{\star} = I_{m_x} \otimes I_{m_y} \otimes \delta_z^{\star -1} D_z. \tag{6.21c}$$

In contrast to the Coulomb and Gibbs gauges, the Lorenz gauge needs a termination of the simulation domain with PMLs. For the EM fields we adopt the complex-frequency shifted (CFS) PML with a recursive convolution [25], known as the CPML. Similar as in Chapter 4, the PML is interpreted as a complex coordinate stretch. First, the complex coordinate stretching is introduced:

$$\frac{\partial}{\partial u} \rightarrow \frac{1}{s_u}\frac{\partial}{\partial u}, \quad \text{for} \quad u \in \{x, y, z\}, \tag{6.22}$$

where the coordinate stretching factor is defined as:

$$s_u(\omega) = \kappa_u + \frac{\sigma_u}{\gamma_u + \jmath\omega\epsilon_0}. \tag{6.23}$$

Next, this complex frequency stretch is inserted into the frequency domain counterparts of (2.7b) and (2.16):

$$\tilde{\boldsymbol{E}} = -\jmath\omega\tilde{\boldsymbol{A}} - \boldsymbol{\nabla}\tilde{\phi}, \tag{6.24a}$$

$$\boldsymbol{\nabla}\cdot\tilde{\boldsymbol{A}} + \frac{1}{c^2}\jmath\omega\tilde{\phi} = 0, \tag{6.24b}$$

where $\tilde{\boldsymbol{E}}$, $\tilde{\boldsymbol{A}}$, and $\tilde{\phi}$ are the frequency domain analogues of $\boldsymbol{E}$, $\boldsymbol{A}$, and ϕ, respectively. Finally, a straightforward reordering analogous to [26] and subsequent transformation to the time domain, yields:

$$\frac{\partial A_u}{\partial t} = -E_u - \frac{1}{\kappa_u}\left(\frac{\partial\phi}{\partial u} + \phi_u\right), \tag{6.25}$$

and

$$-\frac{1}{c^2}\frac{\partial \phi}{\partial t} = \frac{1}{\kappa_x}\left(\frac{\partial A_x}{\partial x} + A_{xx}\right) + \frac{1}{\kappa_y}\left(\frac{\partial A_y}{\partial y} + A_{yy}\right) + \frac{1}{\kappa_z}\left(\frac{\partial A_z}{\partial z} + A_{zz}\right), \quad (6.26)$$

with additional auxiliary differential equations:

$$\left(\alpha_u + \epsilon_0 \frac{\partial}{\partial t}\right) A_{uu} = -\frac{\sigma_u}{\kappa_u}\frac{\partial A_u}{\partial u}, \quad (6.27a)$$

$$\left(\alpha_u + \epsilon_0 \frac{\partial}{\partial t}\right) \phi_u = -\frac{\sigma_u}{\kappa_u}\frac{\partial \phi}{\partial u}, \quad (6.27b)$$

where

$$\alpha_u = \gamma_u + \frac{\sigma_u}{\kappa_u}. \quad (6.28)$$

The discretization of (6.25) and (6.26) is given by:

$$\begin{aligned} A_x|^{n+\frac{1}{2}}_{i+\frac{1}{2},j,k} = A_x|^{n-\frac{1}{2}}_{i+\frac{1}{2},j,k} - \Delta t E_x|^n_{i+\frac{1}{2},j,k} \\ - \frac{\Delta t}{\kappa_x|_{i+\frac{1}{2}}}\left(\frac{\phi|^n_{i+1,j,k} - \phi|^n_{i,j,k}}{\Delta x_{i+1}} + \phi_x|^n_{i+\frac{1}{2},j,k}\right), \end{aligned} \quad (6.29)$$

and

$$\begin{aligned} \phi|^{n+1}_{i,j,k} = \phi|^n_{i,j,k} - \frac{c^2\Delta t}{\kappa_x|_i}\left(\frac{A_x|^{n+\frac{1}{2}}_{i+\frac{1}{2},j,k} - A_x|^{n+\frac{1}{2}}_{i-\frac{1}{2},j,k}}{\Delta x^\star_i} + A_{xx}|^{n+\frac{1}{2}}_{i,j,k}\right) \\ - \frac{c^2\Delta t}{\kappa_y|_j}\left(\frac{A_y|^{n+\frac{1}{2}}_{i,j+\frac{1}{2},k} - A_y|^{n+\frac{1}{2}}_{i,j-\frac{1}{2},k}}{\Delta y^\star_j} + A_{yy}|^{n+\frac{1}{2}}_{i,j,k}\right) \\ - \frac{c^2\Delta t}{\kappa_z|_k}\left(\frac{A_z|^{n+\frac{1}{2}}_{i,j,k+\frac{1}{2}} - A_z|^{n+\frac{1}{2}}_{i,j,k-\frac{1}{2}}}{\Delta z^\star_k} + A_{zz}|^{n+\frac{1}{2}}_{i,j,k}\right). \end{aligned} \quad (6.30)$$

Following the derivation in [26], we find the updates for the auxiliary variables which are equivalent to the CPML in [25]:

$$\phi_x|^n_{i+\frac{1}{2},j,k} = a_x|_{i+\frac{1}{2}}\phi_x|^{n-1}_{i+\frac{1}{2},j,k} + b_x|_{i+\frac{1}{2}}\frac{\phi|^n_{i+1,j,k} - \phi|^n_{i,j,k}}{\Delta x_{i+1}}, \quad (6.31)$$

$$A_{xx}|^{n+\frac{1}{2}}_{i,j,k} = a_x|_i A_{xx}|^{n-\frac{1}{2}}_{i,j,k} + b_x|_i \frac{A_x|^{n+\frac{1}{2}}_{i+\frac{1}{2},j,k} - A_x|^{n+\frac{1}{2}}_{i-\frac{1}{2},j,k}}{\Delta x^\star_i}, \quad (6.32)$$

with analogous expressions for ϕ_y, ϕ_z, A_{yy}, and A_{zz}. The coefficients a_x and b_x are given by:

$$a_x = e^{-\frac{\alpha_x \Delta t}{\epsilon_0}} \quad \text{and} \quad b_x = -\frac{\sigma_x}{\alpha_x \kappa_x}(1-a_x). \tag{6.33}$$

The parameters κ_u, σ_u, and γ_u are polynomially graded as proposed in [26].

Stability

For the Lorenz and the Gibbs gauges the stability can be determined straightforwardly. Consider that for both systems, the update equation can be schematically written as:

$$\begin{bmatrix} L_{11} & 0 \\ L_{21} & L_{22} \end{bmatrix} \boldsymbol{x}|^n = \begin{bmatrix} R_{11} & \\ & R_{22} \end{bmatrix} \boldsymbol{x}|^{n-1}, \tag{6.34}$$

where $\boldsymbol{x}|^n$ is given by:

$$\begin{bmatrix} \boldsymbol{e}|^n \\ \boldsymbol{h}|^{n+\frac{1}{2}} \\ \boldsymbol{a}|^{n+\frac{1}{2}} \\ \boldsymbol{\phi}|^{n+1} \end{bmatrix}, \quad \text{and} \quad \begin{bmatrix} \boldsymbol{e}|^n \\ \boldsymbol{h}|^{n+\frac{1}{2}} \\ \boldsymbol{a}|^{n+\frac{1}{2}} \end{bmatrix}, \tag{6.35}$$

for the Lorenz and Gibbs gauge, respectively. The stability of this system is guaranteed if the iteration matrix A, which is given by:

$$A = \begin{bmatrix} L_{11}^{-1} & 0 \\ -L_{22}^{-1} L_{21} L_{11}^{-1} & L_{22}^{-1} \end{bmatrix} \begin{bmatrix} R_{11} & 0 \\ 0 & R_{22} \end{bmatrix} = \begin{bmatrix} L_{11}^{-1} R_{11} & 0 \\ -L_{22}^{-1} L_{21} L_{11}^{-1} R_{11} & L_{22}^{-1} R_{22} \end{bmatrix}, \tag{6.36}$$

has a spectral radius smaller than 1. Since A is lower block triangular, its eigenvalues are given by the eigenvalues of the blocks on the diagonals. Note that these blocks $L_{22}^{-1} R_{11}$ and $L_{22}^{-1} R_{22}$ are the iteration matrices of the $(\boldsymbol{e}, \boldsymbol{h})$ system (6.4) and $(\boldsymbol{a}, \boldsymbol{\phi})$ system, respectively. The stability of the complete $(\boldsymbol{e}, \boldsymbol{h}, \boldsymbol{a}, \boldsymbol{\phi})$ system is thus guaranteed by guaranteeing the stability of the separate systems.

Stability for the $(\boldsymbol{e}, \boldsymbol{h})$ system is guaranteed for Δt satisfying (6.10). For the Gibbs gauge, only the stability of (6.18) has to be considered with $\boldsymbol{e} = 0$ such that the iteration matrix is I_{n_e}. Therefore, the eigenvalues are all 1 and the system is stable, independent of the time step. The Lorenz gauge is slightly more involved. We collect the Lorenz update equations (6.12) and (6.19) with $\boldsymbol{e} = 0$ as:

$$\begin{bmatrix} I_{n_e} & 0 \\ \Delta\tau D^\star & I_{n_\phi} \end{bmatrix} \begin{bmatrix} \boldsymbol{a}|^{n+\frac{1}{2}} \\ \frac{1}{c}\boldsymbol{\phi}|^{n+1} \end{bmatrix} = \begin{bmatrix} I_{n_e} & \Delta\tau D^T \\ 0 & I_{n_\phi} \end{bmatrix} \begin{bmatrix} \boldsymbol{a}|^{n-\frac{1}{2}} \\ \frac{1}{c}\boldsymbol{\phi}|^{n} \end{bmatrix}, \tag{6.37}$$

where $\Delta\tau = c\Delta t$. As in Chapter 5, we will employ the method of [27] to determine the stability. First, (6.37) is transformed using the transformation matrix:

$$W = \begin{bmatrix} \delta_x \otimes \delta_y^\star \otimes \delta_z^\star & & & \\ & \delta_x^\star \otimes \delta_y \otimes \delta_z^\star & & \\ & & \delta_x^\star \otimes \delta_y^\star \otimes \delta_z & \\ & & & \delta_x^\star \otimes \delta_y^\star \otimes \delta_z^\star \end{bmatrix}, \quad (6.38)$$

to

$$\begin{bmatrix} I_{n_e} & 0 \\ \tilde{D} & I_{n_\phi} \end{bmatrix} \begin{bmatrix} \tilde{\boldsymbol{a}}|^{n+\frac{1}{2}} \\ \tilde{\boldsymbol{\phi}}|^{n+1} \end{bmatrix} = \begin{bmatrix} I_{n_e} & \tilde{D}^T \\ 0 & I_{n_\phi} \end{bmatrix} \begin{bmatrix} \tilde{\boldsymbol{a}}|^{n-\frac{1}{2}} \\ \tilde{\boldsymbol{\phi}}|^{n} \end{bmatrix}, \quad (6.39)$$

where

$$\begin{bmatrix} \tilde{\boldsymbol{a}} \\ \tilde{\boldsymbol{\phi}} \end{bmatrix} = W^{\frac{1}{2}} \begin{bmatrix} \boldsymbol{a} \\ \frac{1}{c}\boldsymbol{\phi} \end{bmatrix}, \quad (6.40)$$

with

$$\tilde{D} = \Delta\tau \left(\delta_x^\star \otimes \delta_y^\star \otimes \delta_z^\star\right)^{-\frac{1}{2}} D \begin{bmatrix} \delta_x \otimes \delta_y^\star \otimes \delta_z^\star & & \\ & \delta_x^\star \otimes \delta_y \otimes \delta_z^\star & \\ & & \delta_x^\star \otimes \delta_y^\star \otimes \delta_z \end{bmatrix}^{\frac{1}{2}}. \quad (6.41)$$

Second, the update equation (6.39) is recast as:

$$(E+F) \begin{bmatrix} \tilde{\boldsymbol{a}}|^{n+\frac{1}{2}} \\ \tilde{\boldsymbol{\phi}}|^{n+1} \end{bmatrix} = (E-F) \begin{bmatrix} \tilde{\boldsymbol{a}}|^{n-\frac{1}{2}} \\ \tilde{\boldsymbol{\phi}}|^{n} \end{bmatrix}, \quad (6.42)$$

with

$$E = \begin{bmatrix} I_{n_e} & \frac{1}{2}\tilde{D}^T \\ \frac{1}{2}\tilde{D} & I_{n_\phi} \end{bmatrix}, \quad \text{and} \quad F = \begin{bmatrix} 0 & -\frac{1}{2}\tilde{D}^T \\ \frac{1}{2}\tilde{D} & 0 \end{bmatrix}. \quad (6.43)$$

Next, according to [27], and since E is real and symmetric and F real, the system (6.42) is stable if $F + F^T$ is positive semi-definite and E is positive definite. It is clear that $F + F^T$ is positive semi-definite since it is the zero matrix. The eigenvalues z of E are determined by solving $\det\left(E - zI_{n_e+n_\phi}\right) = 0$. This is transformed, using the Schur complement [28], to:

$$\det\left((1-z)I_{n_\phi} - \frac{1}{4(1-z)}\tilde{D}\tilde{D}^T\right) = 0, \quad (6.44)$$

and

$$\det\left((1-z)I_{n_e}\right) = 0. \quad (6.45)$$

The latter immediately yields eigenvalues:

$$z = 1. \quad (6.46)$$

From (6.44) the eigenvalues z are related to the eigenvalues σ^2 of $\tilde{D}\tilde{D}^T$ by:

$$(1-z)^2 - \frac{1}{4}\sigma^2 = 0. \tag{6.47}$$

Note that σ are the singular values of $\tilde{D}$. For E to be positive definite, we require:

$$z = 1 - \frac{\sigma}{2} > 0. \tag{6.48}$$

Since the matrix 2-norm is equal to the maximum singular value, we finally obtain the following stability criterion:

$$2 > \left\|\tilde{D}\right\|_2 = \sqrt{\left\|\tilde{D}\tilde{D}^T\right\|_2}, \tag{6.49}$$

where we have used that $\left\|A\,A^T\right\|_2 = \|A\|_2^2$. Since the matrix 2-norm of a symmetric matrix is equal to the spectral radius, we get:

$$\sqrt{\left\|\tilde{D}\tilde{D}^T\right\|_2} = \Delta\tau\sqrt{\rho\left(\tilde{D}_x\tilde{D}_x{}^T \oplus \tilde{D}_y\tilde{D}_y{}^T \oplus \tilde{D}_z\tilde{D}_z{}^T\right)}, \tag{6.50}$$

where $\tilde{D}_u$ for $u \in \{x,y,z\}$ is defined in (4.29). Now, we write the spectral radius of the Kronecker sum as the sum of the spectral radii by virtue of (5.28a) and by using that the $D_u D_u^T$ are positive definite (5.27)[1]:

$$\rho\left(\tilde{D}_x\tilde{D}_x{}^T \oplus \tilde{D}_y\tilde{D}_y{}^T \oplus \tilde{D}_z\tilde{D}_z{}^T\right) = \sum_{u\in\{x,y,z\}} \rho\left(\tilde{D}_u\tilde{D}_u{}^T\right). \tag{6.51}$$

Now, set $\rho(\tilde{D}\tilde{D}^T) = \rho(\delta_u^{\star-1}D_u\delta_u^{-1}D_u^T)$, such that the stability of $\boldsymbol{a}$ and $\boldsymbol{\phi}$ is guaranteed by:

$$\Delta t < \frac{2}{c\sqrt{\sum_{u\in\{x,y,z\}} \rho\left(\delta_u^{\star-1}D_u\delta_u^{-1}D_u^T\right)}}. \tag{6.52}$$

The time step is now compared to the criterion for $\boldsymbol{e}$ and $\boldsymbol{h}$ (6.10). By using the submultiplicativity of the matrix 2-norm [28, eq. 9.3.4], (6.10) is be approximated by:

$$\Delta t < \frac{2}{\frac{1}{\sqrt{\epsilon_{\min}\mu_{\min}}}\left\|M^{\star-\frac{1}{2}}CM^{-\frac{1}{2}}\right\|_2}. \tag{6.53}$$

Further, in [27], it is shown that:

$$\left\|M^{\star-\frac{1}{2}}CM^{-\frac{1}{2}}\right\|_2^2 = \sum_{u\in\{x,y,z\}} \left\|\tilde{D}_u\right\|_2^2, \tag{6.54}$$

[1] Eq. (5.27) only shows that $\tilde{D}_u\tilde{D}_u{}^T$ is positive semi-definite. However, it is easy to see that $\|\tilde{D}_u{}^T\boldsymbol{x}\|_2$ is zero if and only if $\boldsymbol{x} = \boldsymbol{0}$. As such, $\tilde{D}_u\tilde{D}_u{}^T$ is positive definite.

This matrix norm is again rewritten as:

$$\left\|\tilde{D}_u\right\|_2^2 = \left\|\tilde{D}_u \tilde{D}_u{}^T\right\|_2 = \rho\left(\delta_u^{\star -1} D_u \delta_u^{-1} D_u^T\right), \tag{6.55}$$

such that the stability of $\boldsymbol{e}$ and $\boldsymbol{h}$ is guaranteed for:

$$\Delta t < \frac{2}{\frac{1}{\sqrt{\epsilon_{\min}\mu_{\min}}}\sqrt{\sum_{u\in\{x,y,z\}} \rho\left(\delta_u^{\star -1} D_u \delta_u^{-1} D_u^T\right)}}. \tag{6.56}$$

From (6.52) and (6.56), it is clear that the dependence on the spatial steps is the same for the $(\boldsymbol{e}, \boldsymbol{h})$ and $(\boldsymbol{a}, \boldsymbol{\phi})$ systems. However, condition (6.56) depends on the maximum phase velocity $1/\sqrt{\epsilon_{\min}\mu_{\min}}$, while (6.52) is always limited by the speed of light c. Nonetheless, these two values will coincide in free space and thus also in many practical applications.

To conclude this discussion on stability, it is insightful to derive a Courant-like stability criterion by replacing the spectral radius with the infinity norm. For (6.52), this results in:

$$\Delta t < \frac{1}{c\sqrt{\frac{1}{\widehat{\Delta x}^2} + \frac{1}{\widehat{\Delta y}^2} + \frac{1}{\widehat{\Delta z}^2}}}, \tag{6.57}$$

where

$$\frac{1}{\widehat{\Delta x}^2} = \max_i \left(\frac{1}{2\Delta x_i^\star}\left(\frac{1}{\Delta x_i} + \frac{1}{\Delta x_{i+1}}\right)\right), \tag{6.58}$$

and similar for $\widehat{\Delta y}$ and $\widehat{\Delta z}$. Criterion (6.57) very closely resembles the regular Courant condition (3.20).

6.3 The minimally-coupled Schrödinger equation

In this section, we propose a novel method to solve the time-dependent minimally-coupled Schrödinger or Kohn-Sham equations. Since, formally, the Kohn-Sham equations correspond to many single-particle Schrödinger equations but with self-consistently determined potentials, the numerical time propagation of a Kohn-Sham orbital is identical to that of a single-particle wave function [29]. The differences between single-particle and many-particle systems will be addressed in Section 6.4.

6.3.1 Nonuniform grids

The minimally-coupled single-particle Schrödinger equation (2.40) is again discretized on the nonuniform tensor-product grid as in Chapters 4 and 5. The leap-frog explicit scheme is extended to include an arbitrary time-dependent vector potential $\boldsymbol{A}$ and scalar potential ϕ. The wave function is split in its real and imaginary

parts as $\psi = r + \jmath s$, yielding two coupled equations:

$$\hbar \frac{\partial s}{\partial t} = -\hat{H}_0 r + \hat{H}_1 s, \tag{6.59a}$$

$$\hbar \frac{\partial r}{\partial t} = \hat{H}_0 s + \hat{H}_1 r, \tag{6.59b}$$

where the Hamiltonian $\hat{H}$ is split into its real and imaginary part as $\hat{H} = \hat{H}_0 + \jmath \hat{H}_1$, with:

$$\hat{H}_0 = -\frac{\hbar^2}{2m}\nabla^2 + v + \frac{q^2}{2m}\boldsymbol{A}^2 + q\phi, \tag{6.60}$$

$$\hat{H}_1 = \frac{q\hbar}{2m}(2\boldsymbol{A}\cdot\nabla + (\boldsymbol{\nabla}\cdot\boldsymbol{A})). \tag{6.61}$$

The operator $\hat{H}_0$ is symmetric and $\hat{H}_1$ is skew-symmetric. The temporal discretization using second-order accurate central differences and averages yields:

$$\left(1 - \frac{\Delta t}{2\hbar}\hat{H}_1|^{n-\frac{1}{2}}\right)s|^n = \left(1 + \frac{\Delta t}{2\hbar}\hat{H}_1|^{n-\frac{1}{2}}\right)s|^{n-1} - \frac{\Delta t}{\hbar}\hat{H}_0|^{n-\frac{1}{2}} r|^{n-\frac{1}{2}}, \tag{6.62a}$$

$$\left(1 - \frac{\Delta t}{2\hbar}\hat{H}_1|^{n}\right)r|^{n+\frac{1}{2}} = \left(1 + \frac{\Delta t}{2\hbar}\hat{H}_1|^{n}\right)r|^{n-\frac{1}{2}} + \frac{\Delta t}{\hbar}\hat{H}_0|^{n} s|^{n}. \tag{6.62b}$$

The operator $\hat{H}_0$ is further split into $\hat{H}_0 = \hat{H}_s + \hat{H}_d$, where:

$$\hat{H}_s = -\frac{\hbar^2}{2m}\nabla^2 + v, \tag{6.63}$$

is static, and

$$\hat{H}_d = \frac{q^2}{2m}\boldsymbol{A}^2 + q\phi, \tag{6.64}$$

can vary as a function of time. An alternative derivation of (6.62), based on the well-known exponential mid-point rule [30], is given in Appendix 6.A.1.

After spatial discretization, the update equations are concisely written in matrix form as:

$$\begin{bmatrix} I_{n_\psi} - \frac{\Delta\eta}{2}H_1|^{n-\frac{1}{2}} & 0 \\ -\Delta\eta H_0|^{n} & I_{n_\psi} - \frac{\Delta\eta}{2}H_1|^{n} \end{bmatrix}\begin{bmatrix} \boldsymbol{s}|^{n} \\ \boldsymbol{r}|^{n+\frac{1}{2}} \end{bmatrix} = \\ \begin{bmatrix} I_{n_\psi} + \frac{\Delta\eta}{2}H_1|^{n-\frac{1}{2}} & -\Delta\eta H_0|^{n-\frac{1}{2}} \\ 0 & I_{n_\psi} + \frac{\Delta\eta}{2}H_1|^{n} \end{bmatrix}\begin{bmatrix} \boldsymbol{s}|^{n-1} \\ \boldsymbol{r}|^{n-\frac{1}{2}} \end{bmatrix}, \tag{6.65}$$

where the operators $\hat{H}_0$, $\hat{H}_1$, $\hat{H}_s$, and $\hat{H}_d$ are replaced by their discrete counterparts, i.e., the matrices H_0, H_1, H_s, and H_d, respectively. We define the diagonal matrices:

$$\Phi \in \mathbb{R}^{n_\phi \times n_\phi}, \quad \text{and} \quad A_u \in \mathbb{R}^{n_{e_u} \times n_{e_u}}, \quad \text{for} \quad u \in \{x, y, z\}, \tag{6.66}$$

which contain $\boldsymbol{\phi}$ and $\boldsymbol{a}_u$ on their diagonal, respectively. The matrix H_s is the static Hamiltonian matrix (5.5) as:

$$H_s = T_x \oplus T_y \oplus T_z + V, \tag{6.67}$$

and H_d is the diagonal matrix:

$$H_d = q\Phi + \frac{q^2}{2m}\Big(B_x^2 + B_y^2 + B_z^2\Big), \tag{6.68}$$

where the matrix B_x contains A_x averaged to the nodes of the grid on its diagonal and likewise for B_y and B_z. This is expressed in matrix notation by introducing the matrices U_x and L_x:

$$U_x = \begin{pmatrix} 0 & 1 & & & \\ & 0 & 1 & & \\ & & \ddots & \ddots & \\ & & & 0 & 1 \\ & & & & 0 \end{pmatrix}_{m_x \times n_x}, \quad \text{and} \quad L_x = \begin{pmatrix} 1 & 0 & & & \\ & 1 & 0 & & \\ & & \ddots & \ddots & \\ & & & 1 & 0 \\ & & & & 1 \end{pmatrix}_{m_x \times n_x}. \tag{6.69}$$

as:

$$\begin{aligned} B_x = \frac{1}{2}\Big(&\Big(L_x \otimes I_{m_y} \otimes I_{m_z}\Big) A_x \Big({L_x}^T \otimes I_{m_y} \otimes I_{m_z}\Big) \\ &+ \Big(U_x \otimes I_{m_y} \otimes I_{m_z}\Big) A_x \Big({U_x}^T \otimes I_{m_y} \otimes I_{m_z}\Big)\Big). \end{aligned} \tag{6.70}$$

The matrix H_1 is given by:

$$\begin{aligned} H_1 = \frac{q\hbar}{2m}\Bigg(&\Big(\big(\delta_x^\star\big)^{-1} U_x \otimes I_{m_y m_z}\Big) A_x \Big({L_x}^T \otimes I_{m_y m_z}\Big) \\ &- \Big(\big(\delta_x^\star\big)^{-1} L_x \otimes I_{m_y m_z}\Big) A_x \Big({U_x}^T \otimes I_{m_y m_z}\Big) \\ &+ \Big(I_{m_x} \otimes \big(\delta_y^\star\big)^{-1} U_y \otimes I_{m_z}\Big) A_y \Big(I_{m_x} \otimes {L_y}^T \otimes I_{m_z}\Big) \\ &- \Big(I_{m_x} \otimes \big(\delta_y^\star\big)^{-1} L_y \otimes I_{m_z}\Big) A_y \Big(I_{m_x} \otimes {U_y}^T \otimes I_{m_z}\Big) \\ &+ \Big(I_{m_x m_y} \otimes \big(\delta_z^\star\big)^{-1} U_z\Big) A_z \Big(I_{m_x m_y} \otimes {L_z}^T\Big) \\ &- \Big(I_{m_x m_y} \otimes \big(\delta_z^\star\big)^{-1} L_z\Big) A_z \Big(I_{m_x m_y} \otimes {U_z}^T\Big)\Bigg). \end{aligned} \tag{6.71}$$

Since (6.71) is not very transparent, $(H_1\boldsymbol{\psi})|_{(i,j,k)}$ is written in scalar notation as:

$$\begin{aligned} (H_1\boldsymbol{\psi})|_{(i,j,k)} = \frac{q\hbar}{2m}\Bigg(&\frac{A_x|_{i+\frac{1}{2},j,k}}{\Delta x_i^\star}\psi|_{i+1,j,k} - \frac{A_x|_{i-\frac{1}{2},j,k}}{\Delta x_i^\star}\psi|_{i-1,j,k} \\ &+ \frac{A_y|_{i,j+\frac{1}{2},k}}{\Delta y_j^\star}\psi|_{i,j+1,k} - \frac{A_y|_{i,j-\frac{1}{2},k}}{\Delta y_j^\star}\psi|_{i,j-1,k} \\ &+ \frac{A_z|_{i,j,k+\frac{1}{2}}}{\Delta z_k^\star}\psi|_{i,j,k+1} - \frac{A_z|_{i,j,k-\frac{1}{2}}}{\Delta z_k^\star}\psi|_{i,j,k-1}\Bigg). \end{aligned} \tag{6.72}$$

Note that (6.72) is a very light-weight discretization of the rather complicated $(q\hbar/2m)(2\boldsymbol{A}\cdot\nabla+(\boldsymbol{\nabla}\cdot\boldsymbol{A}))\psi$ term present in the minimally-coupled Schrödinger equation.

Stability

The stability of the novel scheme for potentials that are constant as a function of time can be readily determined. Analogous to Section 5.3, the update equations are symmetrized using the diagonal transformation matrix Q (4.26). Left multiplication of (6.65) with $I_2 \otimes Q^{1/2}$ results in:

$$\begin{aligned}&\begin{bmatrix} Q^{\frac{1}{2}} & \\ & Q^{\frac{1}{2}} \end{bmatrix}\begin{bmatrix} I_{n_\psi}-\frac{\Delta\eta}{2}H_1 & 0 \\ -\Delta\eta H_0 & I_{n_\psi}-\frac{\Delta\eta}{2}H_1 \end{bmatrix}\begin{bmatrix} Q^{-\frac{1}{2}} & \\ & Q^{-\frac{1}{2}} \end{bmatrix}\tilde{\boldsymbol{x}}|^n \\ &\quad=\begin{bmatrix} Q^{\frac{1}{2}} & \\ & Q^{\frac{1}{2}} \end{bmatrix}\begin{bmatrix} I_{n_\psi}+\frac{\Delta\eta}{2}H_1 & -\Delta\eta H_0 \\ 0 & I_{n_\psi}+\frac{\Delta\eta}{2}H_1 \end{bmatrix}\begin{bmatrix} Q^{-\frac{1}{2}} & \\ & Q^{-\frac{1}{2}} \end{bmatrix}\tilde{\boldsymbol{x}}|^{n-1},\end{aligned} \tag{6.73}$$

which simplifies to the symmetrized update equation:

$$\begin{bmatrix} I_{n_\psi}-\frac{\Delta\eta}{2}\tilde{H}_1 & 0 \\ -\Delta\eta\tilde{H}_0 & I_{n_\psi}-\frac{\Delta\eta}{2}\tilde{H}_1 \end{bmatrix}\tilde{\boldsymbol{x}}|^n=\begin{bmatrix} I_{n_\psi}+\frac{\Delta\eta}{2}\tilde{H}_1 & -\Delta\eta\tilde{H}_0 \\ 0 & I_{n_\psi}+\frac{\Delta\eta}{2}\tilde{H}_1 \end{bmatrix}\tilde{\boldsymbol{x}}|^{n-1}, \tag{6.74}$$

with $\tilde{\boldsymbol{x}}|^n$ defined as (5.17) and

$$\tilde{H}_0=\tilde{T}_x\oplus\tilde{T}_y\oplus\tilde{T}_z+V+q\Phi+\frac{q^2}{2m}\Big(B_x^2+B_y^2+B_z^2\Big), \tag{6.75}$$

$$\begin{aligned}\tilde{H}_1=\frac{q\hbar}{2m}\Bigg(&\Big(\big(\delta_x^\star\big)^{-\frac{1}{2}}U_x\otimes I_{m_ym_z}\Big)A_x\Big({L_x}^T\big(\delta_x^\star\big)^{-\frac{1}{2}}\otimes I_{m_ym_z}\Big)\\&-\Big(\big(\delta_x^\star\big)^{-\frac{1}{2}}L_x\otimes I_{m_ym_z}\Big)A_x\Big({U_x}^T\big(\delta_x^\star\big)^{-\frac{1}{2}}\otimes I_{m_ym_z}\Big)\\&+\Big(I_{m_x}\otimes\big(\delta_y^\star\big)^{-\frac{1}{2}}U_y\otimes I_{m_z}\Big)A_y\Big(I_{m_x}\otimes{L_y}^T\big(\delta_y^\star\big)^{-\frac{1}{2}}\otimes I_{m_z}\Big)\\&-\Big(I_{m_x}\otimes\big(\delta_y^\star\big)^{-\frac{1}{2}}L_y\otimes I_{m_z}\Big)A_y\Big(I_{m_x}\otimes{U_y}^T\big(\delta_y^\star\big)^{-\frac{1}{2}}\otimes I_{m_z}\Big)\\&+\Big(I_{m_xm_y}\otimes\big(\delta_z^\star\big)^{-\frac{1}{2}}U_z\Big)A_z\Big(I_{m_xm_y}\otimes{L_z}^T\big(\delta_z^\star\big)^{-\frac{1}{2}}\Big)\\&-\Big(I_{m_xm_y}\otimes\big(\delta_z^\star\big)^{-\frac{1}{2}}L_z\Big)A_z\Big(I_{m_xm_y}\otimes{U_z}^T\big(\delta_z^\star\big)^{-\frac{1}{2}}\Big)\Bigg).\end{aligned} \tag{6.76}$$

Note that $\tilde{H}_0$ is symmetric and $\tilde{H}_1$ is skew-symmetric. Following again the approach from [27], the update equations (6.65) are cast as $(E+F)\tilde{\boldsymbol{x}}|^n=(E-F)\tilde{\boldsymbol{x}}|^{n-1}$ with:

$$E=\begin{bmatrix} I_{n_\psi} & -\frac{\Delta t}{2\hbar}\tilde{H}_0 \\ -\frac{\Delta t}{2\hbar}\tilde{H}_0 & I_{n_\psi} \end{bmatrix},\quad\text{and}\quad F=\frac{\Delta t}{2\hbar}\begin{bmatrix} -\tilde{H}_1 & \tilde{H}_0 \\ -\tilde{H}_0 & -\tilde{H}_1 \end{bmatrix}. \tag{6.77}$$

Since E is real symmetric and F is real, the scheme is stable if E is positive definite and $F + F^T$ is positive semi-definite. The latter is trivially satisfied because $F + F^T$ is the zero matrix. The former is satisfied if the time step satisfies:

$$\Delta t < \frac{2\hbar}{\left\|\tilde{H}_0\right\|_2}. \tag{6.78}$$

To prove this, consider that E is positive definite if:

$$\boldsymbol{x}^T E \boldsymbol{x} > 0, \quad \forall \boldsymbol{x} \in \mathbb{R}^{2n_\psi} \setminus \mathbf{0}. \tag{6.79}$$

By rewriting E, the positive definiteness condition (6.79) yields:

$$\frac{\Delta t}{2\hbar} \frac{\boldsymbol{x}^T \left(\begin{bmatrix} 0 & 1 \\ 1 & 0 \end{bmatrix} \otimes \tilde{H}_0 \right) \boldsymbol{x}}{\|\boldsymbol{x}\|_2^2} < 1. \tag{6.80}$$

We now use the fact that the maximum eigenvalue $\lambda_{\max}$ of a real symmetric matrix $A \in \mathbb{R}^{n \times n}$ is [28, eq. 8.4.3]:

$$\lambda_{\max}(A) = \max_{\boldsymbol{x} \in \mathbb{R}^{2n} \setminus \mathbf{0}} \frac{\boldsymbol{x}^T A \boldsymbol{x}}{\|\boldsymbol{x}\|_2^2}. \tag{6.81}$$

As such, (6.80) yields:

$$\frac{\Delta t}{2\hbar} \max_{\boldsymbol{x} \in \mathbb{R}^{2n} \setminus \mathbf{0}} \left(\frac{\boldsymbol{x}^T \left(\begin{bmatrix} 0 & 1 \\ 1 & 0 \end{bmatrix} \otimes \tilde{H}_0 \right) \boldsymbol{x}}{\|\boldsymbol{x}\|_2^2} \right) = \frac{\Delta t}{2\hbar} \lambda_{\max} \left(\begin{bmatrix} 0 & 1 \\ 1 & 0 \end{bmatrix} \otimes \tilde{H}_0 \right) \tag{6.82a}$$

$$= \frac{\Delta t}{2\hbar} \rho(\tilde{H}_0) \tag{6.82b}$$

$$= \frac{\Delta t}{2\hbar} \left\|\tilde{H}_0\right\|_2. \tag{6.82c}$$

Consequently, (6.80) yields the stability condition (6.78). In going from equation (6.82a) to (6.82b), we used (5.28b) which states that the eigenvalues of a Kronecker product are the products of the eigenvalues, such that the spectral radius $\rho(H_0) = \max(|\lambda_{\min}(H_0)|, |\lambda_{\max}(H_0)|)$, and to go from (6.82b) to (6.82c) it was used that the matrix 2-norm of a symmetric matrix is equal to its spectral radius. Note that the stability criterion does not include any gradients of potentials but only their magnitude, which are much easier to predict. As such, the obtained criterion is easily applied in simulations.

The stability criterion can again be approximated by using the infinity norm. We assume:

$$v|_{i,j,k} + q\phi|_{i,j,k} + \frac{q^2}{2m} \left(\mathcal{A}|_{i,j,k} \right)^2 \geq -\frac{\hbar^2}{m} \left(\frac{1}{\lambda_{i,j,k}} \right)^2, \tag{6.83}$$

where $\lambda_{i,j,k}$ is defined in (4.33), and

$$\left(\mathcal{A}|_{i,j,k}\right)^2 = \frac{1}{4}\Bigg(\left(A_x|_{i+\frac{1}{2},j,k} + A_x|_{i-\frac{1}{2},j,k}\right)^2 + \left(A_y|_{i,j+\frac{1}{2},k} + A_y|_{i,j-\frac{1}{2},k}\right)^2 + \left(A_z|_{i,j,k+\frac{1}{2}} + A_z|_{i,j,k-\frac{1}{2}}\right)^2\Bigg), \tag{6.84}$$

such that the Courant-like stability condition is given as:

$$\Delta t < \frac{2\hbar}{\max\limits_{i,j,k}\left(\frac{\hbar^2}{m}\left(\frac{1}{\lambda_{i,j,k}}\right)^2 + v|_{i,j,k} + q\phi|_{i,j,k} + \frac{q^2}{2m}\left(\mathcal{A}|_{i,j,k}\right)^2\right)}. \tag{6.85}$$

6.3.2 Higher-order accuracy on uniform grids

In this section, higher-order spatially accurate methods are developed. This is more involved compared to Chapter 4 because we wish that the discretized Hamiltonian $H = H_0 + \jmath H_1$ is Hermitian for two reasons. First, in this way a physical property of the system is directly translated into the discrete realm and second, the stability proof of Section 6.3.1 required that H_1 is skew-symmetric. This property has to hold for arbitrary vector potentials $\boldsymbol{A}$. The update scheme is identical to (6.65) but with a redefinition of H_0 and H_1 to higher-order accurate finite differences. The stability is again guaranteed for Δt satisfying (6.78).

Fourth-order accuracy

The fourth-order accurate spatial discretization of $\hat{H}_0$ can be easily determined. The effect of H_s and H_d on ψ is given by:

$$(H_s\boldsymbol{\psi})|_{(i,j,k)} = -\frac{\hbar^2}{2m}(L\boldsymbol{\psi})|_{(i,j,k)} + v|_{i,j,k}\,\psi|_{i,j,k}, \tag{6.86a}$$

$$(H_d\boldsymbol{\psi})|_{(i,j,k)} = \left(\frac{q^2}{2m}\Bigg(\left((M_x\boldsymbol{a}_x)|_{(i,j,k)}\right)^2 + \left((M_y\boldsymbol{a}_y)|_{(i,j,k)}\right)^2 + \left((M_z\boldsymbol{a}_z)|_{(i,j,k)}\right)^2\Bigg) + q\phi|_{i,j,k}\right)\psi|_{i,j,k}, \tag{6.86b}$$

where L is the higher-order discretized Laplacian L_H (4.10) from Chapter 4 on uniform grids with the coefficients given by:

$$d^x_{-2}|_i = d^x_2|_i = -\frac{1}{12\Delta x^2}, \quad \text{and} \quad d^x_{-1}|_i = d^x_1|_i = \frac{4}{3\Delta x^2}, \tag{6.87}$$

and where $(M_x\boldsymbol{a}_x)|_{(i,j,k)}$ is the fourth-order accurate average of A_x around the point (x_i, y_j, z_k), i.e.:

$$(M_x\boldsymbol{a}_x)|_{(i,j,k)} = \frac{-A_x|_{i-\frac{3}{2},j,k} + 9A_x|_{i-\frac{1}{2},j,k} + 9A_x|_{i+\frac{1}{2},j,k} - A_x|_{i+\frac{3}{2},j,k}}{16}. \tag{6.88}$$

The coefficients for the fourth-order accurate Laplacian and the averages in the y- and z-directions are calculated similarly.

The discretization of H_1 is somewhat more involved. Besides the skew-symmetry condition, the stencil should leverage the vector potential in a symmetric way. This condition implies that if $A_x|_{i+l,j,k}$ is applied to $\psi|_{i+m,j,k}$, then $A_x|_{i-l,j,k}$ is applied to $\psi|_{i-m,j,k}$. By imposing these two conditions, the x-dependent part of H_1 is approximated as:

$$\begin{aligned} 2A_x \frac{\partial \psi}{\partial x} + \left(\frac{\partial A_x}{\partial x}\right)\psi\Big|_{i,j,k} \\ \approx \Big(\beta A_x|_{i+\frac{1}{2},j,k} + \gamma A_x|_{i+\frac{3}{2},j,k}\Big)\psi|_{i+2,j,k} \\ + \Big(\alpha A_x|_{i+\frac{1}{2},j,k} + \delta A_x|_{i+\frac{3}{2},j,k} + \epsilon A_x|_{i-\frac{1}{2},j,k}\Big)\psi|_{i+1,j,k} \\ - \Big(\alpha A_x|_{i-\frac{1}{2},j,k} + \delta A_x|_{i+\frac{1}{2},j,k} + \epsilon A_x|_{i-\frac{3}{2},j,k}\Big)\psi|_{i-1,j,k} \\ - \Big(\beta A_x|_{i-\frac{3}{2},j,k} + \gamma A_x|_{i-\frac{1}{2},j,k}\Big)\psi|_{i-2,j,k}, \end{aligned} \tag{6.89}$$

where the coefficients can be determined by Taylor expanding (6.89), yielding:

$$\alpha = \frac{5}{4\Delta x}, \quad \beta = \gamma = -\frac{1}{12\Delta x}, \quad \text{and} \quad \delta = \epsilon = \frac{1}{24\Delta x}, \tag{6.90}$$

which results in a fourth-order accurate $\mathcal{O}\left(\Delta x^4\right)$ discretization of (6.89). Careful investigation shows that the update equations are indeed skew symmetric.

Sixth-order accuracy

By extending the stencil with two extra points for ψ in the three cardinal directions, the accuracy can be increased from fourth-order accuracy to sixth-order accuracy. The effect of H_s and H_d on ψ is again given by (6.86) but where the matrix L now leverages the well known sixth-order accurate discretization for the Laplacian term as used in, e.g., [31], and where $(M_x \boldsymbol{a}_x)|_{(i,j,k)}$ is the sixth-order accurate average of A_x around (x_i, y_j, z_k), i.e.:

$$(M_x \boldsymbol{a}_x)|_{(i,j,k)} = \sum_{m=-\frac{5}{2}}^{\frac{5}{2}} a_m^x A_x|_{i+m,j,k}, \tag{6.91}$$

with coefficients:

$$a^x_{-\frac{5}{2}} = a^x_{\frac{5}{2}} = \frac{3}{256}, \quad a^x_{-\frac{3}{2}} = a^x_{\frac{3}{2}} = -\frac{25}{256}, \quad \text{and} \quad a^x_{-\frac{1}{2}} = a^x_{\frac{1}{2}} = \frac{75}{128}. \tag{6.92}$$

The averages in the y- and z-directions are calculated similarly.

For the matrix H_1 we use:

$$(H_1\boldsymbol{\psi})|_{(i,j,k)} = (H_1^x\boldsymbol{\psi})|_{(i,j,k)} + (H_1^y\boldsymbol{\psi})|_{(i,j,k)} + (H_1^z\boldsymbol{\psi})|_{(i,j,k)}, \tag{6.93}$$

where

$$\begin{aligned}(H_1^x\boldsymbol{\psi})|_{(i,j,k)} = \frac{9}{640\Delta x}\Big(& h^x_{1,3}|_{i,j,k}\psi|_{i+3,j,k} + h^x_{1,2}|_{i,j,k}\psi|_{i+2,j,k} \\ & + h^x_{1,1}|_{i,j,k}\psi|_{i+1,j,k} + h^x_{1,-1}|_{i,j,k}\psi|_{i-1,j,k} \\ & + h^x_{1,-2}|_{i,j,k}\psi|_{i-2,j,k} + h^x_{1,-3}|_{i,j,k}\psi|_{i-3,j,k}\Big),\end{aligned} \tag{6.94}$$

with coefficients:

$$h^x_{1,3}|_{i,j,k} = \frac{10}{27}A_x|_{i+\frac{3}{2},j,k} + A_x|_{i+\frac{1}{2},j,k} + A_x|_{i+\frac{5}{2},j,k}, \tag{6.95a}$$

$$h^x_{1,2}|_{i,j,k} = -10\Big(A_x|_{i+\frac{1}{2},j,k} + A_x|_{i+\frac{3}{2},j,k}\Big) - \frac{2}{3}\Big(A_x|_{i-\frac{1}{2},j,k} + A_x|_{i+\frac{5}{2},j,k}\Big), \tag{6.95b}$$

$$h^x_{1,1}|_{i,j,k} = \frac{290}{3}A_x|_{i+\frac{1}{2},j,k} + 5\Big(A_x|_{i+\frac{3}{2},j,k} + A_x|_{i-\frac{1}{2},j,k}\Big), \tag{6.95c}$$

$$h^x_{1,-1}|_{i,j,k} = -\frac{290}{3}A_x|_{i-\frac{1}{2},j,k} - 5\Big(A_x|_{i-\frac{3}{2},j,k} + A_x|_{i-\frac{1}{2},j,k}\Big), \tag{6.95d}$$

$$h^x_{1,-2}|_{i,j,k} = 10\Big(A_x|_{i-\frac{1}{2},j,k} + A_x|_{i-\frac{3}{2},j,k}\Big), + \frac{2}{3}\Big(A_x|_{i+\frac{1}{2},j,k} + A_x|_{i-\frac{5}{2},j,k}\Big), \tag{6.95e}$$

$$h^x_{1,-3}|_{i,j,k} = -\frac{10}{27}A_x|_{i-\frac{3}{2},j,k} - A_x|_{i-\frac{1}{2},j,k} - A_x|_{i-\frac{5}{2},j,k}. \tag{6.95f}$$

The discretizations $(H_1^y\boldsymbol{f})|_{(i,j,k)}$ and $(H_1^z\boldsymbol{f})|_{(i,j,k)}$ are determined analogously.

6.3.3 Numerical probability conservation

Since the real and imaginary parts are staggered in time, we need to perform an interpolation to acquire the density. As such, the probability density is calculated as follows [2]:

$$n|^n_{i,j,k} = r|^{n+\frac{1}{2}}_{i,j,k} r|^{n-\frac{1}{2}}_{i,j,k} + \Big(s|^n_{i,j,k}\Big)^2, \tag{6.96}$$

where we have used the geometric instead of the arithmetic mean, with the advantage that it requires less computations. It is also accurate up to second order in time. Moreover, the norm N calculated using this definition for the density is exactly conserved when no EM fields are present.

The norm N of the probability density is defined as:

$$N|^n = \Big(\boldsymbol{r}|^{n+\frac{1}{2}}\Big)^T\Big(\delta_x^\star \otimes \delta_y^\star \otimes \delta_z^\star\Big)\boldsymbol{r}|^{n-\frac{1}{2}} + \Big(\boldsymbol{s}|^n\Big)^T\Big(\delta_x^\star \otimes \delta_y^\star \otimes \delta_z^\star\Big)\boldsymbol{s}|^n \tag{6.97}$$

$$= \Big(\tilde{\boldsymbol{r}}|^{n+\frac{1}{2}}\Big)^T\tilde{\boldsymbol{r}}|^{n-\frac{1}{2}} + \Big(\tilde{\boldsymbol{s}}|^n\Big)^T\tilde{\boldsymbol{s}}|^n, \tag{6.98}$$

where $\tilde{\boldsymbol{r}}$ and $\tilde{\boldsymbol{s}}$ are defined as $\left(\delta_x^\star \otimes \delta_y^\star \otimes \delta_z^\star\right)^{1/2}\boldsymbol{r}$ and $\left(\delta_x^\star \otimes \delta_y^\star \otimes \delta_z^\star\right)^{1/2}\boldsymbol{s}$, respectively. The time evolution of this norm is studied for constant potentials. We define $\Delta\eta\check{H}_0 = \check{H}_0$, and $\Delta\eta\check{H}_1/2 = \check{H}_1$ and insert the symmetrized update equations (6.74) into (6.98), yielding:

$$\begin{aligned} N|^n &= \left(\left(I_{n_\psi} - \check{H}_1\right)^{-1}\left(\check{H}_0\tilde{\boldsymbol{s}}|^n + \left(I_{n_\psi} + \check{H}_1\right)\tilde{\boldsymbol{r}}|^{n-\frac{1}{2}}\right)\right)^T \tilde{\boldsymbol{r}}|^{n-\frac{1}{2}} \\ &\quad + \left(\tilde{\boldsymbol{s}}|^n\right)^T\left(I_{n_\psi} - \check{H}_1\right)^{-1}\left(\left(I_{n_\psi} + \check{H}_1\right)\tilde{\boldsymbol{s}}|^{n-1} - \check{H}_0\tilde{\boldsymbol{r}}|^{n-\frac{1}{2}}\right) \end{aligned} \tag{6.99a}$$

$$\begin{aligned} &= (\tilde{\boldsymbol{s}}^n)^T\left(\check{H}_0\left(I_{n_\psi} + \check{H}_1\right)^{-1} - \left(I_{n_\psi} - \check{H}_1\right)^{-1}\check{H}_0\right)\tilde{\boldsymbol{r}}|^{n-\frac{1}{2}} \\ &\quad + \left(\tilde{\boldsymbol{r}}|^{n-\frac{1}{2}}\right)^T\left(I_{n_\psi} - \check{H}_1\right)\left(I_{n_\psi} + \check{H}_1\right)^{-1}\tilde{\boldsymbol{r}}|^{n-\frac{1}{2}} \\ &\quad + \left(\tilde{\boldsymbol{s}}|^n\right)^T\left(I_{n_\psi} - \check{H}_1\right)^{-1}\left(I_{n_\psi} + \check{H}_1\right)\tilde{\boldsymbol{s}}|^{n-1} \end{aligned} \tag{6.99b}$$

$$\begin{aligned} &= (\tilde{\boldsymbol{s}}^n)^T\left(\check{H}_0\left(I_{n_\psi} + \check{H}_1\right)^{-1} - \left(I_{n_\psi} - \check{H}_1\right)^{-1}\check{H}_0\right)\tilde{\boldsymbol{r}}|^{n-\frac{1}{2}} \\ &\quad + \left(\tilde{\boldsymbol{r}}|^{n-\frac{1}{2}}\right)^T\left(\left(I_{n_\psi} + \check{H}_1\right)^{-1}\check{H}_0 - \check{H}_0\left(I_{n_\psi} - \check{H}_1\right)^{-1}\right)\tilde{\boldsymbol{s}}|^{n-1} \\ &\quad + \left(\tilde{\boldsymbol{r}}|^{n-\frac{1}{2}}\right)^T\tilde{\boldsymbol{r}}|^{n-\frac{3}{2}} + \left(\tilde{\boldsymbol{s}}|^{n-1}\right)^T\tilde{\boldsymbol{s}}|^{n-1}. \end{aligned} \tag{6.99c}$$

Without vector potential ($\check{H}_1 = 0$), the norm is thus exactly conserved:

$$N|^n = \left(\tilde{\boldsymbol{r}}|^{n-\frac{1}{2}}\right)^T\tilde{\boldsymbol{r}}|^{n-\frac{3}{2}} + \left(\tilde{\boldsymbol{s}}|^{n-1}\right)^T\tilde{\boldsymbol{s}}|^{n-1} = N|^{n-1}. \tag{6.100}$$

However, with EM a vector potential, the norm is not exactly conserved. This analysis is equally valid for the fourth- and sixth-order accurate schemes on uniform grids presented in Section 6.3.2. In Section 6.5.1, the norm conservation for the leapfrog scheme is compared to the Crank-Nicolson (CN) method and a collocated-explicit (CE) method based on the scheme presented in Chapter 4.

6.4 Self-consistent coupling

In this section, we discuss the self-consistency of our update schemes. First, the subject of self-consistency for the Kohn-Sham equations in TDDFT is discussed. Second, the fully-coupled scheme with mutual interaction between EM fields and a quantum mechanical system, is analyzed.

6.4.1 Kohn-Sham

In TDDFT, the Kohn-Sham equations constitute a system of many single-particle Schrödinger equations where the exchange-correlation $v_{\text{xc}}[n]$ and Hartree $v_H[n]$ potentials are determined self-consistently. In the following, we write everything only for a single wave function to not complicate notation too much. However,

as explained in Section 2.3, the total probability density n (2.52) or probability current density J_p (2.59) is obtained by summing the densities of the individual wave functions, e.g.:

$$n|^n_{i,j,k} = \sum_m n_m|^n_{i,j,k} = \sum_m r_m|^{n+\frac{1}{2}}_{i,j,k} r_m|^{n-\frac{1}{2}}_{i,j,k} + \left(s_m|^n_{i,j,k}\right)^2, \tag{6.101}$$

where the subscript m labels the individual single-particle wave functions.

Since TDDFT does not accommodate magnetic fields, the leapfrog scheme (6.65) is used without a vector potential:

$$\boldsymbol{r}|^{n+\frac{1}{2}} = \boldsymbol{r}|^{n-\frac{1}{2}} + \Delta\eta H_0|^n \boldsymbol{s}|^n, \tag{6.102a}$$

$$\boldsymbol{s}|^{n+1} = \boldsymbol{s}|^n - \Delta\eta H_0|^{n-\frac{1}{2}} \boldsymbol{r}|^{n+\frac{1}{2}}. \tag{6.102b}$$

However, to determine $H_0|^n$ in (6.102a) the still unknown density n at $t = n\Delta t$ is required. This discrepancy can be addressed by extrapolating the density or by using a predictor-corrector scheme. Alternatively, the probability density is predicted from the probability current density using the continuity equation, which is discretized as:

$$n|^n_{i,j,k} = n|^{n-1}_{i,j,k} - \Delta t\Big((C_x \boldsymbol{j}_{p,x})|^{n-\frac{1}{2}}_{(i,j,k)} + (C_y \boldsymbol{j}_{p,y})|^{n-\frac{1}{2}}_{(i,j,k)} + (C_z \boldsymbol{j}_{p,z})|^{n-\frac{1}{2}}_{(i,j,k)}\Big), \tag{6.103}$$

where $\boldsymbol{j}_{p,x}$ is the x-directed row-major vectorized probability current density and $(C_x \boldsymbol{j}_{p,x})|^n_{i,j,k}$ is the derivative in the x-direction of $J_{x,p}$ centered at (x_i, y_j, z_k). For a nonuniform grid, C_x is given by:

$$C_x = \left(\delta^\star_x\right)^{-1} D_x, \tag{6.104}$$

with D_x defined in (4.24). On a uniform grid, the fourth- or sixth-order accurate differences can be used such that:

$$(C_x \boldsymbol{j}_{p,x})|_{(i,j,k)} = \sum_m g^x_m J_{p,x}|_{i+m}, \tag{6.105}$$

where the coefficients are given in Table 6.1. The y- and z-directed terms are calculated analogously.

The probability current is calculated from (2.24) which can be rewritten in terms of the real and imaginary parts of the wave function as:

$$\boldsymbol{J}_p = \frac{\hbar}{m}(r\boldsymbol{\nabla}s - s\boldsymbol{\nabla}r). \tag{6.106}$$

The spatial discretization of (6.106) for the x-component is given by:

$$\begin{aligned} J_{p,x}|^{n-\frac{1}{2}}_{i+\frac{1}{2},j,k} = \frac{\hbar}{m}\Big(&(M^\star_x \boldsymbol{r})|^{n-\frac{1}{2}}_{(i+\frac{1}{2},j,k)} (G^\star_x \boldsymbol{s})|^{n-\frac{1}{2}}_{(i+\frac{1}{2},j,k)} \\ &- (M^\star_x \boldsymbol{s})|^{n-\frac{1}{2}}_{(i+\frac{1}{2},j,k)} (G^\star_x \boldsymbol{r})|^{n-\frac{1}{2}}_{(i+\frac{1}{2},j,k)}\Big), \end{aligned} \tag{6.107}$$

Table 6.1: The coefficients for the approximate derivative used in (6.105) for the fourth- and sixth-order accurate schemes on a uniform grid are determined using traditional finite-difference methods.

	$g^x_{-5/2}$	$g^x_{-3/2}$	$g^x_{-1/2}$	$g^x_{1/2}$	$g^x_{3/2}$	$g^x_{5/2}$
4th order	0	$\frac{1}{24\Delta x}$	$-\frac{27}{24\Delta x}$	$\frac{27}{24\Delta x}$	$-\frac{1}{24\Delta x}$	0
6th order	$-\frac{3}{640\Delta x}$	$\frac{25}{384\Delta x}$	$-\frac{75}{64\Delta x}$	$\frac{75}{64\Delta x}$	$-\frac{25}{384\Delta x}$	$\frac{3}{640\Delta x}$

where $(M^\star_x \boldsymbol{r})|_{(i+\frac{1}{2},j,k)}$ and $(G^\star_x \boldsymbol{r})|_{(i+\frac{1}{2},j,k)}$ are the average and gradient in the x-direction of r (similar for s) around $(x_{i+\frac{1}{2}}, y_j, z_k)$, respectively. These are given by:

$$(M^\star_x \boldsymbol{r})|_{(i+\frac{1}{2},j,k)} = \sum_m a^x_m r|_{i+\frac{1}{2}+m}, \tag{6.108a}$$

$$(G^\star_x \boldsymbol{r})|_{(i+\frac{1}{2},j,k)} = \sum_m g^x_m r|_{i+\frac{1}{2}+m}. \tag{6.108b}$$

For the nonuniform case, a two-point average is considered, resulting in:

$$J_{p,x}|^{n-\frac{1}{2}}_{i+\frac{1}{2},j,k} = \frac{\hbar}{m\Delta x_{i+1}}\Bigg(r|^{n-\frac{1}{2}}_{i,j,k}\Big(s|^n_{i+1,j,k} + s|^{n-1}_{i+1,j,k}\Big) - \Big(s|^n_{i,j,k} + s|^{n-1}_{i,j,k}\Big) r|^{n-\frac{1}{2}}_{i+1,j,k}\Bigg). \tag{6.109}$$

The coefficients for the fourth- and sixth-order accurate schemes on a uniform grid are given in Table 6.2. Note that the derivative coefficients g^x_m for uniform grid are the same as used in (6.105). The imaginary part s of the wave function in (6.107) is interpolated via:

$$s|^{n-\frac{1}{2}}_{i,j,k} = \frac{1}{2}\Big(s|^n_{i,j,k} + s|^{n-1}_{i,j,k}\Big). \tag{6.110}$$

The probability current densities in the y- and z-directions are computed analogously.

In (6.102b), we also need the density at a point in the future. This is addressed in the same way, using:

$$J_{p,x}|^n_{i+\frac{1}{2},j,k} = \frac{\hbar}{m}\Bigg((M^\star_x \boldsymbol{r})|^n_{(i+\frac{1}{2},j,k)} (G^\star_x \boldsymbol{s})|^n_{(i+\frac{1}{2},j,k)} - (M^\star_x \boldsymbol{s})|^n_{(i+\frac{1}{2},j,k)} (G^\star_x \boldsymbol{r})|^n_{(i+\frac{1}{2},j,k)}\Bigg), \tag{6.111}$$

and

$$n|^{n+\frac{1}{2}}_{i,j,k} = n|^{n-\frac{1}{2}}_{i,j,k} - \Delta t\Big((C_x \boldsymbol{j}_{p,x})|^n_{(i,j,k)} + (C_y \boldsymbol{j}_{p,y})|^n_{(i,j,k)} + (C_z \boldsymbol{j}_{p,z})|^n_{(i,j,k)}\Big), \tag{6.112}$$

Table 6.2: The averaging coefficients used in (6.108) for the fourth- and sixth-order accurate schemes on a uniform grid are determined using traditional finite-difference methods.

	$a^x_{-5/2}$	$a^x_{-3/2}$	$a^x_{-1/2}$	$a^x_{1/2}$	$a^x_{3/2}$	$a^x_{5/2}$
4th order	0	$-\frac{1}{16}$	$\frac{9}{16}$	$\frac{9}{16}$	$-\frac{1}{16}$	0
6th order	$\frac{3}{256}$	$-\frac{25}{256}$	$\frac{75}{128}$	$\frac{75}{128}$	$-\frac{25}{256}$	$\frac{3}{256}$

where now the real part of the wave function r is interpolated as:

$$r|^n_{i,j,k} = \frac{1}{2}\left(r|^{n+\frac{1}{2}}_{i,j,k} + r|^{n-\frac{1}{2}}_{i,j,k}\right). \tag{6.113}$$

As such, we calculate a probability current density every half time step, and store two probability densities, i.e., one at integer time steps and one at half-integer time steps.

6.4.2 Maxwell-Schrödinger and Maxwell-Kohn-Sham

Electromagnetic fields influence the behavior of quantum systems through minimal coupling. In turn, the quantum system acts as a source for the EM fields. In order to compute the combined behavior, the Yee scheme (6.4) for EM and the leapfrog scheme for QM have to be unified into a single computational framework.

As explained in Section 2.4, the quantum current density $\boldsymbol{J}_q$ links the QM system back to the EM fields. Therefore, the discretization of $\boldsymbol{J}_q$ should be done accurately. Also, due to the presence of EM fields, the probability current density needs to be altered to (2.41) which results in the discretized probability current density:

$$\begin{aligned}\boldsymbol{j}_{p,x}|^{n-\frac{1}{2}} = \frac{\hbar}{m}\Big((M^\star_x \boldsymbol{r}|^{n-\frac{1}{2}}) \circ (G^\star_x \boldsymbol{s}|^{n-\frac{1}{2}}) - (M^\star_x \boldsymbol{s}|^{n-\frac{1}{2}}) \circ (G^\star_x \boldsymbol{r}|^{n-\frac{1}{2}})\Big) \\ - \frac{q}{m}\boldsymbol{a}_x|^{n-\frac{1}{2}} \circ (M^\star_x \boldsymbol{n}|^{n-\frac{1}{2}}),\end{aligned} \tag{6.114}$$

where $\circ$ is the Hadamard or point-wise product, and the row-major vectorized probability density $\boldsymbol{n}|^{n-\frac{1}{2}}$ is determined as:

$$\boldsymbol{n}|^{n-\frac{1}{2}} = \boldsymbol{r}|^{n-\frac{1}{2}} \circ \boldsymbol{r}|^{n-\frac{1}{2}} + \boldsymbol{s}|^{n} \circ \boldsymbol{s}|^{n-1}. \tag{6.115}$$

To determine the quantum current density, we need to consider how the Yee algorithm (6.4) treats current sources. Although the Yee scheme only leverages Maxwell's curl equations (2.2), the divergence equations (2.3) are nonetheless automatically satisfied on a discrete level as long as the source is charge conserving.

Consider the discrete version of Gauss's electric law in free space:

$$\rho|^n_{i,j,k} = \epsilon_0 \left(\frac{E_x|^n_{i+\frac{1}{2},j,k} - E_x|^n_{i-\frac{1}{2},j,k}}{\Delta x^\star_i} + \frac{E_y|^n_{i,j+\frac{1}{2},k} - E_y|^n_{i,j-\frac{1}{2},k}}{\Delta y^\star_j} + \frac{E_z|^n_{i,j,k+\frac{1}{2}} - E_z|^n_{i,j,k-\frac{1}{2}}}{\Delta z^\star_k} \right). \tag{6.116}$$

By using the discretized Ampère's law from (6.4) to rewrite (6.116) in terms of $\boldsymbol{E}$ at $t = (n-1)\Delta t$, and $\boldsymbol{H}$ and $\boldsymbol{J}$ at $t = (n-1/2)\Delta t$ yields[2]:

$$\rho|^n_{i,j,k} = \rho|^{n-1}_{i,j,k} - \Delta t \left(\frac{J_x|^{n-\frac{1}{2}}_{i+\frac{1}{2},j,k} - J_x|^{n-\frac{1}{2}}_{i-\frac{1}{2},j,k}}{\Delta x^\star_i} + \frac{J_y|^{n-\frac{1}{2}}_{i,j+\frac{1}{2},k} - J_y|^{n-\frac{1}{2}}_{i,j-\frac{1}{2},k}}{\Delta y^\star_j} + \frac{J_z|^{n-\frac{1}{2}}_{i,j,k+\frac{1}{2}} - J_z|^{n-\frac{1}{2}}_{i,j,k-\frac{1}{2}}}{\Delta z^\star_k} \right). \tag{6.117}$$

To have a consistently coupled scheme, the probability density and (quantum) charge density should be related by $\rho_q|_{i,j,k} = qn|_{i,j,k}$. As such, (6.117) has to be reconciled with (6.103). In the nonuniform case with only a two point stencil, we can simply set:

$$\boldsymbol{j}_q = q\boldsymbol{j}_p, \tag{6.118}$$

where $\boldsymbol{j}_q$ is the row-major vectorized current density source in (6.4).

However, the higher-order accurate continuity equation on a uniform grid for the Schrödinger equation (6.103) predicts a different density than (6.117) if we would simply apply (6.118). To solve this discrepancy, the second-order accurate divergence of $\boldsymbol{j}_q$ is equated with the higher-order accurate divergence of $\boldsymbol{j}_p$:

$$\frac{J_{q,x}|^{n-\frac{1}{2}}_{i+\frac{1}{2},j,k} - J_{q,x}|^{n-\frac{1}{2}}_{i-\frac{1}{2},j,k}}{\Delta x} = q \sum_{m=-\frac{M-1}{2}}^{\frac{M-1}{2}} g^x_m J_{p,x}|^{n-\frac{1}{2}}_{i+m,j,k}. \tag{6.119}$$

We further expand $\boldsymbol{j}_q$ in terms of $\boldsymbol{j}_p$:

$$J_{q,x}|^{n-\frac{1}{2}}_{i+\frac{1}{2},j,k} = q \sum_{l=-\frac{L-1}{2}+1}^{\frac{L-1}{2}} \Delta x\, d^x_l\, J_{p,x}|^{n-\frac{1}{2}}_{i+l,j,k}. \tag{6.120}$$

Plugging (6.120) into (6.119) yields:

$$\sum_{m=-\frac{M-1}{2}}^{\frac{M-1}{2}} g^x_m J_{p,x}|^{n-\frac{1}{2}}_{i+m,j,k} = \sum_{l=-\frac{L-3}{2}}^{\frac{L-1}{2}} d^x_l J_{p,x}|^{n-\frac{1}{2}}_{i+l,j,k} - \sum_{l=-\frac{L-3}{2}}^{\frac{L-1}{2}} d^x_l J_{p,x}|^{n-\frac{1}{2}}_{i+l-1,j,k}. \tag{6.121}$$

[2]This is because FDTD preserves the exact sequence of the de Rham complex [32, 33].

Table 6.3: The coefficients for calculating the quantum current density $\boldsymbol{j}_q$ from the probability current density $\boldsymbol{j}_p$ for the fourth- and sixth-order accurate schemes on a uniform grid are determined using traditional finite-difference methods.

	$d^x_{-3/2}$	$d^x_{-1/2}$	$d^x_{1/2}$	$d^x_{3/2}$	$d^x_{5/2}$
4th order	0	$-\frac{1}{24\Delta x}$	$\frac{26}{24\Delta x}$	$-\frac{1}{24\Delta x}$	0
6th order	$\frac{3}{640\Delta x}$	$-\frac{29}{480\Delta x}$	$\frac{1067}{960\Delta x}$	$-\frac{29}{480\Delta x}$	$\frac{3}{640\Delta x}$

Shifting the summation index results in:

$$\sum_{m=-\frac{M-1}{2}}^{\frac{M-1}{2}} g^x_m J_{p,x}|^{n-\frac{1}{2}}_{i+m,j,k} = \sum_{l=-\frac{L-1}{2}+1}^{\frac{L-1}{2}} d^x_l J_{p,x}|^{n-\frac{1}{2}}_{i+l,j,k} - \sum_{l=-\frac{L-1}{2}}^{\frac{L-1}{2}-1} d^x_{l+1} J_{p,x}|^{n-\frac{1}{2}}_{i+l,j,k}, \quad (6.122)$$

which simplifies to:

$$\begin{aligned}\sum_{m=-\frac{M-1}{2}}^{\frac{M-1}{2}} g^x_m J_{p,x}|^{n-\frac{1}{2}}_{i+m,j,k} = \sum_{l=-\frac{L-3}{2}}^{\frac{L-3}{2}} \left(d^x_l - d^x_{l+1}\right) J_{p,x}|^{n-\frac{1}{2}}_{i+l,j,k} \\ - d^x_{-\frac{L-3}{2}} J_{p,x}|^{n-\frac{1}{2}}_{i-\frac{L-1}{2}} + d^x_{\frac{L-1}{2}} J_{p,x}|^{n-\frac{1}{2}}_{i+\frac{L-1}{2}}.\end{aligned} \quad (6.123)$$

Equating the coefficients for $J_{p,x}$ yields:

$$d^x_m = d^x_{m+1} + g^x_m \quad \text{for} \quad m = \left\{-\frac{M-3}{2}, \ldots, \frac{M-3}{2}\right\}, \quad (6.124)$$

with

$$d^x_{\frac{M-1}{2}} = g^x_{\frac{M-1}{2}}. \quad (6.125)$$

The resulting coefficients for the fourth- and sixth-order accurate discretizations are summarized in Table 6.3. Using this averaging, the charge density ρ calculated with (6.116) is the same as the charge density qn calculated with (6.103).

The fully coupled schemes for the Coulomb, Lorenz, and Gibbs gauges are summarized in Fig. 6.2. To update $\boldsymbol{r}|^{n+\frac{1}{2}}$ the vector potential $\boldsymbol{a}_x|^n$ is averaged in time and to update $\boldsymbol{j}_p|^n$ we use:

$$\begin{aligned}\boldsymbol{j}_{p,x}|^n = \frac{\hbar}{m}\Big((M^\star_x \boldsymbol{r}|^n) \circ (G^\star_x \boldsymbol{s}|^n) - (M^\star_x \boldsymbol{s}|^n) \circ (G^\star_x \boldsymbol{r}|^n) \Big) \\ - \frac{q}{m} \boldsymbol{a}_x|^n \circ \left(M^\star_x \boldsymbol{n}|^n\right),\end{aligned} \quad (6.126)$$

where $\boldsymbol{a}|^n$ and $\boldsymbol{r}|^n$ have to be averaged in time. The Gibbs gauge scheme requires the least amount of computations since no scalar potential has to be calculated.

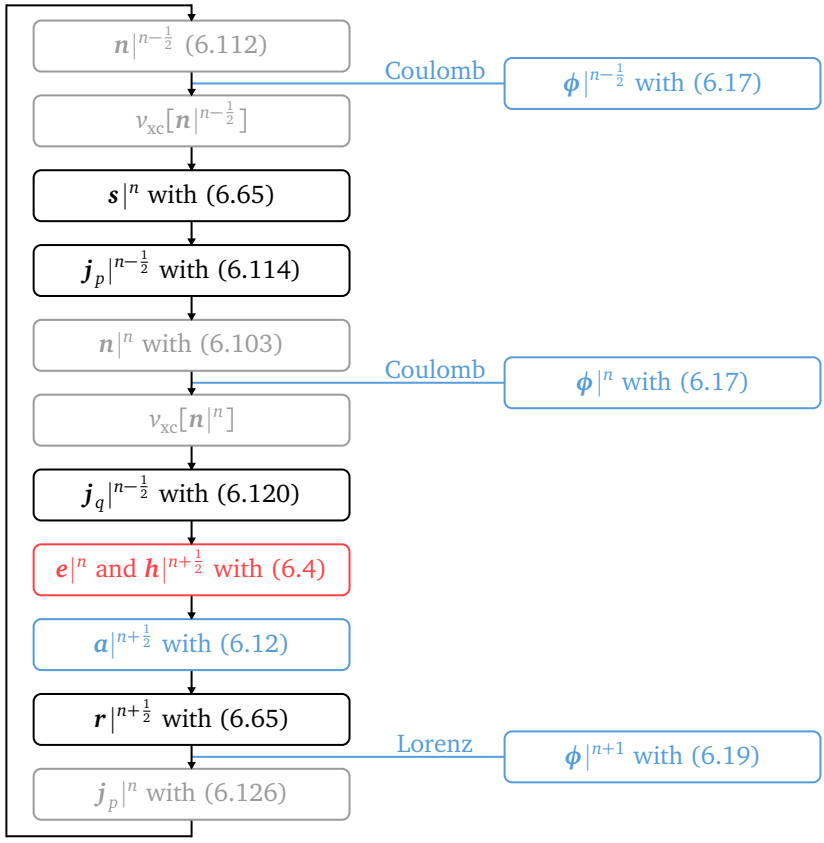

Figure 6.2: The flowchart shows all the steps required for performing a single iteration of the FDTD scheme for a Maxwell-Kohn-Sham system. For the Gibbs gauge the left column can be followed straight down, while the Coulomb gauge and Lorenz gauge require extra steps. The black and grey boxes concern the quantum system, the red box is the Yee algorithm and the blue fields are the updates for the EM potentials. In case no exchange-correlation potential is applied, the grey boxes can be omitted for the Lorenz and Gibbs gauges.

For the Coulomb gauge, the scalar potential $\boldsymbol{\phi}$ is computed with the biconjugate gradient stabilized (BiCGSTAB) method with multipole correction (6.17) twice per iteration. Even though the previous solution is taken as initial guess, this still takes up a large portion of the computational time. For the Lorenz gauge, the update for $\boldsymbol{s}|^{n}$ has to average $\boldsymbol{\phi}|^{n-1/2}$ in time. However, the update equation for $\boldsymbol{\phi}|^{n+1}$ with (6.19) is explicit and only has to be performed once per iteration, making it much faster than the Coulomb gauge.

Furthermore, in the Lorenz and Gibbs gauge, if no exchange-correlation potential is used, self-consistency is automatically achieved without using the continuity equation. Consequently, the grey boxes in Fig. 6.2 can be omitted resulting in a more compact and efficient scheme. In contrast, only the calculation of v_{xc} can be skipped when using the Coulomb gauge.

6.5 Results

In this section, we discuss the results obtained for the minimally-coupled update scheme for the Schrödinger equation and also those obtained for coupled EM-QM systems. The results for the minimally-coupled scheme were run on an Intel(R) Xeon(R) CPU E5-2650 v2 @ 2.60 GHz with 125 GiB of RAM memory and the methods were implemented in Python 2.7.17. The results for coupled EM-QM systems were run on an Intel(R) Xeon(R) Gold 6226 CPU @ 2.70 GHz with 512 GiB of RAM memory and the methods were implemented in C code.

6.5.1 The harmonic oscillator

In this section, we simulate a particle in a harmonic oscillator (HO) like in Section 4.5.3. First, some prescribed EM potentials are applied to the particle and we compare the presented method to solve the minimally-coupled Schrödinger equation to two other methods that are described in Appendix 6.A.2, i.e., the CE and the CN method. Second, the particle in a HO is fully coupled with the electromagnetic field and the influence of the gauge condition is discussed.

Applied potentials

Two sets of simulations are performed. First, a uniform magnetic field is applied. Second, the gauge invariance of the different schemes is tested without EM fields ($\boldsymbol{E} = 0$, $\boldsymbol{B} = 0$), but where the EM potentials are nonetheless nonzero.

The HO described in Section 4.5.3 is considered but the particle is initialized as a coherent state centered at $x = 2\,\mathrm{nm}$, $y = z = 0\,\mathrm{nm}$. A grid of $20\,\mathrm{nm} \times 15\,\mathrm{nm} \times 15\,\mathrm{nm}$ is constructed consisting of $40 \times 30 \times 30$ uniform cells. Additionally, the particle is placed in a z-directed magnetic field with strength $B = 450.617 \times 10^{-6}\,\mathrm{a\,u} = 105.895\,\mathrm{T}$. The vector potential is given by:

$$\boldsymbol{A} = -yB\boldsymbol{u}_x. \tag{6.127}$$

To verify the long-time accuracy of the schemes with different spatially accurate discretizations, we perform a simulation of 120 fs. The classically predicted path for the particle in this applied magnetic field results in a star shaped trajectory in the xy-plane. In Fig. 6.3, it is shown that the higher-order accurate schemes

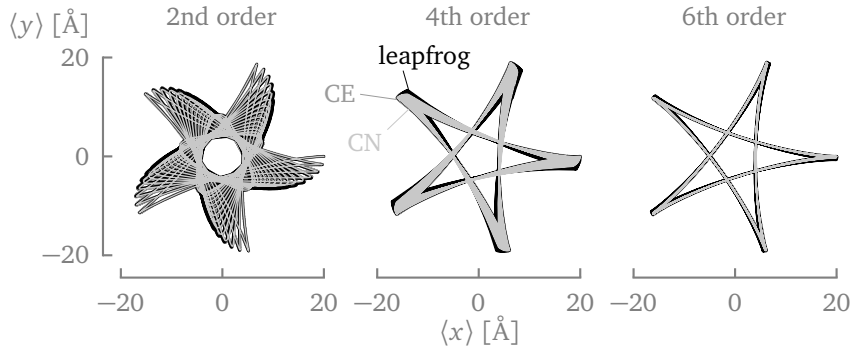

Figure 6.3: The classically predicted star-shaped path of a particle in a magnetic field can be predicted more accurately with higher-order accurate spatial differences. The leapfrog, collocated-explicit (CE) and Crank-Nicolson (CN) schemes yield very similar results.

converge to the classical path. Moreover, the results for all three time integration schemes are very similar.

Now we check gauge invariance with the following applied potentials $(\boldsymbol{A}_1, \phi_1)$ and $(\boldsymbol{A}_2, \phi_2)$ which do not give rise to an electric or magnetic field:

$$\boldsymbol{A}_1 = a_1\big(y\boldsymbol{u}_x + x\boldsymbol{u}_y\big)f(t), \quad \text{and} \quad \phi_1 = -xya_1\frac{\mathrm{d}f}{\mathrm{d}t}, \tag{6.128}$$

and

$$\begin{aligned}\boldsymbol{A}_2 &= a_2\left(\cos\left(\pi\frac{x}{L_x}\right)\boldsymbol{u}_x + \cos\left(\pi\frac{y}{L_y}\right)\boldsymbol{u}_y + \cos\left(\pi\frac{z}{L_z}\right)\boldsymbol{u}_z\right)f(t),\\ \phi_2 &= -\frac{a_2}{\pi}\left(L_x\sin\left(\pi\frac{x}{L_x}\right) + L_y\sin\left(\pi\frac{y}{L_y}\right) + L_z\sin\left(\pi\frac{z}{L_z}\right)\right)\frac{\mathrm{d}f}{\mathrm{d}t},\end{aligned} \tag{6.129}$$

with $f(t)$ a ramped unit step function at $t_0 = 5.0\,\mathrm{fs}$ and $a_1 = 250.0\times10^{-6}\,\mathrm{a\,u}$ and $a_2 = 5.0\times10^{-2}\,\mathrm{a\,u}$ for (6.128) and (6.129), respectively. In theory, the amplitude of $\boldsymbol{A}$ and ϕ is irrelevant since they do not result in an electric or magnetic field. However, the numerical schemes will not exactly obey the gauge invariance. Therefore, note that the Cartesian components of $\boldsymbol{A}_1$ are similar in magnitude to the magnetic field case (6.127). The simulations leverage the sixth-order accurate spatial discretization and are run for 20 fs.

The theoretical trajectory for both $(\boldsymbol{A}_1, \phi_1)$ and $(\boldsymbol{A}_2, \phi_2)$ is an oscillation in the x-direction according to (4.A.6). However, the gauge transformations will induce deviations from the theoretical trajectory caused by the discretization. As expected, in Fig. 6.4(a), we can see that the potentials $(\boldsymbol{A}_1, \phi_1)$ cause a deviation in the

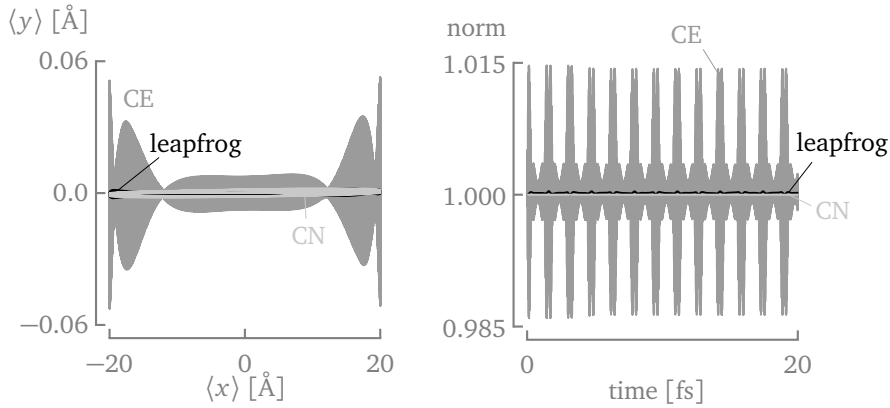

(a) Trajectory in xy-plane.

(b) Calculated norm.

Figure 6.4: The trajectory and norm for the potentials $\boldsymbol{A}_1$ and ϕ_1 from (6.128) show that the leapfrog and CN schemes are more robust to a change of gauge compared to the CE method and conserve the norm better. Sixth-order accurate differences were used for all schemes.

y-position for all three time-integration schemes. However, the deviation is much larger for the CE scheme than for the CN and leapfrog schemes. Moreover, in Fig. 6.4(b), it is shown that the norm for the CE schemes oscillates rapidly, while the norm for the leapfrog scheme and CN schemes is much better conserved.

In Fig. 6.5, the trajectory and norm are shown for the potentials $\boldsymbol{A}_2$ and ϕ_2. After $t_0 = 5\,\mathrm{fs}$, the trajectory changes from oscillating in the x-direction to an elliptical motion for all three schemes. However, the CE scheme exhibits again strong oscillations between time steps on top of this orbital motion. Interestingly, the norm of the CE scheme oscillates less after the potentials are applied. Still, the leapfrog and CN oscillate even less strongly.

Maxwell-Schrödinger system

We now study the fully coupled case, where external EM fields excite a QM system which in turn influences the EM fields. The particle is initialized as the ground state of the HO and a y-polarized plane wave traveling in the x-direction is used as an EM source. The temporal profile of the source is given by:

$$E_y^{\text{source}}(t) = -E_0\sqrt{2}e^{\frac{1}{2}}\frac{t-t_0}{t_w}\exp\left(-\left(\frac{t-t_0}{t_w}\right)^2\right), \tag{6.130}$$

with $E_0 = 1.0\times10^{-3}\,\mathrm{a\,u} = 514.2\,\mathrm{MV\,m^{-1}}$, $t_0 = 4\,\mathrm{fs}$, and $t_w = 1.008\,\mathrm{fs}$. The value of t_w ensures that the bandwidth of the source $b_w = 2/\pi t_w$ is twice the natural

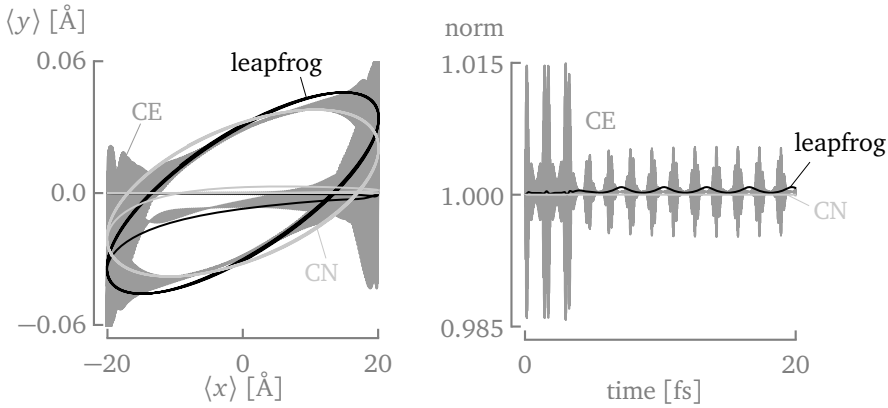

(a) Trajectory in xy-plane.

(b) Calculated norm.

Figure 6.5: The trajectory and norm for the potentials $\boldsymbol{A}_2$ and ϕ_2 from (6.129) show that the CE scheme exhibits strong oscillations but the overall trajectory is closer to the leapfrog and CN schemes compared to the potentials $\boldsymbol{A}_1$ and ϕ_1. Note that, surprisingly, the norm of the CE scheme is better conserved after the potentials are applied. Sixth-order accurate differences were used for all schemes.

oscillating frequency $f = 3.158 \times 10^{14}$ Hz of the HO. For the particle in the HO, a grid of 50 cells in every direction is constructed with uniform cells of $\Delta x = \Delta y = \Delta z = 0.5$ nm. For the EM fields and potentials, a larger grid consisting of 60 cells in every direction is considered to accommodate a total-field scattered-field (TFSF) source, which is additionally terminated by 5 PML layers in every direction.

We run the simulation for 50 fs with a time step equal to $\Delta t = 9.629\,166 \times 10^{-4}$ fs. The results are summarized in Fig. 6.6. The x- and y-positions and the total energy are plotted as a function of time calculated with the Coulomb, Gibbs, and Lorenz gauges. The total energy (2.72) at $t = 0$ is shifted to zero. First, we can see that the Gibbs gauge quickly starts to deviate from the Coulomb, and Lorenz gauges and eventually, the simulation becomes unstable. It is expected that this occurs mainly due to the integrating effect of the Gibbs gauge (6.18). Large values of the vector potential result in larger errors for the Schrödinger equation which are again used as source terms. Eventually, these errors accumulate and result in an unstable scheme. Next, even though a y-polarized plane wave was used, there is a small, yet noticeable oscillation in the x-direction. This can be explained by considering that the magnetic field of the plane wave generates a magnetic force $\boldsymbol{F}_M = q\boldsymbol{v} \times \boldsymbol{B}$, with $\boldsymbol{v}$ the velocity of the particle. As such, we get an x-directed force $F_x = qv_yB_z$. Since v_y first has to increase, the oscillation in the x-direction shows a small initial delay compared to the y-direction. Then, at around 4 fs, E_y, B_z, and v_y switch sign such that the sign of F_x stays the same, which explains the "double hump" in the x-position. Lastly, the total energy in both the Coulomb and

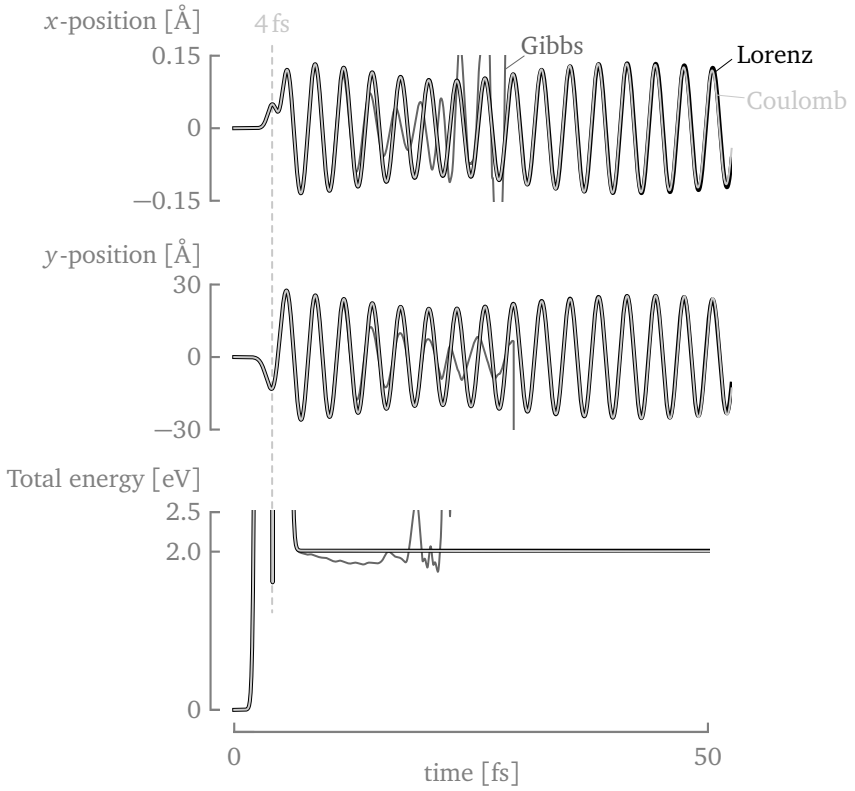

Figure 6.6: The harmonic oscillator Maxwell-Schrödinger system is simulated using the Coulomb, Gibbs, and Lorenz gauge conditions. The Coulomb and Lorenz gauges yield very similar results but the Gibbs gauge quickly diverges and becomes unstable.

Lorenz gauge attains a constant value after the source has died out. This attests to their accuracy.

The Coulomb and Lorenz gauges mainly differ in their calculation of the scalar EM potential ϕ which results in different computation times T_{CPU} as detailed in Table 6.4. The Coulomb gauge is more than 36 times slower than the Lorenz gauge because the former has to solve the Poisson equation at every iteration.

6.5.2 A jellium model for atomic clusters

In this section, a metallic cluster is simulated using a jellium model. A spherical jellium cluster consists of N interacting electrons moving in an external potential of a homogeneously charged sphere with a positive background charge. The positive

Table 6.4: The simulation times for the harmonic oscillator Maxwell-Schrödinger system.

gauge condition	T_{CPU}
Coulomb	4524 min
Gibbs	110 min
Lorenz	124 min

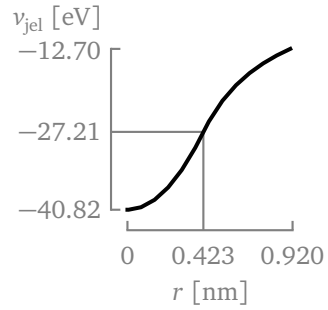

Figure 6.7: The electrostatic potential energy v_{jel} of an electron in a positive background charge is shown as a function of the radial distance r. The parameters in (6.132) are $r_s = 4$ and $Z = 8$, resulting in $R = 0.423\,\text{nm}$.

background charge is distributed as:

$$n_+(r) = n_0 \Theta(|R - r|), \tag{6.131}$$

with Θ the Heaviside function and R the cluster radius. The electrostatic potential energy of an electron in this background charge is given by:

$$v_{\text{jel}}(r) = \begin{cases} \frac{3e^2 Z}{8\pi\epsilon_0 R^3}\left(\frac{r^2}{3} - R^2\right), & \text{for} \quad r < R, \\ \frac{e^2 Z}{4\pi\epsilon_0 r}, & \text{elsewhere,} \end{cases} \tag{6.132}$$

with Z the total charge of the ionic background. For the neutral clusters that we discuss here, $Z = N$ and $R = N^{1/3} a_0 r_s$ where the Wigner-Seitz radius is defined as:

$$n_0 = \frac{3}{4\pi r_s^3 a_0^3}, \tag{6.133}$$

with n_0 the density of the homogeneous electron gas and a_0 the Bohr radius.

The example treated here is a cluster with $r_s = 4$ and $Z = 8$ such that $R = 0.423\,\text{nm}$. The electrostatic potential v_{jel} is illustrated in Fig. 6.7. A grid of 24 cells in every direction is constructed with uniform cells of $\Delta x = \Delta y = \Delta z = 0.0756\,\text{nm}$. This

Table 6.5: The simulation times for the jellium Maxwell-Kohn-Sham system.

gauge condition	T_{CPU}
Coulomb	3678 min
Gibbs	152 min
Lorenz	158 min

system is excited by a y-polarized plane wave traveling in the x-direction with a Gaussian-modulated sine wave temporal profile:

$$E_y^{\mathrm{source}}(t) = E_0 \sin(2\pi f_c(t-t_0)) \exp\left(-\left(\frac{t-t_0}{t_w}\right)^2\right), \tag{6.134}$$

with $E_0 = 2\times10^{-4}\,\mathrm{a\,u} = 102.8\,\mathrm{MV\,m^{-1}}$, $f_c = 6.315\times10^{14}\,\mathrm{Hz}$, $t_0 = 10\,\mathrm{fs}$, and $t_w = 2.016\,\mathrm{fs}$. With this value of t_w, the bandwidth is equal to half the central frequency. For the EM fields and potentials, a larger grid consisting of 32 cells in every direction is considered to accommodate a total-field scattered-field (TFSF) source, which is additionally terminated by 5 PML layers in every direction. The simulation is run for 50 fs with a time step $\Delta t = 1.455\,867\times10^{-4}\,\mathrm{fs}$. In Fig. 6.8, the x- and y-directed dipole moments:

$$d_x(t) = \int x\, n(t)\,\mathrm{d}\boldsymbol{r}\,, \quad \text{and} \quad d_y(t) = \int y\, n(t)\,\mathrm{d}\boldsymbol{r}\,, \tag{6.135}$$

are shown together with the total energy as a function of time. First, we again see that the dipole moments for the Gibbs gauge deviates from both the Coulomb and Lorenz gauges. This is also reflected in the total energy which differs significantly from the expected conserved energy. Second, the dipole moments for the Coulomb gauge are very similar to the Lorenz gauge. The total energy (2.83), however, starts similarly for Coulomb and Lorenz gauges but diverges after many iterations. We suspect that a continuous build-up of small errors related to the instantaneous nature of the Coulomb potential eventually results in nonphysical behavior when coupled to the vector potential. As such, the numerical gauge invariance still has to be further investigated. Furthermore, the Coulomb gauge is a lot less efficient as illustrated by the computation times T_{CPU} detailed in Table 6.5.

6.6 Conclusions

In this chapter, we proposed three schemes, starting from the Yee algorithm on nonuniform grids, to calculate the EM potentials based on different gauge conditions: Coulomb, Gibbs, and Lorenz. From a physical point of view, there is no difference between these gauge conditions. However, in electromagnetism the Lorenz gauge is often preferred because then the scalar and vector potential are manifestly Lorentz invariant. In contrast, the Coulomb gauge is often preferred in

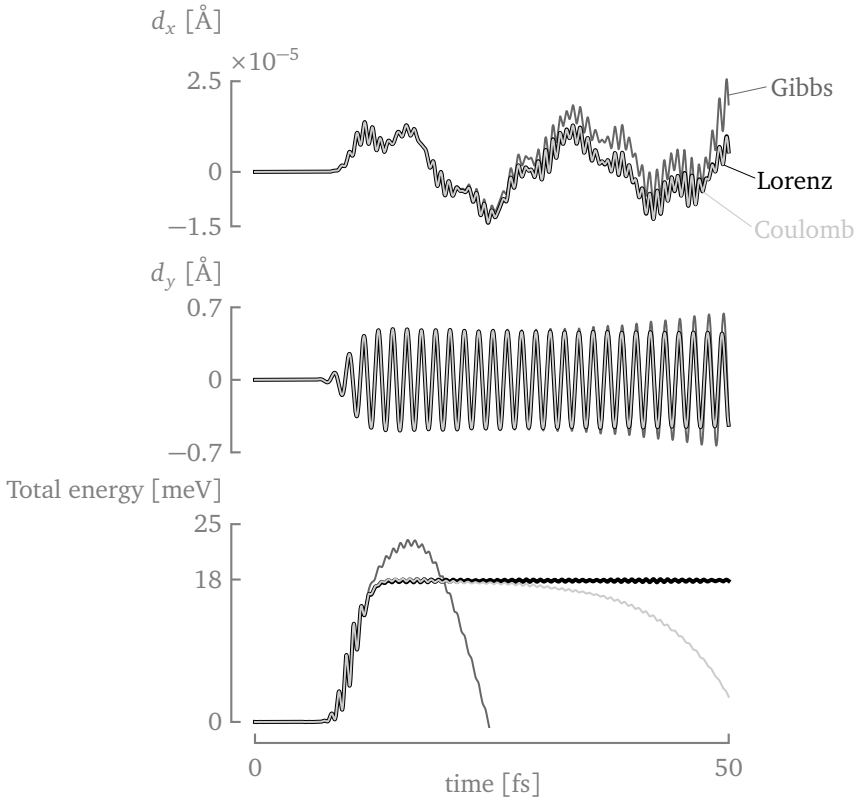

Figure 6.8: The jellium Maxwell-Kohn-Sham system is simulated using the Coulomb, Gibbs, and Lorenz gauges conditions. The dipole moments for the Coulomb and Lorenz gauge are very similar but the Gibbs gauge slowly diverges. After the source has died out, the energy for the Lorenz gauge shows only a small oscillations around a constant value, while both the Coulomb and Gibbs gauge conditions behave nonphysically.

electronic structure calculations, where, additionally, a static approximation is applied. However, the instantaneous nature of the Coulomb scalar potential meshes less neatly into an FDTD scheme than the explicit updates obtained when applying the Gibbs or Lorenz gauge. Furthermore, in the Coulomb gauge, the Poisson equation needs to be solved every time step, which significantly decreases its efficiency. Additionally, we presented a perfectly-matched layer (PML) for the Lorenz gauge which is easily implemented. The stability of the schemes for the Gibbs and Lorenz gauge was studied. It was found that the stability of the Yee algorithm and the new update schemes for the EM potentials can be treated independently. As such, the stability was guaranteed when adopting the well-known stability criterion for the Yee algorithm in free space.

Next, we proposed a new leapfrog scheme for the minimally-coupled Schrödinger equation for arbitrary vector potentials. A two-point stencil on nonuniform grids was proposed along with fourth- and sixth-order spatial differences on uniform grids. We determined the stability condition and found that the conservation of physical symmetries in the discrete scheme are key to obtain a (provably) stable scheme. Further, we validated the method through numerical experiments by comparing it with two alternative time integration schemes: the collocated-explicit (CE) and Crank-Nicolson (CN) methods. The three schemes yielded comparable results but the CE method did not conserve probability as well and the CN is very slow.

Finally, we constructed coupled QM and EM schemes based on the three gauge conditions described earlier. Numerical experiments found that the Gibbs gauge, while very efficient, performed very poorly, even resulting in an unstable coupled system. The Coulomb gauge and Lorenz gauge yielded very similar dipole moments despite their very different numerical schemes. However, the Coulomb gauge did not conserve the total energy for the Maxwell-Kohn-Sham system. We expect that the instantaneous nature of the scalar potential in the Coulomb gauge results in a gradual accumulation of errors, eventually resulting in nonphysical behavior. Furthermore, the Lorenz gauge scheme was more than an order of magnitude faster for both Maxwell-Schrödinger and Maxwell-Kohn-Sham systems and could conserve the total energy much better. Therefore, we clearly find that the Lorenz gauge is the better candidate to simulate coupled EM/QM systems leveraging the FDTD method.

6.A Appendices

6.A.1 Leapfrog Schrödinger FDTD from exponential midpoint rule

In this appendix, an alternative derivation of the update equations for the (minimally-coupled) Schrödinger equation (6.62) is given. As a starting point, we use the exponential midpoint rule. This propagator is second-order accurate in Δt, symplectic and it preserves time-reversal symmetry [34]. It is also well known in a physical-chemistry context. It states that:

$$\psi|^n = \exp\left(-\jmath \frac{\Delta t}{\hbar} \hat{H}|^{n-\frac{1}{2}}\right) \psi|^{n-1}. \tag{6.A.1}$$

Now, $\hat{H}$ is again split in $\hat{H}_0$ and $\hat{H}_1$ such that:

$$\psi|^n = e^{\frac{\Delta t}{2}\hat{H}_1|^{n-\frac{1}{2}}} e^{-\jmath \Delta t \hat{H}_0|^{n-\frac{1}{2}}} e^{\frac{\Delta t}{2}\hat{H}_1|^{n-\frac{1}{2}}} \psi|^{n-1}. \tag{6.A.2}$$

This splitting introduces an error because $\hat{H}_0$ and $\hat{H}_1$ do not commute, but the error is of order $\mathcal{O}\big(\Delta t^2\big)$. We rewrite (6.A.2) as a two-step procedure:

$$e^{-\frac{\Delta t}{2}\hat{H}_1|^{n-\frac{1}{2}}}\psi|^n = e^{-\jmath\frac{\Delta t}{2}\hat{H}_0|^{n-\frac{1}{2}}}\psi|^{n-\frac{1}{2}}, \tag{6.A.3}$$

$$e^{\frac{\Delta t}{2}\hat{H}_1|^{n-\frac{1}{2}}}\psi|^{n-1} = e^{\jmath\frac{\Delta t}{2}\hat{H}_0|^{n-\frac{1}{2}}}\psi|^{n-\frac{1}{2}}. \tag{6.A.4}$$

Taking the real part of both equations and subtracting yields:

$$e^{-\frac{\Delta t}{2}\hat{H}_1|^{n-\frac{1}{2}}}r|^n = e^{\frac{\Delta t}{2}\hat{H}_1|^{n-\frac{1}{2}}}r|^{n-1} + 2\sin\left(\frac{\Delta t}{2}\hat{H}_0|^{n-\frac{1}{2}}\right)s|^{n-\frac{1}{2}}. \tag{6.A.5}$$

Taking the imaginary part of both equations and subtracting yields:

$$e^{-\frac{\Delta t}{2}\hat{H}_1|^{n-\frac{1}{2}}}s|^n = e^{\frac{\Delta t}{2}\hat{H}_1|^{n-\frac{1}{2}}}s|^{n-1} - 2\sin\left(\frac{\Delta t}{2}\hat{H}_0|^{n-\frac{1}{2}}\right)r|^{n-\frac{1}{2}}. \tag{6.A.6}$$

If we now make a Taylor expansion of (6.A.5) and (6.A.6), neglect terms of second order or higher in Δt, and shift (6.A.5) half a time step, we obtain again the proposed update scheme (6.62). As such, we have shown that this new scheme can be interpreted as a modification of the well-known exponential-midpoint rule and that it is second-order accurate in time.

6.A.2 The collocated-explicit and Crank-Nicolson methods

We present two alternative schemes for the minimally-coupled Schrödinger equation, i.e., the collocated-explicit (CE) method:

$$\boldsymbol{\psi}|^{n+1} = -2\jmath\Delta t(H_0 + \jmath H_1)\boldsymbol{\psi}|^n + \boldsymbol{\psi}|^{n-1}, \tag{6.A.7}$$

and the Crank-Nicolson (CN) method:

$$\left(I_{n_\psi} + \jmath\frac{\Delta t}{2}(H_0 + \jmath H_1)\right)\boldsymbol{\psi}|^{n+1} = \left(I_{n_\psi} - \jmath\frac{\Delta t}{2}(H_0 + \jmath H_1)\right)\boldsymbol{\psi}|^n. \tag{6.A.8}$$

For simplicity, the methods are only discussed on uniform grids, but the discussion can easily be modified for the nonuniform discretization presented in Section 6.3.1.

Stability

The CE method is simply an extension of the explicit method (4.12) presented in Chapter 4 to include arbitrary vector potentials. The stability is again guaranteed if Δt satisfies:

$$\Delta t \leq \frac{\hbar}{\rho(H)}, \tag{6.A.9}$$

where the proof in Section 4.3 can be repeated with $H = H_0 + \jmath H_1$ and since H is Hermitian by design, the eigenvalues are real. The stability condition can again be approximated (for a second-order accurate scheme) as:

$$\Delta t < \min_{i,j,k}\left(\left(\frac{2}{m}\left(\frac{1}{\Delta x^2}+\frac{1}{\Delta y^2}+\frac{1}{\Delta z^2}\right)+v|_{i,j,k}+q\phi|_{i,j,k} + \frac{q^2}{2m}\left(\mathcal{A}|_{i,j,k}\right)^2+\frac{q}{m}\left(\frac{\tilde{A}_x|_{i,j,k}}{\Delta x}+\frac{\tilde{A}_y|_{i,j,k}}{\Delta y}+\frac{\tilde{A}_z|_{i,j,k}}{\Delta z}\right)\right)^{-1}\right), \tag{6.A.10}$$

where

$$\tilde{A}_x|_{i,j,k} = \max\left(\left|A_x|_{i+\frac{1}{2},j,k}\right|, \left|A_x|_{i-\frac{1}{2},j,k}\right|\right), \tag{6.A.11}$$

and similar for the y- and z-components. In contrast to the result in [9], this time step is rigorously derived and cannot yield a time step of infinity. Moreover, in case the EM potentials are zero, (6.A.10) simplifies to the correct time step (4.41) unlike the result in [9], which only yields half the time step.

For the CN method, the eigenvalues of the iteration matrix all lie on the unit circle and the method is unconditionally stable. This can be proven by considering that:

$$\begin{aligned}
&\left(I_{n_\psi}+\jmath\frac{\Delta t}{2}(H_0+\jmath H_1)\right)^{-1}\left(I_{n_\psi}-\jmath\frac{\Delta t}{2}(H_0+\jmath H_1)\right)\\
&\qquad=\left(I_{n_\psi}+\jmath\frac{\Delta t}{2}U\Lambda_H U^\dagger\right)^{-1}\left(I_{n_\psi}-\jmath\frac{\Delta t}{2}U\Lambda_H U^\dagger\right) &\text{(6.A.12a)}\\
&\qquad=U\left(I_{n_\psi}+\jmath\frac{\Delta t}{2}\Lambda_H\right)^{-1}U^\dagger U\left(I_{n_\psi}-\jmath\frac{\Delta t}{2}\Lambda_H\right)U^\dagger &\text{(6.A.12b)}\\
&\qquad=U\left(I_{n_\psi}+\jmath\frac{\Delta t}{2}\Lambda_H\right)^{-1}\left(I_{n_\psi}-\jmath\frac{\Delta t}{2}\Lambda_H\right)U^\dagger, &\text{(6.A.12c)}
\end{aligned}$$

where $U\Lambda_H U^\dagger$ is the eigendecomposition of $H = H_0 + \jmath H_1$ with the unitary matrix U. As such, all eigenvalues λ_A of the iteration matrix are of the form:

$$\lambda_A = \frac{1-\jmath\frac{\Delta t}{2}\lambda_H}{1+\jmath\frac{\Delta t}{2}\lambda_H}, \quad \text{and thus} \quad |\lambda_A| = 1. \tag{6.A.13}$$

References

1. Askar, A. & Cakmak, A. S. Explicit integration method for the time-dependent Schrödinger equation for collision problems. *The Journal of Chemical Physics* **68,** 2794–2798 (1978).
2. Visscher, P. A fast explicit algorithm for the time-dependent Schrödinger equation. *Computers in Physics* **5,** 596–598 (1991).
3. Sullivan, D. M. & Citrin, D. Determination of the eigenfunctions of arbitrary nanostructures using time domain simulation. *Journal of Applied Physics* **91,** 3219–3226 (2002).
4. Moxley III, F. I., Zhu, F. & Dai, W. A Generalized FDTD Method with Absorbing Boundary Condition for Solving a Time-Dependent Linear Schrödinger Equation. *American Journal of Computational Mathematics* **2,** 163–172 (2012).
5. Bigaouette, N., Ackad, E. & Ramunno, L. Nonlinear grid mapping applied to an FDTD-based, multi-center 3D Schrödinger equation solver. *Computer Physics Communications* **183,** 38–45 (2012).
6. Pierantoni, L., Mencarelli, D. & Rozzi, T. Boundary immittance operators for the Schrödinger–Maxwell problem of carrier dynamics in nanodevices. *IEEE transactions on Microwave Theory and Techniques* **57,** 1147–1155 (2009).
7. Takeuchi, T., Ohnuki, S. & Sako, T. Hybrid Simulation of Maxwell-Schrödinger Equations for Multi-Physics Problems Characterized by Anharmonic Electrostatic Potential. *Progress In Electromagnetics Research* **148,** 73–82 (2014).
8. Takeuchi, T., Ohnuki, S. & Sako, T. Comparison between Maxwell–Schrödinger and Maxwell–Newton hybrid simulations for multi-well electrostatic potential. *IEEE Journal of Quantum Electronics* **50,** 334–339 (2014).
9. Ryu, C. J., Liu, A. Y., Wei, E. & Chew, W. C. Finite-difference time-domain simulation of the Maxwell–Schrödinger system. *IEEE Journal on Multiscale and Multiphysics Computational Techniques* **1,** 40–47 (2016).
10. Chen, Y. P. *et al.* A unified Hamiltonian solution to Maxwell-Schrödinger equations for modeling electromagnetic field-particle interaction. *Computer Physics Communications* **215,** 63–70 (2017).
11. Zhang, L., Zeng, H. & Chen, R.-S. Full-quantum numerical scheme of finite difference time domain method for high-order harmonic generation. *IEEE Journal on Multiscale and Multiphysics Computational Techniques* **3,** 74–79 (2018).
12. Xiang, C., Kong, F., Li, K. & Liu, M. A high-order symplectic FDTD scheme for the Maxwell-Schrodinger system. *IEEE Journal of Quantum Electronics* **54,** 1–8 (2017).
13. Xie, G. *et al.* Universal vector–scalar potential framework for inhomogeneous electromagnetic system and its application in semiclassical quantum electromagnetics. *IEEE Transactions on Plasma Science* **49,** 3459–3471 (2021).

14. Sato, S. A. & Yabana, K. Maxwell+TDDFT multi-scale simulation for laser-matter interactions. *Journal of Advanced Simulation in Science and Engineering* **1,** 98–110 (2014).

15. Li, Y., He, S., Russakoff, A. & Varga, K. Accurate time propagation method for the coupled Maxwell and Kohn-Sham equations. *Physical Review E* **94,** 023314 (2016).

16. Yamada, S., Noda, M., Nobusada, K. & Yabana, K. Time-dependent density functional theory for interaction of ultrashort light pulse with thin materials. *Physical Review B* **98,** 245147 (2018).

17. Yamada, A. & Yabana, K. Multiscale time-dependent density functional theory for a unified description of ultrafast dynamics: Pulsed light, electron, and lattice motions in crystalline solids. *Physical Review B* **99,** 245103 (2019).

18. You, J. W. & Panoiu, N. C. Analysis of the interaction between classical and quantum plasmons via FDTD–TDDFT method. *IEEE Journal on Multiscale and Multiphysics Computational Techniques* **4,** 111–118 (2019).

19. Gabay, D. *et al.* Lorenz gauge formulation for time-dependent density functional theory. *Physical Review B* **101,** 235101 (2020).

20. Takeuchi, T., Ohnuki, S. & Sako, T. Maxwell-Schrödinger hybrid simulation for optically controlling quantum states: A scheme for designing control pulses. *Physical Review A* **91,** 033401 (2015).

21. Taflove, A. & Hagness, S. C. *Computational electrodynamics: the finite-difference time-domain method* (Artech House, 2005).

22. Van Londersele, A., De Zutter, D. & Vande Ginste, D. An in-depth stability analysis of nonuniform FDTD combined with novel local implicitization techniques. *Journal of Computational Physics* **342,** 177–193 (2017).

23. Castro, A., Rubio, A. & Stott, M. Solution of Poisson's equation for finite systems using plane-wave methods. *Canadian Journal of Physics* **81,** 1151–1164 (2003).

24. Gabay, D., Boag, A. & Natan, A. Optimizing kernel methods for Poisson integrals on a uniform grid. *Computer Physics Communications* **215,** 1–6 (2017).

25. Roden, J. A. & Gedney, S. D. Convolution PML (CPML): An efficient FDTD implementation of the CFS–PML for arbitrary media. *Microwave and Optical Technology Letters* **27,** 334–339 (2000).

26. Gedney, S. D. *Introduction to the Finite-Difference Time-Domain (FDTD) Method for Electromagnetics* (Morgan & Claypool, 2011).

27. Denecker, B., Knockaert, L., Olyslager, F. & De Zutter, D. A new state-space-based algorithm to assess the stability of the finite-difference time-domain method for 3D finite inhomogeneous problems. *AEU-International Journal of Electronics and Communications* **58,** 339–348 (2004).

28. Bernstein, D. S. *Matrix Mathematics* (Princeton University Press, 2009).

29. Ullrich, C. A. *Time-Dependent Density-Functional Theory* (Oxford University Press, 2012).

30. Castro, A., Marques, M. A. & Rubio, A. Propagators for the time-dependent Kohn–Sham equations. *The Journal of Chemical Physics* **121,** 3425–3433 (2004).

31. Mennemann, J.-F. & Jüngel, A. Perfectly Matched Layers versus discrete transparent boundary conditions in quantum device simulations. *Journal of Computational Physics* **275,** 1–24 (2014).

32. Bochev, P. & Robinson, A. Matching Algorithms with Physics: Exact Sequences. *Collected Lectures on the Preservation of Stability Under Discretization* **109,** 145 (2002).

33. Van Londersele, A. *Novel Finite-Difference Time-Domain Techniques to Model Multiscale Electromagnetic Problems* PhD thesis (Ghent University, 2018).

34. Gomez Pueyo, A., Marques, M. A., Rubio, A. & Castro, A. Propagators for the time-dependent Kohn–Sham equations: Multistep, Runge–Kutta, exponential Runge–Kutta, and commutator free Magnus methods. *Journal of Chemical Theory and Computation* **14,** 3040–3052 (2018).

CHAPTER 7

AN ALTERNATING-DIRECTION HYBRID IMPLICIT-EXPLICIT FDTD METHOD FOR THE ELECTROMAGNETIC POTENTIALS

"Just believe everything I tell you, and it will all be very, very simple."

— DOUGLAS ADAMS, Life, the Universe and Everything (1982)

In this chapter, the Yee-like algorithm for the EM fields and EM potentials developed in Chapter 6 is expanded with local implicitization to relax the stability criterion. The theory and examples are based on "A Hybrid EM/QM Framework Based on the ADHIE-FDTD Method for the Modeling of Nanowires" by Pieter Decleer and Dries Vande Ginste, as published in *IEEE Journal on Multiscale and Multiphysics Computational Techniques*, **7**, 236-251 (2022).

7.1 Introduction

In multiscale problems, where one or two directions are finely sampled, the time steps dictated by (6.10) and (6.49) lead to an oversampling in time, slowing down the computation. Therefore, many alternatives have been proposed that are unconditionally stable [1–3]. The main problem is that the implicitization results in more computationally expensive time stepping, oftentimes resulting in longer overall computation times. More recently, techniques have been developed to apply the implicitization locally, so that specific cells are eliminated from the stability criterion on nonuniform grids [4–9]. As a result, the time step is increased while minimizing the computational cost per time step, resulting in a much more efficient scheme.

The multiscale problem is exacerbated in multiphysics EM/QM problems, where there is a large mismatch between the allowed time steps of the different subsystems. Therefore, we present a novel ADHIE method for the EM potentials in the Lorenz gauge which is based on and also uses the ADHIE method presented in [6] for the EM fields. One of the main advantages of the ADHIE method is that it retains the linear complexity of fully explicit methods. Moreover, it is accurate, time and memory efficient and scalable to computationally large problems.

The stability of the method is determined and the numerical dispersion error is investigated. Furthermore, the applicability of our modeling approach is proven through several numerical experiments of quasi 1-D quantum systems, including a single-particle Maxwell-Schrödinger (MS) system as well as a Maxwell-Kohn-Sham (MKS) system within the TDDFT framework. Both types of experiments pertain to a nanotube which has to be finely sampled along its axis. They confirm that the novel ADHIE method drastically decreases the computation time while retaining the accuracy, leading to efficient and accurate simulations of light-matter interactions in multiscale nanoelectronic devices.

This chapter is structured as follows. First, the method is presented in Section 7.2. The method for $\boldsymbol{E}$ and $\boldsymbol{H}$ from [6] is illustrated after which the novel ADHIE method for $\boldsymbol{A}$ and ϕ is presented. Next, its stability is discussed in Section 7.3. In Section 7.4, the numerical dispersion relation is derived. In Section 7.5, we present the results for coupled EM/QM systems and, lastly, we make some final remarks in Section 7.6.

7.2 The ADHIE scheme

7.2.1 The electromagnetic fields

The electromagnetic fields are computed using the ADHIE method proposed in [6], which we briefly restate here for lossless materials:

$$\begin{aligned}&\begin{bmatrix} \frac{M_\epsilon}{\Delta t} + \frac{\Delta t}{4\alpha^2} C_1 M_\mu^{-1} {C_1}^T & 0 \\ C^T & \frac{M_\mu}{\Delta t} + \frac{\Delta t}{4\alpha^2} {C_2}^T M_\epsilon^{-1} C_2 \end{bmatrix} \begin{bmatrix} \hat{\boldsymbol{e}}|^n \\ \hat{\boldsymbol{h}}|^{n+\frac{1}{2}} \end{bmatrix} \\ &= \begin{bmatrix} \frac{M_\epsilon}{\Delta t} + \frac{\Delta t}{4\alpha^2} C_1 M_\mu^{-1} {C_1}^T & C \\ 0 & \frac{M_\mu}{\Delta t} + \frac{\Delta t}{4\alpha^2} {C_2}^T M_\epsilon^{-1} C_2 \end{bmatrix} \begin{bmatrix} \hat{\boldsymbol{e}}|^{n-1} \\ \hat{\boldsymbol{h}}|^{n-\frac{1}{2}} \end{bmatrix} + \begin{bmatrix} \hat{\boldsymbol{s}}|^{n-\frac{1}{2}} \\ 0 \end{bmatrix},\end{aligned} \tag{7.1}$$

where α is a tunable parameter, and where the curl splitting matrices C_1 and C_2 are determined based on the desired local implicitization and time step. The ADHIE scheme (7.1) is stable for:

$$\Delta t < \frac{2\left(1-\alpha^2\right)}{\left\| M_\epsilon^{-\frac{1}{2}} C_0 M_\mu^{-\frac{1}{2}} \right\|_2}, \tag{7.2}$$

where $C = C_0 + C_1 + C_2$. The ADHIE method generalizes the regular alternating-direction implicit (ADI) method to a hybrid implicit-explicit method. Both the regular ADI-FDTD and Yee-FDTD methods are special cases of the ADHIE-FDTD method (7.1). For $C_1 = C_2 = 0$, the conditionally stable Yee-FDTD method (6.4) is

retrieved while for:

$$C_1 = \begin{bmatrix} 0 & 0 & I_{n_x} \otimes D_y \otimes I_{m_z} \\ I_{m_x} \otimes I_{n_y} \otimes D_z & 0 & 0 \\ 0 & D_x \otimes I_{m_y} \otimes I_{n_z} & 0 \end{bmatrix}, \tag{7.3}$$

$$C_2 = \begin{bmatrix} 0 & -I_{n_x} \otimes I_{m_y} \otimes D_z & 0 \\ 0 & 0 & -D_x \otimes I_{n_y} \otimes I_{m_z} \\ -I_{m_x} \otimes D_y \otimes I_{n_z} & 0 & 0 \end{bmatrix}, \tag{7.4}$$

and $\alpha = 1$, the fully implicit and unconditionally stable ADI method is found. Now, it is possible to implicitize certain directions fully or partially by modifying C_1 and C_2 to only include derivatives that have to be implicitized. For example, partial implicitization in the z-direction can be accomplished with C_1 and C_2 given by:

$$C_1 = \begin{bmatrix} 0 & 0 & 0 \\ I_{m_x} \otimes I_{n_y} \otimes D_z R_z & 0 & 0 \\ 0 & 0 & 0 \end{bmatrix}, \tag{7.5}$$

$$C_2 = \begin{bmatrix} 0 & -I_{n_x} \otimes I_{m_y} \otimes D_z R_z & 0 \\ 0 & 0 & 0 \\ 0 & 0 & 0 \end{bmatrix}, \tag{7.6}$$

where R_z is defined as $R_z = I_{n_z} - P_z$ and P_z defined as (5.7). The stability condition (7.2) now depends on C_0 instead of C in (6.10), where:

$$C_0 = \begin{bmatrix} 0 & -I_{n_x} \otimes I_{m_y} \otimes D_z P_z & I_{n_x} \otimes D_y \otimes I_{m_z} \\ I_{m_x} \otimes I_{n_y} \otimes D_z P_z & 0 & -D_x \otimes I_{n_y} \otimes I_{m_z} \\ -I_{m_x} \otimes D_y \otimes I_{n_z} & D_x \otimes I_{m_y} \otimes I_{n_z} & 0 \end{bmatrix}. \tag{7.7}$$

As such, it is clear that $\left[P_z\right]_{k,k} = 0$ removes the primary step Δz_k from the stability criterion and that the traditional Courant limit is relaxed, without implicitizing the entire z-direction. For $\boldsymbol{e}_x$, $\boldsymbol{e}_z$, $\boldsymbol{h}_x$, and $\boldsymbol{h}_z$, the resulting update equations are identical to the Yee scheme – thus explicit – while for $\boldsymbol{e}_y$ and $\boldsymbol{h}_y$, the update equations are given by:

$$\begin{aligned} A_1 \boldsymbol{e}_y|^n = A_1 \boldsymbol{e}_y|^{n-1} &+ \Big(I_{m_x} \otimes I_{n_y} \otimes (\delta_z^\star)^{-1} D_z\Big) \boldsymbol{h}_x|^{n-\frac{1}{2}} \\ &- \Big((\delta_x^\star)^{-1} D_x \otimes I_{n_y} \otimes I_{m_z}\Big) \boldsymbol{h}_z|^{n-\frac{1}{2}}, \end{aligned} \tag{7.8a}$$

$$\begin{aligned} A_2 \boldsymbol{h}_y|^{n+\frac{1}{2}} = A_2 \boldsymbol{h}_y|^{n-\frac{1}{2}} &+ \Big(I_{n_x} \otimes I_{m_y} \otimes (\delta_z)^{-1} D_z^T\Big) \boldsymbol{e}_x|^n \\ &- \Big((\delta_x)^{-1} D_x^T \otimes I_{m_y} \otimes I_{n_z}\Big) \boldsymbol{e}_z|^n, \end{aligned} \tag{7.8b}$$

with the matrices A_1 and A_2 given by:

$$A_1 = \frac{\left[\epsilon_y\right]}{\Delta t} + \frac{\Delta t}{4\alpha^2} \Big(I_{m_x n_y} \otimes (\delta_z^\star)^{-1} D_z\Big) \left[\mu_x\right]^{-1} \Big(I_{m_x n_y} \otimes R_z {\delta_z}^{-1} D_z^T\Big), \tag{7.9a}$$

$$A_2 = \frac{\left[\mu_y\right]}{\Delta t} + \frac{\Delta t}{4\alpha^2} \Big(I_{n_x m_y} \otimes R_z {\delta_z}^{-1} D_z^T\Big) \left[\epsilon_x\right]^{-1} \Big(I_{n_x m_y} \otimes (\delta_z^\star)^{-1} D_z R_z\Big). \tag{7.9b}$$

The diagonal material matrices $\left[\epsilon_u\right]$ and $\left[\mu_u\right]$ are the averaged permittivity and permeability for $\boldsymbol{e}_u$ and $\boldsymbol{h}_u$, respectively. The update equations (7.8) constitute tridiagonal linear systems which are smaller compared to their fully implicit counterpart. As such, the complexity is reduced w.r.t. the ADI-FDTD method while the time-step is increased w.r.t the Yee-FDTD method, resulting in a very efficient scheme.

7.2.2 The electromagnetic potentials

In this section, an ADHIE scheme is developed for the EM potentials in the Lorenz gauge which is compatible with the ADHIE scheme for the EM fields. The novel update scheme is:

$$\begin{bmatrix} I_{n_e} & 0 \\ \Delta\tau D^\star & G \end{bmatrix} \begin{bmatrix} \boldsymbol{a}|^{n+\frac{1}{2}} \\ \frac{1}{c}\boldsymbol{\phi}|^{n+1} \end{bmatrix} = \begin{bmatrix} I_{n_e} & \Delta\tau D^T \\ 0 & G \end{bmatrix} \begin{bmatrix} \boldsymbol{a}|^{n-\frac{1}{2}} \\ \frac{1}{c}\boldsymbol{\phi}|^{n} \end{bmatrix} - \begin{bmatrix} \boldsymbol{e}|^n \\ 0 \end{bmatrix}, \tag{7.10}$$

where

$$G = G_x \otimes G_y \otimes G_z, \tag{7.11}$$

with

$$G_u = \left(I_{m_u} + \frac{\Delta\tau^2}{4\alpha^2} \delta_u^{\star -1} D_u^\star \left(I_{n_u} - P_u\right) \delta_u{}^{-1} D_u^T \right) \quad \text{for} \quad u \in \{x, y, z\}. \tag{7.12}$$

The parameter α in (7.12) is again a tunable parameter. However, it will be shown in Section 7.3 that, in contrast to the ADHIE method for $\boldsymbol{E}$ and $\boldsymbol{H}$ (7.1), it can be chosen arbitrarily close to 1, drastically reducing the splitting error.

A fully explicit scheme, as the one presented in [10], is retrieved when $[P_u]_{i,i} = 1$ for all u and i. In contrast, the x-direction is completely implicitized by setting $[P_x]_{i,i} = 0$ for all $i = 1, \ldots, n_x$. As a result, the matrix $G = G_x \otimes I_{m_y} \otimes I_{m_z}$ that has to be inverted, only contains spatial cells in the x-direction.

To solve (7.10) efficiently, the update for $\boldsymbol{\phi}$ is split in several steps given by:

$$\left(G_x \otimes I_{m_y} \otimes I_{m_z}\right) \boldsymbol{\phi}|^{(1)} = -c^2 \Delta t D^\star \boldsymbol{a}|^{n+\frac{1}{2}}, \tag{7.13a}$$

$$\left(I_{m_x} \otimes G_y \otimes I_{m_z}\right) \boldsymbol{\phi}|^{(2)} = \boldsymbol{\phi}|^{(1)}, \tag{7.13b}$$

$$\left(I_{m_x} \otimes I_{m_y} \otimes G_z\right) \boldsymbol{\phi}|^{(3)} = \boldsymbol{\phi}|^{(2)}, \tag{7.13c}$$

$$\boldsymbol{\phi}|^{n+1} = \boldsymbol{\phi}|^n + \boldsymbol{\phi}|^{(3)}. \tag{7.13d}$$

Consequently, the system can be solved using the tridiagonal matrix algorithm, such that the complexity remains of linear order $\mathcal{O}(n)$ [11].

The method is further elucidated by rewriting the update equations in a more accessible scalar notation. The vector potential is updated explicitly with (6.12) which results in:

$$A_x|^{n+\frac{1}{2}}_{i+\frac{1}{2},j,k} = A_x|^{n-\frac{1}{2}}_{i+\frac{1}{2},j,k} - \frac{\Delta t}{\Delta x_{i+1}}\Big(\phi|^{n}_{i+1,j,k} - \phi|^{n}_{i,j,k}\Big) - \Delta t E_x|^{n}_{i+\frac{1}{2},j,k}, \tag{7.14}$$

and similar for A_y and A_z. The update for $\boldsymbol{\phi}$ (7.13) is written as:

$$\begin{aligned}\Big(\zeta_x|_i\ \phi|^{(1)}_{i+1,j,k} + \eta_x|_i\ \phi|^{(1)}_{i,j,k} + \theta_x|_i\ \phi|^{(1)}_{i-1,j,k}\Big) = \\ - \frac{c^2\Delta t}{\Delta x^\star_i}\Big(A_x|^{n+\frac{1}{2}}_{i+\frac{1}{2},j,k} - A_x|^{n+\frac{1}{2}}_{i-\frac{1}{2},j,k}\Big) \\ - \frac{c^2\Delta t}{\Delta y^\star_j}\Big(A_y|^{n+\frac{1}{2}}_{i,j+\frac{1}{2},k} - A_y|^{n+\frac{1}{2}}_{i,j-\frac{1}{2},k}\Big) \\ - \frac{c^2\Delta t}{\Delta z^\star_k}\Big(A_z|^{n+\frac{1}{2}}_{i,j,k+\frac{1}{2}} - A_z|^{n+\frac{1}{2}}_{i,j,k-\frac{1}{2}}\Big),\end{aligned} \tag{7.15a}$$

$$\Big(\zeta_y|_j\ \phi|^{(2)}_{i,j+1,k} + \eta_y|_j\ \phi|^{(2)}_{i,j,k} + \theta_y|_j\ \phi|^{(2)}_{i,j-1,k}\Big) = \phi|^{(1)}_{i,j,k}, \tag{7.15b}$$

$$\Big(\zeta_z|_k\ \phi|^{(3)}_{i,j,k+1} + \eta_z|_k\ \phi|^{(3)}_{i,j,k} + \theta_z|_k\ \phi|^{(3)}_{i,j,k-1}\Big) = \phi|^{(2)}_{i,j,k}, \tag{7.15c}$$

$$\phi|^{n+1}_{i,j,k} = \phi|^{n}_{i,j,k} + \phi|^{(3)}_{i,j,k}, \tag{7.15d}$$

where

$$\zeta_x|_i = \big(p_x|_{i+1} - 1\big)\frac{\Delta\tau^2}{4\Delta x^\star_i \Delta x_{i+1}}, \tag{7.16a}$$

$$\theta_x|_i = \big(p_x|_i - 1\big)\frac{\Delta\tau^2}{4\Delta x^\star_i \Delta x_i}, \tag{7.16b}$$

$$\eta_x|_i = 1 - (\zeta_x|_i + \theta_x|_i). \tag{7.16c}$$

The update scheme (7.14)–(7.15) written in this scalar notation, makes it very evident that the update for the scalar potential (7.15) constitutes at most three tridiagonal implicit systems, which can be solved very efficiently.

7.3 Stability

As discussed in Section 6.2, the stability of the combined $(\boldsymbol{e}, \boldsymbol{h}, \boldsymbol{a}, \boldsymbol{\phi})$ system can be studied by considering the stability of the separate systems because the ADHIE system can also be written as (6.34). Since the stability of (7.1) has been determined in [6], we only need to concern ourselves with the stability of the novel ADHIE scheme for $\boldsymbol{A}$ and $\boldsymbol{\phi}$ with $\boldsymbol{e} = 0$. The system is symmetrized in the same way as (6.37) with the transformation matrix W from (6.38), resulting in:

$$\begin{bmatrix} I_{n_e} & 0 \\ \tilde{D} & \tilde{G} \end{bmatrix}\begin{bmatrix} \tilde{\boldsymbol{a}}|^{n+\frac{1}{2}} \\ \tilde{\boldsymbol{\phi}}|^{n+1} \end{bmatrix} = \begin{bmatrix} I_{n_e} & \tilde{D}^T \\ 0 & \tilde{G} \end{bmatrix}\begin{bmatrix} \tilde{\boldsymbol{a}}|^{n-\frac{1}{2}} \\ \tilde{\boldsymbol{\phi}}|^{n} \end{bmatrix}, \tag{7.17}$$

where

$$\tilde{G} = \bigotimes_{u\in\{x,y,z\}} \left(I_{m_u} + \frac{\Delta\tau^2}{4\alpha^2}\tilde{D}_u\big(I_{n_u} - P_u\big)\tilde{D}_u^T \right). \tag{7.18}$$

Now, the update equations are recast as $(E+F)\boldsymbol{x}|^n = (E-F)\boldsymbol{x}|^{n-1}$ with:

$$E = \begin{bmatrix} I_{n_e} & \frac{1}{2}\tilde{D}^T \\ \frac{1}{2}\tilde{D} & \tilde{G} \end{bmatrix}, \quad \text{and} \quad F = \begin{bmatrix} 0 & -\frac{1}{2}\tilde{D}^T \\ \frac{1}{2}\tilde{D} & 0 \end{bmatrix}. \tag{7.19}$$

Since the matrix F is identical to the explicit case, we only need to consider the positive definiteness of E. The matrix E is split as:

$$E = E' + \begin{bmatrix} 0 & 0 \\ 0 & K \end{bmatrix}, \tag{7.20}$$

where

$$E' = \begin{bmatrix} I_{n_e} & \frac{1}{2}\tilde{D}^T \\ \frac{1}{2}\tilde{D} & I_{n_\phi} + \frac{1}{4\alpha^2}\tilde{D}\big(I_{n_e} - P\big)\tilde{D}^T \end{bmatrix}, \tag{7.21}$$

with

$$P = \begin{bmatrix} P_x \otimes I_{m_y} \otimes I_{m_z} & & \\ & I_{m_x} \otimes P_y \otimes I_{m_z} & \\ & & I_{m_x} \otimes I_{m_y} \otimes P_z \end{bmatrix}, \tag{7.22}$$

and

$$\begin{aligned} K = {} & \frac{\Delta\tau^4}{16\alpha^4}\tilde{D}_x R_x \tilde{D}_x^T \otimes \tilde{D}_y R_y \tilde{D}_y^T \otimes I_{m_z} + \frac{\Delta\tau^4}{16\alpha^4}\tilde{D}_x R_x \tilde{D}_x^T \otimes I_{m_y} \otimes \tilde{D}_z R_z \tilde{D}_z^T \\ & + \frac{\Delta\tau^4}{16\alpha^4} I_{m_x} \otimes \tilde{D}_y R_y \tilde{D}_y^T \otimes \tilde{D}_z R_z \tilde{D}_z^T \\ & + \frac{\Delta\tau^6}{64\alpha^6}\tilde{D}_x R_x \tilde{D}_x^T \otimes \tilde{D}_y R_y \tilde{D}_y^T \otimes \tilde{D}_z R_z \tilde{D}_z^T. \end{aligned} \tag{7.23}$$

All four terms in K are positive semi-definite since, e.g., the first term satisfies:

$$\begin{aligned} & \boldsymbol{x}^T\Big(\tilde{D}_x R_x \tilde{D}_x^T \otimes \tilde{D}_y R_y \tilde{D}_y^T \otimes I_{m_z}\Big)\boldsymbol{x} \\ & \quad = \boldsymbol{x}^T\big(\tilde{D}_x R_x \otimes \tilde{D_y} R_y \otimes I_{m_z}\big)\big(R_x \tilde{D}_x^T \otimes R_y \tilde{D_y}^T \otimes I_{m_z}\big)\boldsymbol{x} \end{aligned} \tag{7.24}$$

$$\quad = \big\|\big(R_x \tilde{D}_x^T \otimes R_y \tilde{D_y}^T \otimes I_{m_z}\big)\boldsymbol{x}\big\|_2^2 \geq 0, \quad \forall \boldsymbol{x} \in \mathbb{R}^{n_\phi}, \tag{7.25}$$

where we have used that R_u is idempotent. Similarly, all other terms in K can be proven to be positive semi-definite, and thus, only the positive definiteness of E'

has to be investigated. Matrix E' is recast as:

$$E' = \begin{bmatrix} \alpha^2(I_{n_e}-P) & \frac{1}{2}(I_{n_e}-P)\tilde{D}^T \\ \frac{1}{2}\tilde{D}(I_{n_e}-P) & \frac{1}{4\alpha^2}\tilde{D}(I_{n_e}-P)\tilde{D} \end{bmatrix} + \begin{bmatrix} I_{n_e}-\alpha^2\big(I_{n_e}-P\big) & \frac{1}{2}P\tilde{D}^T \\ \frac{1}{2}\tilde{D}P & I_{n_\phi} \end{bmatrix} \tag{7.26a}$$

$$= \overbrace{\begin{bmatrix} \alpha\big(I_{n_e}-P\big) & 0 \\ \frac{1}{2\alpha}\tilde{D}(I_{n_e}-P) & 0 \end{bmatrix}}^{\triangleq J} \overbrace{\begin{bmatrix} \alpha\big(I_{n_e}-P\big) & \frac{1}{2\alpha}(I_{n_e}-P)\tilde{D}^T \\ 0 & 0 \end{bmatrix}}^{=J^T} + \underbrace{\begin{bmatrix} I_{n_e}-\alpha^2\big(I_{n_e}-P\big) & \frac{1}{2}P\tilde{D}^T \\ \frac{1}{2}\tilde{D}P & I_{n_\phi} \end{bmatrix}}_{\triangleq E^*}. \tag{7.26b}$$

The first part JJ^T is positive semi-definite by construction, so we have to determine when E^* is positive definite. Similar to Section 6.2, the eigenvalues z of E^* are the solutions of $\det\Big(E^* - zI_{n_e+n_\phi}\Big) = 0$, yielding:

$$\det\left((1-z)I_{n_\phi} - \frac{1}{4}\tilde{D}P\big((1-z)I_{n_e} - \alpha^2\big(I_{n_e}-P\big)\big)^{-1}P\tilde{D}^T\right) = 0, \tag{7.27}$$

and

$$\det\big((1-z)I_{n_e} - \alpha^2\big(I_{n_e}-P\big)\big) = 0. \tag{7.28}$$

The latter immediately yields eigenvalues:

$$z = 1 \quad \text{and} \quad z = 1-\alpha^2. \tag{7.29}$$

The diagonal matrix $P\big((1-z)I_{n_e} - \alpha^2\big(I_{n_e}-P\big)\big)^{-1}P$ in (7.27) can be simplified by recognizing that:

$$\Big[P\big((1-z)I_{n_e} - \alpha^2\big(I_{n_e}-P\big)\big)^{-1}P\Big]_{i,i} = \begin{cases} [P]_{i,i}, & \text{for} \quad [P]_{i,i} = 0, \\ \frac{[P]_{i,i}}{1-z}, & \text{for} \quad [P]_{i,i} = 1, \end{cases} \tag{7.30}$$

such that (7.27) is simplified to:

$$\det\left((1-z)I_{n_\phi} - \frac{1}{4(1-z)}\tilde{D}P\tilde{D}^T\right) = 0, \tag{7.31}$$

which – following the derivation in Section 7.3 – immediately yields the condition:

$$\Delta t < \frac{2}{c\sqrt{\left\|\tilde{D}P\tilde{D}^T\right\|_2}}. \tag{7.32}$$

Condition (7.29) states that α can be chosen arbitrarily close to 1 while still leaving E^* positive definite. Note that the stability criterion (7.32) does not depend

on a splitting factor α in contrast to the ADHIE method for the EM fields (6.10). Moreover, because α can be set arbitrarily close to 1 for the potentials, the splitting error is reduced.

From (7.32), it is straightforward to derive a Courant-like stability criterion. Therefore, an upper bound for the 2-norm is derived:

$$\sqrt{\left\|\tilde{D}P\tilde{D}^T\right\|_2} \leq \sqrt{\|D^\star PD^T\|_\infty}, \tag{7.33a}$$

$$\begin{aligned} &= \max_{i,j,k}\left(\frac{2}{\Delta x_i^\star}\left(\frac{p_{x,i}}{\Delta x_i}+\frac{p_{x,i+1}}{\Delta x_{i+1}}\right)\right. \\ &\qquad + \frac{2}{\Delta y_j^\star}\left(\frac{p_{y,j}}{\Delta y_j}+\frac{p_{y,j+1}}{\Delta y_{j+1}}\right) \\ &\qquad \left. + \frac{2}{\Delta z_k^\star}\left(\frac{p_{z,k}}{\Delta z_k}+\frac{p_{z,k+1}}{\Delta z_{k+1}}\right)\right)^{\frac{1}{2}}. \end{aligned} \tag{7.33b}$$

Consequently, the system is stable for:

$$\Delta t < \frac{1}{c\sqrt{\frac{1}{\widehat{\Delta x}^2}+\frac{1}{\widehat{\Delta y}^2}+\frac{1}{\widehat{\Delta z}^2}}}, \tag{7.34}$$

where

$$\frac{1}{\widehat{\Delta x}^2} = \max_i\left(\frac{1}{2\Delta x_i^\star}\left(\frac{p_{x,i}}{\Delta x_i}+\frac{p_{x,i+1}}{\Delta x_{i+1}}\right)\right), \tag{7.35}$$

and similar for $\widehat{\Delta y}$ and $\widehat{\Delta z}$. With this Courant-like formula, it is evident that the ADHIE scheme can remove spatial steps from the stability criterion.

7.4 Numerical dispersion

The accuracy of the novel ADHIE scheme for the EM potentials $\boldsymbol{A}$ and ϕ is investigated by assessing the numerical dispersion. Because a dispersion analysis requires constant coefficients, the grid is assumed uniform and we introduce the coefficients:

$$p_u = \begin{cases} 0, & \text{for } u\text{-direction implicit} \\ 1, & \text{for } u\text{-direction explicit} \end{cases} \qquad \text{for } u \in \{x,y,z\}. \tag{7.36}$$

The elements of P_u are set equal to p_u, i.e., $\left[P_u\right]_{i,i} = p_u$ for all i. For example, $p_x = 0$, $p_y = 1$, and $p_z = 1$ means that the x-direction is implicit while both

the y- and z-directions are treated explicitly. We also introduce the central finite-difference notations:

$$\delta_t f|^n_{i,j,k} = \frac{f|^{n+\frac{1}{2}}_{i,j,k} - f|^{n-\frac{1}{2}}_{i,j,k}}{\Delta t}, \tag{7.37a}$$

$$\delta_x f|^n_{i,j,k} = \frac{f|^n_{i+\frac{1}{2},j,k} - f|^n_{i-\frac{1}{2},j,k}}{\Delta x}, \tag{7.37b}$$

$$\delta_{xx} f|^n_{i,j,k} = \frac{f|^n_{i+1,j,k} - 2f|^n_{i,j,k} + f|^n_{i-1,j,k}}{\Delta x^2}. \tag{7.37c}$$

As such, we can rewrite the sourceless ADHIE equations (7.10) with full implicitization in an arbitrary direction as:

$$\delta_t A_x|^n_{i+\frac{1}{2},j,k} + \delta_x \phi|^n_{i+\frac{1}{2},j,k} = 0 \tag{7.38a}$$

$$\delta_t A_y|^n_{i,j+\frac{1}{2},k} + \delta_y \phi|^n_{i,j+\frac{1}{2},k} = 0 \tag{7.38b}$$

$$\delta_t A_z|^n_{i,j,k+\frac{1}{2}} + \delta_z \phi|^n_{i,j,k+\frac{1}{2}} = 0 \tag{7.38c}$$

$$\frac{1}{c^2}\prod_u \left(1 + (1-p_u)\Delta\tau^2\delta_{uu}\right)\delta_t \phi|^{n+\frac{1}{2}}_{i,j,k} + \sum_u \delta_u A_u|^{n+\frac{1}{2}}_{i,j,k} = 0. \tag{7.38d}$$

Plane-wave solutions of the form:

$$f|^n_{i,j,k} = f_0 e^{j\left(\omega n\Delta t - k_x i\Delta x - k_y j\Delta y - k_z k\Delta z\right)}, \tag{7.39}$$

are substituted for $A_x|^n_{i+1/2,j,k}$, $A_y|^n_{i,j+1/2,k}$, $A_z|^n_{i,j,k+1/2}$, and $\phi|^{n+1/2}_{i,j,k}$, which immediately yields:

$$\begin{bmatrix} s_t & & & -s_x \\ & s_t & & -s_y \\ & & s_t & -s_z \\ -c^2 s_x & -c^2 s_y & -c^2 s_z & t_x t_y t_z s_t \end{bmatrix} \begin{bmatrix} A_{x0} \\ A_{y0} \\ A_{z0} \\ \phi_0 \end{bmatrix} = \begin{bmatrix} 0 \\ 0 \\ 0 \\ 0 \end{bmatrix}, \tag{7.40}$$

where

$$s_t = \frac{1}{\Delta t}\sin\left(\frac{\omega\Delta t}{2}\right), \tag{7.41a}$$

$$s_u = \frac{1}{\Delta u}\sin\left(\frac{k_u\Delta u}{2}\right), \quad \text{for} \quad u \in \{x, y, z\}, \tag{7.41b}$$

and

$$t_u = 1 + (1-p_u)\Delta\tau^2 s_u^2, \quad \text{for} \quad u \in \{x, y, z\}. \tag{7.41c}$$

By setting the determinant of the system matrix equal to zero, we find the dispersion relation:

$$\frac{1}{c^2}s_t^2 = \frac{s_x^2 + s_y^2 + s_z^2}{t_x t_y t_z}. \tag{7.42}$$

In the limit of $\Delta t, \Delta x, \Delta y, \Delta z \to 0$, and since:

$$\lim_{\Delta u \to 0} \frac{1}{\Delta u} \sin\left(\frac{k_u \Delta u}{2}\right) = \frac{k_u}{2} \quad \text{for} \quad u \in \{x, y, z\}, \tag{7.43}$$

and, similarly,

$$\lim_{\Delta t \to 0} \frac{1}{\Delta t} \sin\left(\frac{\omega \Delta t}{2}\right) = \frac{\omega}{2}, \tag{7.44}$$

the exact dispersion relation:

$$\omega^2 = c^2\left(k_x^2 + k_y^2 + k_z^2\right), \tag{7.45}$$

is retrieved.

The numerical phase error (NPE) introduced by the discretization is expressed as:

$$\text{NPE}(\%) = 100 \left| \frac{\tilde{k} - k_0}{k_0} \right|, \tag{7.46}$$

where $k_0 = \omega/c$ and $\tilde{k}$ is the magnitude of the numerical wave vector calculated by numerically solving (7.42) after conversion to spherical coordinates. The NPE for a plane wave traveling in the first quadrant of the xy-plane, i.e., making an angle ϕ ($0 \leq \phi \leq 90°$) with the x-axis, is shown in Fig. 7.1. We compare the fully explicit method to the fully implicit ADI scheme and to the hybrid implicit-explicit method with implicitization in the y-direction.

In Fig. 7.1(a), we use an equal discretization of $\Delta x = \Delta y = \Delta z = \lambda/50$ (with $\lambda = 2\pi/k_0$) and a time step $\Delta t_{\text{CFL}} = 1/\left(c\sqrt{1/\Delta x^2 + 1/\Delta y^2 + 1/\Delta z^2}\right)$ at the traditional Courant limit. A plane wave traveling in the x-direction ($\tilde{k} = \tilde{k}_x$) looks identical for the explicit scheme and the ADHIE-y scheme. As such, they result in the same error NPE $= 0.044\,\%$. In contrast, a plane wave traveling in the y-direction ($\tilde{k} = \tilde{k}_y$) looks identical for the ADI scheme and the ADHIE-y scheme resulting in NPE $= 0.110\,\%$.

In Fig. 7.1(b), an unequal discretization of $\Delta x = \Delta z = \lambda/20$, and $\Delta y = \lambda/50$ is considered. The explicit scheme uses the Courant limit Δt_{CFL} for the new discretization, while the ADI and ADHIE-y schemes go beyond the Courant limit and use $\Delta t = 1/\left(c\sqrt{1/\Delta x^2 + 1/\Delta z^2}\right) = 2.03\Delta t_{\text{CFL}}$. It is clear that the explicit scheme has again a very small error in the y-direction due to the fine sampling. Still, the error for the ADHIE-y scheme is well within acceptable limits (NPE $\leq 0.48\,\%$). Moreover, the error in the x-direction for the ADHIE-y scheme actually becomes smaller than for the explicit scheme. This is because the larger time step is closer

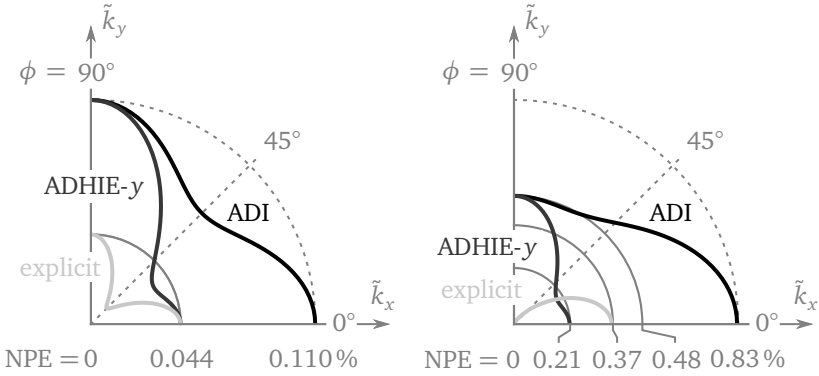

(a) Equal discretization in space and time.

(b) Unequal discretization in space and time.

Figure 7.1: The numerical phase error (NPE) of the ADHIE scheme with only implicitization in the y-direction lies in between the NPE of the fully explicit scheme and of the fully implicit ADI scheme. The NPE for a plane wave traveling in the first quadrant of the xy-plane is calculated in (a) for a discretization of $\Delta x = \Delta y = \Delta z = \lambda/50$ and a time step equal to the Courant limit $\Delta t_{\text{CFL}} = 1/\left(c\sqrt{1/\Delta x^2 + 1/\Delta y^2 + 1/\Delta z^2}\right)$ and in (b) for $\Delta x = \Delta z = \lambda/20$, and $\Delta y = \lambda/50$. The time step for the explicit scheme is chosen at the Courant limit $\Delta t_{\text{CFL}} = 1/\left(c\sqrt{1/\Delta x^2 + 1/\Delta y^2 + 1/\Delta z^2}\right)$ while for the ADHIE-y and ADI schemes, the time steps are chosen well beyond the Courant limit: $\Delta t = 1/\left(c\sqrt{1/\Delta x^2 + 1/\Delta z^2}\right) = 2.03\Delta t_{\text{CFL}}$.

to the 1-D magic time step $\Delta t = \Delta x/c$ which is unstable for the fully explicit scheme. Furthermore, while the ADI scheme supports even larger time steps (beyond the magic time step), these will decrease the accuracy as there are too little temporal samples. In conclusion, the numerical dispersion relation suggests that in multiscale environments the ADHIE method is more efficient than either ADI or the explicit scheme while also having a low numerical error.

7.5 Results

The results discussed in this section were all run on an Intel(R) Xeon(R) Gold 6226 CPU @ 2.70 GHz with 512 GiB of RAM memory. The methods were implemented in C code. All examples were run on a single core and only required a small fraction of the available memory.

7.5.1 Maxwell-Schrödinger system

As a first validation example, we will replicate the results of [10] but with the much more efficient proposed scheme. A hybrid implicit-explicit discretization will

be compared to a fully explicit calculation. The fully explicit calculation is nearly identical to [10]. Note that this example is also treated in [12] and [13].

A quasi 1-D nanotube, placed at $x = y = 0\,\text{nm}$ and oriented along the z-direction, is illuminated by a z-polarized plane wave. The nanotube has an electrostatic confining potential $v(z)$ defined by:

$$v(z) = v_0\left(\frac{z}{z_{\max}}\right)^4, \tag{7.47}$$

where $v_0 = 5 \times 10^3\,\text{eV}$ and $z_{\max} = 1.0\,\text{nm}$. The wave function ψ is discretized on a uniform grid with $\Delta z = 0.01\,\text{nm}$ consisting of $n_z = 100\,\text{cells}$. The nanotube is embedded in a uniform 3-D grid with identical discretization in the z-direction and $n_x = n_y = 20\,\text{cells}$ of $\Delta x = \Delta y = 1\,\text{nm}$ in the x- and y-direction, respectively. An additional 10 layers of PML are added in every direction. The wave function is normalized as:

$$\Delta x \Delta y \int |\psi|^2\,\mathrm{d}z = 1. \tag{7.48}$$

We also assume that the vector potential $\boldsymbol{A}$ and scalar potential ϕ are uniform along the transversal dimensions of the nanotube.

To transform a system in initial state $\psi(t=0)$ to a final state ψ_f, the electric field pulse $E_z^{(\text{in})}(t)$ is generated "on the fly" based on the wave function $\psi(t)$ at that time t. According to [10], this is achieved with the following pulse:

$$E_z^{(\text{in})}(t) = -2\frac{E_0}{m}\,\text{Im}\left(\left\langle\tilde{\psi}'\middle|\hat{W}qz\middle|\tilde{\psi}'\right\rangle\right), \tag{7.49}$$

where

$$\hat{W} = \left|\psi_f\right\rangle\left\langle\psi_f\right|, \quad \tilde{\psi}'(t) = e^{-\jmath\frac{q}{\hbar}A_z(z,t)z}\psi(t), \tag{7.50}$$

and

$$E_0 = \eta\exp\left(-\frac{(t-\tau)\Theta(t-\tau)}{\sigma}\right). \tag{7.51}$$

Here, $\sigma = 3\,\text{fs}$, $\tau = 10\,\text{fs}$ and $\eta = 5 \times 10^9\,\text{V/m}$. This pulse takes the EM fields generated by the moving charge inside the nanotube into account and it is generated by the following z-directed electric current sheet source which is uniform in the yz-plane and placed at $x_s = -2\,\text{nm}$:

$$j_z^s(x_s) = -\frac{2}{\Delta x_i Z_0}E_z^{(\text{in})}. \tag{7.52}$$

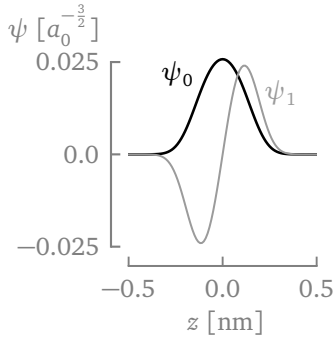

Figure 7.2: The first excited state ψ_1 of the 1-D nanotube is the wanted final state for an initial state $\psi(t=0) = \sqrt{0.9999}\psi_0 + \sqrt{0.0001}\psi_1$, where ψ_0 is the ground state. The wave function is expressed in atomic units.

Table 7.1: Maxwell-Schrödinger simulation parameters and results.

	Explicit	ADHIE-z
Δt	3.335×10^{-5} fs	4.500×10^{-4} fs
$\Delta t / \Delta t_{\text{CFL}}$	1.0	13.5
T_{CPU}	26 649 s	2398 s
speed-up	—	11-fold
RMSE_{Ω_1}	—	2.82×10^{-4}

The initial state is $\psi(t=0) = \sqrt{0.9999}\psi_0 + \sqrt{0.0001}\psi_1$, where ψ_0 is the ground state and ψ_1 is the first exited state. The ground state ψ_0 and the first excited state ψ_1 are determined by numerically calculating the eigenvectors of H_s^{1d}, where H_s^{1d} is the 1-D version of H_s leveraging the sixth-order accurate spatial differences (6.86). The resulting wave functions are shown in Fig. 7.2.

Using this set-up, the goal is to design a laser pulse that transforms the initial state $\psi(t=0)$ to the first excited state ψ_1 and to compare the fully explicit method with the novel ADHIE method. Here, the ADHIE scheme implicitizes the entire z-direction with splitting parameter $\alpha = 0.899$ for the $(\boldsymbol{e},\boldsymbol{h})$ system (7.1), resulting in the ADHIE-z scheme. To quantitatively compare both schemes we calculate the projections onto the ground state and first excited state as a function of time:

$$\Omega_0(t) = |\langle\psi(t)|\psi_0\rangle|^2, \quad \text{and} \quad \Omega_1(t) = |\langle\psi(t)|\psi_1\rangle|^2, \tag{7.53}$$

and compute the root-mean-square error (RMSE) for $\Omega_1(t)$ of the ADHIE-z scheme w.r.t. the explicit scheme during the first 30 fs. The used time steps for both the explicit and ADHIE-z schemes are given in Table 7.1. We also give the total CPU time T_{CPU}, the obtained speed-up and the RMSE. Note that the time step for the

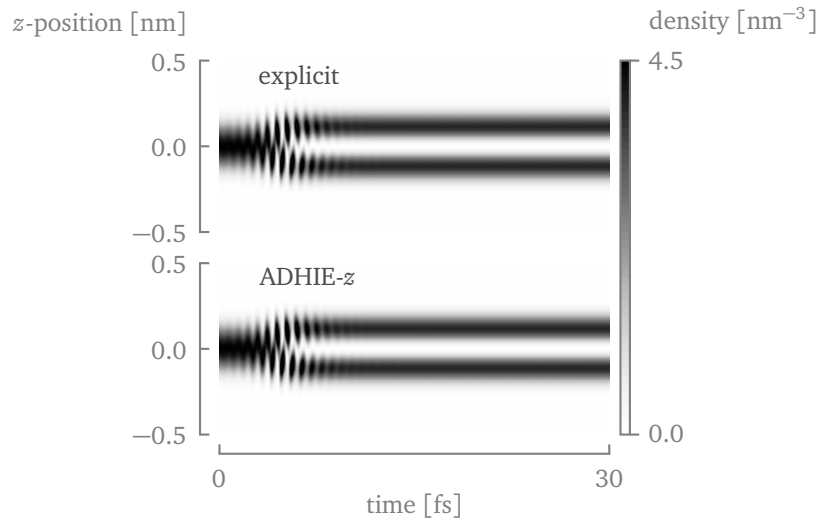

Figure 7.3: The explicit scheme and ADHIE-z schemes exhibit identical behavior for the density $|\psi(t)|^2$ as a function of time. The final density clearly shows that the wave function is in its first excited state ψ_1. The main difference is that the explicit scheme has to use a time step $\Delta t_{\text{exp}} = 3.335 \times 10^{-5}$ fs, while the ADHIE-z scheme can use $\Delta t_{\text{adhie}} = 4.5 \times 10^{-4}$ fs.

ADHIE-z scheme is much closer to the maximum time step for the QM part:

$$\Delta t_{\text{qm}} = 4.650 \times 10^{-4}\,\text{fs}. \tag{7.54}$$

In Table 7.1, it is shown that the ADHIE-z scheme results in an 11-fold increase in efficiency for a time step that is approximately 13.5 times larger. This shows that the ADHIE method does not create much overhead. In Fig. 7.3, the probability density distribution $|\psi(t)|^2$ as a function of time is compared for the explicit scheme and the ADHIE-z scheme. It is clear that the behavior of the ADHIE-z scheme is the same despite the much larger time step. In Fig. 7.4, the projections $\Omega_0(t)$ and $\Omega_1(t)$ are shown for both schemes. It is observed that the projections are identical which is confirmed by the low RMSE_{Ω_1} in Table 7.1. As such, we have demonstrated that the novel ADHIE scheme can be used as a much more efficient alternative to the explicit method to design a laser pulse that transforms the ground state into the first excited state.

7.5.2 Maxwell-Kohn-Sham system

In this section, the novel ADHIE scheme for the potentials is tested for multiple electrons in a quasi 1-D nanowire within the TDDFT framework.

The model for the nanowire was developed in [14–16] and also recently applied in [17]. It is defined as an N electron system subjected to a transverse confining

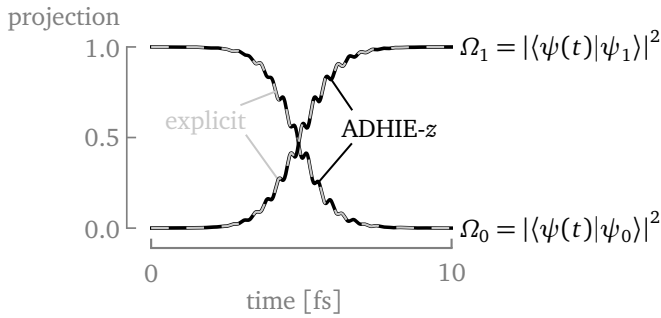

Figure 7.4: The projection of the wave function onto the ground state Ω_0 and onto the first excited state Ω_1 shows that both the explicit scheme and the ADHIE-z scheme can design a laser pulse that transforms the ground state into the first excited state.

harmonic potential $v_{\text{conf}}(x, y)$:

$$v_{\text{conf}}(x, y) = \frac{1}{2} m\omega_{\text{conf}}^2 \left(x^2 + y^2\right). \tag{7.55}$$

Only the first transverse subband is occupied for densities satisfying $r_s > \pi b/4$, where $b^2 = \hbar/(2m\omega_{\text{conf}})$ determines the confinement and $r_s = 1/2\rho_{1d}$ is the 1-D Wigner-Seitz radius [16]. The 1-D density ρ_{1d} is the 3-D density ρ integrated over the transverse plane using the transverse wave function:

$$\chi_{\text{tran}}(x, y) = \frac{1}{2\pi b^2} e^{-\frac{x^2+y^2}{4b^2}}. \tag{7.56}$$

In [14], the resulting 1-D interelectron potential is derived as:

$$v_{\text{int}}(z) = \frac{\sqrt{\pi}}{2} \frac{q^2}{4\pi\epsilon b} \exp\left(\frac{z^2}{4b^2}\right) \text{erfc}\left(\frac{z}{2b}\right), \tag{7.57}$$

where erfc is the complementary error function and ϵ is the background permittivity. The Hartree potential v_H is given by:

$$v_H[\rho_{1d}](z) = \int_{-\infty}^{\infty} v_{\text{int}}\left(\left|z - z'\right|\right) \rho_{1d}(z')\, \mathrm{d}z'. \tag{7.58}$$

The corresponding ALDA parametrization for the exchange correlation potentials was determined in [15]. We follow the implementation from [17], where the exchange energy density is given as:

$$\epsilon_{\text{x}}^{\text{hom}}[n] = -\frac{1}{2} n(z) g(b\pi n), \tag{7.59}$$

Table 7.2: The used values for the expansion coefficients in (7.61).

m	a_m	b_m	c_m
0	1.211 392 168	1.0	0
1	$1.324\,542\,501 \times 10^{-1}$	$1.666\,666\,667 \times 10^{-1}$	−1.288 61
2	$2.760\,196\,114 \times 10^{-2}$	$3.333\,333\,333 \times 10^{-2}$	−0.166 666 67
3	$5.332\,833\,200 \times 10^{-3}$	$5.952\,380\,952 \times 10^{-3}$	0.1
4	$8.927\,499\,490 \times 10^{-4}$	$9.259\,259\,259 \times 10^{-4}$	−0.142 857
5	$1.297\,097\,549 \times 10^{-4}$	$1.262\,626\,263 \times 10^{-4}$	0.333 333 333
6	$1.655\,591\,905 \times 10^{-5}$	$1.526\,251\,526 \times 10^{-5}$	−1.090 909 090 91
7	0	0	4.615 38

with

$$g(z) = \frac{1}{2z^2}\left(-\gamma + \exp\left(z^2\right)\mathrm{Ei}(-z^2) - 2\ln(z) + G^{2,2}_{2,3}\left(z^2 \middle| \begin{matrix} 1, \frac{3}{2} \\ 1, 1, \frac{1}{2} \end{matrix}\right)\right), \tag{7.60}$$

where γ is the Euler-Mascheroni constant and G is the Meijer G-function. Since g is unstable, it is expanded for small and large z:

$$g(z) \approx \begin{cases} \sum_{m=0}^{7} (a_m - b_m \ln(z)) z^{2m} & z \le z_0 \\ \frac{\pi^{3/2}}{2z} - \frac{\ln(z)}{z^2} + \sum_{m=0}^{7} c_m z^{-2m} & z > z_0 \end{cases} \tag{7.61}$$

with $z_0 = 1.68$. The coefficients are given in Table 7.2. The b_m coefficients satisfy:

$$b_m = \frac{1}{m!(2m+1)(m+1)}. \tag{7.62}$$

The exchange potential is thus given by:

$$v_{\mathrm{x}}^{\mathrm{LDA}} = 2\epsilon_{\mathrm{x}}^{\mathrm{hom}} - \frac{n^2}{2}\frac{\partial z}{\partial n}\frac{\partial g(z)}{\partial z} \tag{7.63}$$

$$= 2\epsilon_{\mathrm{x}}^{\mathrm{hom}} + \frac{1}{2b\pi}\begin{cases} \sum_{m=0}^{7} z^{2m+1}(b - 2a_m m + 2b_m m \ln(z)), & z \le z_0 \\ \frac{\pi^{3/2}}{2} - \frac{2\ln(z)-1}{z} + 2\sum_{m=1}^{7} m c_m z^{-2m+1}, & z > z_0 \end{cases} \tag{7.64}$$

In [15], the correlation energy for the interaction potential (7.57) was parameterized for several values of b. The resulting correlation energy is given by:

$$\epsilon_{\mathrm{c}}^{\mathrm{hom}}(r_s) = -\frac{1}{2}\frac{r_s \ln\left(1 + \alpha r_s + \beta r_s^m\right)}{A + B r_s^n + C r_s^2}, \tag{7.65}$$

with correlation potential:

$$v_{\mathrm{c}}^{\mathrm{LDA}}(r_s) = -\frac{1}{2} r_s^2 \frac{\partial}{\partial r_s}\left(\frac{\ln\left(1+\alpha r_s+\beta r_s^m\right)}{A+Br_s^n+Cr_s^2}\right) \tag{7.66}$$

$$= \epsilon_{\mathrm{c}}^{\mathrm{hom}}\left(\frac{2Cr_s^2+nBr_s^n}{A+Cr_s^2+Br_s^n} - \frac{\alpha r_s+m\beta r^m}{(1+\alpha r_s+\beta r^m)\ln\left(1+\alpha r_s+\beta r_s^m\right)}\right). \tag{7.67}$$

The values for the parameters are given in [15].

For the specific example treated here, the electrons are confined in the longitudinal direction as in [16] by:

$$v(z) = \frac{2^{\beta+1}\hbar^2}{mL^{\beta+2}}|z|^\beta, \tag{7.68}$$

where $\beta = 6$. We also set $b = 0.1\,a_B$, $L = 4\,a_B$, $\epsilon = 11\,\epsilon_0$, $m = 0.063\,m_{\mathrm{e}}$, where $a_B = 4\pi\epsilon\hbar^2/mq^2$ is the effective Bohr radius. Moreover, the number of electrons equals $N = 6$, such that there are three doubly occupied Kohn-Sham orbitals. This set-up coincides with one of the examples in [16]. To find the ground state, the imaginary time propagation method is used [18–21]. For this, the wave functions are discretized on a uniform grid consisting of $n_z = 160$ cells with $\Delta z = 0.04\,a_B \approx 0.739\,\mathrm{nm}$ and the sixth-order accurate finite-differences are used as described in Section 6.3.2. The resulting ground state is shown in Fig. 7.5.

The quasi 1-D nanowire is embedded in a 3-D uniform electromagnetic grid consisting of $n_x = n_y = 20$ cells with $\Delta x = \Delta y = 6.55\,\mathrm{nm}$ in the transversal directions and $n_z = 170$ cells with $\Delta z = 0.04\,a_B$ in the longitudinal direction. The grid is terminated by a 15 layers thick PML. With these dimensions, the square cross section of the nanowire has the same surface as a disk with radius $2b$. Since the particle is assumed to be in the transversal ground state, approximately 86 % of the density is contained within this disk. However, we assume, for simplicity, that the density is uniformly distributed within the square with cross section $\Delta x \Delta y$. A possible method to more accurately incorporate the transversal profile is proposed in Section 7.A.2. The nanowire is excited with a z-directed uniform current sheet density in the yz-plane at $x_s = 32.75\,\mathrm{nm}$ with temporal profile:

$$j_z(x_s, t) = j_0 \sin(2\pi f_c(t-t_0))\exp\left(-\frac{t-t_0}{2\sigma^2}\right), \tag{7.69}$$

where $j_0 = 7000\,\mathrm{A\,m^{-1}}$, $f_c = 14.5\times10^{12}\,\mathrm{Hz}$, $\sigma = 45.0\,\mathrm{fs}$ and $t_0 = 200\,\mathrm{fs}$.

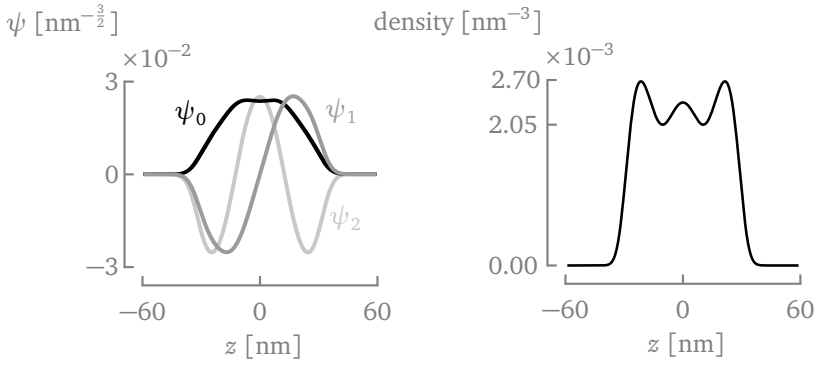

(a) Kohn-Sham orbitals.

(b) Ground state density.

Figure 7.5: The three doubly occupied Kohn-Sham orbitals ψ_0, ψ_1 and ψ_2 in Fig. 7.5(a), are used as the initial states for the multiphysics time-dependent calculation. The corresponding probability density is shown in Fig. 7.5(b).

Since the polarizability of a system is related to the dielectric constant, it is of particular interest in electronic structure calculations. Additionally, the electric field along the nanowire is of interest in photonics where field enhancement is related to plasmons and result in many interesting optical effects [22]. Therefore, we calculate the dipole moment of this nanowire and the local electric field. In particular, the z-directed electric dipole moment $p_z(t) = q\int z\rho(t)\,\mathrm{d}V$ of the nanowire and the z-component of the electric field at the center of the nanowire E_z are calculated using both the fully explicit discretization and the ADHIE method with implicitization in the z-direction. With these, the amplitude of the zz-component of the polarizability tensor α_{zz}:

$$\alpha_{zz}(\omega) = \frac{\tilde{p}_z(\omega)}{\tilde{E}_0(\omega)}, \tag{7.70}$$

and the squared amplitude of the normalized electric field at the center of the nanotube:

$$\mathcal{S} = \left|\frac{\tilde{E}_z(\omega)}{\tilde{E}_0(\omega)}\right|^2 \tag{7.71}$$

are calculated, where $\tilde{p}_z$, $\tilde{E}_z$, and $\tilde{E}_0$ are the Fourier transforms of the z-directed dipole moment p_z, the calculated electric field, and the incident electric field, respectively. The simulation parameters and results are summarized in Table 7.3. The ADHIE-z method support an almost 6 times larger time step for a splitting parameter $\alpha = 0.85$. The achieved speed-up with the ADHIE-z method is a 4.5 fold increase. In Fig. 7.6, the obtained results for α_{zz} and $\mathcal{S}$ are shown. Both for α_{zz} and $\mathcal{S}$, the ADHIE-z method yields very similar results to the much more time-consuming

Table 7.3: Maxwell-Kohn-Sham simulation parameters and results.

	Explicit	ADHIE-z
$\Delta x = \Delta y$	6.55 nm	6.55 nm
Δz	0.739 nm	0.739 nm
Δt	2.43×10^{-3} fs	14.05×10^{-3} fs
$\Delta t / \Delta t_{\mathrm{CFL}}$	1.0	5.77
T_{CPU}	419 805 s	93 920 s
speed-up	—	4.5-fold
$\mathrm{RMSE}_{\alpha_{zz}}$	—	4.352×10^{-18} cm^3
$\mathrm{RMSE}_{\mathcal{S}}$	—	11.53

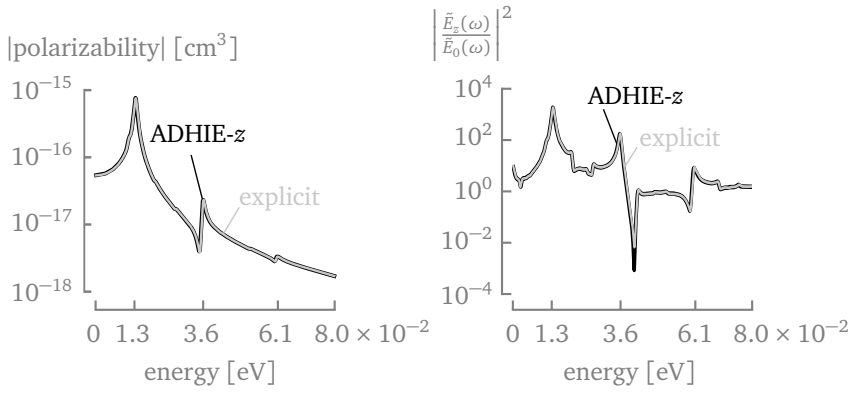

(a) Polarizability.

(b) Electric field spectrum.

Figure 7.6: The absolute value of the polarizability (Fig. 7.6(a)) and the squared normalized spectrum of E_z (Fig. 7.6(b)) show that the ADHIE-z method gives very similar results to the fully explicit method. The polarizability is calculated as in (7.70) and is expressed in cgs units. The electric field at the center of the nanowire was used to calculate the spectrum and was normalized w.r.t. the incident electric field.

fully explicit method, which is confirmed by their RMSEs given in Table 7.3. Consequently, the novel ADHIE method is shown to be very applicable to multiscale geometries in a multiphysics TDDFT context.

7.6 Conclusions

A novel alternating-direction hybrid implicit-explicit (ADHIE) method was developed for the EM potentials which neatly meshes with the existing ADHIE method

for the EM fields. The novel method retains all the flexibility of the original method as it can apply local implicitization in preferred directions on nonuniform grids to relax the time step. Moreover, by leveraging the tridiagonal matrix algorithm, the number of calculations per time step, still scales linear, similar to the fully explicit methods. As such, the method is highly applicable for large problems in multiscale geometries.

The stability of the ADHIE scheme was rigorously derived, resulting in tight upper bounds for the stability. It is noteworthy that the stability of the new ADHIE method for the potentials does not include a splitting parameter that reduces the maximum time step, as was the case for the ADHIE method for the EM fields.

The applicability of the method was tested for the multiphysics simulation of quasi 1-D nanowires. It was shown that the time step can be drastically increased both for Maxwell-Schrödinger systems as for many-particle Maxwell-Kohn-Sham systems while preserving a high accuracy. However, the ADI method upon which the HIE scheme was based – while very efficient – is less accurate than the explicit method. Therefore, possible future work might include the investigation of alternative hybridization techniques. Also, the method is very suited to investigate the interactions between multiple quasi 1-D quantum systems.

7.A Appendices

7.A.1 Stability for $\alpha = 1$

In this appendix, the stability of the ADHIE scheme for the EM potentials (6.37) for $\alpha = 1$ is investigated when preferred directions are entirely implicitized instead of locally. The coefficient p_u determines the implicitization as in (7.36). Therefore, the diagonal implicitization matrices P_u from (5.7) are replaced with these scalar p_u. The singular-value decomposition (SVD) of $\tilde{D}_u$ is defined as:

$$\Delta\tau\tilde{D}_u = U_u \Sigma_u V_u^T, \quad \text{for} \quad u \in \{x, y, z\}, \tag{7.A.1}$$

where Σ_u is a rectangular diagonal matrix containing the singular values $\sigma_{u,i}$. The matrix E' from (7.21) with $\alpha = 1$ is transformed using the orthogonal matrix:

$$S = \begin{bmatrix} V_x \otimes U_y \otimes U_z & & & \\ & U_x \otimes V_y \otimes U_z & & \\ & & U_x \otimes U_y \otimes V_z & \\ & & & U_x \otimes U_y \otimes U_z \end{bmatrix}, \tag{7.A.2}$$

to

$$SE'S^T = \begin{bmatrix} I_{n_{e_x}} & & & \frac{1}{2}\Sigma_1^T \\ & I_{n_{e_y}} & & \frac{1}{2}\Sigma_2^T \\ & & I_{n_{e_z}} & \frac{1}{2}\Sigma_3^T \\ \frac{1}{2}\Sigma_1 & \frac{1}{2}\Sigma_2 & \frac{1}{2}\Sigma_3 & I_\phi + \frac{1}{4}\left(\tilde{\Sigma}_x\tilde{\Sigma}_x^T \oplus \tilde{\Sigma}_y\tilde{\Sigma}_y^T \oplus \tilde{\Sigma}_z\tilde{\Sigma}_z^T\right) \end{bmatrix}, \quad (7.A.3)$$

with

$$\tilde{\Sigma}_u = (1-p_u)\Sigma_u, \quad \text{for} \quad u \in \{x,y,z\}, \quad (7.A.4)$$

and

$$\Sigma_1 = \Sigma_x \otimes I_{m_y} \otimes I_{m_z}, \quad (7.A.5a)$$

$$\Sigma_2 = I_{m_x} \otimes \Sigma_y \otimes I_{m_z}, \quad (7.A.5b)$$

$$\Sigma_3 = I_{m_x} \otimes I_{m_y} \otimes \Sigma_z. \quad (7.A.5c)$$

We similarly define:

$$\tilde{\sigma}_{u,i} = (1-p_u)\sigma_{u,i}, \quad \text{for} \quad u \in \{x,y,z\}. \quad (7.A.6)$$

The matrix $SE'S^T$ from (7.A.3) can be transformed to block diagonal form by using elementary row and column operations, yielding:

$$\text{diag}\left(1,\ldots,1,\begin{bmatrix} 1 & 0 & 0 & \frac{\sigma_{x,i}}{2} \\ 0 & 1 & 0 & \frac{\sigma_{y,j}}{2} \\ 0 & 0 & 1 & \frac{\sigma_{z,k}}{2} \\ \frac{\sigma_{x,i}}{2} & \frac{\sigma_{y,j}}{2} & \frac{\sigma_{z,k}}{2} & 1+\frac{\tilde{\sigma}_{x,i}+\tilde{\sigma}_{y,j}+\tilde{\sigma}_{z,k}}{4} \end{bmatrix},\ldots\right), \quad (7.A.7)$$

where there are $n_e - 3n_\phi$ 1's and n_ϕ square blocks of size 4. Matrix E is positive definite when the eigenvalues λ of these blocks are strictly positive. These eigenvalues are either 1 or:

$$\lambda = \frac{1}{8}t \pm \frac{1}{8}\sqrt{t^2 - 16(4-u)}, \quad (7.A.8)$$

with

$$t = 8 + \tilde{\sigma}_{x,i}^2 + \tilde{\sigma}_{y,j}^2 + \tilde{\sigma}_{z,k}^2, \quad (7.A.9)$$

$$u = p_x\sigma_{x,i}^2 + p_y\sigma_{y,j}^2 + p_z\sigma_{z,k}^2. \quad (7.A.10)$$

The eigenvalues λ from (7.A.8) are strictly positive for:

$$u = p_x\sigma_{x,i}^2 + p_y\sigma_{y,j}^2 + p_z\sigma_{z,k}^2 < 4. \quad (7.A.11)$$

Since this has to be valid for any combination of $\sigma_{x,i}, \sigma_{y,j}, \sigma_{z,k}$, we obtain the stability condition:

$$1 < \frac{2}{\sqrt{p_x\sigma_x^2 + p_y\sigma_y^2 + p_z\sigma_z^2}} \quad (7.A.12)$$

where

$$\sigma_x = \max_i\left(\sigma_{x,i}\right) = \Delta\tau\left\|\tilde{D}_x\right\|_2, \tag{7.A.13a}$$

$$\sigma_y = \max_j\left(\sigma_{y,j}\right) = \Delta\tau\left\|\tilde{D}_y\right\|_2, \tag{7.A.13b}$$

$$\sigma_z = \max_k\left(\sigma_{z,k}\right) = \Delta\tau\left\|\tilde{D}_z\right\|_2. \tag{7.A.13c}$$

As such, we have proven – at least in case where directions are either completely explicitly or implicitly updated – that E' is positive definite as opposed to just positive semi-definite despite $\alpha = 1$.

7.A.2 Taking the transverse profile into account

This section we investigates how the transverse profile of the quasi 1-D nanowire of Section 7.5.2 can be better taken into account. We start from the general 3-D minimally-coupled Schrödinger equation (2.40). We assume that the wave function ψ remains in the transversal eigenstate $\chi(x,y)$ with eigenenergy ϵ_t at all times and that the potential v is separable as $v(x,y,z) = v_t(x,y) + v_l(z)$. The resulting transverse wave function $\chi(x,y)$ is a real valued eigenstate of the static 2-D Schrödinger equation. The wave function is split as:

$$\psi = \chi(x,y)e^{-\jmath\frac{\epsilon_t t}{\hbar}}\varphi(z,t), \tag{7.A.14}$$

resulting in:

$$\begin{aligned}\jmath\hbar e^{-\jmath\frac{\epsilon_t}{\hbar}t}\chi\left(-\jmath\frac{\epsilon_t}{\hbar}+\frac{\partial}{\partial t}\right)\varphi \\ = e^{-\jmath\frac{\epsilon_t}{\hbar}t}\Bigg(\epsilon_t\chi\varphi - \chi\frac{\hbar^2}{2m}\frac{\partial^2}{\partial z^2}\varphi + \jmath\frac{\hbar}{2m}(\boldsymbol{\nabla}\cdot\boldsymbol{A})\chi\varphi \\ + \jmath\frac{\hbar}{m}\boldsymbol{A}\cdot\boldsymbol{\nabla}(\chi\varphi) + \frac{q^2}{2m}\boldsymbol{A}^2\chi\varphi + (q\phi+v_l)\chi\varphi\Bigg),\end{aligned} \tag{7.A.15}$$

where the explicit dependence on the coordinates is removed. The wave function is assumed to be strongly confined, so that it remains in its ground state. Also, it was used that the transverse wave function is an eigenstate of the static 2-D Schrödinger equation without EM coupling. Simplifying (7.A.15) yields:

$$\begin{aligned}\jmath\hbar\chi\frac{\partial\varphi}{\partial t} = -\chi\frac{\hbar^2}{2m}\frac{\partial^2}{\partial z^2}\varphi + \jmath\frac{\hbar}{2m}(\boldsymbol{\nabla}\cdot\boldsymbol{A})\chi\varphi \\ + \jmath\frac{\hbar}{m}\boldsymbol{A}\cdot\boldsymbol{\nabla}(\chi\varphi) + \left(\frac{q^2}{2m}\boldsymbol{A}^2 + q\phi + v_l\right)\chi\varphi.\end{aligned} \tag{7.A.16}$$

This is multiplied by $\chi^* = \chi$ and integrated over the xy-plane, resulting in:

$$\jmath\hbar\frac{\partial\varphi}{\partial t} = -\frac{\hbar^2}{2m}\frac{\partial^2\varphi}{\partial z^2} + \jmath\frac{\hbar}{2m}(c_1+2c_2)\varphi + \jmath\frac{\hbar}{m}c_3\frac{\partial\varphi}{\partial z} + c_4\varphi, \tag{7.A.17}$$

where the following coefficients are introduced:

$$c_1(z,t) = \iint |\chi|^2 \boldsymbol{\nabla}\cdot\boldsymbol{A}\,\mathrm{d}x\,\mathrm{d}y\,, \tag{7.A.18a}$$

$$c_2(z,t) = \iint \chi\left(A_x\frac{\partial\chi}{\partial x} + A_y\frac{\partial\chi}{\partial y}\right)\mathrm{d}x\,\mathrm{d}y\,, \tag{7.A.18b}$$

$$c_3(z,t) = \iint |\chi|^2 A_z\,\mathrm{d}x\,\mathrm{d}y\,, \tag{7.A.18c}$$

$$c_4(z,t) = \iint |\chi|^2\left(\frac{q^2}{2m}\boldsymbol{A}^2 + q\phi + v_l\right)\mathrm{d}x\,\mathrm{d}y\,. \tag{7.A.18d}$$

It was also used that the transverse wave function χ is normalized as:

$$\iint |\chi|^2\,\mathrm{d}x\,\mathrm{d}y = 1. \tag{7.A.19}$$

The coefficients c_1 and c_2 are rewritten as:

$$c_1 = \iint |\chi|^2\left(\frac{\partial A_x}{\partial x} + \frac{\partial A_y}{\partial y} + \frac{\partial A_z}{\partial z}\right)\mathrm{d}x\,\mathrm{d}y\,, \tag{7.A.20}$$

$$c_2 = -\iint \left(\frac{\partial}{\partial x}(\chi A_x)\chi + \frac{\partial}{\partial y}(\chi A_y)\chi\right)\mathrm{d}x\,\mathrm{d}y \tag{7.A.21}$$

$$= -\iint \left(|\chi|^2\left(\frac{\partial A_x}{\partial x} + \frac{\partial A_y}{\partial y}\right) + \chi\left(A_x\frac{\partial\chi}{\partial x} + A_y\frac{\partial\chi}{\partial y}\right)\right)\mathrm{d}x\,\mathrm{d}y \tag{7.A.22}$$

$$= -c_2 - \iint \left(\frac{\partial}{\partial x}(A_x)|\chi|^2 + \frac{\partial}{\partial y}(A_y)|\chi|^2\right)\mathrm{d}x\,\mathrm{d}y\,, \tag{7.A.23}$$

such that c_2 is given by:

$$c_2 = -\frac{1}{2}\iint |\chi|^2\left(\frac{\partial A_x}{\partial x} + \frac{\partial A_y}{\partial y}\right)\mathrm{d}x\,\mathrm{d}y\,. \tag{7.A.24}$$

Consequently, the terms $\jmath\hbar c_1\varphi + 2\jmath\hbar c_2\varphi$ are combined as:

$$\jmath\frac{\hbar}{2m}(c_1 + 2c_2)\varphi = \jmath\frac{\hbar}{2m}\frac{\partial}{\partial z}\left(\iint |\chi|^2 A_z\,\mathrm{d}x\,\mathrm{d}y\right)\varphi. \tag{7.A.25}$$

The resulting Schrödinger equation is hence:

$$\begin{aligned}\jmath\hbar\frac{\partial\varphi}{\partial t} = -\frac{\hbar^2}{2m}\frac{\partial^2\varphi}{\partial z^2} + \jmath\frac{\hbar}{2m}\frac{\partial\widetilde{A}_z}{\partial z}\varphi + \jmath\frac{\hbar}{m}\widetilde{A}_z\frac{\partial\varphi}{\partial z} \\ + \left(\frac{q^2}{2m}\widetilde{(\boldsymbol{A}^2)} + q\widetilde{\phi} + \widetilde{v_l}\right)\varphi,\end{aligned} \tag{7.A.26}$$

where the $\widetilde{\cdots}$ stands for the weighted average with the transverse density. Under the assumption that the fields are uniform over the extent of the nanowire, the following 1-D Schrödinger equation is obtained:

$$\jmath\hbar\frac{\partial\varphi}{\partial t} = \frac{1}{2m}\left(-\jmath\hbar\frac{\partial}{\partial z} - qA_z\right)^2\varphi\left(\frac{q^2}{2m} + \left(A_x^2 + A_y^2\right) + q\phi + v_l\right)\varphi, \qquad (7.A.27)$$

where the potentials are only evaluated at the position of the nanotube and depend on z and t.

Similarly, the probability current density is weighted over a single cell:

$$J_{p,z}|_{i,j,k+\frac{1}{2}} = J^{1d}_{p,z}|_{i,j,k+\frac{1}{2}} \int_{x_{i-\frac{1}{2}}}^{x_{i+\frac{1}{2}}} \int_{y_{j-\frac{1}{2}}}^{y_{j+\frac{1}{2}}} |\chi(x,y)|^2 \,\mathrm{d}x\,\mathrm{d}y\,, \qquad (7.A.28)$$

where $J^{1d}_{p,x}$ is the 1-D probability current density and $x_{i+\frac{1}{2}} = (x_{i+1} + x_i)/2$.

References

1. Namiki, T. A new FDTD algorithm based on alternating-direction implicit method. *IEEE Transactions on Microwave Theory and techniques* **47,** 2003–2007 (1999).
2. Sun, C. & Trueman, C. Unconditionally stable Crank-Nicolson scheme for solving two-dimensional Maxwell's equations. *Electronics Letters* **39,** 595–597 (2003).
3. Tierens, W. & De Zutter, D. An unconditionally stable time-domain discretization on cartesian meshes for the simulation of nonuniform magnetized cold plasma. *Journal of Computational Physics* **231,** 5144–5156 (2012).
4. Chen, J. & Wang, J. A 3D hybrid implicit-explicit FDTD scheme with weakly conditional stability. *Microwave and Optical Technology Letters* **48,** 2291–2294 (2006).
5. Zhang, Q., Zhou, B. & Wang, J. A novel hybrid implicit–explicit FDTD algorithm with more relaxed stability condition. *IEEE Antennas and Wireless Propagation Letters* **12,** 1372–1375 (2013).
6. Van Londersele, A., De Zutter, D. & Vande Ginste, D. An in-depth stability analysis of nonuniform FDTD combined with novel local implicitization techniques. *Journal of Computational Physics* **342,** 177–193 (2017).
7. Van Londersele, A., De Zutter, D. & Vande Ginste, D. A new hybrid implicit–explicit FDTD method for local subgridding in multiscale 2-D TE scattering problems. *IEEE Transactions on Antennas and Propagation* **64,** 3509–3520 (2016).
8. Van Londersele, A., De Zutter, D. & Vande Ginste, D. Full-wave analysis of the Shielding Effectiveness of Thin Graphene Sheets with the 3D Unidirectionally Collocated HIE-FDTD Method. *International Journal of Antennas and Propagation* **2017,** 1–8 (2017).
9. Van Londersele, A., De Zutter, D. & Vande Ginste, D. A Collocated 3-D HIE-FDTD Scheme With PML. *IEEE Microwave and Wireless Components Letters* **27,** 609–611 (2017).
10. Takeuchi, T., Ohnuki, S. & Sako, T. Maxwell-Schrödinger hybrid simulation for optically controlling quantum states: A scheme for designing control pulses. *Physical Review A* **91,** 033401 (2015).
11. Süli, E. & Mayers, D. F. *An Introduction to Numerical Analysis* (Cambridge University Press, 2008).
12. Xie, G. *et al.* Universal vector–scalar potential framework for inhomogeneous electromagnetic system and its application in semiclassical quantum electromagnetics. *IEEE Transactions on Plasma Science* **49,** 3459–3471 (2021).
13. Xiang, C., Kong, F., Li, K. & Liu, M. A quantum state controller based on the electromagnetic potentials. *IEEE Access* **7,** 42006–42013 (2019).

14. Friesen, W. & Bergersen, B. Dielectric response of a one-dimensional electron gas. *Journal of Physics C: Solid State Physics* **13,** 6627 (1980).

15. Casula, M., Sorella, S. & Senatore, G. Ground state properties of the one-dimensional Coulomb gas using the lattice regularized diffusion Monte Carlo method. *Physical Review B* **74,** 245427 (2006).

16. Abedinpour, S. H., Polini, M., Xianlong, G. & Tosi, M. Density-functional theory of inhomogeneous electron systems in thin quantum wires. *The European Physical Journal B* **56,** 127–134 (2007).

17. Grossi, J., Musslimani, Z. H., Seidl, M. & Gori-Giorgi, P. Kohn–Sham equations with functionals from the strictly-correlated regime: investigation with a spectral renormalization method. *Journal of Physics: Condensed Matter* **32,** 475602 (2020).

18. Lehtovaara, L., Toivanen, J. & Eloranta, J. Solution of time-independent Schrödinger equation by the imaginary time propagation method. *Journal of Computational Physics* **221,** 148–157 (2007).

19. Sudiarta, I. W. & Geldart, D. W. Solving the Schrödinger equation using the finite difference time domain method. *Journal of Physics A: Mathematical and Theoretical* **40,** 1885 (2007).

20. Moxley III, F. I., Byrnes, T., Fujiwara, F. & Dai, W. A generalized finite-difference time-domain quantum method for the N-body interacting Hamiltonian. *Computer Physics Communications* **183,** 2434–2440 (2012).

21. Flamant, C., Kolesov, G., Manousakis, E. & Kaxiras, E. Imaginary-time time-dependent density functional theory and its application for robust convergence of electronic states. *Journal of Chemical Theory and Computation* **15,** 6036–6045 (2019).

22. Fafin, A., Camelio, S., Pailloux, F. & Babonneau, D. Surface plasmon resonances and local field enhancement in aluminum nanoparticles embedded in silicon nitride. *The Journal of Physical Chemistry C* **123,** 13908–13917 (2019).

CHAPTER 8

CONCLUSIONS

"But it be the strangeness you see that pulls you to the next horizon."

— ROBERT JORDAN, The Eye of the World (1990)

8.1 Conclusions

The miniaturization of electronic devices and incorporation of novel low-dimensional materials is complicated by the appearance of possibly unexpected quantum mechanical effects. Hence, new modeling tools have to be developed that can describe such effects, either to sidestep them or to exploit them. Therefore, we proposed in this dissertation several advancements for the finite-difference time-domain (FDTD) method focused on quantum mechanical (QM) systems and also on QM problems coupled to an electromagnetic (EM) system. The required physical backbone was presented in Chapter 2. Further, in Chapter 3, we presented the very basics of the FDTD method and introduced quintessential concepts such as stability, convergence, and dispersion.

In Chapters 4 and 5, we presented two novel methods to solve the time-dependent Schrödinger equation on nonuniform grids. While the Yee algorithm is one of the most popular (time-dependent) methods for EM problems by virtue of the second-order accurate staggered grid resulting in fast explicit time integration, no such favoritism is seen for the Schrödinger and Kohn-Sham equations and many variations are used [1–7]. In Chapter 4, based on [1], we presented a collocated explicit (CE) method that applies nonuniform grids and higher-order spatial discretizations to increase the accuracy and efficiency. From the numerical dispersion relation, it was seen that small spatial steps or higher-order accurate differences are needed to obtain accurate results. Besides providing a rigorous stability criterion, we also amended the stability criterion of [8], which was too restrictive.

The proposed spatial discretization is not limited to a specific time-integration method and can be applied to others as well. We also showed that the method is, in fact, equivalent to the FDTD method with staggered real and imaginary parts of the wave function, originally proposed in [2]. This leapfrog method however,

Table 8.1: A comparison of the allowed time steps for the time-dependent Schrödinger equation.

Method	$\Delta t_{\max}$
CE (Ch. 4)	$\frac{\hbar}{\rho(H)}$
leapfrog (Ch. 4)	$\frac{2\hbar}{\rho(H)}$
CN [10]	—
ADI (Ch. 5)	$\frac{2\hbar}{\max_i(\lvert[V]_{i,i}\rvert)}$
ADHIE (Ch. 5)	$\frac{2\hbar}{\left\lVert\tilde{U}_x\oplus\tilde{U}_y\oplus\tilde{U}_z+V\right\rVert_2}$

only requires half the memory and number of operations.

Next, in Chapter 5, we started from the leapfrog method to address one of its flaws, i.e., the allowed time step on nonuniform grids is often overly restrictive. Inspired by [9], our novel scheme applies local implicit updates based on a novel alternating-direction implicit (ADI) method to the leapfrog explicit scheme. The so-called alternating-direction hybrid implicit-explicit (ADHIE) scheme applies implicitization in one part of the grid and solves the remainder explicitly. It compensates for its more expensive implicit updates – only applied to a small portion of the grid – by increasing the allowed time step significantly. Unique to the ADI method that we developed here, is that it is not unconditionally stable but it is limited by the potential. This is no real hindrance because the time step should be smaller than the stability dictates to obtain a high enough accuracy. Instead, it has the distinct advantage that the implicit part of the calculation remains unchanged throughout the simulation even when time-dependent excitations are used.

A comparison of the allowed time steps for the different schemes we used in this first part is given in Table 8.1. The Hamiltonian matrix H is given by:

$$H = T_x \oplus T_y \oplus T_z + V. \tag{8.1}$$

The kinetic energy matrices T_x, T_y, and T_z contain discretizations of the Laplacian and V is the potential matrix. The matrices $\tilde{U}_x$, $\tilde{U}_y$, and $\tilde{U}_z$ are the symmetrized kinetic energy matrices (for lower-order discretizations) but with small spatial steps removed to increase the time step. Removing no cells results in the leapfrog scheme and removing all cells yields the ADI scheme.

In Chapters 6 and 7, we coupled the Schrödinger equation with Maxwell's equations. Furthermore, we extended the scope to include many-particle systems using the time-dependent Kohn-Sham equations. In Chapter 6, we again started from the leapfrog scheme for the QM part and applied higher-order spatial discretizations on the minimally-coupled Schrödinger equation on uniform grids. We also

proposed a lower-order accurate discretization on nonuniform grids. This spatial discretization was validated by comparing with a straightforward generalization of the CE method presented in Chapter 4 and the implicit Crank-Nicolson method. The leapfrog scheme is particularly useful when the vector potential is expected to be small.

The electromagnetic part was tackled using the regular Yee algorithm and extended to compute the EM potentials for three different gauge conditions: the Coulomb, Gibbs, and Lorenz gauges. With widely varying efficiencies and methods come wildly varying results. For a Maxwell-Schrödinger system, we obtained similar results between the Coulomb gauge and Lorenz gauge but produced instabilities in the Gibbs gauge. The Coulomb gauge, however, was much less efficient than the Lorenz gauge because it needs to solve the Poisson equation twice every iteration. For a Maxwell-Kohn-Sham system the Gibbs gauge again yields nonphysical results, while the Coulomb gauge yields results similar to the Lorenz gauge. However, the total energy in the Coulomb gauge also starts to deviate after many time iterations. It is expected that a continuous build-up of small errors related to the instantaneous nature of the Coulomb potential eventually results in nonphysical behavior. As such, the gauge invariance of the proposed methods still has to be investigated further.

Chapter 7 endeavors to overcome the overly restrictive time step of the Yee algorithm encountered in Chapter 6 for multiscale and multiphysics simulations. To achieve this, we employed the ADHIE method for the EM fields described in [9] and developed a similar method for the EM potentials. Unlike the original leapfrog scheme, the new method is a multistep scheme. Nevertheless, the method similarly succeeds in applying local implicitization in different directions while still resulting in tridiagonal linear systems whose computational complexity scales linearly with the size of the implicitized dimension. Interestingly, the stability condition of the new scheme is not limited by a splitting parameter α compared to the ADHIE method for the EM fields and thus increases accuracy and efficiency. Tests on quasi 1-D Maxwell-Schrödinger and Maxwell-Kohn-Sham systems showed that the new ADHIE method indeed increases the efficiency of multiphysics problems in multiscale environments.

We again provide an overview of the allowed time steps $\Delta t_{\max}$ of the presented methods for the minimally-coupled Schrödinger equation and for the EM potentials in Table 8.2. The Hamiltonian matrix is defined as $H = H_0 + \jmath H_1$ where:

$$H_0 = T_x \oplus T_y \oplus T_z + V + q\Phi + \frac{q^2}{2m}A^2, \tag{8.2}$$

and H_1 contains a discretization of the $2\boldsymbol{A}\cdot\boldsymbol{\nabla} + (\boldsymbol{\nabla}\cdot\boldsymbol{A})$ term. The $\tilde{D}\tilde{D}^T$ corresponds to the symmetrized Laplacian and $\tilde{D}P\tilde{D}^T$ is also this Laplacian, but with small cells removed.

Table 8.2: A comparison of the allowed time steps of hybrid EM/QM-FDTD methods for the minimally-coupled Schrödinger equation and the EM potentials.

Method	$\Delta t_{\max}$
CE (Ch. 6)	$\frac{\hbar}{\rho(H_0+\jmath H_1)}$
leapfrog (Ch. 6)	$\frac{2\hbar}{\rho(H_0)}$
CN (Ch. 6)	—
$\text{Yee}_{\text{Coulomb}}$ (Ch. 6)	unknown
$\text{Yee}_{\text{Gibbs}}$ (Ch. 6)	$\frac{2\sqrt{\epsilon_{\min}\mu_{\min}}}{\sqrt{\left\|\tilde{D}\tilde{D}^T\right\|_2}}$
$\text{Yee}_{\text{Lorenz}}$ (Ch. 6)	$\frac{2}{c\sqrt{\left\|\tilde{D}\tilde{D}^T\right\|_2}}$
$\text{ADHIE}_{\text{Lorenz}}$ (Ch. 7)	$\frac{2}{c\sqrt{\tilde{D}P\tilde{D}^T}}$

8.2 Future work

Many novel methods and ideas were proposed in this dissertation. However, there are more than equally many ideas that still warrant further investigation. Therefore, we propose a non-exhaustive list in no particular order of possible research avenues.

Alternative discretization schemes

In Chapter 4, we stated that the derivation of the stability condition could be repeated for other spatial discretizations. Therefore, an interesting approach might be to apply higher-order compact schemes for the discretization of the Laplacian term in the Hamiltonian. These schemes can achieve higher-order accuracy in higher dimensions by leveraging a cube-like stencil instead of the star-shaped stencils developed in this work. However, these will lose the attractive property that the discretized kinetic energy operator can be expressed as a Kronecker sum of their 1-D counterparts. Alternatively, a finite-element discretization on Cartesian grids can also lead to higher accuracies.

Higher-order accurate discretization of the minimally-coupled Schrödinger equation on nonuniform grids

The spatial discretization of the minimally-coupled Hamiltonian for arbitrary vector potentials was performed in Chapter 6 on a nonuniform grid only with a 2-point stencil for the vector potential and a 3-point stencil for the wave function. A systematic extension to larger stencils would greatly increase its accuracy and the increased flexibility of nonuniform grids would increase the efficiency similar to Chapter 4.

Kohn-Sham nanotubes with finite transverse radius

In Section 7.5.2, we embedded the Kohn-Sham nanotube in a single cell of the EM grid. However, as explained in Section 7.A.2, the transverse profile is known and could be properly averaged. Furthermore, by also introducing the nanowire as a 3-D object, a full comparison can be made to assess the validity of the quasi 1-D model.

Also in Section 7.5.2, we assumed that the background medium of the wire with permittivity ϵ is infinitely extended. In practice, however, nanowires are embedded in different materials. To go beyond this approximation the theory has to be modified. First, the static interelectron interaction should be determined for electrons in wires with finite cross sections. Next, the exchange energy for a wire with given confinement potential should be determined and the correlation energy parameterized. These tools would enable the calculation of the properties of more realistic nanowires.

Generalized Lorenz gauge condition

In semiconductors, we consider a (possibly inhomogeneous) background medium with $\epsilon_r > 1$. Therefore, it is more natural to incorporate this material also in the gauge condition by leveraging, e.g., a generalized Lorenz gauge [11–13]:

$$\epsilon^{-1}\boldsymbol{\nabla}\cdot(\epsilon\boldsymbol{A}) = -\mu\epsilon\frac{\partial\phi}{\partial t}. \tag{8.3}$$

In homogeneous media with $\epsilon_r > 1$, it is easy to see that the resulting numerical scheme supports a larger time step. However, the influence on the accuracy should be thoroughly investigated.

Multi time stepping

The allowed time step for the Yee algorithm limits the efficiency for Maxwell-Schrödinger and Maxwell-Kohn-Sham systems. This causes the QM part to be heavily over-sampled in time. To overcome this, it is possible to introduce different time steps for the EM and QM parts. While this will increase the efficiency significantly, ensuring the self-consistency of the coupled schemes might prove problematic.

Stability of the ADHIE method for the EM potentials

For the ADHIE method for the potentials, it was proven that $\alpha = 1$ yields a stable scheme if an entire direction is implicitized. However, when only local implicitization is applied, we only proved that α can be arbitrarily close to 1. It remains to be proven (or disproven) that $\alpha = 1$ is also allowed.

References

1. Askar, A. & Cakmak, A. S. Explicit integration method for the time-dependent Schrödinger equation for collision problems. *The Journal of Chemical Physics* **68,** 2794–2798 (1978).
2. Visscher, P. A fast explicit algorithm for the time-dependent Schrödinger equation. *Computers in Physics* **5,** 596–598 (1991).
3. Sullivan, D. M. & Citrin, D. Determination of the eigenfunctions of arbitrary nanostructures using time domain simulation. *Journal of Applied Physics* **91,** 3219–3226 (2002).
4. Castro, A., Marques, M. A. & Rubio, A. Propagators for the time-dependent Kohn–Sham equations. *The Journal of Chemical Physics* **121,** 3425–3433 (2004).
5. Moxley III, F. I., Zhu, F. & Dai, W. A Generalized FDTD Method with Absorbing Boundary Condition for Solving a Time-Dependent Linear Schrödinger Equation. *American Journal of Computational Mathematics* **2,** 163–172 (2012).
6. Bigaouette, N., Ackad, E. & Ramunno, L. Nonlinear grid mapping applied to an FDTD-based, multi-center 3D Schrödinger equation solver. *Computer Physics Communications* **183,** 38–45 (2012).
7. Gomez Pueyo, A., Marques, M. A., Rubio, A. & Castro, A. Propagators for the time-dependent Kohn–Sham equations: Multistep, Runge–Kutta, exponential Runge–Kutta, and commutator free Magnus methods. *Journal of Chemical Theory and Computation* **14,** 3040–3052 (2018).
8. Dai, W., Li, G., Nassar, R. & Su, S. On the stability of the FDTD method for solving a time-dependent Schrödinger equation. *Numerical Methods for Partial Differential Equations: An International Journal* **21,** 1140–1154 (2005).
9. Van Londersele, A., De Zutter, D. & Vande Ginste, D. An in-depth stability analysis of nonuniform FDTD combined with novel local implicitization techniques. *Journal of Computational Physics* **342,** 177–193 (2017).
10. Goldberg, A., Schey, H. M. & Schwartz, J. L. Computer-generated motion pictures of one-dimensional quantum-mechanical transmission and reflection phenomena. *American Journal of Physics* **35,** 177–186 (1967).
11. Chew, W. C. Vector potential electromagnetics with generalized gauge for inhomogeneous media: Formulation. *Progress In Electromagnetics Research* **149,** 69–84 (2014).
12. Ryu, C. J., Liu, A. Y., Wei, E. & Chew, W. C. Finite-difference time-domain simulation of the Maxwell–Schrödinger system. *IEEE Journal on Multiscale and Multiphysics Computational Techniques* **1,** 40–47 (2016).
13. Xie, G. *et al.* Universal vector–scalar potential framework for inhomogeneous electromagnetic system and its application in semiclassical quantum electromagnetics. *IEEE Transactions on Plasma Science* **49,** 3459–3471 (2021).